A NUMERICAL STUDY OF PULSE-COMBUSTOR JET IMPINGEMENT HEAT TRANSFER

A Dissertation
Presented to
The Academic Faculty

by

Wichit Liewkongsataporn

In Partial Fulfillment
of the Requirements for the Degree
Doctor of Philosophy in the
George W. Woodruff School of Mechanical Engineering

Georgia Institute of Technology
May 2008

A NUMERICAL STUDY OF PULSE-COMBUSTOR JET IMPINGEMENT HEAT TRANSFER

Approved by:

Dr. Tim Patterson, Co-Advisor
School of Mechanical Engineering

Dr. Fred Ahrens, Co-Advisor
School of Mechanical Engineering

Dr. Cyrus Aidun
School of Mechanical Engineering

Dr. Jeff Empie
School of Chemical and Biomolecular Engineering

Dr. Jim Frederick
School of Chemical and Biomolecular Engineering

Date Approved: March 12, 2008

To My Parents

ACKNOWLEDGEMENTS

I would like to give many thanks to my co-advisors, Drs. Fred Ahrens and Tim Patterson, for their guidance, support, and patience throughout the long process of my graduate study. Dr. Ahrens' attention to detail is amazing. His fundamental questions have kept me learning while Dr. Patterson's clear perspective of the research and the project has given me a very good idea of the big picture and kept me moving forward. I would like to thank the committee members, Drs. Cyrus Aidun, Jeff Empie, and Jim Frederick, for their comments and suggestions with the proposal and the dissertation. I also wish to thank Jim Loughran for his help in the laboratory during the early phase of the research. I am grateful to the Institute of Paper Science and Technology (IPST) for financial support since the beginning of my study. Finally, I would like to express my appreciation to the IT staff of IPST, especially Charles Andry, for the help with both hardware and software for the research.

TABLE OF CONTENTS

LIST OF TABLES

LIST OF FIGURES

LIST OF SYMBOLS

Letter Symbols

A	cross-sectional area, m^2
B	slot nozzle width, m
D	tailpipe diameter, m
E	specific total energy, J/kg
H	nozzle-to-surface spacing, m
L	tailpipe length, m
Pr	Prandtl number
R	gas constant, J/kg.K
Re	Reynolds number, $\rho u_m S/\mu_j$
S	hydraulic diameter of nozzle, D or $2B$, m
St	Strouhal number, fS/u_m
T	temperature, K
a,b	coefficients of a linear function of enthalpy ($h = aT+b$)
c	speed of sound, m/s
c_p	constant pressure specific heat, J/kg.K
c_v	constant volume specific heat, J/kg.K
f	oscillation frequency, 1/s
g	relative opening area
h	specific enthalpy, J/kg
k	thermal conductivity, W/m.K
$\dot{m}$	mass flow rate, kg/s
p	absolute pressure, N/m^2
q''	heat flux, W/m^2
$\dot{q}$	heat source, W
r	radial distance, m

t	time, s
u	x-velocity or axial velocity, m/s
v	y-velocity or radial velocity, m/s
x	distance in x-axis, m
y	distance in y-axis, m

Greek Symbols

α	energy ratio of heat source, $\dot{q}_{CA}/\dot{q}_{Cm}$
β	volume ratio of Helmholtz pulse combustor, V_C/V_T
γ	specific heat ratio, c_p/c_v
ε	velocity ratio of velocity oscillation, u_A/u_m
ϕ	equivalence ratio of fuel and air
λ	acoustic wavelength, m
μ	viscosity, N.s/m^2
ρ	density, kg/m^3
τ	normalized cycle time, cycle time/cycle period
$\overset{=}{\tau}$	stress tensor
ω	radian frequency, 1/s

Subscripts

A	oscillation amplitude
C	of combustion chamber
T	of tailpipe
a	atmospheric pressure or ambient temperature
j	of jet at tailpipe exit, or
	for jet temperature, maximum value in an oscillation cycle
m	space- and time-averaged
s	of impingement surface

1	at combustion chamber inlet
2	at tailpipe inlet or combustion chamber exit
3	at tailpipe exit

Symbols Specific for Turbulence Models

k	turbulence kinetic energy
ε	dissipation rate of turbulence kinetic energy
ω	specific dissipation rate of turbulence kinetic energy, k/ε
v^2	normal velocity fluctuation
f	elliptic relaxation function

SUMMARY

A pulsating jet generated by a pulse combustor has been experimentally demonstrated as a technique for impingement heat transfer enhancement relative to a steady jet. The enhancement factor was as high as 2.5. Despite such potential, further studies of this technique have been limited, let alone industrial applications. The ultimate goal of the Pulsed Air Drying project at the Institute of Paper Science and Technology is to develop this technique to commercialization for industrial applications such as paper drying. The main objective of the research in this dissertation is to provide a fundamental basis for the development of the technology. Using CFD simulations, the research studied the characteristics of pulsating single-slot-nozzle jet impingement flows and heat transfer on stationary and moving surfaces. In addition, in order to understand basic flow characteristics of pulse-combustor jets, a simplified model of Helmholtz pulse combustors was developed. The model was used to recommend a strategy to generate a pulsating jet having large amplitude of velocity oscillation. And based on this model, pulsating jets in the simulations were characterized as those at the tailpipe exit of a pulse combustor. The impingement conditions were similar to those in conventional impingement hoods for paper drying. Parameter studies included the effects of jet velocity oscillation amplitude, pulsation frequency, mean jet velocity, tailpipe width, and impingement surface velocity. Simulation results showed that the amplitude of jet velocity oscillation was the most important parameter for heat transfer enhancement, in which two mechanisms were identified: high impinging jet velocity during the positive cycle and strong re-circulating flows in the impingement zone during the negative cycle of jet velocity oscillation. As for the improvement by the pulsating jets relative to steady jets, the maximum heat transfer enhancement and energy saving factors were 1.8 and 3.0, respectively, which were very encouraging for further development of the technology.

CHAPTER 1

INTRODUCTION

Research work in this dissertation is a part of a project called Pulsed Air Drying (PAD) at the Institute of Paper Science and Technology (IPST), a multidisciplinary research center specializing in forest products at the Georgia Institute of Technology, Atlanta, Georgia. The ultimate goal of the PAD project is to develop a pulsating jet impingement drying technique for industrial applications, especially paper manufacturing processes. As an early phase of this project, the research presented here is focused on the fundamental characteristics of flow and heat transfer of pulsating single-slot-nozzle jet impingement on a flat surface.

1.1 Pulsed Air Drying Project

The PAD project was initiated by Procter & Gamble Company (P&G) for drying improvement in the tissue manufacturing process. Later, in 2002, P&G donated this technology to IPST for further development. In essence, the PAD technology is an impingement drying technique utilizing pulsating jets generated by pulse combustion. The assumption is that pulsating jets can significantly increase drying rate as compared to the steady jets used in conventional impingement drying techniques. One of the most comprehensive investigations of pulse combustion impingement technology was documented in a series of publications by a combustion research group at Sandia National Laboratories (Eibeck et al., 1993). The work experimentally demonstrated a stagnation point heat transfer enhancement factor as high as 2.5.

In the paper industry, impingement drying has commonly been used in coating and tissue drying (Yankee dryer) processes. A Yankee dryer consists of a large-diameter steam cylinder partially surrounded by an impingement hood. The drying process employed in most paper products uses a series of steam cylinders, which is a 200-year-old technology. Typically, an impingement hood has a higher drying rate than steam cylinders: 50-120 vs. 15-35 kg of water/h.m^2 (Kuhasalo et al., 2000). With the increased emphasis on high speed in modern paper machines, impingement drying has received increased attention for applications on non-tissue grades. An impingement drying hood could be installed between steam cylinders, e.g., Vertical OptiDry by Metso (Johansson, 2005), or combined with a steam cylinder similar to a Yankee dryer, e.g., Papridry™ by Paprican (Pikulik et al., 2006). Key benefits from impingement drying combined with or replacing steam-cylinder drying are increased drying capacity, hence, machine speed and production capacity or reduced size of the overall drying section for the same drying capacity.

As for energy efficiency, the energy consumption rates from both conventional drying techniques are not much different (Sundqvist and Kiiskinen, 2000). The theoretical value of the energy required for water evaporation in a paper machine is approximately 3 GJ per ton of paper produced (solids content from 40% to 95%). The overall energy consumption rate of a steam-cylinder drying system is a typically 4 GJ per ton of paper produced (Hill, 1983 and Kuhasalo et al., 2000). The significance of energy efficiency in drying systems can be appreciated by considering data from the Manufacturing Energy Consumption Survey 2002 by the Department of Energy. According to the survey, the pulp and paper industry is the third highest in energy consumption, approximately 10% of total energy consumption by all industries surveyed. Papermaking comprises about 85% of energy consumed by the pulp and paper manufacturing processes combined. Drying systems consume about 60% of total energy used by overall papermaking processes, according to the energy distribution in Pulp and Paper Industry Energy Bandwidth Study by Kinstrey & White (2006). Therefore, the contribution of the PAD technology, if successfully developed, is the combination of a higher drying rate compared to conventional steam-cylinder drying systems and higher energy efficiency due to heat transfer enhancement compared to conventional impingement drying systems.

The Pulsed Air Drying concept is based on pulse combustion technology, which has been successfully applied in residential heating and industrial drying systems (Zinn, 1996 and Kudra and Mujumdar, 2002). Those applications benefit from pulsating flows within the tailpipe or a chamber connected to the tailpipe. As for jet impingement configurations, pulse-combustor jets have never been reported for commercial applications despite the Sandia demonstration that a pulsating jet has the potential for a high heat transfer enhancement factor. Although the concept is simple, i.e., replacing steady jets with pulsating jets in a conventional impingement hood, the implementation for practical applications is more complicated than that for other types of pulse combustion drying. A number of factors must be considered, including the generation of pulsating jets with large oscillation amplitude by an array of nozzles, the control of jet temperature suitable for drying materials, and the re-circulation system of exhaust gas. However, as an early phase of the PAD project, the present work aims toward the creation of optimum conditions of impingement geometry for maximum heat transfer.

1.2 Scope and Objective of Research

The research in the PAD project can be divided into three parts: the design of pulse combustors with multiple nozzles or tailpipes, the optimization of impingement geometry, and the transport phenomena in the moving web. The design of pulse combustors to generate multiple pulsating jets is probably most challenging because, as will be shown later, the oscillation amplitude of the pulsating jets has to be large enough to cause flow reversal in order to provide high heat transfer. An early design of pulse combustors with an array of nozzles could not generate pulsating jets with flow reversal (Patterson et al., 2003). As discussed later, the characteristics of pulse combustion and resulting pulsating flows are largely affected by the geometry and dimensions of the pulse combustor. The optimization of impingement geometry is typically based on the characteristics of pulsating impingement flows. The parameters of impingement geometry, i.e., type of nozzles, diameter or width of nozzles, and relative opening area could be different than those of a conventional steady-jet impingement hood. Finally, the study of transport phenomena of fluids inside the wet web subjected to pulsating jet impingement is necessary to fundamentally evaluate the effects of unsteady high-intensity surface heat transfer on paper qualities. Results from the web response study could provide the limitations of pulsating jets characteristics, e.g., maximum jet temperature and velocity, for achieving a high drying rate but not degrading paper qualities.

The research in this dissertation is a numerical study, focusing on fundamental characteristics of pulsating jet flow and heat transfer in the impingement zone. The numerical study is preferable to laboratory experiments in this phase because, as discussed in the following chapter, it is more difficult to independently vary each parameter of a pulsating jet generated by a laboratory pulse combustor. In addition, laboratory measurements of unsteady high-temperature flows are difficult and expensive. A goal of the numerical study is to find an optimum condition of impingement geometry for maximum heat transfer from multiple pulsating jets so that a maximum heat transfer enhancement factor can be achieved compared to the optimum condition of steady jet impingement typically used in impingement drying hoods. However, as the fundamental characteristics of this type of flow are not clearly understood, it is useful to start from single jet impingement flows. Hence, the scope of the research is limited to single jet impingement with confinement. The type of tailpipes or nozzles is also limited to the two-dimensional slot type so that computational domains for numerical simulations remain two-dimensional when a moving surface is used.

The main purpose of the study with single nozzles is to provide fundamental insights for further investigation with multiple-nozzle geometry. Therefore, an objective of the dissertation is to identify the mechanisms responsible for heat transfer enhancement. The other main objective is to delineate the effects of the parameters of both pulsating jet and impingement geometry on surface heat transfer. In general, the parameters of single-nozzle impingement condition include nozzle type (circular or slot), nozzle diameter or width, nozzle-to-surface spacing, confinement condition, impingement angle, and surface speed. Typical parameters of a pulsating jet include the mean value and amplitude of velocity oscillation, oscillation frequency, and jet temperature. The parameters for the numerical study in this dissertation are the amplitude of velocity oscillation, mean velocity, frequency, nozzle width, and surface velocity. The nozzle-to-surface spacing is kept constant for all cases because, in practice, such distance is the minimum distance allowed for the operation of an impingement drying hood. Only a confined impingement condition is considered, as unconfined impingement would be impractical for industrial applications.

1.3 Dissertation Outline

Chapter 2 provides a background for the numerical study of impingement heat transfer from a pulsating jet generated by a pulse combustor. Since the number of studies, either experimental or numerical, directly related to the present work are very limited, the literature review focuses on several areas separately. These areas include experimental and numerical studies of steady jet impingement heat transfer, studies of various types of pulsating jets for impingement heat transfer, and basic characteristics of pulse combustors. The literature review also includes simplified models of Helmholtz pulse combustors as a background for the development of the model in Chapter 4. Chapter 3 reviews and discusses results of preliminary laboratory experiments and numerical simulations, which led to a numerical approach for the simulations in this dissertation. Chapter 4 develops a simplified model of Helmholtz pulse combustors, used to study the effects of various parameters on velocity oscillation at the tailpipe exit. The model is further simplified and adapted to calculate inlet boundary conditions for the simulations in following chapters.

Chapter 5 discusses the numerical approach and describes the numerical procedure for the simulations. The numerical approach and procedure are then validated with surface heat flux data measured in an experiment with a laboratory pulse combustor of the PAD project. Chapter 6 explains the design of numerical experiments and the ranges of parameters. Simulation results of the base case are presented in this chapter. The discussion includes basic characteristics of pulsating impingement flows and the effects of the amplitude of velocity oscillation as well as the mechanisms responsible for heat transfer enhancement. Chapter 7 discusses simulation results of the parameter study, i.e., effects of pulsation frequency, mean jet velocity, and tailpipe width. In addition, from simulation results of various tailpipe widths, two optimum conditions for multiple-nozzle geometry are identified, based on certain simplifying assumptions. The criteria for these conditions are maximum heat transfer enhancement at the same mean energy input rate and maximum energy saving at the same heat transfer level. Chapter 8 presents simulation results for an impingement condition with a moving surface and discusses the effects of surface velocity on impingement heat transfer. Conclusions and recommendations for future work are included in Chapters 9 and 10, respectively.

1.4 Summary of Significant Findings

The key characteristic for producing high heat transfer enhancement in pulsating flows is a strong re-circulating flow in the impingement zone close to the stagnation point during the negative cycle of the jet oscillation. From the literature review, coherent vortex structures in other types or conditions of pulsating jet impingement flows did not develop into strong re-circulating flows, but rather small vortex rings moving along the impingement surface and merging with a larger bubble or weak re-circulating flow located farther away from the stagnation point. It was found that the size of re-circulating flows is governed by the maximum velocity of the jet oscillation from the fluid at the centerline of the tailpipe exit. In other words, the size of the re-circulating flow is relatively the same for different nozzle widths or different mean velocities as long as maximum velocity and frequency are the same. As for the effects of frequency, the re-circulating flows are smaller for a higher frequency due to shorter cycle period. For a moving surface, high heat transfer enhancement can still be achieved as long as the velocity amplitude of the jet oscillation is high enough to generate strong re-circulating flows.

Using practical values of pulsating jet velocity ratio and frequency ($\varepsilon = 4.4$ and $f = 160$ Hz), the enhancement factor from the optimum condition for maximum heat transfer was found to be approximately 1.8. This number is based on area-averaged heat fluxes and compared to the optimum condition of steady jet impingement (within the range studied). For the same level of area-averaged heat fluxes, the maximum energy saving factor is approximately 3.0. Although these numbers are based on simplifying assumptions that allow applying results from a single-jet to multiple-jet impingement, these preliminary results are encouraging for the possible significant improvement of drying processes.

CHAPTER 2

BACKGROUND

The literature on impingement heat transfer from a pulsating jet generated by a pulse combustor is very limited. Thus, in order to provide a background for the numerical study in this dissertation, this chapter briefly reviews selected publications relevant to jet impingement heat transfer and pulse combustors separately. The subjects are divided into five groups. The first section discusses the basic characteristics of steady jet impingement heat transfer. The next section reviews the performance of turbulence models for predicting jet impingement heat transfer. The third section reviews impingement heat transfer from various types of pulsating jets. The following section gives an overview of flow characteristics in pulse combustors. The final section reviews some of the simplified models of pulse combustors.

2.1 Steady Jet Impingement Heat Transfer

A large number of reports have been published for both experimental and numerical studies of steady jet impingement flow and heat transfer for a wide range of applications and parameters. The main interest for this research is impingement drying applications, i.e., hot air or gas jet impingement with confinement. Although practical applications involve a moving surface and an array of nozzles, basic flow and heat transfer characteristics of single jet impingement onto a stationary surface is reviewed as an important background for more complex flows. Extensive reviews of impingement heat transfer have been reported on numerous occasions, for example, Martin (1977), Polat et al. (1989), Polat (1993), Viskanta (1993), and Garimella (2000). Steady jet impingement flows and heat transfer are affected by several parameters, e.g., Reynolds number, Prandtl number, velocity profile, turbulence level, nozzle type and configuration, impingement geometry, confinement, entrainment, and coherent structures. The basic characteristics of jet impingement flows are shown in Figure 2.1.

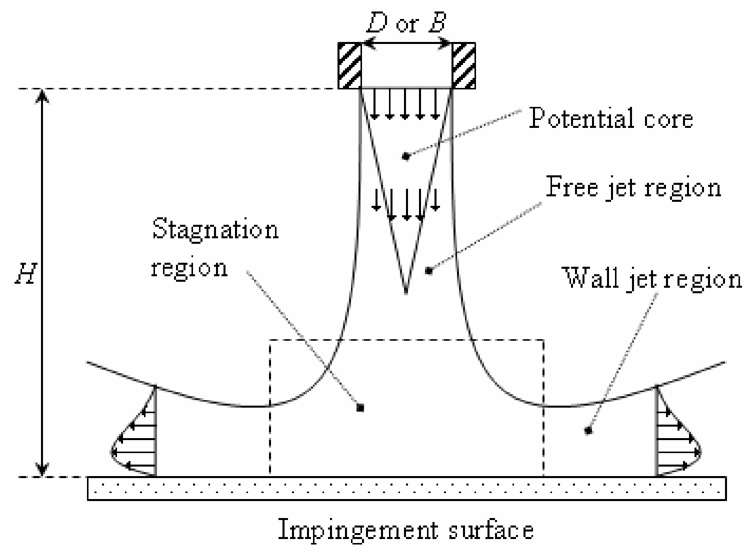

Figure 2.1: Basic characteristics of jet impingement flow.

A single jet impingement flow on a stationary surface is divided into three regions: free jet region, stagnation region, and wall jet region. The free jet region could also be divided into two or three more regions depending on the spacing between the nozzle and the impingement surface: potential core, developing flow, and developed flow. The potential core is the region where the jet velocity is still equal to the velocity at nozzle exit. The maximum width of the potential core is equal to the nozzle width or diameter and decreases along the jet length as the mixing layer between the jet and the ambient fluid grows. The length of the potential core largely depends on flow characteristics at the nozzle exit, i.e., velocity profile, turbulence level, and temperature level. Typically, the potential core length is about 5-8 times the diameter of the nozzle. Jet turbulence intensity remains relatively low within the potential core and increases and reaches a maximum in the developing or transition flow region. The nozzle-to-surface spacing for maximum heat transfer at the stagnation point coincides with the axial distance where the jet turbulence intensity is peak (Kataoka et al., 1987a, Lee et al., 2004).

The stagnation region is where the jet velocity decelerates due to the presence of the surface, and then deflects and accelerates along the surface due to the favorable pressure gradient. Theoretically, the thickness of boundary layers on the impingement surface remains constant in this region. At the end of the stagnation region or the beginning of the wall jet region where the pressure gradient becomes zero, the jet velocity decelerates again and the boundary layers grow. The turbulence intensity dramatically increases in the wall region because of the mixing of free stream fluids. For confined impingement geometry, if the confinement plate is long enough, the wall jet layer reaches the confinement plate resulting in re-circulating bubbles between the impinging jet and the outflow (Polat et al., 1989). The center of the re-circulating bubble moves away from the impinging jet as the Reynolds number or the nozzle-to-surface spacing increases (Garimella, 2000).

The profile of local heat transfer on the surface from single jet impingement is typically a bell shape, i.e., maximum at the stagnation point, then monotonically decreasing along the surface. Secondary peaks in local heat transfer profiles can occur with small nozzle-to-surface spacing. It is generally accepted that the secondary peaks occur when the laminar flow in the stagnation region begins transition to turbulence (Viskanta, 1993). However, there is an argument that coherent vortex rings, caused by the Kelvin-Helmholtz instability in shear layers between the jet and surrounding fluids, are also responsible for secondary peaks by periodically impinging onto the surface. Such argument is supported by visualization and heat transfer measurement from Popiel and Trass (1991), Meola et al. (1996), and Angioletti et al. (2003). Narayanan et al. (2004) measured heat transfer, pressure, and velocity variance on an impingement surface at two nozzle-to-surface distances, H/S = 0.5 and 3.5, i.e., within the potential core and transition regions of a slot jet, respectively. The variation of pressure on the surface also supported the idea of vortices impinging on the surface causing the secondary peak in local heat transfer profile for the case with H/S = 0.5. Nevertheless, the authors stated that further studies were still required for the verification of this hypothesis.

Kataoka et al. (1987b) showed a visualization of a water free jet with coherent vortex rings and large-scale eddies. The vortex rings were well organized within the length of the jet potential core (4.5*D*). Beyond such axial distance, the vortex rings broke down to less-coherent large-scale eddies which reached and passed over the centerline of the jet then decayed further downstream. It was found that stagnation point heat transfer was maximum at $H/D = 6$, coinciding with the axial distance where the large-scale eddies had the highest turbulence intensity and the highest passing frequency. In other words, the increase in heat transfer was not only caused by high turbulence level but also caused by the sweeping behavior of the large-scale eddies, i.e., repeatedly removing boundary layers, which were basically a resistance to surface heat transfer. The latter behavior was referred to as a surface renewal effect. The importance of large-scale eddies was also shown by Hwang et al. (2001), in which the structures of coherent vortices and large-scale eddies were modified by controlling secondary flows around the main impinging jet and by acoustic excitation. When the secondary flows were in the same direction (blowing) as the main jet, the breakdown of vortex rings to large-scale eddies was delayed to further downstream. On the other hand, the breakdown occurred earlier (upstream) if the secondary flows were in the opposite direction (suction). The effects of acoustic excitation were more complex, i.e., the axial distance where vortex rings broke down had a nonlinear relationship with the excitation frequency. However, results showed that the nozzle-to-surface spacing where stagnation point heat transfer was maximum coincided with the axial distance where vortex rings broke down for each respective jet condition.

In practice, area-averaged heat transfer is more important than local profiles for industrial applications such as paper drying, in which impingement hoods employ arrays of nozzles. Generally, area-averaged heat transfer from arrays of nozzles is higher than that from single nozzles due to the increase in turbulence level resulting from interactions between adjacent wall jets (Can, 2003). Impingement heat transfer using air jets with arrays of slot or round nozzles has been studied by several groups, for example, Chance

(1974), Wedel (1979), Polat and Douglas (1990), Saad et al. (1992), Can et al. (2002), and Can (2003). These studies included the effects of nozzle type, impingement geometry, jet temperature, crossflow, throughflow, and surface motion. Basically, the objectives of such studies were to derive a correlation and find an optimum condition for maximum heat transfer or energy efficiency. According to Polat (1993), the well-known correlations by Martin (1977) are generally applicable to the conditions of impingement hoods for the prediction of area-averaged heat transfer. The Martin correlations were derived from a large collection of data on impingement heat and mass transfer. Nevertheless, most data were based on controlled conditions of laboratory experiments, e.g., stationary surface and small difference between jet and surface temperatures. These factors could be different in practical applications and could affect impingement heat transfer or predictions from the correlations. In order to account for these factors, correction factors are usually incorporated into the correlations of heat transfer. The decrease in heat transfer could be as high as 10% due to water evaporation (Sundqvist and Kiiskinen, 2000). Increasing jet temperature typically results in an increase in surface heat flux. However, in terms of heat transfer coefficient in which net heat flux is divided by temperature difference, experimental data showed that measured heat transfer coefficients were lower than those predicted by Martin correlation when jet temperatures were in the range of drying impingement hoods, 100-700°C (Heikkilä and Milosavljevic, 2002). The difference between measured and predicted heat transfer coefficients increased with increasing jet temperature. The difference was close to 0% at the jet temperature of 100°C and up to nearly 20% with the jet temperature of 500-700°C (Heikkilä and Milosavljevic, 2002 and 2003). The effects of crossflow are presumably accounted for in the Martin correlations for arrays of nozzles because the results are area-averaged heat transfer. Typically, crossflow interference from neighboring jets disrupted impinging jets and decreased heat transfer (Chance, 1974; Huang et al., 1984). On the other hand, overall heat transfer increased if gas was partially allowed to flow through a permeable surface. The enhancement of heat transfer linearly depended on the amount of throughflow gas (Polat and Douglas, 1990; Polat et al., 1991a and 1991b). Such effect plays an important role for one important tissue drying process, so-called through-air drying.

The effects of surface velocity on impingement heat transfer have been studied for both single nozzles and arrays of nozzles, mostly slot type. A key parameter is the surface-to-jet velocity ratio (surface velocity/jet velocity) or M_{vs}. Polat and Douglas (1990) studied the effects of surface motion (and throughflow) using three slot nozzles with exhaust exits in between nozzles (no crossflow effects). The nozzle width was 10 mm and the nozzle-to-nozzle spacing and the nozzle-to-surface spacing were 50 mm. The ranges of jet velocity and surface-to-jet velocity ratio were 14-44 m/s and 0.019-0.38, respectively. Within this range, the effect of surface motion in terms of the correction factor for area-averaged heat transfer was $(1+M_{vs})^{-0.69}$. That is, the decrease in heat transfer could be up to 17% for $M_{vs} = 0.3$ compared to the case with a stationary surface. Polat et al. (1991b) studied the effects of surface motion with single slot jet impingement with confinement. The nozzle width and the nozzle-to-surface spacing were 20 and 50 mm, respectively, and $M_{vs} = 0.03\text{-}0.35$. Results for area-averaged heat transfer were not much different from those with three nozzles, i.e., the correction factor was $(1+M_{vs})^{-0.89}$. As for the effects on local heat transfer profile, the moving surface only affected the upstream or approaching side of the impinging jets. The magnitude of heat transfer decreased with increasing surface velocity. In addition, the location of a secondary peak was closer to the nozzle centerline with increasing surface velocity. On the other side where the surface was moving away from the impinging jet, the magnitude of heat transfer decreased only slightly but the location of the secondary peak moved farther away from the nozzle centerline with increasing surface velocity. The magnitude of surface heat transfer in the area close to the nozzle centerline was least affected by surface motion.

2.2 Turbulence Models for Jet Impingement Heat Transfer

For fundamental studies, numerical simulations using computational fluid dynamics (CFD) techniques could offer details of flow fields too difficult or expensive to measure in laboratory experiments. For engineering applications, CFD simulations could be used as a tool for the design or optimization of a process or equipment or for solving a particular problem. Numerical simulation techniques are assessed by the accuracy of solutions and the computational performance, e.g., convergence rate, stability, and the requirement of computational power resource (processors and memory capacity). The accuracy of numerical simulations mainly depends on the physical validity of the governing equations. For laminar flows of Newtonian fluids, the conservation equations of mass (and species), momentum, and energy are adequate to predict accurate solutions. However, most flows in practical applications are turbulent. The three conservation equations are technically adequate but the length scale of grid cells has to be extremely small to capture turbulence characteristics which are unsteady, three-dimensional, and somewhat chaotic. This technique, so-called direct numerical simulation (DNS), would require a great deal of computational power resources, which makes this technique impractical for most cases. A less computationally burdensome technique for simulating turbulent flows is large eddy simulation (LES), which models small scales of turbulence and physically simulates larger scales. Yet, the LES models are still not practical enough for flows in industrial applications. The solutions from the simulations with DNS and LES models are considered accurate and often used as a benchmark or validation for other turbulence models.

In order that simulations of turbulent flows are practical and useful, certain simplifying assumptions are required to represent turbulence characteristics with just a few variables. A widely-used assumption is Reynolds averaging. The resulting governing equations are so-called Reynolds-averaged Navier-Stokes (RANS) equations. Extra terms in standard Navier-Stokes or momentum equations are Reynolds stresses, which represent components of turbulence velocity fluctuations. Turbulence models which solve for these terms are called Reynolds stress models (RSM). A further simplifying assumption is the Boussinesq hypothesis, used in most turbulence models. With this hypothesis, assuming isotropic eddy viscosity, Reynolds stress terms are reduced to one scalar parameter, i.e., eddy or turbulent viscosity, analogous to the viscosity of fluids. Turbulence models are used to calculate the turbulent viscosity, which is regarded as a flow field property and can have different values over the flow field.

The turbulence model which is most commonly used for practical purposes is the standard k-ε model, where k is the turbulent kinetic energy and ε is its dissipation rate. It is called a two-equation model due to the need for two additional differential equations, for the k and ε parameters. This model is applicable for simple external and internal flows where near-wall characteristics are not of interest. Other versions of the k-ε model also exist, for example, RNG k-ε model and realizable k-ε model. The predictions from these models are supposedly better than the standard model for more complex flows. For applications which require accurate near-wall characteristics such as surface heat transfer, a wall function or a modification to the model is needed. A wall function may use different parameters as a bridge to the gap between the walls and bulk flows. A modification of the standard model, a so-called low-Re version, provides a smooth transition of parameters from bulk flows down to the walls.

Another group of two-equation turbulence models is k-ω models where ω is the specific dissipation rate of turbulence kinetic energy. Two versions of k-ω models are commonly used and available in commercial software: Wilcox's standard k-ω (Wilcox, 1994) and Menter's shear stress transport (SST) k-ω (Menter, 1994). The standard or original k-ω model has been known to be sensitive to boundary conditions but performs much better for boundary layer flows than k-ε models. The SST k-ω model is a hybrid model employing the advantages of k-ε models and the standard k-ω model. For more accurate solutions of wall-bounded flows, low-Re or transitional versions are also required to resolve the viscous sublayer at the walls.

A relatively new turbulence model, the so-called v^2-f or V2F model, has emerged as a good candidate for jet impingement flows and other complex flows. The V2F model, developed by Durbin (1991 and 1995), is a four-equation model consisting of the two conventional k and ε parameters plus two more parameters: wall normal velocity fluctuation (v^2) and elliptic relaxation function (f). Basically, the V2F model is a low-Re version of the k-ε models. The additional parameters are based on more realistic physical assumptions than other versions of low-Re k-ε models. Thus, the predictions from this model are presumably better than those from the two-equation models. Behnia et al. (1998 and 1999) demonstrated the performance of the V2F model for unconfined and confined single round jet impingement heat transfer. The original V2F model has been known to be difficult to converge due to numerical instability and thus requires more advanced numerical techniques. Several "code-friendly" versions were developed to enhance the numerical stability (Lien and Kalitzin, 2001 and Laurence et al., 2004). The V2F model available in FLUENT software (Fluent, 2003) is the version used in Lien and Kalitzin (2001).

Jet impingement flows and heat transfer are often used to test the performance of various turbulence models due to rather complex flow characteristics but simple geometry for computational domains. In essence, there are no universal turbulence models that can accurately predict impingement heat transfer for wide ranges of flows and impingement conditions. The main reason is that the isotropic assumption of three-dimensional turbulence eddies employed by most turbulence models are not very accurate physically. Another possible reason is that parameters of those models have been calibrated with certain flow types, which may not be applied as well as other types or ranges of flows. Note that the Reynolds numbers referred in this section follow the original publications, which were usually based on the diameter (*D*) of round nozzles or the width (*B*) of slot nozzles, not the hydraulic diameter (*S*) of slot nozzles. The other key parameter for jet impingement geometry is *H/D* or *H/B*, where *H* is the nozzle-to-surface spacing. Craft et al. (1993) tested four turbulence models, a low-Re k-ε model and three versions of RSM models, with four conditions of unconfined single round jet impingement heat transfer. The best model was a RSM model, in which solutions were in agreement with two conditions of experimental results (*Re* = 23000 and *H/D* = 2 & 6). For the cases with *Re* = 70000 and *H/D* = 2 & 6, results from the RSM model were not quite as accurate as those for the other two cases but were still much better than from other models. The predictions from the low-Re k-ε model were poor for all cases.

Shi et al. (2002) used the FLUENT software to test two turbulence models, standard k-ε and RSM, to simulate two conditions of confined slot jet impingement heat transfer, *B* = 6.2 and 14.1 mm with *H* = 37 mm and *Re* ~ 11000. Results showed that both models performed quite well for the case with *B* = 6.2 mm or larger *H/B*. For the case with *B* = 14.1 mm, predictions from both models were poor, i.e., overpredicting heat transfer at and near the stagnation point. At this condition, the standard k-ε model failed to predict a secondary peak whereas the RSM model was able to predict the secondary peak but at a different location compared to experimental data. Wang and Mujumdar (2005) also used the FLUENT software to test five versions of low-Re k-ε models with similar experimental data. Results were similar to Shi et al. (2002), i.e., all five models performed well for the case with *H/B* = 6 but overpredicted heat transfer for the case with *H/B* = 2.6.

Coussirat et al. (2005a) tested three k-ε models, the V2F model, and the Spalart-Allmaras model, which is a one-equation turbulence model, using the FLUENT software, with several conditions of single slot and round jets. Simulation results varied from case to case. The performance of all models was slightly better for the round jets than for the slot jets. The authors concluded that there was no best overall model. However, the authors also noted that the V2F model performed well for predicting flow velocities for most cases and predicted acceptable results for the cases with a lower Reynolds number (*Re* = 23000 vs. 70000 for round jets). The V2F model was able to capture secondary peaks for round jets but not for the cases with slot jets whereas other models failed to capture secondary peaks for any cases. Coussirat et al. (2005b) continued to test the turbulence models, including the standard k-ω model, with two and three slot nozzles. Local heat transfer profiles and area-averaged heat transfer from all models except for the k-ω model were acceptable with experimental data for both two and three nozzles. The k-ω model strongly overpredicted heat transfer especially in the area near the stagnation point. The V2F model predicted excellent results near the stagnation point but overpredicted heat transfer at the area where two jets met.

For three-dimensional computational domains, Yan and Saravanan (2004) simulated a pair of unconfined round jets using the RNG k-ε and the V2F models in the FLUENT software. The Reynolds number of the jets was 23000. The nozzle-to-surface spacing ratio, *H/D*, was 2, 4, 6, and 10. The nozzle-to-nozzle spacing was 1.75*D*, 3.5*D*, 5.25D, and 7*D*. Simulation results showed that the V2F model was in excellent agreement with experimental data for most studied cases and much better than the RNG model. Ibrahim and Kochuparambil (2005) simulated single and multiple round jets using the FLUENT software and three turbulence models: standard k-ε, standard k-ω, and V2F. For the single jet, the Reynolds number was 23000 and *H/D* = 2, 4, 6, 10, and 14. For multiple jets, two sets of jet arrangements were simulated: one row of seven jets with Re = 3000-20000 and *H/D* = 2 and three rows of seven jets each with *Re* = 1000 and *H/D* = 5. Simulation results showed that the V2F model gave the best overall performance although not very accurate in terms of local heat transfer profiles for the single jet and one row of multiple jets. The k-ω model was better than the k-ε model which always overpredicted heat transfer. As for the case with three rows of multiple jets, all three models performed reasonably well except for the magnitude of stagnation point heat transfer for each jet or local maximum heat transfer. In addition, the V2F model failed to predict a significant decrease in local maximum heat transfer due to crossflow effects whereas the other two models could qualitatively capture such a characteristic.

Zuckerman and Lior (2005) reviewed the performance of several turbulence models for impingement heat transfer. The authors recommended two most suitable models, V2F and SST k-ω, respectively, in terms of accuracy and the requirement of moderate computational power. However, for some reason, the k-ω models, especially the SST model, have not been used or tested as widely as other turbulence models in available literature for jet impingement heat transfer, despite the potential of better performance and the availability in commercial software. Based on the Zuckerman and Lior recommendation and available simulation results from the V2F model and other models, the V2F model is chosen for the numerical simulations in this dissertation. The V2F model also performed reasonably well for steady and unsteady internal flows (Iaccarino, 2001; Lien and Kalitzin, 2001: Scotti and Piomelli, 2002; and Cokljat et al., 2003), which is important because the computational domains in this dissertation include tailpipes and inlet chambers for pulsating flows.

It is noteworthy that, in general, the numerical simulations of "steady" jets with RANS-based turbulence models could not capture unsteady behaviors, i.e., vortex rings induced by shear layer instability, evidenced in laboratory experiments. This is probably one of the reasons that predictions were not accurate for the cases with small nozzle-to-surface spacing. In order to simulate such flow behaviors, more sophisticated and physically accurate models such as LES or DNS would be required as shown, for example, by Chung and Luo (2002), which used a DNS technique to simulate six conditions of confined single slot jet impingement with Re = 300, 500, and 100 and H/B = 4 and 10. The coherent vortex structure caused oscillations of impingement heat transfer, although not perfectly periodic ones. And the magnitude of oscillation amplitude increased with increasing Reynolds number. Although such behaviors are more physically accurate, these techniques are not yet practical for fluid flows in the range of industrial applications, with current computational technology and resources.

2.3 Pulsating Jet Impingement Heat Transfer

Although there have been few publications concerning pulse-combustor jet impingement heat transfer, other types of pulsating jet impingement heat transfer have been relatively well studied. However, most of those pulsating jets had small amplitudes of velocity oscillation or relatively low frequencies. In some cases, pulsating jets were just intermittent, not continuously oscillating. Literature review in this section focuses on the studies of pulse-combustor jet impingement heat transfer by Sandia National Laboratories. Then, heat transfer with other types of pulsating jets will be briefly reviewed for background purposes.

The experiments on pulsating jet impingement heat transfer at Sandia National Laboratories (Keller et al., 1993 and Eibeck et al., 1993) were limited to only one operating condition of the pulsating jet. The pulse combustor had a round tailpipe with length L = 880 mm and diameter D = 50 mm. The volume ratio of the combustion chamber to the tailpipe was approximately 1.0. The operating conditions were as follows: mean mass flow rate, $\dot{m}_m$ = 9 g/s; pulsation frequency, f = 100 Hz; pressure amplitude in the combustion chamber, p_A = 10 kPa; and maximum jet temperature at the tailpipe exit, T_j = 1400 K. With these parameters and the calculation described in Chapter 4, the jet velocity oscillation at the tailpipe exit was: mean velocity, u_m = 20 m/s and velocity amplitude, u_A = 94 m/s (jet velocity ratio, $u_A/u_m = \varepsilon$ = 4.7). The magnitude of the velocity oscillation calculated in the reference was lower, i.e., u_m = 9 m/s and u_A = 60 m/s because the authors simply assumed incompressible plug flow and used time-averaged jet temperature for the calculation. Such assumptions are not entirely satisfied for pulse-combustor flows, especially for the calculation of mean velocity, as discussed in the following chapter.

The key characteristic of the pulsating jet at the tailpipe exit was the presence of coherent toroidal vortices around the free jet, resulting in a large amount of ambient air entrainment and a rapid decrease in jet temperature along the axial distance from the tailpipe exit. The primary vortex was created during the positive cycle of jet velocity oscillation and continued to propagate downstream even during the negative cycle or flow reversal. The flows at the tailpipe exit during flow reversal showed the characteristic of a sink flow, i.e., fluids around the tailpipe exit entered the tailpipe from every direction instead of straight flow like exiting jet flow during the positive cycle. A secondary, smaller vortex was created at the end of the positive cycle. This vortex appeared not to be moving downstream due to the counter effects of the sink flow. A third, weak vortex was also visible very late in the cycle. The oscillation cycle of jet temperature at the distance of half the tailpipe diameter downstream from the tailpipe exit showed the maximum temperature at 1400 K and the minimum temperature at 350 K, which were temperatures of the combustion products and of the ambient air, respectively. The time-averaged temperature was approximately 700 K.

The impingement condition was unconfined. Three conditions of nozzle-to-surface spacing, H/D = 2, 3, and 4, were tested. Both pulsating and steady jets were used for impingement heat transfer measurement. The steady jet had the same mean mass flow rate as the pulsating jet. The temperature of the steady jet at the tailpipe exit was 1200 K. Thus, the velocity of the steady jet was about 16 m/s. The comparison between pulsating and steady jet impingement heat transfer was based on the heat transfer coefficient, which was intended to be an unbiased method of comparison because the temperatures along the impinging jets down to the surface were quite different. Due to vortices and air entrainment, jet temperature and surface heat flux would be lower for the pulsating jet than for the steady jet. The calculation of heat flux and heat transfer coefficient was based on surface temperature measured by thermocouples and infrared thermometry. Time-averaged surface heat fluxes were calculated from the historical trend of surface temperature assuming one-dimensional heat transfer of a semi-infinite solid. The reference temperature for calculating heat transfer coefficient was the adiabatic surface temperature at the stagnation point for each respective case, i.e., for steady jet/pulsating jet temperature: 1185/582, 1007/444, and 868/390 K for H/D = 2, 3, and 4, respectively. Time-averaged profiles of local heat transfer coefficient were shown for each case. In order to calculate meaningful heat transfer enhancement factors, area-averaged heat transfer coefficients were calculated from those data and are shown in Figure 2.2.

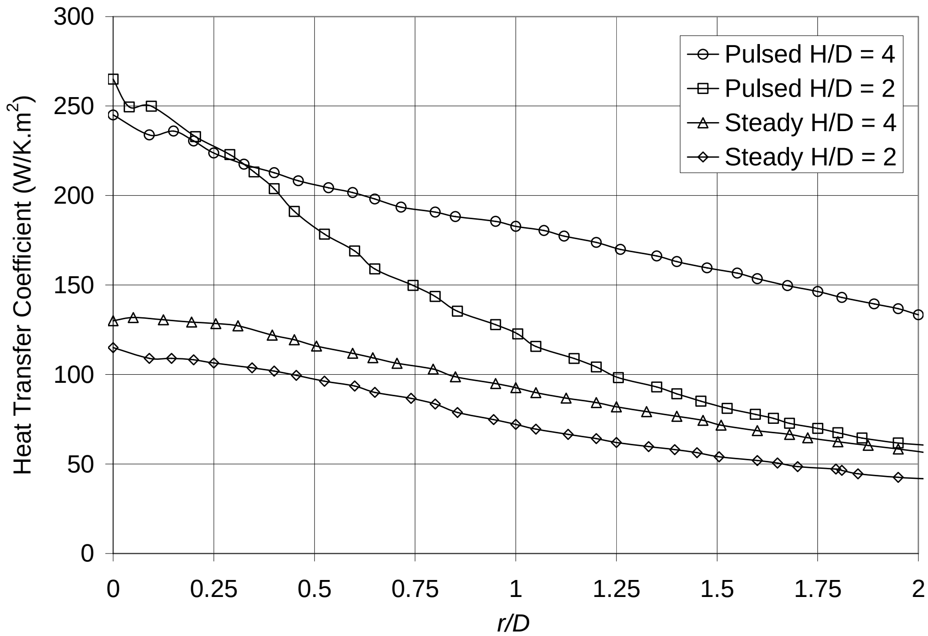

Figure 2.2: Time-averaged profiles of area-averaged heat transfer coefficient calculated from the profiles of local heat transfer in Eibeck et al. (1993).

The patterns of heat transfer profiles at different *H/D* from the steady jet were similar. But the profiles from the pulsating jet were quite different, i.e., the bell shape of the local profile for the case with *H/D* = 4 had a wider base than for the case with *H/D* = 2 (and *H/D* = 3). The magnitudes of heat transfer coefficient at the stagnation point for both cases were relatively the same, about 250 W/K.m^2. The magnitude of the local heat transfer coefficient for the case with *H/D* = 2 decreased rapidly along the radial distance and reached the same level as that for the steady jet at *r/D* = 1.5. As for the case with *H/D* = 4, the magnitude of the local heat transfer coefficient from the pulsating jet remained significantly higher than that from the steady jet up to a distance of *r/D* = 5. Based on the area-averaged profiles in Figure 2.2, heat transfer enhancement factors from the stagnation point up to *r/D* = 2 were 2.3 down to 1.5 for the case with *H/D* = 2 and 1.8 up to 2.3 for the case with *H/D* = 4. The authors explained that the difference in heat transfer profiles of the pulsating jet was caused by different characteristics of the impinging jet and vortices with different nozzle-to-surface spacing. With *H/D* = 2, both the pulsating jet and the vortices strongly impinged on the surface during the positive cycle. With *H/D* = 4, the impinging jet during the positive cycle was weaker but the vortices reached the surface during the negative cycle resulting in a more uniform profile of heat transfer. According to these explanations, the pulsating jet had an impact on surface heat transfer during only half of the oscillation cycle for both cases. Yet, the enhancement factors were as high as 2.3. Such a high enhancement factor was a motivation for the PAD project. However, the parameter of interest for practical applications is surface heat flux, which is directly related to drying rate. The comparison of heat transfer coefficient was based on a very large difference in the reference temperature, which could have different effects on heat flux of pulsating and steady jets. In addition, the impingement geometry was different from industrial applications such as paper drying hoods, which utilize impinging jets onto a moving surface from arrays of nozzles with confinement. An objective of the present work is to investigate the effects of flow parameters on surface heat flux with more practical conditions of flow and impingement geometry. Another objective is to identify the mechanisms for heat transfer enhancement, if any, in such conditions.

Other available data of jet impingement applications with pulse combustors were experiments of paper drying rates. Patterson et al. (2003) experimentally investigated the performance of three pulse combustor systems with various types of nozzle configurations. The pulsation frequency was about 90 Hz for all systems. Only the first system, equipped with slot nozzles, could generate pulsating jets with flow reversal. The pulsating jets from the other two systems appeared to have small velocity ratios. And only the third system had the capability to generate steady jets. Various types of paper were tested. Samples were passed through an investigated impinging jet. The evaporation rates from the first system with slot nozzles were significantly higher than those from the other two systems despite having a lower firing rate and lower mass flow rates. However, this could be the effect of higher jet temperature because the first system was operated close to the stoichiometric ratio whereas the other systems had a high ratio of excess air.

The direct comparison between pulsating and steady jets from the third system showed no heat transfer enhancement.

Wu et al. (2006) and Wu (2007) used a small-scale pulse combustor for impingement drying of paper samples and impingement heat transfer experiments. The impingement geometry was unconfined single round nozzle (tailpipe) with *H/D* = 1.27, 2.96, 4.68, and 6.36. The pulsation frequency was 250 Hz. Although pressure oscillations in the combustion chamber were measured, it was not clear whether the velocity amplitudes of pulsating jets were large enough to have flow reversal. Results showed that the surface area for effective heat transfer or drying for those conditions was limited to *r/D* = 3 due to the effects of ambient air entrainment. Evidence of vortices impinging on the surface could be seen from the profiles of local heat transfer at different *H/D*. While stagnation point heat transfer slightly decreased with increasing *H/D*, heat transfer at *r/D* = 1 increased, presumably due to the effects of vortices. However, there was no steady jet impingement heat transfer or drying for direct comparison in those experiments.

Another type of pulsating jet that can have large velocity oscillation amplitude is a so-called synthetic jet, which is usually generated from a cavity, like a Helmholtz resonator, by the mechanical movement of an actuator such as a piston or diaphragm. As with pulse-combustor jets, the key characteristic of synthetic jets is vortices formed at the edge of cavity exit (Smith and Glezer, 1998). One of the applications of synthetic jets is materials cooling, especially electronic components (Li, 2005; Pavlova and Amitay, 2006; and Trávníček and Vít, 2006). Because there is only one open end of the cavity, the mean mass flow rate of a synthetic jet is zero. Thus, the characteristic jet velocity commonly used is the mean jet discharge velocity: the integration of the velocity oscillation in the positive cycle divided by the cycle time period (thus, $1/\pi$ of peak velocity for a perfect sinusoidal pattern).

Li (2005) numerically studied the characteristics of micro-synthetic jets and impingement heat transfer using CFD simulations. The turbulence model was the SST k-ω model. Results showed that vortices propagated downstream, impinged onto the surface, and moved further along with the wall jets, and finally merged with large re-circulation flows between the impingement surface and the confinement surface. The location of the center of the recirculating flows increased with increasing nozzle-to-surface spacing. For a comparison with steady jet impingement heat transfer at the same mean discharge jet velocity, the enhancement factor for area-averaged heat transfer over the area up to $r/D = 10$ was approximately 1.5 whereas the enhancement factor at the stagnation point was approximately 1.6. The condition of synthetic jet impingement was $H/D = 4$, $D = 6.35$ mm, $u_m = 18$ m/s, and $f = 80$ Hz. The effects of frequency were studied with a slightly different flow and impingement condition. The range of frequency was 250-1250 Hz. The magnitude of heat transfer increased with increasing frequency from 250, 320, to 500 Hz. The local maximum heat transfer coefficient, at $r/D = 0.6$, was approximately 430, 475, and 510 W/K.m^2 for $f = 250$, 320, and 500 Hz, respectively. However, the local profiles for $f = 500$, 1000, and 1250 Hz were not much different.

Pavlova and Amitay (2006) experimentally studied synthetic jet impingement heat transfer for surface cooling. The ranges of key parameters were $f = 420$ and 1200 Hz and $H/D = 1.9$-38.1. The heat transfer enhancement factors at $H/D = 4.75$ were 1.9 and 2.6 for $f = 420$ and 1200 Hz, compared to an equivalent steady jet. Heat transfer from the jet with $f = 1200$ Hz compared to that with $f = 420$ Hz was higher for $H/D = 3$-9, then about the same for $H/D = 10$-15, and became lower for $H/D > 15$. An interesting characteristic was that, at $H/D = 9.5$, vortices from the higher frequency merged with each other and broke down to smaller structures before impinging onto the surface whereas vortices from the lower frequency impinged onto the surface separately.

Trávníček and Vít (2006) experimentally measured impingement mass transfer using a steady jet, a synthetic jet, and a hybrid synthetic jet, which was a synthetic jet but with a mean mass flow rate. All three jets were generated by using a chamber consisting of two diaphragms on opposite sides for the synthetic jet and an auxiliary channel for the steady jet. The hybrid jet was generated by operating both diaphragms and the auxiliary channel. In essence, a hybrid synthetic jet is similar to a pulse-combustor jet, i.e., having a mean mass flow rate or velocity and flow reversal. The velocity ratio of the hybrid jet was approximately 3.0. The diameter of the round nozzle was 8 mm. The mean discharge jet velocity was about 8 and 10 m/s and the frequency was 75 and 95 Hz for synthetic and hybrid jets, respectively. The velocity of the steady jet was 10 m/s. The authors focused on the comparison between the synthetic and hybrid jets. With $H/D = 6$, stagnation point mass transfer of the hybrid jet was 17% higher than that of the synthetic jet due to the increase in mean jet velocity. For the comparison between the hybrid and steady jets, it was approximately 21% higher for the hybrid jet at the stagnation point. The magnitude of the whole profile of local mass transfer (up to $r/D = 8$) for the hybrid jet was higher than that for the steady jet.

Pulsating jets without flow reversal have also been studied for the effects on impingement heat transfer. Nevins and Ball (1961) used a function generator and a pneumatic controller to generate pulsating jets in sinusoidal, square, and triangular patterns. The ranges of mean velocity, velocity ratio, and frequency were 3-30 m/s, 0-1 and 0-18 Hz, respectively. The nozzle-to-surface spacing ratio was $H/D = 8$, 16, and 32. Results showed that heat transfer from the pulsating jets was about the same as that from corresponding steady jets over the whole ranges of velocity ratio and frequency. In fact, heat transfer even decreased for the cases with the velocity ratio close to 1.0. Azevedo et al. (1994) used a rotating valve in a chamber before a nozzle to periodically cut off the flow. However, the pattern of the velocity of impinging jets was not exactly a square wave. The ranges of Reynolds number and frequency were 4,000-40,000 and 0-200 Hz, respectively. Results showed that stagnation point heat transfer from pulsating jets was lower than that from steady jets, up to 25% in some conditions. Sailor et al. (1999) used a valve mechanism to vary the duty cycle of pulsating jets. The duty cycle was defined by "on" time duration divided by the cycle period. The ranges of Reynolds number, frequency, and duty cycle were 21000-31000 and 20-60 Hz, and 0.25-0.5, respectively. The nozzle-to-surface spacing ratio was $H/D = 4$, 6, and 8. Results showed that a lower duty cycle gave higher stagnation point heat transfer than the regular square wave or 50%

duty cycle did. Maximum heat transfer enhancement, about 60-65%, occurred at f = 25-30 Hz with the duty cycle of 0.33 and 0.25 for H/D = 4 and 6, respectively. For H/D = 8, heat transfer from the pulsating jets was about the same as that from the steady jets.

Zumbrunnen and Aziz (1993) generated intermittent impinging jets using rotating blades located beneath a nozzle exit to periodically cut off water slot jets. The ranges of Reynolds number and frequency were 6500-16000 and 30-142 Hz, respectively. Results showed that pulsating jet impingement heat transfer directly depended on the intermittent frequency and that there was a threshold frequency, in which heat transfer enhancement could occur, for a given Reynolds number. For the tested conditions, the maximum heat transfer enhancement factor was about 2 at the stagnation point with Re = 9450 and f = 130 Hz. The authors explained that heat transfer enhancement was due to the effects of boundary layer renewal. Mladin and Zumbrunnen (1997) generated pulsating slot air jets using the combination of steady flows and pulsating flows caused by a rotating ball valve. The ranges Re, f, and H/B were 1000-11000, 23-80 Hz, and 3-10 respectively. The velocity ratio, ε, was up to 0.5. The comparison between pulsating and steady jets showed both a decrease and an increase in stagnation point heat transfer, within the range of $\pm$12%, depending on flow and impingement conditions. The enhancement was due to boundary layer renewal effects by large vortex structures. The key parameter seemed to be the product of Strouhal number and velocity ratio (Mladin and Zumbrunnen, 2000). The decrease in heat transfer was due to nonlinear dynamic effects according to theoretical modeling within boundary layers of pulsating stagnation flows by Mladin and Zumbrunnen (1995). The nonlinear dynamic behavior resulted in non-equilibrium between momentum and energy equations within the boundary layers. A key result was that stagnation point heat transfer decreased with increasing velocity ratio (maximum at 1.0, i.e., no flow reversal). Another experiment with pulsating air jets was an array of nine round nozzles (Sheriff and Zumbrunnen, 1999). The ranges of parameters were Re = 2500-10000, f = 0-65 Hz, ε = 0-0.6, and H/D = 2-6. Results showed that pulsating jets yielded lower heat transfer than steady jets and that pulsating jet impingement heat transfer decreased with increasing velocity ratio despite the existence of coherent structures and the increase in turbulence level. The decrease was about 18% for the condition with $\varepsilon = 0.6$, $H/D = 6$, $Re = 5000$, and $f = 10$ & 25 Hz. The explanation for this behavior was that the effects of nonlinear dynamic effects in boundary layers were probably stronger than the effects of surface renewal and increased turbulence intensity.

Numerical simulations of laminar small-amplitude pulsating jets have been performed to study the effects of velocity ratio and frequency. The behavior of vortices propagating from nozzle exit to surface was evidenced in these simulations. Chaniotis and Poulikakos (2001) simulated pulsating slot air jet impingement with confinement. An increase of 14% was reported for heat transfer from a pulsating jet with $\varepsilon = 1.0$ for compared to a corresponding steady jet. Chaniotis et al. (2003) simulated single and dual slot air jets with confined impingement geometry. Similar results were reported, i.e., heat transfer increased with the velocity ratio for both single and dual jets. As for the effects of pulsating frequency, results from Chaniotis and Poulikakos (2001) showed that, although enhancement factors were very small (0.12-3.41%), there was an optimum frequency for maximum enhancement. The magnitude of the fluctuation of surface heat transfer decreased with increasing frequency. Similar behavior was found for round water jet impingement with confinement (Poh et al., 2005). The range of frequency was 1-20 Hz. At "high" frequencies, 10 and 20 Hz, there was no oscillation of surface heat transfer. The enhancement factors were also very small. The pulsation amplitude was not varied in that numerical study.

In summary, the key characteristic of pulsating jets for heat transfer enhancement appeared to be the well-organized vortex structures. And the key parameters appeared to be the frequency and the velocity ratio. The enhancement factors from pulsating jets without flow reversal were much lower than those from pulsating jets with flow reversal. Most conditions of pulsating jets and impingement geometry in the literature were quite different from the conditions of interest, i.e., in impingement hoods for paper drying processes. In addition, for industrial applications, area-averaged heat transfer is more important than local heat transfer at a single point. The design of numerical experiment for the present work will consider all these parameters and conditions, as discussed in Chapter 6.

2.4 Helmholtz Pulse Combustor Flow Characteristics

The objective of this section is to provide basic flow characteristics of pulse combustors and a background for the derivation and applications of the simplified model of Helmholtz pulse combustors in Chapter 4. The literature review in this section is mainly based on publications by a research group at the Combustion Research Facility, Sandia National Laboratories, Livermore, CA. The operations of pulse combustion were also extensively studied by, among others, a combustion research group at the Georgia Institute of Technology led by Professor Ben Zinn. The historical developments of designs and applications of pulse combustors were reviewed in Putnam et al. (1986) and Zinn (1996). The recognition of this technology dates back to "singing flame" experiments in 1777. An interesting application was the V-1 rocket or the buzz bomb in World War II. As for drying applications, various types of pulse combustion dryers were reviewed and discussed in Kudra and Mujumdar (2002). Some applications in the pulp and paper industry were the drying of sawdust and waste materials. Needs for further research and development in the area of pulse combustion drying was addressed in Wu and Mujumdar (2006). Obviously, an example is impingement drying applications as the ultimate goal of the PAD project and the present work.

Pressure oscillation and pulsating flow in a pulse combustor are driven by a self-sustained and self-oscillating combustion process, coupled with the acoustic resonance of the system. Three types of pulse combustor exist, i.e., Schmidt, Rijke, and Helmholtz (Zinn, 1996 and Kudra and Mujumdar, 2002). The Schmidt or quarter-wave tube pulse combustor has one closed end and one open end. The combustion occurs in the zone at the closed end. The Rijke pulse combustor has two open ends and, hence, has a half-wave characteristic. The combustion occurs at a quarter of the pipe length from the inlet end.

The Helmholtz type consists of a relatively large combustion chamber (closed end) and a tailpipe (open end). Thus, a Helmholtz pulse combustor has a quarter-wave acoustic characteristic, similar to the Schmidt type.

The operating principles of pulse combustors are basically the same for all three types. The literature review focuses on the Helmholtz type used in pulsating jet impingement heat transfer and drying experiments. A main component of a pulse combustor is one-directional supply valves for reactants, i.e., air and fuel. Three types of one-directional valves commonly used for pulse combustors are flapper valves, rotating valves, and aerodynamic valves (Putnam et al., 1986 and Kudra and Mujumdar, 2002). The reactants could be pre-mixed in a mixing chamber or separately fed to the combustion chamber. The operation of a one-directional supply valve is based on the pressure difference across the valve, i.e., between the supply lines and the combustion chamber. Typically, the supply pressure is small compared to the amplitude of pressure oscillation in the chamber. A diagram of a pulse combustion cycle is shown in Figure 2.3 When the pressure in the chamber is lower than the supply pressure, the valves open and reactants enter (Phase 1). The reactants are heated by mixing with remaining hot combustion products from previous cycles (Phase 2). As the combustion reaction occurs, the pressure in the chamber increases, and the valves close (Phase 3). As exhaust gas continues to flow through the tailpipe and the combustion rate slows down, the combustion chamber pressure decreases (Phase 4). When the pressure becomes lower than the supply pressure of reactants, the valves open again, reactants flow in, and a new cycle begins. The corresponding direction of the flow at the tailpipe inlet for each phase is also shown in the diagram. According to the momentum equation, and also shown by the measurement in Dec et al. (1991), the phase of the tailpipe velocity oscillation lags that of pressure oscillation by a quarter of the cycle.

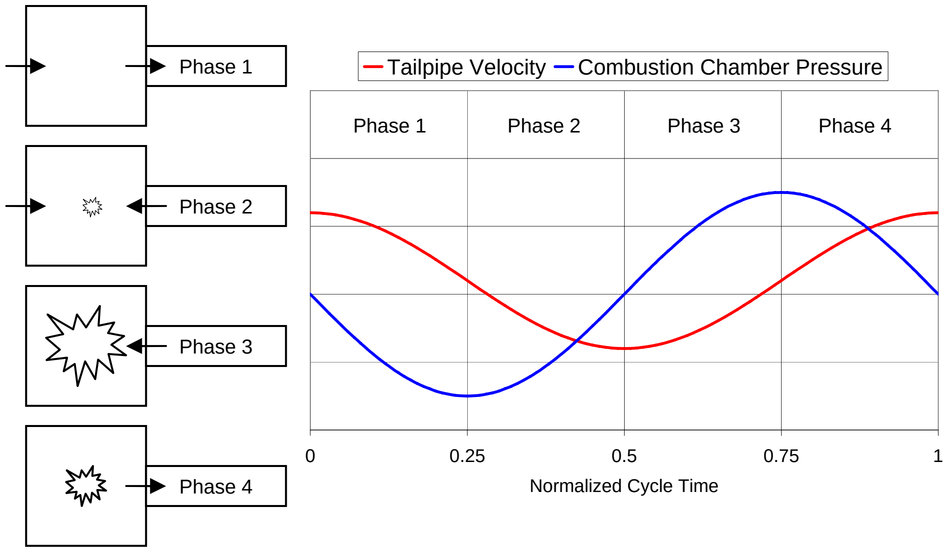

Figure 2.3: Diagram of pulse combustion cycle.

The stable oscillation of a pulse combustion process follows the Rayleigh criterion (Lord Rayleigh, 1945), which requires heat to be released or added during the positive cycle of pressure oscillation (Zinn, 1996). This criterion has been verified by experiments, for example, Reuter et al. (1986), Keller et al. (1989), Tang et al. (1995), and Fernandes and Heitor (1996). In this case, heat is added by combustion of the reactants. From the operation of the one-directional valve, reactants can only enter the combustion zone during the negative cycle of pressure oscillation. Thus, the combustion reaction has to be delayed until the positive cycle. The total delay time is the sum of three characteristic times: time for mixing between reactants, time for mixing between reactants and combustion products from previous cycles, and time for the combustion reaction (Keller et al., 1989). For a pulse combustor to have a stable oscillation, the total delay time has to be long enough such that the peak of heat release occurs during the positive cycle of pressure oscillation. The majority of the total delay time is the characteristic time for mixing between reactants and combustion products. Such characteristic time or the mixing rate could be controlled by modifying the fluid dynamics of the reactants. This can be achieved by placing a small stagnation plate in the flow path of the reactants so that the reactants would impinge onto the plate and form vortex structures, as shown in Keller et al. (1990).

The position of the stagnation plate or the spacing between the inlet port of reactants and the plate has significant effects on the characteristics of heat release (Keller et al., 1989). Typically, the pattern of heat release rate versus time is somewhat bell shaped. In other words, the combustion process does not occur all at once. One characteristic of heat release is the height of the bell-shape pattern, which could be normalized by the mean value to define the amplitude ratio of heat release rate. While the mean value of heat release is determined by the mean mass flow rate of fuel, the heat release amplitude ratio could be controlled by the stagnation plate position or the port-to-plate spacing. Keller et al. (1989) showed that decreasing such spacing increased the mixing rate or decreased the mixing time resulting in earlier start of heat release, thus yielding a smaller amplitude and the heat release being less in-phase with the pressure oscillation. In this experiment, the reactants were premixed and both mean mass flow rate and air/fuel ratio were kept constant. Results showed that the amplitude ratio of heat release had a direct effect on the magnitude of pressure oscillation amplitude. In essence, the relationship between the heat release amplitude ratio and the pressure amplitude follows the Rayleigh criterion, i.e., the strongest pulsation occurs when the heat release is totally in phase with the pressure oscillation, which results in the highest heat release amplitude ratio.

According to the authors, the total delay time of combustion process also determined the cycle period, i.e., decreasing the delay time decreased the cycle period and thus, increased the pulsation frequency. However, according to linear acoustic theory, the resonant frequency depends on the wavelength of the system and the mean speed of sound. The system wavelength is typically determined by the dimensions of the pulse combustor, whereas the mean speed of sound typically depends on the mean temperature of the fluid in the tailpipe, which is also affected by heat losses at tailpipe wall and by the temperature of ambient fluid entering the tailpipe during flow reversal. A smaller amplitude of pressure oscillation causes a smaller velocity amplitude and, thus, less heat loss at the walls, weaker flow reversal and less ambient fluid entering the tailpipe, resulting in higher mean temperature. This could be another reason for the higher frequency when the delay time was decreased. However, data on tailpipe fluid temperature were not provided in the reference. Nevertheless, the results showed that the resonant frequency had significant effects on the pulsation frequency of the pulse combustor, i.e., the pulsation frequency decreased with increasing volume of the combustion chamber even if the position of the stagnation plate was the same. The concept of the resonant frequency discussed here is used in deriving the simplified model of Helmholtz pulse combustors in Chapter 4.

For heating and drying applications, it is desirable that the magnitude of pressure oscillation amplitude in the combustion chamber be large enough to cause the pulsating flow in the tailpipe to have flow reversal, which is the key factor for heat transfer enhancement inside and outside the tailpipe, including jet impingement. However, the flow parameters of a pulse combustor are nonlinearly coupled with one another. Dec and Keller (1986) varied total mean mass flow rate (air and fuel) and equivalence ratio of a Helmholtz pulse combustor one factor at a time and measured pressure oscillation amplitude in the combustion chamber, velocity oscillation amplitude in the tailpipe, and oscillation frequency. There were two systems of air and fuel injection: separate (non-premixed) and premixed. For the non-premixed injection, the trends of results were consistently the same, i.e., increasing mean mass flow rate or equivalence ratio resulted in a decrease in pressure amplitude and velocity amplitude and an increase in frequency. Increasing total mean mass flow rate increased firing rate and mean temperature, resulting in higher frequency or shorter cycle period. Thus, the delay time for heat release had to be shorter resulting in lower heat release amplitude ratio (broader and shorter bell shape) and lower oscillation amplitudes of pressure and velocity. Similarly, increasing equivalence ratio increased firing rate and mean temperature. Thus, the response of the system had similar trends. Data also showed that only one condition for each test had flow reversal. For the premixed injection, the trends were inconsistent. With increasing mean mass flow rate, pressure and velocity amplitude first increased and then decreased, whereas frequency first remained the same and then increased. The explanation for the first response was that heat release amplitude ratio increased while the cycle period remained the same. This was probably because there was flow reversal in this regime, causing a balance between effects of higher mean velocity and higher velocity amplitude, resulting in unchanged temperature and frequency. After this regime, there was probably no flow reversal. The trends and the explanation were similar to the tests with the non-premixed injection. For the other test, increasing equivalence ratio up to 1.0 resulted in relatively small amplitude of pressure and velocity oscillation and relatively high frequency, displaying the instability of pulse combustion with these conditions. Then, the trends were reversed when the equivalence ratio was greater than 1.0. As there was a reduced amount of air for combustion reaction with the fuel, firing rate and temperature were lower, resulting in a lower frequency. A longer cycle period required a longer delay time for heat release, higher heat release amplitude ratio (narrower and taller bell shape), and higher pressure amplitude.

Similar to the experiments by Keller et al. (1989), Möller and Lindholm (1999) adjusted the position of the stagnation plate in the combustion chamber of a Helmholtz pulse combustor but let the pulse combustor run with a self-aspirating mode by keeping a constant supply pressure of premixed reactants. Results showed that decreasing the port-to-plate spacing resulted in a decrease in energy input rate (fuel flow rate), excess air ratio (air flow rate), pressure amplitude, and heat release amplitude ratio. Although the amount of data for frequency was smaller than that for other parameters, it seemed the frequency only slightly changed. Hence, these trends were similar to the regime in which the frequency remained relatively the same (increasing mass flow rate with premixed injection) in Dec and Keller (1986), discussed earlier. These trends were also similar to the results in Keller et al. (1989), in which decreasing port-to-plate spacing resulted in a decrease in pressure amplitude.

While the combustion process in the combustion chamber of a Helmholtz pulse combustor is rather complex, the characteristics of pulsating flows in the tailpipe are more straightforward, i.e., can be roughly characterized as one-dimensional flows. Dec et al. (1991) experimentally measured instantaneous velocity profiles across the width of the square cross-sectional tailpipe of a Helmholtz pulse combustor. The length and the width of the tailpipe were 880 and 30 mm, respectively. The base operating condition of the pulse combustor was $\dot{m}_m$ = 4 g/s, ϕ = 1.0, p_A = 10.5 kPa, and f = 83 Hz, where ϕ is equivalence ratio. The reactants were premixed. The base location was 540 mm from the tailpipe entrance, in which velocity oscillation at the center of the tailpipe had a mean value of 16.3 m/s and varied from -60 to 95 m/s. The phase of the velocity oscillation lagged the phase of pressure oscillation in the combustion chamber by about a quarter of the cycle period, as predicted by the momentum equation. The oscillation patterns of both pressure and velocity were close to, although not perfectly, sinusoidal. The patterns of the instantaneous velocity profiles over an oscillation cycle were basically uniform like a plug flow, except for boundary layers at the walls. As the momentum of fluid in the boundary layers was much lower than that in bulk flows, fluid in the boundary layers would change direction earlier during the oscillation than those in the bulk flow. Thus, the instantaneous boundary layer thickness of pulsating flows was smaller than that of a steady flow with the same instantaneous bulk velocity. It should be noted that even pulsating laminar flows show similar behavior, i.e., instantaneous velocity profiles are uniform in bulk flows and have a leading phase in boundary layers. Velocity oscillations at three other locations along the tailpipe were also measured (at the center of the tailpipe cross section). Mean velocities decreased along the tailpipe length due to lower temperature as a result of air cooling around the tailpipe walls. The amplitude of velocity oscillations slightly increased along the tailpipe length, as is characteristic of a resonant acoustic tube. However, the velocity wave form along the tailpipe was different from the pressure quarter-wave form. The amplitude of pressure oscillations was maximum at the tailpipe entrance and decreased to zero at the tailpipe exit. On the other hand, the amplitude of velocity oscillations was minimum, but not zero, at the tailpipe entrance and increased along the tailpipe length. As for this case, the authors considered that the increase in velocity amplitude was small and suggested that flow parameters of a Helmholtz pulse combustor could be predicted by a Helmholtz resonator model, which assumes incompressible flow in the tailpipe.

The effects of mean mass flow rate and pressure amplitude on velocity oscillation were also studied. The velocity oscillations were measured at the center of the tailpipe and 540 mm from the entrance for all cases. Increasing mean mass flow rate resulted in an increase in frequency, pressure amplitude, mean velocity, and velocity amplitude but a decrease in velocity ratio. These trends were quite different from the experiments in Dec and Keller (1986). Both pulse combustors were practically the same except for tailpipe length and air cooling around tailpipe walls. Another difference was the operating conditions being reviewed had strong flow reversal and stable oscillations. The underlying physical reasons typically involve heat release characteristics in the combustion chamber. However, such information was not available in these publications. The effects of pressure amplitude were quite expected, i.e., velocity amplitude increased with pressure amplitude at the same frequency.

With the same base operating condition of the same pulse combustor, Dec and Keller (1990) measured instantaneous profiles of temperature oscillations across the tailpipe width at the same base location. The patterns of the profiles were similar throughout the cycle, i.e., uniform in the bulk flows with boundary layers at the walls. The oscillation of temperature at the center of the tailpipe had a quarter-cycle phase shift from the oscillation of velocity. The temperature increased when the velocity was positive, and vice versa, corresponding to gas temperature upstream or downstream. At the moments when the velocity was zero or changing direction either way, temperature dropped dramatically and then recovered rapidly. This behavior corresponded to sudden increases in wall heat transfer at the same moment. The mechanism responsible for this behavior was not well understood at the time. A possible explanation could be the boundary layers or surface renewal effects. As the bulk flows were about to change the direction, the boundary layers previously existing were removed by the phase-leading fluids near the walls. The oscillations of temperature along the tailpipe length were also measured. The pattern of the oscillations was similar to that at the base location. The mean value decreased along the tailpipe length in the downstream direction.

The effects of frequency on velocity and temperature oscillations at the base location were studied in both references. The frequency was changed (67, 74, and 83 Hz) by changing tailpipe length so that pressure amplitude could be at the same level for all cases. Results showed that the patterns of temperature oscillations were similar but the mean values slightly decreased with increasing frequency. The key difference was that the sudden drops in temperature at the times of flow reversal were more prominent at higher frequencies. This may possibly also be explained by the surface renewal effect. As for the effects of frequency on velocity oscillations, increasing frequency by shortening the tailpipe resulted in a slight decrease in mean velocity and an increase in velocity amplitude and velocity ratio. The slight decrease in mean velocity could correspond to the slight decrease in temperature. The evaluation of the mean velocity in the tailpipe of a pulse combustor as related to temperature oscillation is discussed in the following chapter. The explanation for the increase in velocity amplitude was not given in the reference. Typically, if the tailpipe length was constant, increasing frequency would decrease the velocity amplitude. However, as the acoustic relationship between the frequency and the pulse combustor dimensions is nonlinear, as discussed in Chapter 4, the combined effects of the shorter tailpipe and the higher frequency resulted in the increase in velocity amplitude.

Flow reversal is the key factor for heat transfer enhancement by pulsating flows inside the tailpipe of a pulse combustor. Successful industrial applications of pulse combustion are based on such a characteristic inside the tailpipe. Basically, no enhancement occurs if the velocity ratio is less than one and the enhancement factor directly depends on the magnitude of velocity ratio (Hanby, 1969 and Perry and Culick, 1974). Numerous studies about this heat transfer enhancement technique and its applications have been published. Examples of experiments with Helmholtz pulse combustors include Lalwani et al. (1979), Nomura et al. (1989), Dec and Keller (1989), Gemmen et al. (1993), Zbicinski et al. (1998), Liu et al. (2001), and Kudra et al. (2003). The enhancement factor can be as high as 4.6 (Nomura et al., 1989). The dependence of the enhancement factor on pulsation frequency was also studied. However, results were inconsistent, i.e., directly dependent for heat transfer on the tailpipe wall in Dec and Keller (1989) but no obvious trend for mass transfer on a cylinder in the middle of the tailpipe in Gemmen et al. (1993), despite using similar pulse combustors.

In summary, the characteristics of a Helmholtz pulse combustor are rather complex largely due to the unsteady combustion process in the combustion chamber coupled with the acoustic resonance of the tailpipe. For stable oscillating processes, the Rayleigh criterion is required, i.e., heat release oscillation being in-phase with pressure oscillation. The characteristics of heat release can be controlled, within some limits, by adjusting the mixing rate determined by flow characteristics of the entering fresh reactants. Flow parameters, e.g., pressure amplitude, heat release amplitude ratio, frequency, and velocity amplitude, have nonlinear relationships among one another as well as the dimensions of the pulse combustor. Such relationships can be characterized, at least qualitatively if not quantitatively, by the simplified model based on the conservation of energy in the combustion chamber and the acoustic flow solution in the tailpipe, described in Chapter 4.

2.5 Simplified Models of Helmholtz Pulse Combustors

Numerous analytical and numerical studies of pulse combustor operations and applications have been reported. Modeling techniques employed in these studies range from assuming a simple Helmholtz resonator model, to solving one-dimensional transport equations, to simulating full two-dimensional flow fields. The present work requires a simplified model that can predict pressure amplitude and frequency, as well as velocity oscillation, given the dimensions of the Helmholtz pulse combustor and the flow rates of reactants. In order to provide a background for the development, or the simplification, of the model to be presented in Chapter 4, this section briefly reviews some of the previous simplified models for the Helmholtz pulse combustor, focusing on their underlying assumptions and limitations.

As discussed in the previous section, flows in the combustion chamber of a Helmholtz pulse combustor are rather complex due to the vortex structures of reactant flows entering the chamber, which determine the mixing rate between reactants and hot exhaust gas and, thus, the characteristics of heat release. The heat release amplitude ratio directly affects the amplitude of pressure oscillation. Therefore, in order to accurately predict the pressure amplitude, the characteristics of heat release or flow structure have to be accurately modeled. In other words, a full flow field in the combustion chamber has to be simulated, coupling with the reaction kinetics for the combustion process. Examples for two-dimensional simulations are Barr and Keller (1990), Tajiri and Menon (2001), and Wu (2007). Simplified models have no capability to accurately simulate such characteristic. Thus, the heat release process has to be modeled approximately or obtained from experimental data.

The simplest model for a Helmholtz pulse combustor is a Helmholtz resonator, in which the pulsating flow in the tailpipe is assumed to be incompressible or behave like a plug flow. Heat loss and frictional force at the wall could be taken into account. The operating frequency of the system is commonly predicted by the resonant frequency of the Helmholtz resonator determined from pulse combustor dimensions: tailpipe length (L) and volume ratio of the combustion chamber to the tailpipe (β), and the mean speed of sound in the tailpipe (c_m), i.e., $f = c_m \big/ \left(2\pi L\sqrt{\beta}\right)$. A common assumption is that pressure in the combustion chamber is spatially uniform. However, in order to predict the amplitude of pressure oscillation, a submodel is required. Examples of the submodel for pressure amplitude used in literature were a correlation from experimental data, a kinetic rate expression, and a moving flame front. Gill and Bhaduri (1974 and 1978), from the observation of experimental data, divided the pattern of pressure oscillation into three phases: rising, falling, and negative. Each phase was separately expressed by a correlation equation. The pressure amplitude, associated with the time duration of the rising phase, was estimated from the amount of fuel consumed per cycle and the rate of fuel consumption taken from experiments. Coulman et al. (1982) modeled a Helmholtz pulse combustor by solving the conservation equations of mass, energy, and species, and the equation of state of an ideal gas. A kinetic rate expression was used as a heat source in the energy equation. Pressure amplitude and temperature (used for calculating frequency) were sensitive to the values of constant parameters in the kinetic expression.

Ahrens et al. (1978) developed a simplified model, the so-called AKT model, by assuming that the combustion chamber could be divided into two zones, one for cool fresh reactants and one for hot combustion products, separated by a moving flame front. The flow rates of fresh reactants entering the chamber during the negative cycle of pressure oscillation were assumed to be quasi-steady and determined by orifice flow equations. The model resulted in explicit solutions for the pressure amplitude and the burning velocity of the flame front. The pressure amplitude was a linear function of air/fuel ratio and independent of pulse combustor dimensions. It was found that the prediction of pressure amplitude was in reasonable agreement with experimental data when the magnitude of pressure amplitude was relatively small compared to that of mean absolute pressure. This model was further developed to incorporate more realistic valve operation and a modified modeling approach in Bloom et al. (2007). Lee et al. (1985) slightly modified the concept of a moving flame front in the AKT model by introducing two different burning velocities for the open and closed periods of the flapper valves. Another difference was the calculation of valve opening area. While the original AKT model assumed fully open or fully closed valves, this model calculated the opening area from the moving displacement of the flapper valves. In addition, the configuration of the pulse combustor in this work was different from other works, i.e., the pulse combustor with a short tailpipe was connected to a decoupling chamber which was connected to a very long exhaust pipe. However, it was also found that the model agreed with experimental data when the magnitude of pressure amplitude was less than 20% of mean absolute pressure.

The models previously reviewed could be regarded as zero-dimensional models. In order to account for the effects of the geometry of the pulse combustor more accurately, one-dimensional models are required. Most one-dimensional models solve the three basic conservation equations (mass, momentum, and energy), with variable cross-sectional area, and the equation of state of an ideal gas. The most important conditions for a pulse combustor model are the pattern and the rate of heat release, as a heat source in the energy equation, and the injection rates of fresh reactants through one-directional valves. Typically, these conditions still have to be modeled or prescribed. The research group at Sandia National Laboratories successively improved their one-dimensional model using available detailed experimental data especially for the patterns of heat release and reactant injection flows. First, Dwyer et al. (1986) assumed a simple form of injection velocity and used a prescribed pattern of heat release obtained from experimental data. Frequency was also pre-determined. Barr et al. (1987) used prescribed patterns from the experiment for both injection flows and heat release. The heat release was assumed to be spatially uniform in the combustion chamber domain. The frequency prediction was based on a condition satisfying the Rayleigh criterion. Results showed that, while the frequency prediction was somewhat satisfactory, pressure amplitude from the model was more than twice as large as that from the experiment. Barr et al. (1990) further improved the model by introducing three submodels for reactant injection, fluid dynamic mixing, and chemical kinetics, respectively. The injection submodel was based on the operation of a flapper valve. The fluid dynamic mixing submodel, representing the mixing rate between cool fresh reactants and hot exhaust gas, was based on transient jet analysis. The chemical kinetics submodel, representing the combustion reaction, used the so-called HCT (hydrodynamics, chemistry, and transport) code for solving the conservation equations of mass, momentum, energy, and chemical species. The combination of the fluid dynamic mixing and chemical kinetics models gave the pattern of heat release for the main model. The patterns of reactant injection and heat release were dependent on results of the main model, i.e., pressure oscillation pattern and cycle period. Therefore, the main model and the submodels had to be iterated until a stable oscillation was obtained. The output of the model was pressure amplitude and frequency. However, each submodel had constant parameters which needed to be calibrated so that the numerical results matched with experimental data at least at one condition. Results showed that the patterns of reactant injection and heat release were similar to those of the experiment. And, the phases between heat release and pressure oscillation satisfied the Rayleigh criterion.

Other simplified models were developed differently in terms of governing equations and submodels: Clarke and Craigen (1976), Fureby and Lundgren (1993), Neumeier (1993), Narayanaswami and Richards (1996), Richards and Gemmen (1996), and Erickson and Zinn (2002). However, as for the relevance of the present work, the conclusion was the same, i.e., the requirement for specific experimental data depends on the degree of simplification used. The simplified model in Chapter 4 can be regarded as a zero-dimensional model in the combustion chamber and a one-dimensional model in the tailpipe. This is similar to the model in Neumeier (1993), but with a different approach and additional simplifying assumptions. The Neumeier model was in the form of a transfer function developed through a frequency domain analysis, which included both phase and amplitude of heat release oscillation. Frequency prediction was based on an analysis of delay time and chemical reaction time. The solution for tailpipe flow was based on acoustic wave equations. A parameter of the model was the energy ratio, which represented the amplitude ratio of heat release discussed in the previous section. The information from experiments for this model was a linear relationship between the pressure amplitude and the energy ratio. Interestingly, this relationship was inverse, i.e., pressure amplitude decreased with increasing energy ratio. Nevertheless, model predictions were in agreement with experimental data.

In summary, all simplified models require some specific information from experiments or highly approximate burning rate submodels. Therefore, the validity of the predictions is typically within a limited range of operating conditions. The extent to which experimentally obtained information is required depends on the degree of simplification or the underlying assumptions used in the model. The most important factor is the characterization of heat release as a driving force of the pulsation process. It could be assumed that if this characteristic is modeled accurately, the predictions of the Helmholtz pulse combustor model should be accurate because other factors are generally governed by standard conservation equations or submodels.

CHAPTER 3

PRELIMINARY WORK

This chapter reviews and discusses the key results of three preliminary experiments, one laboratory and two numerical simulations. The objective of the preliminary work is to gain basic understanding of the characteristics of pulsating jets generated by pulse combustors, to guide further design of numerical experiments. Laboratory impingement drying results were presented at the 15th International Drying Symposium in Budapest, Hungary (Liewkongsataporn et al., 2006a). Simulation results of pulsating jet impingement heat transfer were presented at the 13th International Heat Transfer Conference, Sydney, Australia (Liewkongsataporn et al., 2006b). The simulation of pulsating flows inside the tailpipe of a pulse combustor was a Master's Thesis (Liewkongsataporn, 2006).

3.1 Impingement Drying Experiment

A main objective for this experiment was to determine the impingement drying enhancement obtained by using a pulsating jet instead of a steady jet. The work used a pulse combustor with a single tailpipe having a diameter, D = 25.4 mm (1″) and length, L = 279.4 mm (11″). The variable examined for the confined impingement condition was nozzle-to-surface distance, H: H/D = 1 and 2. An unconfined impingement condition was also tested at H/D = 1 with both pulsating and steady jets. A diagram of the experimental setup is shown in Figure 3.1. Sample sheets of wet paper with a diameter of 72.6 mm (3″) were put directly under the tailpipe for a range of time periods. The amount of water in the sheet before and after was determined gravimetrically and was used to calculate the amount of evaporated water. For each impingement condition, the drying test was run using a number of exposure times to establish a drying curve. And at each time period, the test was repeated 5-6 times with a new sheet. The characteristics of the pulsating jet were essentially the same for all conditions, except time-averaged temperature at the tailpipe exit, which noticeably changed from case to case (700-950 K). The tailpipe exit temperature was lower at a larger *H/D* or with an unconfined impingement condition. The pulsation frequency was 155 Hz. The mean velocity, u_m, velocity amplitude, u_A, and velocity ratio, $\varepsilon = u_A/u_m$, were evaluated to be 24.8 m/s, 94.1 m/s, and 3.8, respectively, based on the assumptions described in the following chapter. The drying rate results are summarized in Table 3.1, which also includes equivalent heat flux for each respective case.

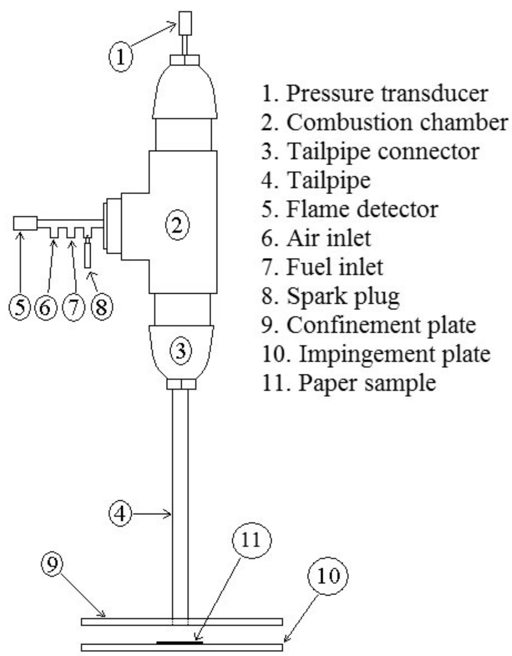

Figure 3.1: Diagram of pulse combustor for drying experiment.

Table 3.1: Drying rates and equivalent heat fluxes from drying experiment

Condition	Jet	H/D	Drying Rate ($kg/h.m^2$)	Equivalent Heat Flux (kW/m^2)
Unconfined	Steady	1	55	35
	Pulsed	1	81	51
Confined	Steady	1	64	40
		2	60	38
	Pulsed	1	130	81
		2	78	49
		3	44	27

The equivalent heat fluxes in Table 3.1 were calculated from the drying rates assuming that all heat transferred from the impinging jet was converted to heat for water evaporation. The value of latent heat used for water evaporation was 2257 J/g. Results showed that the drying enhancement factor for the confined impingement condition with *H/D* = 1 was as high as 2.2, which was an encouraging result. In this experiment, the comparison of drying rates between pulsating and steady jets was based on the same mean mass flow rate and mean temperature at the tailpipe exit for each respective condition. The basis of such comparison was that variations of the temperature of pulsating jets at the tailpipe or nozzle exit in an impingement hood would be small due to the confined impingement geometry of multiple nozzles. In order to achieve such a condition, the confinement wall and the impingement surface were made of a large insulation board so that cool ambient air could not reach the impingement zone around the tailpipe exit. However, it seemed that ambient air did reach the tailpipe exit because of a fracture of the insulation boards yielding an imperfect impingement condition. This conclusion was based on the temperature measurements made along the tailpipe length. For the pulsating jet, the temperature was 1500 K at the tailpipe inlet and 700-950 K at the tailpipe exit. The temperature at the tailpipe exit should be only slightly lower than that at the tailpipe inlet if ambient air was well contained outside the impingement zone. Steady jets were generated by using a short tailpipe (25.4 mm). The temperatures of steady jets were adjusted by adding excess air so that the temperature at the tailpipe exit was about the same as that of the pulsating jet for each respective case. That is, the steady jets had much lower energy rate input or fuel flow rates than the pulsating jet. If the comparison was based on the same energy input rate and the same mean mass flow rate, the temperatures of steady jets would have been higher (so would jet velocity), the drying rates would be higher and the enhancement factor would be lower.

Another factor for the comparison is mean jet velocity. As discussed in a later section, the mean velocity of a pulsating jet at the tailpipe exit corresponds to the maximum temperature in the oscillation cycle, not the mean temperature averaged over the cycle. It could be assumed that the maximum temperature of the pulsating jet in the experiment was much higher than the mean temperature. Hence, the corresponding density for the mean velocity of the pulsating jet was lower than that of the steady jet. That is, the mean velocity of the pulsating jet was possibly higher than that of the steady jet. If this assumption is reasonable, the effects of higher jet temperature and velocity could also help enhance impingement heat transfer as compared to the steady jet. Correction factors can be estimated for surface heat fluxes from steady jets by using the Martin correlation for a single round nozzle, in which the area-averaged Nusselt number is proportional to $Re^{0.574}$. The assumption is that, for a fair comparison with the pulsating jet, the temperature of the steady jet increases from 950 K to 1200 K for the confined impingement condition with $H/D = 1$ and that the surface temperature is 373 K. From the correlation, correction factors due to changes in velocity, temperature, and air properties are 1.14, 1.43, and 0.94, respectively. Thus, the overall correction factor for the steady jet is 1.53. In other words, the enhancement factor for this impingement condition would decrease to about 1.44, which is still an encouraging result considering cool ambient air could reach the impingement zone and might affect surface heat transfer for the pulsating jet.

Psimas et al. (2007) used the same pulse combustor to generate pulsating jets and calculated impingement heat fluxes from historical trends of surface temperatures measured by fast-response temperature sensors embedded in an impingement plate. The concept of comparison between steady and pulsating jets was the same as above (same mean mass flow rate and same mean tailpipe exit temperature). However, the construction and materials for impingement geometry in this experiment were much improved compared to the earlier drying experiment. One condition of pulsating jets was similar to that in the drying experiment (confined impingement with $H/D = 1$). This condition will be used as a validation case for the CFD simulation in Chapter 5.

3.2 Impingement Heat Transfer Simulations

The work presented here is for pulsating jets from a round tailpipe impinging onto an impingement surface with confinement. An objective of the simulations was to preliminarily study the characteristics of pulsating jet impingement flows and heat transfer. The diagram of the computational domain is shown in Figure 3.2. The constant parameters were diameter, D = 25.4 mm, mean velocity, u_m = 50 m/s, frequency, f = 125 Hz, jet temperature (maximum temperature at the tailpipe exit), T_j = 1200 K, and surface temperature, T_s = 373 K (as temperature during drying). The variables were velocity ratio, ε = 2-10, and nozzle-to-surface spacing ratio, H/D = 1-4. The flows were assumed to be incompressible, with temperature-dependent fluid properties, including density. The boundary condition at the inlet was velocity oscillation with a sinusoidal pattern (superimposed on the mean velocity). The backflow temperature at the outlet was 300 K. The turbulence model was a low-Re version of the standard k-ω model. The simulations were performed using the commercial software FLUENT. Simulation results, in general, were as expected, i.e., impingement heat transfer increased with increasing jet velocity amplitude as shown in Figure 3.3. Heat fluxes in Figure 3.3 were time-averaged over one oscillation cycle and area-averaged from the stagnation point up to radial distance, r = 5D.

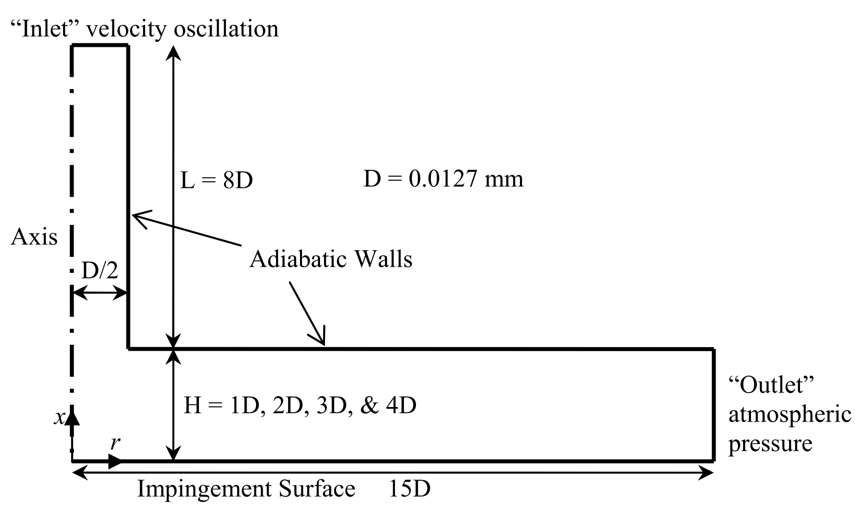

Figure 3.2: Computational domain for preliminary work of impingement heat transfer

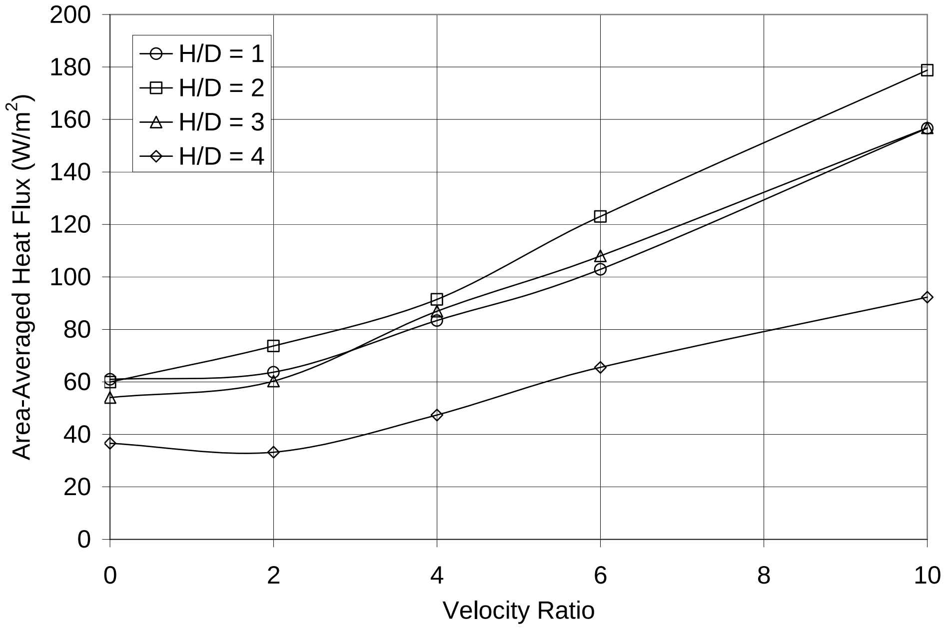

Figure 3.3: Area-averaged heat fluxes up to *r/D* = 5 from preliminary impingement heat transfer simulation.

The cases with $\varepsilon = 4$ are of particular interest because most of the pulsating jets discussed in this dissertation have a velocity ratio close to 4.0. Figures 3.4 and 3.5 show time-averaged profiles of local heat fluxes and area-averaged enhancement factors, respectively. The enhancement factors were calculated from area-averaged heat fluxes up to corresponding locations, compared to those from the steady jet at the same nozzle-to-surface spacing ratio, *H/D*. In general, the enhancement factor increases with radial distance from the stagnation point except for the case with *H/D* = 1, where the enhancement factor drops after *r/D* = 3. This position coincides with the location where the local heat flux drops in Figure 3.4. This is caused by vortex structures and re-circulating flows in the impingement zone as shown in Figure 3.6.

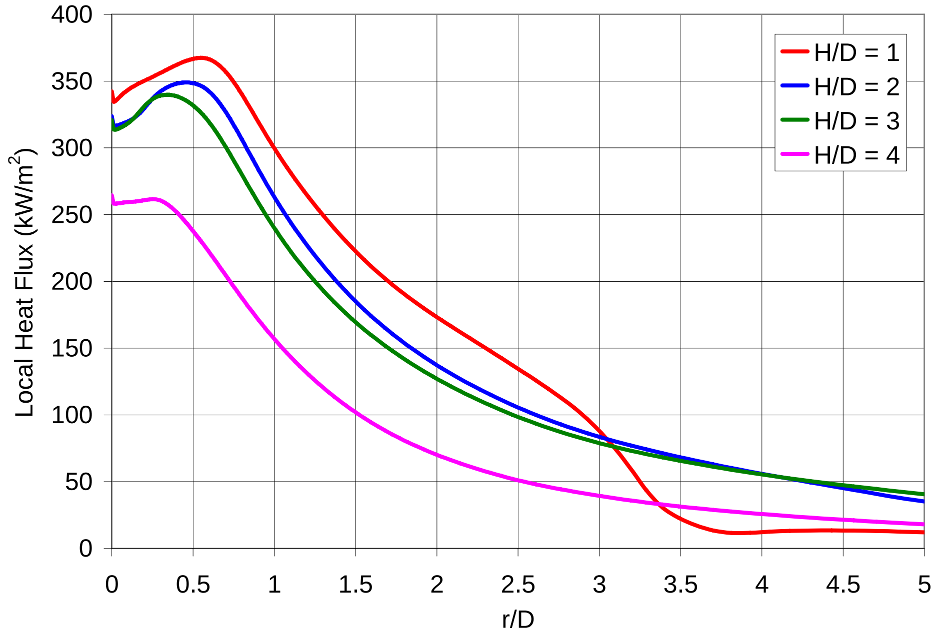

Figure 3.4: Time-averaged profiles of local heat fluxes with $\varepsilon = 4$ from preliminary impingement heat transfer simulation.

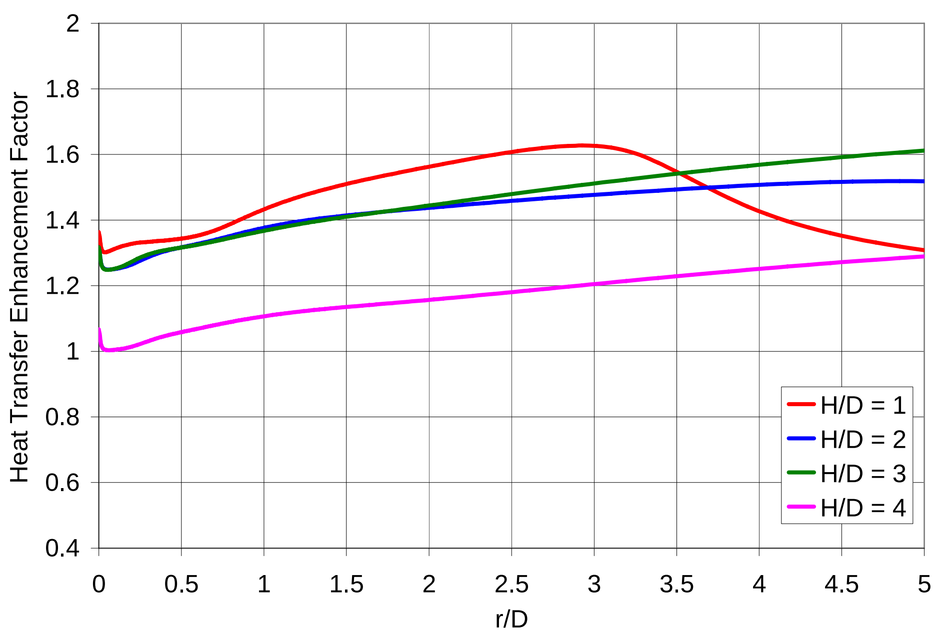

Figure 3.5: Enhancement factors with $\varepsilon = 4$ from preliminary impingement heat transfer simulation.

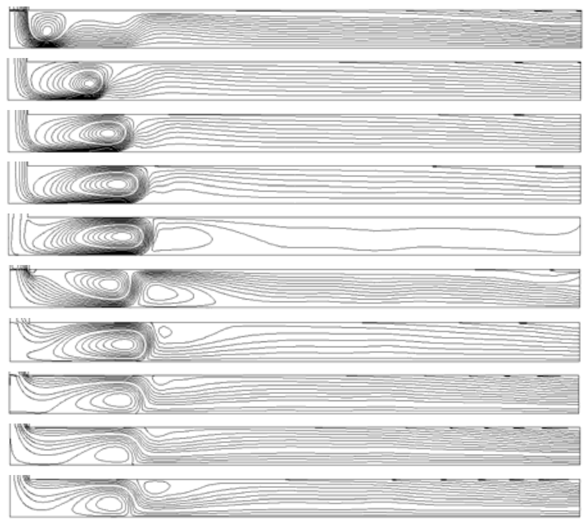

Figure 3.6: Instantaneous stream function with $\varepsilon = 4$ and $H/D = 1$ from preliminary impingement heat transfer simulation.

The normalized cycle time, $\tau = 0.1$, in Figure 3.6 corresponds to the beginning of the positive cycle of velocity oscillation (sine function), in which a toroidal vortex is generated at the edge of tailpipe exit. The primary vortex propagates and impinges onto the surface along with the impinging jet, then moves along with the wall jet. At the beginning of the negative cycle, $\tau = 0.6$, the primary vortex is counteracted by reversed flow entering the tailpipe. The primary vortex is pushed up to the confinement wall and eventually vanishes. A secondary vortex is then generated by the reversed flow. However, these behaviors only occur when the nozzle-to-surface spacing is relatively small. For H/D = 2-4, the primary vortex merges with a larger re-circulating flow in the impingement zone as shown in Figure 3.7 for the case with H/D = 3. The characteristic of the vortex in Figure 3.7 is similar to that of the vortex generated by a synthetic jet impingement flow as shown by simulation results in Li (2005).

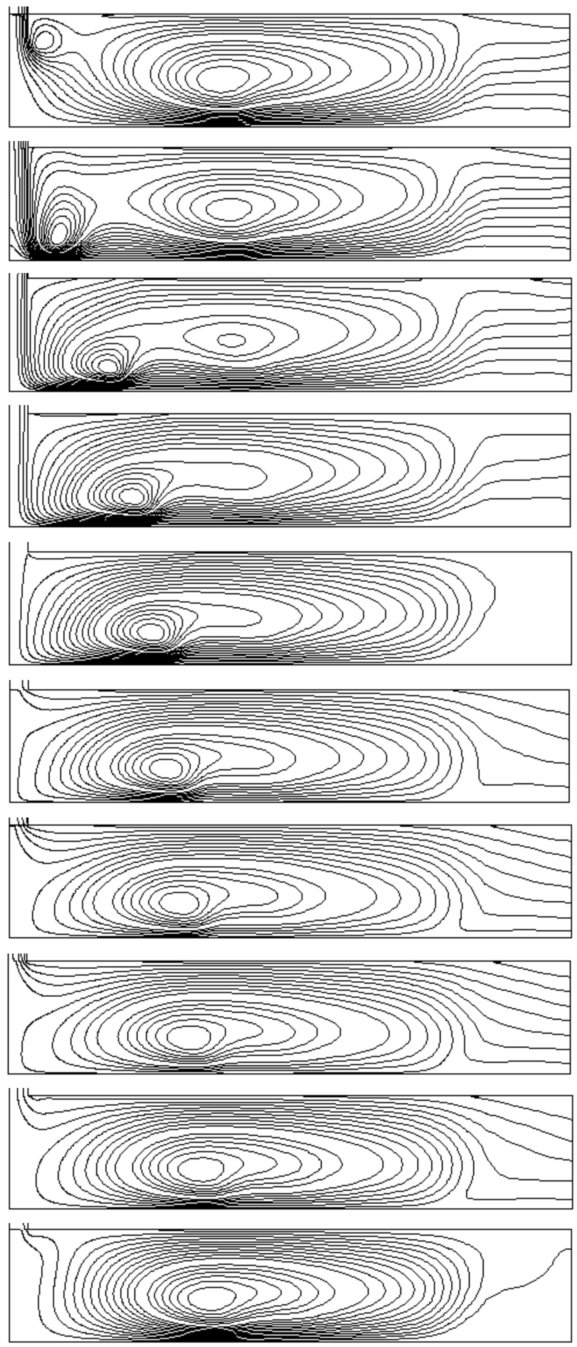

Figure 3.7: Instantaneous stream function with $\varepsilon = 4$ and $H/D = 3$ from preliminary impingement heat transfer simulation.

Instantaneous profiles of local heat flux for the case with $\varepsilon = 4$ and $H/D = 1$ and 3 are shown in Figures 3.8 and 3.9, respectively. Time-averaged profiles for the pulsating jet and the steady jet are also plotted for comparison. In general, the magnitude of surface heat fluxes near the stagnation point during the positive cycle (τ = 0.1-0.5) are higher than that of the steady jet. On the other hand, the magnitude of surface heat fluxes near the stagnation point during the negative cycle (τ = 0.6-1.0) are lower than that of the steady jet. The profiles of heat fluxes correspond to the instantaneous stream function in Figures 3.6 and 3.7, where very little or no flow impinges on the surface in the area near the stagnation point during the negative cycle.

These results suggest that the mechanism of heat transfer enhancement is the higher velocity of the impinging jet during the positive cycle. However, it should be noted that the jet temperature oscillations at the tailpipe exit in these simulations have different characteristics than those produced by an actual pulse combustor. Due to a relatively short tailpipe and high velocity amplitudes, fluid from the tailpipe exit can reach the inlet boundary during the negative cycle. In an actual pulse combustor with a longer tailpipe, all fluids entering the tailpipe during flow reversal would be driven out by fresh upstream gas within one oscillation cycle. Hence, for a portion of the cycle the jet temperature would be the temperature of fluid from around the tailpipe exit and the remainder of the cycle the jet temperature would be the high temperature of fresh gas, as measured in the experiment by Keller et al. (1993). The relative proportion of the two parts depends on the magnitude of velocity ratio, i.e., the duration of the high temperature decreases with increasing velocity ratio for the same oscillation frequency.

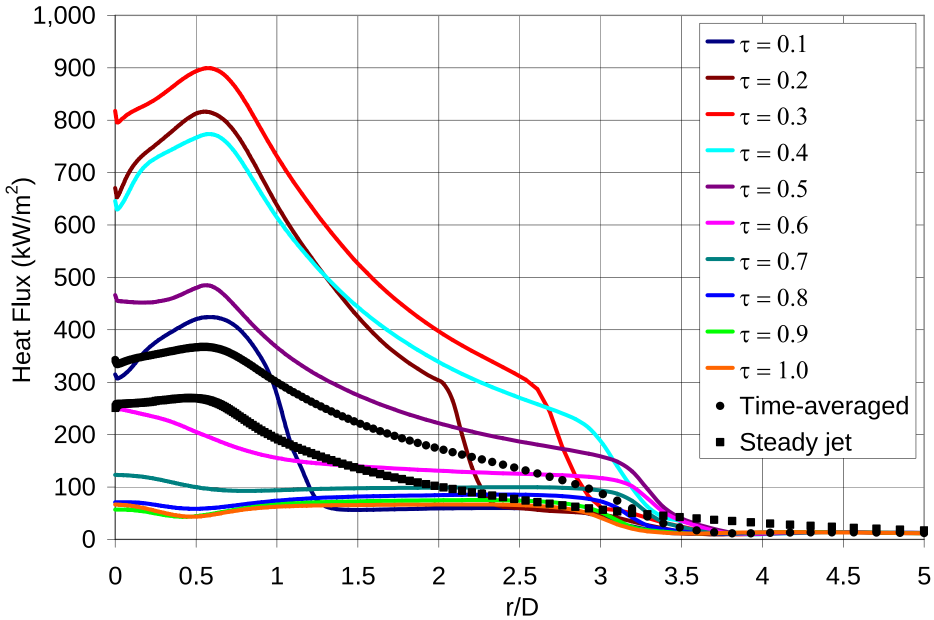

Figure 3.8: Instantaneous profiles of local heat fluxes with ε = 4 and *H/D* = 1 from preliminary impingement heat transfer simulation.

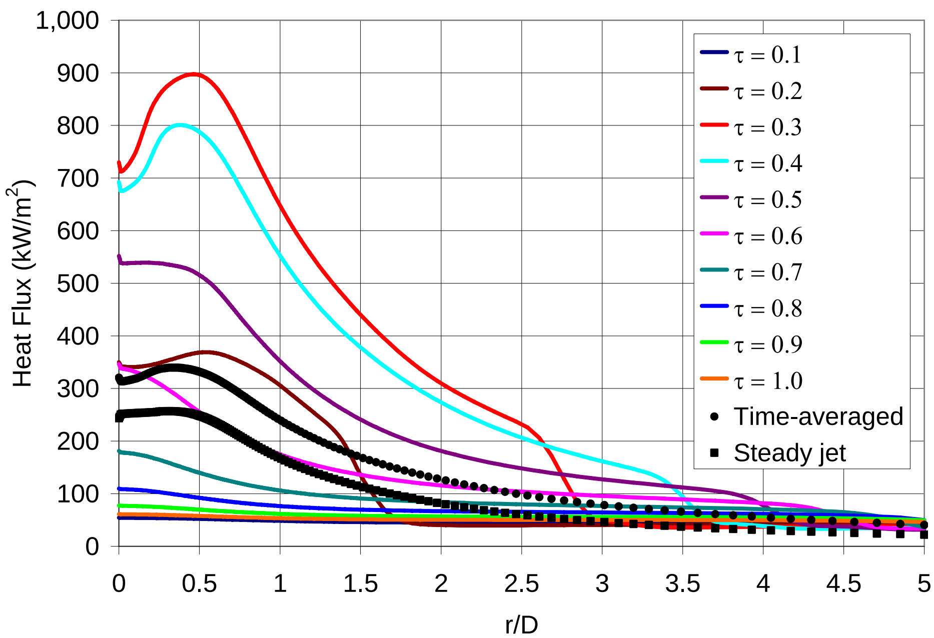

Figure 3.9: Instantaneous profiles of local heat fluxes with ε = 4 and *H/D* = 3 from preliminary impingement heat transfer simulation.

However, for these simulations, the boundary condition at the inlet imposes a high temperature as soon as the velocity is positive and cuts off reversed-flow fluid. In other words, the temperature oscillations have a longer period of high temperature than those in an actual pulse combustor. From the calculation of maximum reversed-flow distance, fluids at the tailpipe exit could flow back beyond the tailpipe inlet in the cases with $\varepsilon = 4$, 6, and 10. Such distances are $0.4L$, $1.6L$, $2.8L$, and $5.3L$ for $\varepsilon = 2$, 4, 6, and 10, respectively, where $L = 8D$ is the tailpipe length in the computational domain. Therefore, heat fluxes from those cases are likely to be higher than those for conditions with longer tailpipes. The degree of this positive bias increases with increasing velocity ratio. Therefore, in order to simulate more realistic behaviors of pulsating jets, the tailpipe in the computational domain must be longer than the maximum reversed-flow distance. Although it could be argued that it might be possible in an actual operating pulse combustor that the flow-reversed fluid could reach beyond the tailpipe length and enter the combustion chamber, flow-reversed fluid would still be driven back out of the pulse combustor during the positive cycle, as a consequence of mass conservation. In any case, for more realistic simulation results, the computational domain for the pulse combustor part must be long or large enough for flow-reversed fluids to flow in and out of the pulse combustor through the tailpipe exit.

In summary, surface heat fluxes from pulsating jets generally increase with increasing velocity ratio. The key characteristics of pulsating jet impingement flows from those simulations are vortex structures generated by pulsating jets merging with re-circulating flows in the impingement zone. With a larger nozzle-to-surface spacing, the re-circulating flow is also larger and located farther away from the stagnation point. The mechanism of heat transfer enhancement seems to be the higher jet velocity impinging onto the surface during the positive cycle. However, due to the forcing function of temperature at the inlet of the tailpipe, the results of surface heat transfer from pulsating jets with high velocity ratios is possibly higher than those with a more realistic condition, i.e., with a longer tailpipe. Such a condition was considered in the design of numerical experiments which are presented later in this dissertation.

3.3 Tailpipe Flow Simulations

The other numerical study was the simulation of pulsating flow inside a pulse combustor tailpipe. Flow conditions followed experimental data from Sandia National Laboratories (Dec and Keller, 1990 and Dec et al., 1991). An objective of the simulations was to compare the performance of incompressible and compressible flow models for this type of flow. The difference between the two flow models was in the characterization of fluid density. The density function for the incompressible flow was a polynomial function dependent on temperature only. For the compressible flow, the density was assumed to follow the ideal gas law and was therefore a function of both pressure and temperature. Another objective was to study the characteristics of the pulsating flow, especially at the tailpipe exit, with different ambient temperatures. The computational domain consisted of a round tailpipe and a relatively large open chamber connected to the tailpipe exit as shown in Figure 3.10. The inlet boundary condition was pressure oscillation with a sinusoidal pattern (superimposed on the mean pressure). Mean mass flow rate, pressure amplitude and oscillation frequency were the same as in the reference, i.e., 4 g/s, 10.5 kPa and 83 Hz, respectively. Note that the tailpipe in the Sandia experiment had a square cross-sectional area of 30x30 mm^2. In order to have a two-dimensional computational domain, a round tailpipe with a similar cross-sectional area (34 mm in diameter) was used for simulations, instead. The tailpipe length, L = 880 mm, was the same as in the reference. In order for the pulsating flow to have the target mean mass flow rate, the mean pressure at the inlet boundary was adjusted manually. The inflow temperature at the inlet boundary was 1500 K. The tailpipe wall temperature was held constant at 500 K. The turbulence model was the V2F model. The simulations were performed using the FLUENT software.

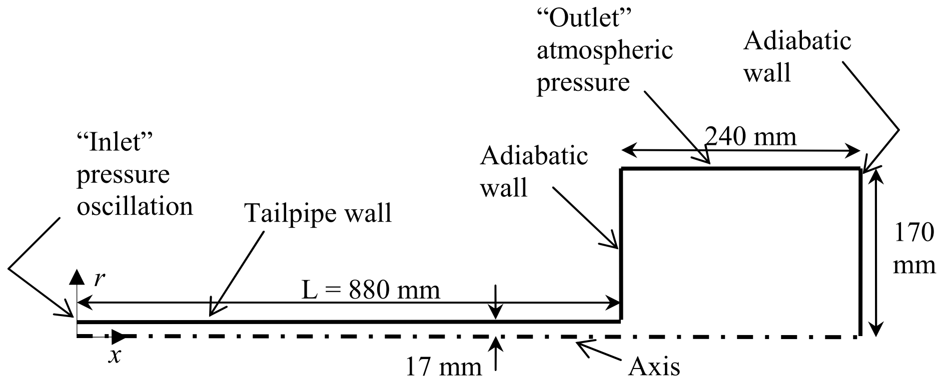

Figure 3.10: Computational domain for tailpipe flow simulations.

Three cases were simulated to study the effects of flow compressibility and ambient temperature (backflow temperature at the outlet boundary). Case 1 was the base case; the density function was the ideal gas law and the ambient temperature was 850 K. Case 2 was the same as Case 1 except that the ambient temperature was 300 K. Case 3 had the same ambient temperature as Case 1 but had a temperature-dependent function for density as for an incompressible flow. Simulation results for these three cases are summarized and compared in Figures 3.11 and 3.12 as profiles along the tailpipe of mean temperature and velocity oscillation, respectively.

From Figure 3.11, the effects of ambient temperature on temperature profiles (between Cases 1 and 2) were quite distinctive at the tailpipe exit, x/L = 1. Due to lower ambient temperature and flow reversal, mean temperatures near the tailpipe exit in Case 2 were significantly lower than those in Case 1. Based on the location where the temperature sharply dropped in the profile of Case 2, it could be deduced that the maximum distance for flow reversal was approximately 0.2L or 176 mm. The profiles for Cases 1 and 3 showed that the density function had no significant effect on mean temperature. These results could be expected. However, more interesting results were the effects of compressibility and ambient temperature on velocity oscillations as shown in Figure 3.12.

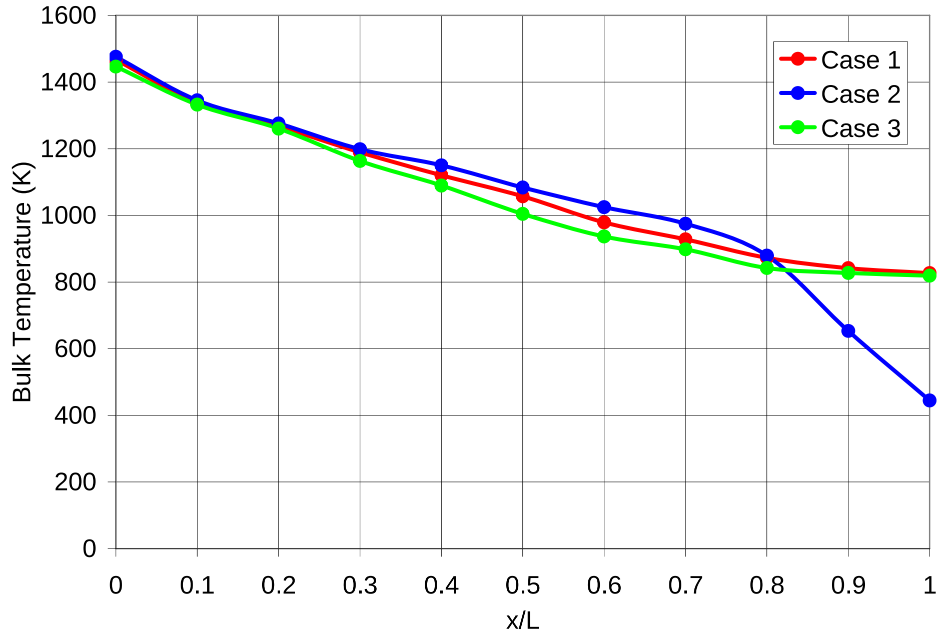

Figure 3.11: Profiles of time-averaged bulk temperature along the tailpipe.

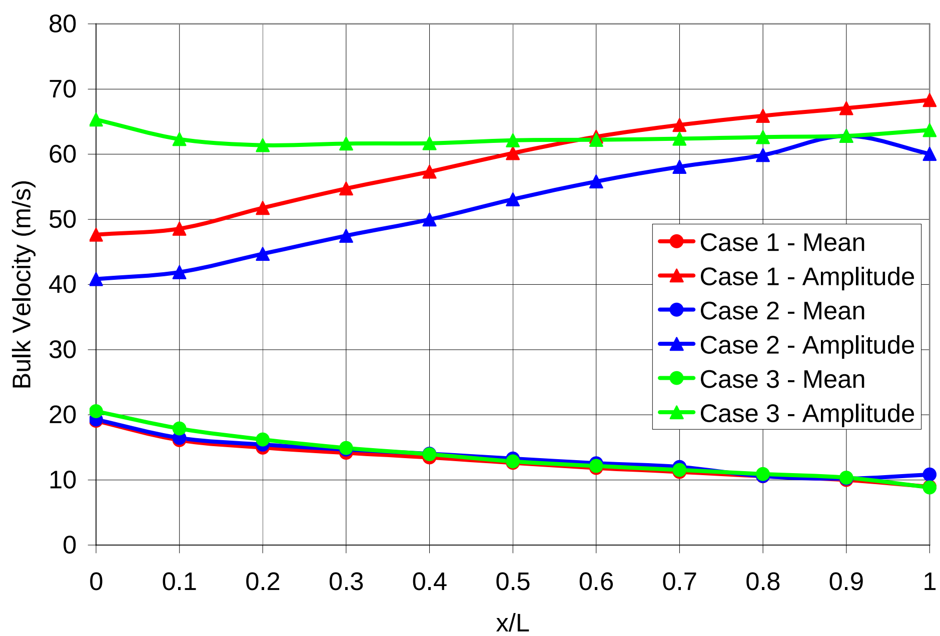

Figure 3.12: Profiles of time-averaged value and amplitude of bulk velocity oscillation along the tailpipe.

First, consider the magnitude of velocity amplitudes along the tailpipe. The difference between the compressible flow (Cases 1 and 2) and the incompressible flow (Case 3) was quite clear. The amplitude along the tailpipe was rather constant for the incompressible flow. This was expected because the conservation of mass for the incompressible flow was satisfied at any point in time, i.e., the pulsating flow behaved like a solid plug flow. The amplitude from the compressible flow increased along the tailpipe, which was consistent with experimental results in the reference. This behavior is also in agreement with the acoustic theory of quarter-wave-tube resonance (Dec et al., 1991), where the oscillation amplitude or the movement of flows is larger at the open end and sinusoidally decreases toward the closed end. However, as a Helmholtz pulse combustor has a combustion chamber at the opposite end of the tailpipe exit, the amplitude of velocity oscillation would not be zero at the tailpipe inlet but rather at the opposite wall of the combustion chamber. (In addition, due to the change in volume from the tailpipe to the combustion chamber, the magnitude of velocity oscillation would be lower in the combustion chamber.)

Mean velocities decreased along the tailpipe due to the decrease in temperature from heat loss to the wall. An interesting result was that mean velocity at the tailpipe exit for Case 2 was approximately the same as that for Case 1 despite having a significantly lower mean temperature than Case 1 (Figure 3.11). In the literature, e.g., Keller et al. (1993), the mean velocity of pulsating flows was commonly calculated from the value of density corresponding to the mean temperature. With such a concept, the mean velocity at the tailpipe exit for Case 2 would be lower than that for Case 1. This result suggests that the mean velocity of a pulsating flow corresponds to the maximum temperature in an oscillation cycle, not the mean temperature, because of the requirement of mass conservation. Figure 3.13 shows instantaneous velocity, temperature, and the integral of mass flow rate at the tailpipe exit over an oscillation cycle of Case 2. In each oscillation cycle, the conservation of mass requires the same amount of fluid mass to flow out of the tailpipe from the inlet through the exit. Thus, all ambient fluid entering the tailpipe during flow reversal has to be driven out within a cycle. Then, the fresh hot fluid from upstream of the tailpipe would exit the tailpipe in the same net amount of fluid that entered the tailpipe inlet. In other words, the mean velocity is responsible for driving out the required amount of fresh hot gas from the upstream end of the tailpipe in each oscillation cycle. And the oscillating part of the velocity is responsible for pulling in and driving out the reversed-flow fluid from the downstream end of the tailpipe.

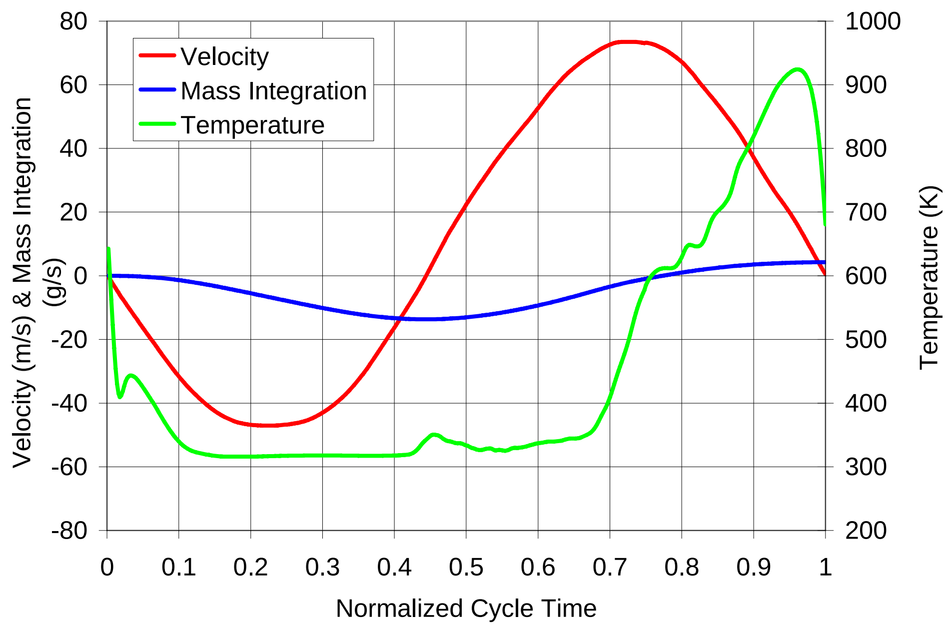

Figure 3.13: Oscillations of velocity and temperature at the tailpipe exit for Case 2, as well as the integral of mass flow rate.

Figure 3.14 shows the profiles of the mean value and oscillation amplitude of mass flow rate along the tailpipe. As expected, mean mass flow rates were the same along the tailpipe for all cases. The oscillation amplitude at the tailpipe exit for Case 2 was much higher than that for the other cases because the density of ambient fluid is higher for Case 2. As discussed earlier, the magnitude of mass flow rate amplitude at the tailpipe exit for Case 2 (~56 g/s) can be calculated from the oscillation amplitude of velocity at the tailpipe exit (~60 m/s) and the density corresponding to the temperature of ambient fluids around the tailpipe exit (~1.01 kg/m^3 and ~320 K, respectively). The mean mass flow rate (~4 g/s) can be calculated from the mean velocity (~11 m/s) and the density corresponding to the temperature of hot fresh gas (~0.41 kg/m^3 and ~850 K, respectively). The concept of these calculations is important for the evaluation of measurement data for laboratory pulse combustors because the velocity oscillation is usually not measured directly but calculated from other measurement data, i.e., total mean mass flow rate of reactants, mean temperature at the tailpipe exit, and the pressure amplitude in the combustion chamber. Accurate approximations or calculations of both mean velocity and velocity amplitude are required for the determination of jet velocity ratio as the key parameter for the heat transfer enhancement factor. The approximation of velocity amplitude in this dissertation is based on a solution of acoustic wave equations and discussed in detail in the following chapter.

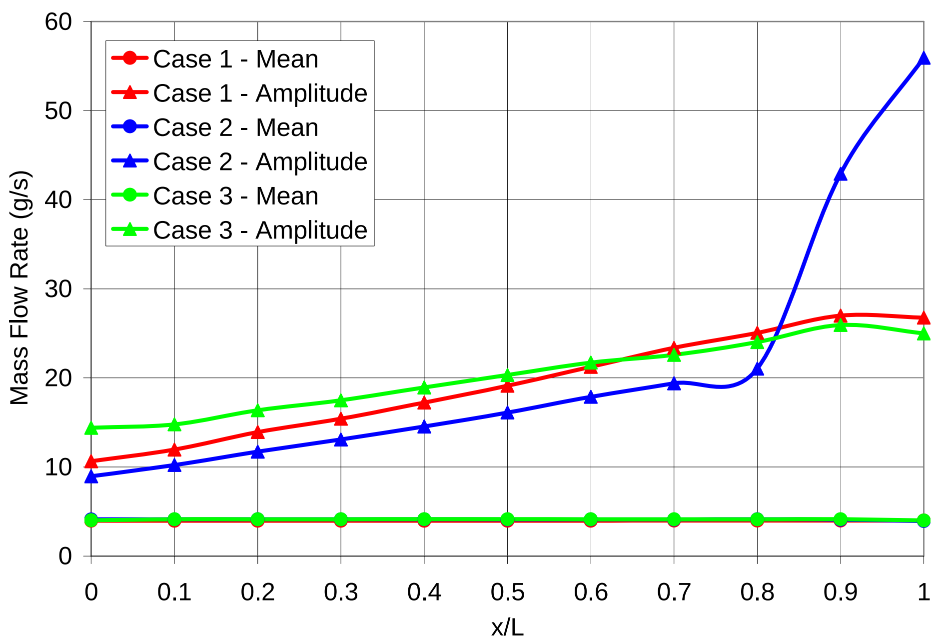

Figure 3.14: Profiles of time-averaged value and amplitude of mass flow rate oscillation along the tailpipe.

Regarding the performance of the simulations, results showed that the simulations using the compressible flow model converged much faster than that using the incompressible flow model, possibly because compressible flows were more physically reasonable or accurate than incompressible flows for this type of pulsating flow, which had relatively large pressure variations. The assumption of incompressible flow is usually satisfied with steady flows or flows with small pressure variations. Therefore, the compressible flow model will be used for the simulations in this dissertation.

Another aspect of the simulations in this preliminary work is the inlet boundary condition of pressure oscillation. In order for the pulsating flows to have the desired mean mass flow rate, the mean value of pressure oscillation at the inlet boundary had to be adjusted manually because it could not be approximated or calculated beforehand. At each step, the simulation had to be run for about 20-30 cycles until the oscillation was stable before the result could be evaluated. Furthermore, in other cases, it was found that the mean mass flow rate was too sensitive to the mean pressure, i.e., the mean mass flow rate dramatically changed even with a small step change in mean pressure when the mean mass flow rate was close to the target value. This indicated the existence of a criterion for stability (or instability) for this kind of boundary condition. It would be possible to write a user-defined code using an optimization algorithm for the simulation software to automatically search for a mean pressure that result in the desired mean mass flow rate. However, it might take quite a long time to reach the target because the evaluation in each step has to wait until the oscillation is stable. In addition, there was no guarantee that a stable condition would exist at the target value. Therefore, another type of inlet boundary condition was required to generate a pulsating flow, with controllable or predictable parameters of velocity oscillation, i.e., both mean velocity and velocity amplitude. After several attempts, the inlet boundary condition in this dissertation was chosen to be a mass flow rate oscillation at the boundary of an inlet chamber, similar to the combustion chamber of a Helmholtz pulse combustor, before the tailpipe. With this condition, the mean velocity at the tailpipe exit could be easily and accurately determined. As for the velocity amplitude, it could be estimated from the dimensions of the inlet chamber and the tailpipe by using simplified balance equations in the inlet chamber and a solution of pulsating tailpipe flow. The calculations of velocity oscillation are described in Chapter 5.

In summary, the compressible flow model yielded more physically reasonable results than the incompressible flow model, i.e., the oscillation amplitude of velocity increased along the tailpipe. From the simulation results, it could be deduced that the mean velocity of a pulsating flow in the tailpipe corresponded to mean mass flow rate and the temperature of hot fresh gas from upstream in the tailpipe. The amplitude of the mass flow rate oscillation corresponded to the amplitude of velocity oscillation and the temperature of cooler reversed-flow fluid from downstream in the tailpipe. As for the performance of the numerical approach with pressure oscillation as the inlet boundary condition, it was difficult to adjust the mean pressure so that the pulsating flow would have the desired mean mass flow rate. Therefore, another inlet boundary condition was required for more effective performance. As discussed in Chapter 5, the inlet boundary condition for this dissertation is a mass flow rate oscillation.

3.4 Summary

Three preliminary studies, one laboratory experiment and two numerical experiments, were conducted in order to gain basic understanding of the characteristics of pulsating flows and jet impingement heat transfer. The drying experiment showed an encouraging result for impingement heat transfer enhancement using a pulsating jet. For the impingement condition with confinement and a nozzle-to-surface spacing of one tailpipe diameter (H/D = 1), the enhancement factor for the drying rate of paper samples was about 2.2, compared to the steady jet with the same mean mass flow rate and mean temperature at the tailpipe exit. The analysis showed that this condition of the steady jet had lower velocity and temperature than the mean velocity and the maximum temperature of the pulsating jet, respectively. A correction factor of 1.53 was calculated from the

Martin correlation for the steady jet having equivalent velocity and temperature to those of the pulsating jet. Thus, the enhancement factor for such condition was evaluated to be about 1.4, which was still an encouraging result considering cool ambient air could reach the impingement zone.

The simulations of pulsating jet impingement flow and heat transfer showed that surface heat fluxes from pulsating jets generally increased with increasing velocity amplitude. The key characteristics of pulsating jet impingement flows were shown to be vortex structures generated by pulsating jets propagating along with the impinging jet and the wall jet then merging with re-circulating flows in the impingement zone. The re-circulating flow was larger and located farther away from the stagnation point with larger nozzle-to-surface spacings. The mechanism of heat transfer enhancement seemed to be the higher jet velocity impinging onto the surface during the positive cycle as heat fluxes were low during the negative cycle. However, due to the boundary condition of temperature at the inlet of the tailpipe, the results of surface heat transfer from pulsating jets with high velocity ratios were possibly higher than those with a more realistic condition, i.e., with a longer tailpipe, because the inlet temperature was forced to be a high value as soon as the velocity was positive.

The simulations of pulsating flows in the tailpipe of a pulse combustor showed that the compressible flow model yielded more physically reasonable flow characteristics than the incompressible flow model, i.e., the magnitude of velocity amplitude increased along the tailpipe. It could be deduced that the mean velocity of a pulsating flow in the tailpipe corresponded to the mean mass flow rate and the temperature of hot fresh gas from upstream in the tailpipe, not the mean temperature, and that the amplitude of mass flow rate oscillation corresponded to the amplitude of velocity oscillation and the temperature of cooler reversed-flow fluid from downstream in the tailpipe.

As for the numerical approach of the simulations in this dissertation, results from those numerical studies suggested that the compressible flow model should be used due to more accurate results and faster convergence rate compared to the incompressible flow model. The tailpipe should be long enough to allow ambient fluids flowing in and out of the tailpipe. For the inlet boundary condition with pressure oscillation, it was difficult to find the mean pressure that resulted in the desired mean mass flow rate of the pulsating flow in the tailpipe. Therefore, another type of inlet boundary condition was required. As discussed in Chapter 5, the inlet boundary condition for this dissertation will be mass flow rate oscillation.

CHAPTER 4

A SIMPLIFIED MODEL OF HELMHOLTZ PULSE COMBUSTORS

This chapter describes the development of a simplified model of Helmholtz pulse combustors, which could be regarded as a zero-dimensional model for the combustion chamber and a one-dimensional model for the tailpipe flow. The primary objective of the model is to provide some basic theoretical considerations for the pulse combustor of the PAD project, in particular, how to produce a pulsating jet with the highest possible velocity ratio. The purpose of the development of this model is by no means to outperform other simplified models. It is developed because information concerning the characteristics of heat release and reactant injection is not available from the laboratory PAD pulse combustor. Therefore, with some simplifying assumptions, the specific information required for this model is reduced to one parameter, i.e., the heat release amplitude ratio (called energy ratio in this chapter), which could be evaluated from one operating condition of the pulse combustor. A useful aspect of this model is that it can be solved within a very short turnaround time using a standard spreadsheet program. Another aspect is that a result from further simplification of the model can be used to design a computational domain for the CFD simulations given a mass flow rate oscillation at the inlet boundary and a target velocity oscillation at the tailpipe exit. The further simplified model for CFD simulations is described in the next chapter.

4.1 Introduction

As discussed in Chapter 2, the characteristics of the flows and combustion process in the combustion chamber of a Helmholtz pulse combustor are complex and coupled with the pulsating flow in the tailpipe. Flow paths and the mixing rate of reactants depend on the geometry of the combustion chamber and the stagnation plate as well as inlet flow parameters, i.e., mean mass flow rate and air/fuel ratio. Pulsating flow parameters, e.g., pressure amplitude, pulsation frequency, and velocity amplitude, have nonlinear relationships with the dimensions of the pulse combustor and couple with one another. These relationships can be predicted, at least qualitatively, with simplified models as reviewed in Chapter 2. However, for accurate predictions within limited ranges of parameters, specific information from experiments is required, especially details of the processes occurring in the combustion chamber, e.g., patterns of heat release and reactant injection. For the PAD project, such information is not available. Therefore, the present model applies simplifying assumptions for the patterns of some parameters, i.e., oscillations of pressure and mass flow rate in the combustion chamber. These assumptions also allow the model to be solved easily and quickly.

Typically, a one-dimensional pulse combustor model has to solve the governing equations of pulsating flow in the combustion chamber and the tailpipe simultaneously. For simplicity, the present work adopts the explicit solution of velocity amplitude along the tailpipe from Ahrens (1979), together with the concept of the calculation of mean velocity in the tailpipe discussed in the previous chapter. The derivation of the solution of tailpipe velocity amplitude, based on acoustic wave equations, was not included in the Ahrens paper, and so is provided in the Appendix. The amplitude of the velocity oscillation in the tailpipe is coupled with the amplitude of the pressure oscillation in the combustion chamber, whereas the mean velocity is coupled with the mean mass flow rate of the pulse combustor.

The pulsating flow in the combustion chamber is obtained by solving the conservation equations of mass and energy. For simplicity, the present work applies the concept of a zero-dimensional model, i.e., pressure, temperature, and heat release are spatially uniform in the combustion chamber. A key assumption for this model is that the pattern of pressure oscillation is perfectly sinusoidal. Although this pattern is not physically accurate, it is a reasonable approximation as shown in Dec et al. (1991). As a result of this assumption, the velocity oscillation in the tailpipe also has a perfect sinusoidal pattern with a quarter-cycle phase lag (see Appendix). Another assumption is that the pattern of reactant injection can be characterized as flow through a valve, i.e., a function of the square-root of pressure difference, or in this case, negative (gauge) pressure in the combustion chamber. As the pattern of pressure oscillation is established, this allows the pattern of reactant injection to be easily determined. The reactant injection and the velocity oscillation at the tailpipe inlet satisfy the mass balance in the combustion chamber.

As for the energy balance, the heat release rate functions as a source term. In some simplified models, the pattern of heat release is provided and the model solves for pressure and velocity oscillations. For this model, as other parameters are already assumed or established, the model will solve for the heat release oscillation. As discussed in Chapter 2, the amplitudes of pressure and heat release are directly related. However, both parameters are not known beforehand for a given set of pulse combustor dimensions and mean mass flow rate. Therefore, one of the two parameters has to be assumed or evaluated from an operating condition of the pulse combustor. In this case, the amplitude of heat release is pre-specified so that the pressure amplitude can be predicted. But as the pressure amplitude is an input parameter of the model, the prediction is done by finding a value of pressure amplitude that matches the solution of the model, i.e., heat release oscillation, with the pre-specified value of heat release amplitude. And because the mean value of heat release ($\dot{q}_m$) can be approximated from the mean mass flow rate of fuel and the heat of combustion, the heat release amplitude ($\dot{q}_A$) is specified in terms of heat release amplitude ratio (α), i.e., $\alpha = \dot{q}_A / \dot{q}_m$. In the remainder of this dissertation, this term is referred to as energy ratio.

The other key parameter is pulsation frequency. Several simplified models simply use the frequency of a Helmholtz resonator as the prediction. More sophisticated models attempt to satisfy the Rayleigh criterion, i.e., take the overall delay time of heat release into account so that heat release oscillation is in phase with pressure oscillation. For the present work, the frequency prediction follows the expression of frequency derived from the acoustic wave equations for tailpipe velocity amplitude in Ahrens (1979). This expression is a generalized form of the expression for the frequency of a Helmholtz resonator, applicable when the volume ratio between the combustion chamber and the tailpipe is arbitrary. As shown in the Appendix, for small volume ratios, the frequency of a Helmholtz resonator is higher than the frequency derived from the acoustic wave equations. As shown later, this acoustic frequency has a linear relationship with the mean speed of sound in the tailpipe but a nonlinear relationship with the dimensions of the pulse combustor, i.e., tailpipe length and volume ratio. In order that the model can use the acoustic frequency as an operating frequency for the pulse combustor, the mean speed of sound in the tailpipe has to be estimated.

The mean speed of sound for this model is calculated from the mean temperature in the tailpipe, which is estimated from the condition of the pulsating flow in the tailpipe, i.e., maximum temperatures at the inlet and the exit, ambient temperature, and velocity ratio. The estimation of the mean temperature is done by assuming that the pulsating flow behaves as a plug flow using the velocity oscillation at the tailpipe exit and that ambient fluid entering the tailpipe during flow reversal does not mix with fluid from upstream in the tailpipe, but maintains two separate compartments of fluid during the oscillation in the tailpipe. This methodology allows the mean temperature in the tailpipe, and the resulting frequency, to change with the velocity ratio at the tailpipe exit. The ambient temperature is usually lower than the temperature of pulsating flow upstream. Hence, the mean temperature and the frequency will be lower when the velocity ratio is higher because cooler ambient fluid can reach farther inside the tailpipe.

The complete simplified model consists of three submodels: combustion chamber pressure and flow oscillations, tailpipe velocity oscillation, and mean tailpipe temperature. Key simplifying assumptions for the model are summarized as follows:

1. Patterns of pressure and velocity oscillation are perfectly sinusoidal.
2. Pressure, temperature, and heat release in the combustion chamber are spatially uniform.
3. Heat transfer to the combustion chamber wall is negligible.

4. The flow of reactants through a one-directional valve behaves like a quasi-steady flow, i.e., the pattern of reactant injection is a function of the square-root of the sinusoidal pressure oscillation.
5. The pulsation frequency follows the acoustic frequency of the pulse combustor.

Additional simplifying assumptions for the derivation of the submodels are provided in the corresponding sections. The diagram of the model and the symbols of key parameters are shown in Figure 4.1: $\dot{m}_1$ and $\dot{m}_2$, mass flow rate at the inlet and the exit of the combustion chamber, respectively; p_C, T_C, and $\dot{q}_C$, pressure, temperature, and heat source in the combustion chamber, respectively; $p_T(x)$ and $u_T(x)$, pressure and velocity along the tailpipe, respectively; u_2 and u_3, velocity at the inlet and the exit of the tailpipe, respectively; x, distance from the tailpipe inlet; and L, tailpipe length.

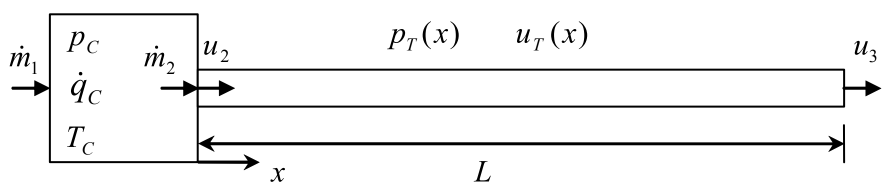

Figure 4.1: Diagram for the simplified model of Helmholtz pulse combustors.

Input parameters for the model are combustion chamber volume, V_C; tailpipe length, L; tailpipe cross-sectional area, A_T; volume ratio, $\beta = V_C/V_T = V_C/(A_T L)$; mean mass flow rate, $\dot{m}_m$; equivalence ratio, ϕ; mean heat release or energy input rate, $\dot{q}_{Cm}$, calculated from $\dot{m}_m$ and ϕ; atmospheric pressure, p_a; pressure amplitude, p_{CA}; adiabatic flame temperature, T_{j2}, corresponding to the equivalence ratio, ϕ, of fuel and air; jet (or maximum) temperature at the tailpipe exit, T_{j3}, and ambient temperature, T_a. The resulting parameters of interest are heat release amplitude, $\dot{q}_{CA}$, and energy ratio, $\alpha = \dot{q}_{CA}/\dot{q}_{Cm}$, from the combustion chamber submodel; mean velocity and velocity amplitude at the tailpipe exit, u_{m3} and u_{A3}, respectively, and velocity ratio, $\varepsilon = u_{A3}/u_{m3}$, from the tailpipe velocity submodel; and mean temperature in the tailpipe, T_{Tm}, and frequency, f, from the mean tailpipe temperature submodel.

The derivation of the three submodels is described in the following sections. After the models are described the available experimental data are applied to the model in order to evaluate the typical range of energy ratio of operating pulse combustors. The final section uses the model to evaluate the energy ratio for an operating condition of the laboratory pulse combustor used in the PAD project and then to study the effects of some input parameters on pulsating flow characteristics, i.e., pressure amplitude in the combustion chamber, frequency, and velocity ratio at the tailpipe exit.

4.2 Combustion Chamber Submodel

The submodel for the combustion chamber is simply the conservation equations of mass and energy. With previously stated and additional assumptions, the result is a solution for the heat source. First, the expressions for pressure oscillation in the combustion chamber and velocity oscillation at the tailpipe inlet are the following.

$$p_C = p_a + p_{CA} \sin(\omega t) \tag{4.1}$$

$$u_2 = u_{m2} - u_{A2} \cos(\omega t) \tag{4.2}$$

From a simplified momentum equation for pulsating flow in the tailpipe, the phase of pressure oscillation leads that of velocity oscillation by a quarter of a cycle. The mean pressure in the combustion chamber is assumed to be equal to atmospheric pressure, p_a. The pressure amplitude in the combustion chamber, p_{CA}, is specified in this model so that the heat source can be determined. The mean velocity at the tailpipe inlet, u_{m2}, is calculated from mean mass flow rate, $\dot{m}_m$, and density corresponding to the maximum temperature in the combustion chamber, which is estimated by the adiabatic flame temperature. The velocity amplitude, u_{A2}, is calculated from the tailpipe velocity submodel in the next section. Consequently, the mass flow rate at the combustion chamber exit or the tailpipe inlet, $\dot{m}_2$, can be calculated as

$$\dot{m}_2 = \rho_C A_T u_2 \tag{4.3}$$

The mass flow rate of the reactants at the inlet of the combustion chamber, $\dot{m}_1$, depends on the type and size of one-directional valves and the pressure difference across the valves. Several simplified models assumed constant area of the valves over the negative pressure period or a quasi-steady flow characteristic, whereas other models modeled the dynamic movement of flapper valves and calculated the corresponding mass flow rates. For this model, the total inlet mass flow rate, as the combination of premixed air and fuel flows, is assumed to behave as a one-directional quasi-steady flow through a valve with the supply pressure equal to the mean pressure in the combustion chamber. That is, when the combustion chamber pressure is greater than the mean value, the valve is closed and the inlet mass flow rate is zero. When the combustion chamber pressure is lower than the mean value, the mass flow rate is equal to a coefficient of flow through the valve multiplied by the square-root of the pressure difference, which is the pressure oscillation in the combustion chamber during the negative cycle. However, as the model input parameter is specified as a mean mass flow rate instead of the supply pressure and valve size, the constant parameters can be lumped together as a new constant and the mean mass flow rate as

$$\dot{m}_1 = \begin{cases} 0 & , \; p_C > p_a \quad (0 \le \omega t \le \pi) \\ C_1\sqrt{-p_{CA}\sin(\omega t)} = C_2 \dot{m}_m \sqrt{-\sin(\omega t)} & , p_C < p_a \quad (\pi \le \omega t \le 2\pi) \end{cases} \tag{4.4}$$

where $C_1 = \sqrt{2\rho_1} c_{D1} A_{v1}$, ρ_1 is the density of premixed reactants, c_{D1} is the discharge coefficient of the reactant valve, and A_{v1} is the effective flow area of the reactant valve (Ahrens et al., 1978). The expression with the second term of the right side requires that the time-average of $\dot{m}_1$ be equal to $\dot{m}_m$. This in turn requires that the constant C_2 have a value of 2.623. Thus, it can be expressed that

$$C_1\sqrt{p_{CA}} = C_2 \dot{m}_m$$

This expression suggests that, as C_1 is constant if the same valve is used, the pressure amplitude could be predicted or calculated directly from the mean mass flow rate through the same valve. However, this might not be the case in an actual operating pulse combustor, as demonstrated by Keller et al. (1989), in which the mean mass flow rate and the equivalence ratio were held constant while the position of the stagnation plate was adjusted resulting in a change in pressure amplitude and frequency. That was probably done by adjusting the supply pressure of reactants so that the pressure difference across the valve was the same for each case. Another possible explanation was that the quasi-steady assumption was not valid for the pulse combustor, as several models used a moving flapper-valve model resulting in a variable flow area, instead of a constant flow area. In any case, for simplification purposes, the second term on the right side of Equation (4.4) is used in the present work so that the mean mass flow rate can be treated as an input parameter. Thus, Equation (4.4) reduces to

$$\dot{m}_1 = \begin{cases} 0 & , \ p_C > p_a \quad (0 \le \omega t \le \pi) \\ 2.623\dot{m}_m\sqrt{-\sin(\omega t)} & , p_C < p_a \quad (\pi \le \omega t \le 2\pi) \end{cases}, \tag{4.5}$$

Given the mean mass flow rate and equivalence ratio of air and fuel, a mean value of energy rate input or heat release can be calculated from the mean mass flow rate and the heat of combustion of the fuel. Likewise, an adiabatic flame temperature can be estimated from the equivalence ratio for a given fuel. From tables of gas properties (Çengel & Boles, 2001), a linear relationship between gas enthalpy and temperature can be established, especially within a typical range of adiabatic flame temperature.

$$h = aT + b \tag{4.6}$$

The values of coefficients, *a* and *b*, for air are 1.2 kJ/kg.K and -159 kJ/kg, respectively, in the range of temperature, T = 800-2200 K. Note that *a* is basically an average value of the specific heat at constant pressure. For this model, these coefficients would be varied with the equivalence ratio and fuel type, being established from the composition of products resulting from complete combustion and excess air, i.e., CO_2, H_2O, O_2 and N_2. In practice, the mean temperature in the combustion chamber is lower than the adiabatic flame temperature due to heat loss at the walls. For simplicity, the heat loss is neglected in this model. For application with experimental data, however, measured values of equivalence ratio and mean temperature in the combustion chamber are used.

Given specific pulse combustor dimensions and the above assumptions, only two variables, temperature and heat source, $\dot{q}_C$, are left to be solved from the conservation equations of mass and energy in the combustion chamber. The variable of interest is the heat source or heat release rate because, for this model, its oscillation amplitude can be interpreted as an indicator of the phase relationship between heat release and pressure oscillations.

It is noteworthy here that the solution of heat source oscillation from this submodel might not be physically accurate in terms of the phase relationship with pressure oscillation, due to several assumptions applied for simplification purposes. From the observation of model results, the heat source oscillations are rather in-phase the with velocity oscillations, i.e., lagging pressure oscillations instead of leading as in actual Helmholtz pulse combustors. However, experimental data in Keller et al. (1989) suggests that there could be a correlation between the amplitude and the phase of heat release rate oscillation. That is, with a longer delay time of the heat release, the oscillation of the heat release rate is more in-phase with the pressure oscillation and the amplitude ratio of the heat release rate is higher. Hence, despite the lack of physical accuracy in terms of heat source oscillation phase, the interpretation of the heat release amplitude ratio from the model will be linked to the phase relationship between heat release rate and pressure, i.e., the Rayleigh criterion.

As the magnitude of heat release rate or heat source is always positive, the amplitude of heat source, $\dot{q}_{CA}$, is defined by the averaged value of the “positive” portion, $\dot{q}_{C+}$, which is higher than the mean value, $\dot{q}_{Cm}$, as

$$\dot{q}_{CA} = \frac{\omega}{2}\int_0^{1/f} \dot{q}_{C+}dt, \qquad \dot{q}_{C+} = \begin{cases} \dot{q}_C - \dot{q}_{Cm} & , \qquad \dot{q}_C > \dot{q}_{Cm} \\ 0 & , \qquad \dot{q}_C < \dot{q}_{Cm} \end{cases} \tag{4.7}$$

where $\dot{q}_{Cm}$ is the mean value of heat source. The ratio between the amplitude and the mean value of heat source was referred to as heat release ratio in previous chapters. For the model, this quantity is referred to as energy ratio, α, following the terminology used in Neumeier (1993).

$$\alpha = \dot{q}_{CA} / \dot{q}_{Cm} \tag{4.8}$$

In practice, the energy ratio is determined by the geometry of the combustion chamber, the stagnation plate position, and the flow rates of reactants. Since the model is highly simplified, the energy ratio can not be predicted or pre-specified from the dimensions of a pulse combustor. In fact, even with most of the one-dimensional models, the energy ratio can not be predicted. That is why the patterns and the magnitude of heat release rate were obtained from experimental data in those models. An objective of the present work is to evaluate the energy ratio of operating pulse combustors from available experimental data in the literature. These results can then be used to define a typical value for predicting pressure amplitude and other variables of a pulse combustor.

Another assumption commonly used for the simplified models of pulse combustors is the ideal-gas behavior of compressible pulsating flows. This assumption is also applied in the present work.

$$p_C = \rho_C R T_C \tag{4.9}$$

where ρ_C is the density of fluid in the combustion chamber and R is a gas constant. For simplicity, a value of the gas constant of air, R = 287 J/kg.K, is used in the present work.

With the above assumptions and definitions, the conservation equations of mass and energy can be manipulated or rearranged to solve for the heat source. First, Equations (4.3) and (4.9) are substituted into the mass balance equation, resulting in Equation (4.10) as follows.

$$V_C \frac{d\rho_C}{dt} = \dot{m}_1 - \dot{m}_2$$

$$\frac{V_C}{R} \frac{d}{dt}\left(\frac{p_C}{T_C}\right) = \dot{m}_1 - \rho_C A_T u_2$$

$$\frac{V_C}{RT_C}\frac{dp_C}{dt} - \frac{V_C p_C}{RT_C^2}\frac{dT_C}{dt} = \dot{m}_1 - \frac{p_C}{RT_C}A_T u_2 \tag{4.10}$$

The energy balance equation, neglecting the kinetic energy term and heat loss, can be written as

$$V_C \frac{d}{dt}\left(\rho_C h_C - p_C\right) = h_1 \dot{m}_1 - h_C \dot{m}_2 + \dot{q}_C$$

$$V_C \rho_C \frac{dh_C}{dt} + V_C h_C \frac{d\rho_C}{dt} - V_C \frac{dp_C}{dt} = h_1 \dot{m}_1 - h_C \dot{m}_2 + \dot{q}_C \tag{4.11}$$

where h_1 = 300 kJ/kg as the enthalpy of cool fresh reactants (using the value of air at 300 K), and h_C is the enthalpy of combustion products.

From a mass balance, $$V_C h_C \frac{d\rho_C}{dt} = h_C\left(\dot{m}_1 - \dot{m}_2\right)$$

Thus, $$V_C \rho_C \frac{dh_C}{dt} - V_C \frac{dp_C}{dt} = h_1 \dot{m}_1 - h_C \dot{m}_1 + \dot{q}_C \tag{4.12}$$

With the assumption, $h_C = aT_C + b$, Equation (4.12) becomes

$$\frac{aV_C p_C}{RT_C}\frac{dT_C}{dt} - V_C \frac{dp_C}{dt} = \left(h_1 - aT_C - b\right)\dot{m}_1 + \dot{q}_C \tag{4.13}$$

Temperature terms are eliminated by multiplying Equation (4.10) by aT_C and combining the result with Equation (4.13), yielding the final equation of this submodel as

$$\dot{q}_C = \frac{V_C}{R}\left(a - R\right)\frac{dp_C}{dt} - \left(h_1 - b\right)\dot{m}_1 + \frac{ap_C A_T u_2}{R} \tag{4.14}$$

The mean value of heat source from Equation (4.14) is basically the energy input rate of the pulse combustor. Although not exactly the same, mean values from this equation are found to be in agreement with the values of energy input rate calculated from the product of the mean mass flow rate and the heat of combustion of fuel. Also note that as the parameter *a* is basically an average value of the specific heat at constant pressure, the term (*a*-*R*) is basically an average value of the specific heat at constant volume.

The equation for temperature oscillation can be derived from the mass balance, Equation (4.10) or substituting the heat source term in Equation (4.13) by Equation

(4.14). Although the model does not require the solution of temperature oscillation from this submodel, the following equation is given for the sake of completion.

$$V_C T_C \frac{dp_C}{dt} - V_C p_C \frac{dT_C}{dt} = RT_C^2 \dot{m}_1 - p_C T_C A_T u_2$$

In summary, the combustion chamber submodel results in an explicit expression for the oscillation of heat source or heat release, Equation (4.14). However, this submodel still requires the solution for velocity oscillation at the tailpipe inlet, u_2, from the tailpipe velocity submodel described in the next section.

4.3 Tailpipe Velocity Submodel

The tailpipe velocity submodel is used to provide solutions for the velocity oscillation at the tailpipe inlet (the combustion chamber exit) for the combustion chamber submodel in the previous section and for the velocity oscillation at the tailpipe exit used in the mean tailpipe temperature submodel developed in the next section. The velocity oscillation at the tailpipe exit is of interest with respect to the velocity ratio of the pulsating jet, a key parameter for impingement heat transfer enhancement. The velocity oscillation consists of two parameters: mean velocity and velocity amplitude. The concept for calculating the mean velocity was discussed in Section 3.3 of the previous chapter. The discussion in this section focuses on the derivation of a solution for the velocity amplitude.

The mean velocity is calculated using the mean mass flow rate, the cross-sectional area of the tailpipe, and the fluid density corresponding to maximum temperature of fresh hot gas from upstream. Fluid densities in the present work are calculated from the ideal-gas law. For simplicity, the pressure used for calculating densities in the tailpipe is the atmospheric pressure, p_a. Therefore, mean velocities at the tailpipe inlet, u_{m2}, and the tailpipe exit, u_{m3}, are as follows.

$$u_{m2} = \frac{\dot{m}_m}{A_T \rho_{j2}} = \frac{\dot{m}_m RT_{j2}}{A_T p_a} \tag{4.15}$$

$$u_{m3} = \frac{\dot{m}_m}{A_T \rho_{j3}} = \frac{\dot{m}_m R T_{j3}}{A_T p_a} \tag{4.16}$$

where T_{j2} and T_{j3} are maximum temperatures in an oscillation cycle at the inlet and the exit of the tailpipe, respectively. As in the previous section, T_{j2} is the adiabatic flame temperature in the combustion chamber. The value of T_{j3}, in practice, depends on T_{j2} and heat loss at the tailpipe wall. For the present work, the value of T_{j3} is given as an input parameter of the model.

From velocity measurement results by Sandia National Laboratories (Dec et al., 1991) and CFD simulation results from preliminary work shown in the previous chapter, the velocity amplitude increases along the tailpipe length from the inlet toward the exit. This behavior is similar to that of the increasing velocity amplitude in an acoustic resonance tube, indicating that a linear acoustic theory could be applied for a solution. Two approaches were applied and both yielded identical solutions. The first approach follows the derivation by Ahrens (1979), the details of which are given in the Appendix. The governing equations are linear wave equations in forms of pressure change (or amplitude) and velocity potential. The boundary condition at the tailpipe inlet is the mass balance between the combustion chamber and the tailpipe. The boundary condition at the tailpipe exit is zero pressure amplitude. The solutions for pressure amplitude, p_{TA}, and velocity amplitude, u_{TA}, along the tailpipe length are as follows:

$$p_{TA}(x) = p_{CA}\left[\cos\left(\frac{\omega x}{c_{Tm}}\right) - \sin\left(\frac{\omega x}{c_{Tm}}\right) / \tan\left(\frac{\omega L}{c_{Tm}}\right)\right] \tag{4.17}$$

$$u_{TA}(x) = \frac{p_{CA}}{\rho_{Tm} c_{Tm}}\left[\cos\left(\frac{\omega x}{c_{Tm}}\right) / \tan\left(\frac{\omega L}{c_{Tm}}\right) + \sin\left(\frac{\omega x}{c_{Tm}}\right)\right] \tag{4.18}$$

where x is distance from the tailpipe inlet, L is tailpipe length, ω is radian frequency, and c_{Tm} and ρ_{Tm} are mean speed of sound and mean density of the fluid in the tailpipe, respectively.

The boundary conditions at the two ends of the tailpipe yielded an important relationship:

$$\frac{\omega L}{c_{Tm}} \tan\left(\frac{\omega L}{c_{Tm}}\right) = \frac{1}{\beta} \tag{4.19}$$

where β is the volume ratio between the combustion chamber and the tailpipe. This relationship can be used to predict or calculate the resonant frequency of the pulse combustor given the speed of sound, c_{Tm}. The estimation of the mean temperature for evaluating the speed of sound is described in the next section. As shown in the Appendix, Equation (4.19) is a generalized form of the resonant frequency of an acoustic tube, ranging from a Schmidt quarter-wave tube (zero volume ratio) to a Helmholtz resonator (very large volume ratio).

The second approach considers the entire Helmholtz pulse combustor as an equivalent quarter-wave tube, where one end is closed (combustion chamber upstream end) and the other end is open (tailpipe exit). The length of this tube is the combination of the tailpipe length (L) and the characteristic length of the combustion chamber (L'), as shown in Figure 4.2. The characteristic length, L', represents the effect of the combustion chamber volume on the acoustic resonance. However, the parameter of interest is the system wavelength, λ, which can be assumed to be four times the overall characteristic length of the Helmholtz pulse combustor, $L + L'$, i.e., $\lambda = 4(L + L')$, according to the basic concept of the quarter-wave tube. As shown later, the system wavelength can be calculated from dimensions of the pulse combustor, i.e., the volume ratio and the tailpipe length.

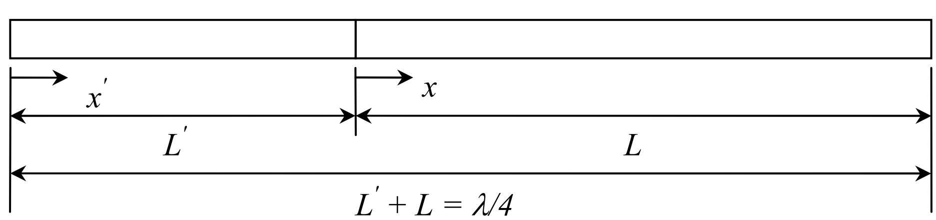

Figure 4.2: Diagram of equivalent quarter-wave tube for a Helmholtz pulse combustor.

From the theory of the quarter-wave tube, the general solutions of the amplitude of pressure and velocity oscillations along the overall length in Figure 4.2 are as follows:

$$p_A(x') = p_A(0)\cos\left(\frac{2\pi x'}{\lambda}\right) \tag{4.20}$$

$$u_A(x') = \frac{p_A(0)}{\rho_{Tm} c_{Tm}}\sin\left(\frac{2\pi x'}{\lambda}\right) \tag{4.21}$$

where x' is the distance from the closed end of the tube. From the perspective of the tailpipe portion, the pressure amplitude at the tailpipe inlet, $x' = L'$, is equal to the pressure amplitude in the combustion chamber, p_{CA}. This relationship is used to determine the relationship between p_{CA} and $p_A(0)$.

$$p_{CA} = p_A(L') = p_A(0)\cos\left(\frac{2\pi L'}{\lambda}\right) = p_A(0)\cos\left(\frac{2\pi\left(\lambda/4 - L\right)}{\lambda}\right)$$

$$p_{CA} = p_A(0)\left[\cos\left(\frac{\pi}{2}\right)\cos\left(\frac{2\pi L}{\lambda}\right) + \sin\left(\frac{\pi}{2}\right)\sin\left(\frac{2\pi L}{\lambda}\right)\right]$$

$$p_{CA} = p_A(0)\sin\left(\frac{2\pi L}{\lambda}\right) \tag{4.22}$$

Hence, Equation (4.20) can be re-written in terms of the pressure amplitude along the actual tailpipe length:

$$p_{TA}(x) = \frac{p_{CA}}{\sin\left(\frac{2\pi L}{\lambda}\right)}\cos\left(\frac{2\pi\left(x + \lambda/4 - L\right)}{\lambda}\right)$$

$$p_{TA}(x) = \frac{p_{CA}}{\sin\left(\frac{2\pi L}{\lambda}\right)}\cos\left(\frac{2\pi(x - L)}{\lambda} + \frac{\pi}{2}\right)$$

$$p_{TA}(x) = \frac{p_{CA}}{\sin\left(\frac{2\pi L}{\lambda}\right)}\sin\left(\frac{2\pi(x - L)}{\lambda}\right) \tag{4.23}$$

Likewise, Equation (4.21) can be re-written as:

$$u_{TA}(x) = \frac{p_{CA}}{\rho_{Tm} c_{Tm}\sin\left(\frac{2\pi L}{\lambda}\right)}\sin\left(\frac{2\pi\left(x + \lambda/4 - L\right)}{\lambda}\right)$$

$$u_{TA}(x) = \frac{p_{CA}}{\rho_{Tm} c_{Tm} \sin\left(\frac{2\pi L}{\lambda}\right)} \sin\left(\frac{2\pi(x-L)}{\lambda} + \frac{\pi}{2}\right)$$

$$u_{TA}(x) = \frac{p_{CA}}{\rho_{Tm} c_{Tm} \sin\left(\frac{2\pi L}{\lambda}\right)} \cos\left(\frac{2\pi(x-L)}{\lambda}\right) \tag{4.24}$$

The acoustic relationship between the system wavelength, the resonance frequency, and the speed of sound is the linkage between the solutions of the two approaches.

$$\lambda = \frac{c_{Tm}}{f} = \frac{2\pi c_{Tm}}{\omega}$$

$$c_{Tm} = \frac{\lambda \omega}{2\pi}$$

Thus,

$$\frac{\omega L}{c_{Tm}} = \frac{2\pi L}{\lambda} \tag{4.25}$$

With Equation (4.25) and some rearrangement, Equation (4.18) can be written as:

$$u_{TA}(x) = \frac{p_{CA}}{\rho_{Tm} c_{Tm} \sin\left(\frac{2\pi L}{\lambda}\right)} \left[\cos\left(\frac{2\pi x}{\lambda}\right)\cos\left(\frac{2\pi L}{\lambda}\right) + \sin\left(\frac{2\pi x}{\lambda}\right)\sin\left(\frac{2\pi L}{\lambda}\right)\right]$$

$$u_{TA}(x) = \frac{p_{CA}}{\rho_{Tm} c_{Tm} \sin\left(\frac{2\pi L}{\lambda}\right)} \cos\left(\frac{2\pi(x-L)}{\lambda}\right)$$

which is identical to Equation (4.24). Likewise, for the solution of pressure amplitude, Equation (4.17) can be rearranged to be identical with Equation (4.23).

Given the pulse combustor dimensions, the system wavelength, λ, can be calculated from the combination of Equations (4.19) and (4.25):

$$\frac{2\pi L}{\lambda} \tan\left(\frac{2\pi L}{\lambda}\right) = \frac{1}{\beta} \tag{4.26}$$

As with the mean velocities, the solutions of velocity amplitude for the model are only required at the inlet and the exit of the tailpipe, i.e., u_{A2} and u_{A3}, respectively.

$$u_{A2} = u_{TA}(0) = \frac{p_{CA}}{\rho_{Tm} c_{Tm} \tan\left(\frac{2\pi L}{\lambda}\right)} \tag{4.27}$$

$$u_{A3} = u_{TA}(L) = \frac{p_{CA}}{\rho_{Tm} c_{Tm} \sin\left(\frac{2\pi L}{\lambda}\right)} \tag{4.28}$$

Initially, the mean temperature for the evaluation of the mean density, ρ_{Tm}, and the mean speed of sound, c_{Tm} was to be the same as from the submodel in the next section. However, from a comparison with experimental data of velocity measurement in Dec et al. (1991), the velocity amplitudes from the model were significantly lower than those from the experiment. This suggests that the mean density should be lower or the corresponding temperature should be higher. The calculation of the mean speed of sound is unchanged because it is also used for the frequency prediction. From trial and error, an appropriate value of mean temperature for the density is the average value between maximum temperatures at the inlet and the exit of the tailpipe, T_{j2} and T_{j3}, respectively. Thus, the mean density in the tailpipe for this submodel is calculated as follows.

$$\rho_{Tm} = \frac{p_a}{R\left(\frac{T_{j2} + T_{j3}}{2}\right)}$$

In summary, the solutions for velocity oscillations are given in terms of mean velocities and velocity amplitudes. For use in the combustion chamber submodel, the mean velocity and the velocity amplitude at the tailpipe inlet can be calculated from Equations (4.15) and (4.27). For the use in the mean tailpipe temperature submodel, the mean velocity and the velocity amplitude at the tailpipe exit can be calculated from Equations (4.16) and (4.28). The system wavelength required for the solution of velocity amplitude can be calculated from Equation (4.26).

4.4 Mean Tailpipe Temperature Submodel

The objective of this submodel is to approximate the mean temperature of a pulsating flow in the tailpipe. The mean tailpipe temperature is then used to evaluate the mean speed of sound, c_{Tm}, for the solution of velocity amplitude in the previous section and for the prediction of the pulsation frequency, which is also required in the combustion chamber submodel. The predicted frequency is the natural frequency of a resonance tube:

$$f = \frac{c_{Tm}}{\lambda} \tag{4.29}$$

where the system wavelength, λ, is calculated from Equation (4.26) for a given pulse combustor.

The approximation of mean tailpipe temperature is done by averaging the profile of temperature along the tailpipe at an instant in time as an instantaneous space-averaged value and then averaging those instantaneous values over an oscillation cycle. Temperature parameters include maximum temperature in the combustion chamber or at the tailpipe inlet, T_{j2}, maximum temperature at the tailpipe exit, T_{j3}, and ambient temperature around the tailpipe exit, T_a. The ambient temperature is taken into account when the velocity amplitude is large enough to cause flow reversal. Given the parameters of the velocity oscillation, the distance that ambient fluid travels into the tailpipe can be calculated. In this section, for the velocity oscillation at the tailpipe exit, Equations (4.16) and (4.28) are used. In addition, for simplicity, the pulsating flow is assumed to be incompressible, i.e., the velocity oscillation is spatially uniform in the tailpipe.

Typically, the average temperature in a flowing fluid is a mass-averaged temperature. However, in this case, instead of directly calculating temperature along the tailpipe, the corresponding density is used so that the average is volume-averaged, or in this case, length-averaged. Another assumption is that ambient fluid entering the tailpipe during flow reversal does not mix with fluids upstream coming from the combustion chamber. Here, this is referred to as a two-compartment model. The concept of this model is shown in Figure 4.3.

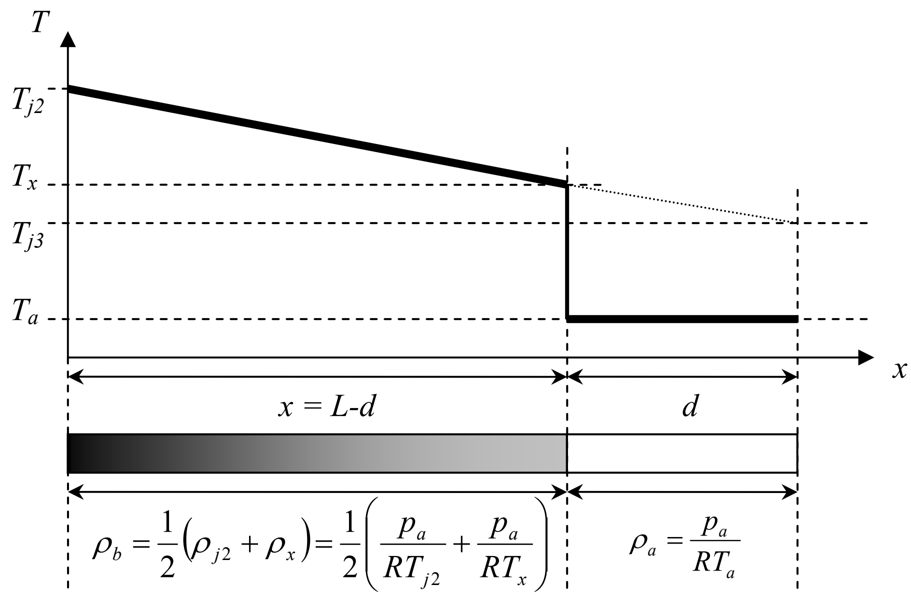

Figure 4.3: Diagram of two-compartment model assumption in the tailpipe.

Figure 4.3 shows an instantaneous profile of temperature along the tailpipe. The compartment for ambient fluids has an instantaneous length of reversed-flow distance, *d*. The sudden change in the temperature profile represents the assumption of non-mixing between the ambient fluid and the fluid upstream. Thus, the density in the ambient fluid compartment, ρ_a, is uniform and corresponds to the ambient temperature, T_a. For the upstream compartment, the mean density, ρ_b, is the mean value between the density at the tailpipe inlet, ρ_{j2}, and the density at the location to where ambient fluid flows back, ρ_x. The temperature used to calculate the density at this location is T_x, based on a linear projection between maximum temperatures at the inlet and the exit of the tailpipe (T_{j2} and T_{j3}, respectively). Typically, T_{j3} is lower than T_{j2}. Hence, heat loss at the tailpipe wall is implicitly accounted for in the model.

With the two-compartment model, the spatially-averaged density at any instantaneous time during a cycle for the whole tailpipe could be estimated as

$$\frac{1}{L}\int_0^L \rho_T dx = \rho_b (L-d) + \rho_a d \tag{4.30}$$

The reversed-flow distance, d, varying with time, is calculated from the velocity oscillation at the tailpipe exit, u_3.

$$u_3 = u_{m3} - u_{A3}\sin(\omega t)$$

This expression of u_3 is used for the simplicity of the calculation of the flow-reversal distance, d, which is straightforward as follows.

$$d = -\int_{t_1^*}^{t_2^*} u_3 dt = \begin{cases} 0 & ,t < t_1^* \\ -u_{m3}t - \dfrac{u_{A3}}{\omega}\cos(\omega t) + C_d & ,t_1^* \le t \le t_2^* \\ 0 & ,t > t_2^* \end{cases} \tag{4.31}$$

$$C_d = u_{m3}t_1^* + \frac{u_{A3}}{\omega}\cos(\omega t_1^*),$$

where t_1^* is time at the first $u_3 = 0$ (from positive to negative) and t_2^* is time where $d = 0$ (all ambient fluid flows out of tailpipe). The value of t_1^* can be simply determined.

$$t_1^* = \frac{1}{\omega}\sin^{-1}\left(\frac{u_{m3}}{u_{A3}}\right) \tag{4.32}$$

The value of t_2^* cannot be explicitly determined but can be solved from Equation (4.31) at the condition when $d(t = t_2^*) = 0$ as follows.

$$u_{m3}t_2^* + \frac{u_{A3}}{\omega}\cos(\omega t_2^*) = u_{m3}t_1^* + \frac{u_{A3}}{\omega}\cos(\omega t_1^*) \tag{4.33}$$

This equation can be solved using numerical methods. The maximum distance ambient fluid could travel is the position where the velocity changes direction from negative to positive, i.e., d at $u_3 = 0$, which can be directly calculated:

$$d_{\max} = d\left(t = \frac{1}{2f} - t_1^*\right) = u_{m3}\left(2t_1^* - \frac{1}{2f}\right) + \frac{2u_{A3}}{\omega}\cos\left(\omega t_1^*\right) \tag{4.34}$$

Finally, the mean temperature, T_{Tm}, and the mean speed of sound, c_{Tm}, in the tailpipe are calculated from the time-averaged value of the spatially-averaged density defined by Equation (4.30), ρ_{cTm}, as follows.

$$\rho_{cTm} = \frac{f}{L}\int_0^{1/f}\int_0^L \rho_T \, dx dt$$

$$T_{Tm} = \frac{p_a}{R\rho_{cTm}}$$

$$c_{Tm} = \sqrt{\gamma R T_{Tm}} \tag{4.35}$$

For convenience, the value of the specific heat ratio of air is used, γ = 1.4. The value of mean speed of sound from Equation (4.35) is then used for the frequency prediction in Equation (4.29) and the solution of velocity amplitude in the previous section.

4.5 Evaluation of Energy Ratio

The objective of the model is to predict pressure amplitude, pulsation frequency, and velocity ratio from input parameters of pulse combustor dimensions, mean mass flow rate, and equivalence ratio. As with other simplified models, the present work requires specific information about the operating conditions of the pulse combustor. For this model, the specific information is the energy ratio, α, defined as the ratio between the amplitude of heat release rate oscillation and the mean heat release rate. The heat release rate amplitude is defined by Equation (4.7), which is basically the average of the portion of heat release rate that is higher than the mean value. The average of the lower portion of heat release rate would yield the same value. The mean heat release rate is typically the energy input rate from the fuel. Theoretically, the heat release during the oscillation cannot have a negative value, being a heat source or heat addition to the flows from the combustion reaction. Therefore, by the definition of the heat release amplitude, the energy ratio is always equal to or less than one (unless the pattern of heat release rate oscillation is an impulse pattern or explosion-like, which is unlikely because, from experimental data in the literature, the typical pattern for stable oscillations is rather like a bell or triangular shape.)

The combustion chamber submodel yields an explicit expression for the heat release rate oscillation as a function of other parameters, which are input parameters and solutions from the other two submodels. The pressure amplitude is an input parameter of the submodel. Therefore, the prediction process is to find a value of pressure amplitude that produces the target (specified) value of the energy ratio. The velocity oscillation and the frequency predicted from the other two submodels are coupled with the pressure amplitude. Therefore, the prediction process would require some iterations until all conditions are satisfied. However, the value of the energy ratio depends on the geometry and the operating condition of the pulse combustor. Therefore, at least one operating condition of the pulse combustor is required to evaluate the value of the energy ratio, or a reasonable value of the energy ratio has to be provided for the model.

The objectives of this section are to evaluate the range of the energy ratio from available data of operating pulse combustors in the literature and to test the prediction capability of the model. The evaluation process is straightforward for the combustion chamber submodel because the solution of the submodel is the heat release oscillation. However, experimental data, especially temperature, were incomplete in most publications. Some parameters must therefore be best-guessed or chosen so that all conditions in the model are satisfied.

The most complete experimental data for Helmholtz pulse combustors were from Sandia National Laboratories (Dec and Keller, 1989 and 1990 and Dec et al., 1991). The cross-section of the pulse combustor was a square shape. The tailpipe width was 30 mm The tailpipe length (L) was 880 mm. Combining the volumes of the mixing chamber and the tailpipe connector with the combustion chamber, the volume ratio (β) was 1.45. The mean mass flow rate ($\dot{m}_m$) and the equivalence ratio (ϕ) were 4.08 g/s and 1.0, respectively, with methane as a fuel. Cooling air was applied around the walls of the tailpipe. Flow and jet temperature at the inlet and the exit of the tailpipe (T_{j2} and T_{j3}, respectively) were approximately 1600 and 700 K, respectively. The end of the tailpipe was connected to a large decoupling chamber. Thus, the ambient temperature (T_a) is assumed to be the same as the jet temperature at the tailpipe exit. The pressure amplitude in the combustion chamber (p_A) was 10.4 kPa. With all these data as input parameters, the model predicts a frequency (f) of 85 Hz, which agrees well with the actual operating frequency of 83 Hz. The velocity amplitudes at the inlet and the exit of the tailpipe from the model are 58 and 80 m/s, respectively, which are consistent with the measured data.

The energy input rate ($\dot{q}_m$) calculated from the heat of combustion of methane is 11.2 kW, based on $\phi = 1.0$, which yields an adiabatic flame temperature of 2300 K. However, the measured temperature in the combustion chamber was only 1600 K. This was probably due to high heat loss at the walls or a mistake in the determination of the equivalence ratio. If negligible heat loss is assumed, the equivalence ratio and the energy input rate corresponding to T_C = 1600 K is 0.58 and 6.6 kW, respectively. With $\phi = 1.0$, the heat loss to the walls would be as high as 4.6 kW, which was unlikely because cooling air was not provided for the combustion chamber. As the parameters used in the model are based on the measured temperature of 1600 K at the tailpipe inlet and the equivalence ratio of 0.58, the mean heat source resulting from the model is also about 6.6 kW. The resulting amplitude of heat release ($\dot{q}_A$) is 4.9 kW. Thus, the energy ratios based on the energy rate inputs of 6.6 and 11.2 kW are 0.75 and 0.44, respectively. The energy ratio, $\alpha = 0.44$ is quite low compared to other pulse combustors reviewed in this section. Thus, for this pulse combustor condition, the energy ratio is more likely to be 0.75.

Another set of experimental data from the same pulse combustor with a longer tailpipe (Dec & Keller, 1986) was used in the model. In this case, L = 2 m, $\beta = 0.64$, f = 49 Hz, $\dot{m}_m$ = 5.06 g/s, p_A = 7.8 kPa, and $\phi = 0.62$. The energy input rate and the combustion chamber temperature are calculated to be 8.8 kW and 1670 K, respectively. In order to match the calculated frequency with the operating value, ambient and jet temperatures at the tailpipe exit are adjusted to be 635 K. The calculated velocity oscillation amplitude at 185 mm from the tailpipe inlet was 30 m/s, which was in agreement with the experimental data (~27 m/s). The resulting energy ratio was 0.67. In these experiments, mean mass flow rate was varied from 4.5-6.8 g/s, with the measured parameters being pressure amplitude, frequency, and velocity amplitude at 185 mm from the tailpipe inlet. As with the first set of data, input parameters were applied to the model and temperature at the tailpipe exit was adjusted to match the frequency data case by case. The tailpipe exit temperature was in the range of 650-900 K and increased with increasing mean mass flow rate. The resulting equivalence ratios were in the range of 0.62-0.68, changing in the same direction as the pressure amplitude.

Another Helmholtz pulse combustor, in which the combustion chamber and the tailpipe had a circular cross-section, was tested at Sandia National Laboratories (Keller et al., 1989). The position of the stagnation plate was varied to change the delay time or mixing rate of reactants with the hot gas remaining in the combustion chamber. The inlet flow parameters were kept constant, $\dot{m}_m$ = 9 g/s and ϕ = 0.78. The tailpipe geometry was 880 mm in length and 47.6 mm in diameter. The measured parameters were pressure amplitude and frequency. There were three cases of interest with the volume ratio of 0.57: the position of the stagnation plate was at 8, 10, and 12 mm from the inlet port of reactants. For all three cases, the jet temperature at the inlet and the exit of the tailpipe, and the ambient temperature used in the model were 1930, 1400 and 400 K, respectively. The measured pressure amplitudes were 10.6, 15.0, and 17.7 kPa for the stagnation plate position of 8, 10, and 12 mm, respectively. Predicted frequencies were in excellent agreement with experimental data, i.e., 141, 133, and 127 Hz, respectively. The resulting energy ratios were 0.60, 0.73, and 1.00, respectively. From the model results, the frequency decreased with increasing pressure amplitude because mean temperature in the tailpipe decreased with increasing velocity amplitude ratio at the tailpipe exit.

In this experiment, with the same volume ratio, the stagnation plate position was adjusted farther up to 20 mm, resulting in relatively constant frequency of 127 Hz, slightly increasing pressure amplitude, and yielding less stable oscillations. A possible explanation from the model perspective is that the energy ratio has reached a maximum value for stable oscillations (α = 1.0) at the stagnation plate position of 12 mm. Beyond this position, the mixing rate between the reactants and the hot gas became too slow during the oscillation cycle, i.e., the delay time became too long. The combustion process probably occurred all at once like an impulse function instead of being distributed smoothly over the cycle period, resulting in less stable oscillations. From the Rayleigh criterion point of view, the longer delay time caused the heat release oscillation to be more out of phase with the pressure oscillation, resulting in less stable oscillations.

From the same experiments, four sizes of the combustion chamber were used, whereas the stagnation plate position remained the same at 12 mm. The volume ratios were 0.57, 0.69, 0.80, and 1.03, with corresponding pressure amplitudes of 17.7, 16.8, 16.0, and 10.6 kPa, and operating frequencies of 127, 122, 118, and 108 Hz, respectively. For this set of data, in order to match predicted frequencies with the experimental data, ambient temperature in the model was adjusted case by case, over the range of 340-470 K. The resulting energy ratios were 1.00, 0.96, 0.91, and 0.74, respectively. As the volume of the combustion chamber increases, the energy ratio decreased with decreasing pressure amplitude and frequency.

The results of the energy ratio evaluation for experimental data produced by the Helmholtz pulse combustors at Sandia National Laboratories are summarized in Table 4.1. The table includes the response of pressure amplitude and frequency to the change in the variable in each experiment. It should be noted that the response of the energy ratio is the same as that of pressure amplitude but to a smaller degree.

Table 4.1: Summary results of energy ratio evaluation

Reference	Variable	Effects of increases in the value of the variable	Range of energy ratio
Dec & Keller (1986)	Mean mass flow rate	Pressure amplitude increased then decreased Frequency increased	0.62-0.68
Keller et al. (1989)	Stagnation plate distance	Pressure amplitude increased Frequency decreased	0.60-1.00
Keller et al. (1989)	Combustion chamber volume	Pressure amplitude decreased Frequency decreased	0.74-1.00

As discussed earlier, the interpretation of the magnitude of the energy ratio can be related to the Rayleigh criterion. First, assume that the frequency or the cycle period is constant and the pressure oscillation cycle begins with the negative phase where reactants enter the combustion chamber. A low energy ratio means that the mixing rate between reactants and hot gas is relatively high, causing the combustion process to begin early and have small variation or amplitude over the cycle. When the mixing rate is lower, the delay time is longer. Thus, the combustion process or heat release occurs later but with higher amplitude for the same mean value. This phenomenon is consistent with the Rayleigh criterion, i.e., a longer delay time means more in-phase oscillations between heat release rate and pressure and, thus, stronger oscillations. If the delay time is too long, however, the heat release oscillation would be out of phase with the pressure oscillation, resulting in unstable or no oscillation. In case the mixing rate and the delay time are constant but the cycle period changes, the concept of the interpretation is still the same, i.e., following the Rayleigh criterion. If the cycle period is relatively long compared to the delay time, the energy ratio would be relatively low. When the cycle period becomes shorter, the oscillations are more in-phase and the energy ratio is higher. In summary, it can be interpreted that the energy ratio is highest when the heat release rate oscillation is entirely in-phase with the pressure oscillation. And the energy ratio is lower when the phase angle between heat release and pressure oscillations becomes larger.

Such interpretation can be used to explain the response of parameters in Table 4.1. It probably can be assumed that the mixing rate mainly depends on the mean mass flow rate and the stagnation plate position. Thus, when the frequency decreased due to a larger combustion chamber, the energy ratio and the pressure amplitude decreased (same delay time but longer cycle period). When the distance between the stagnation plate and the reactants port increased, the delay time increased resulting in higher energy ratio and pressure amplitude. Although the cycle period also increased, the change in the delay time was probably larger than that in the cycle period. As for the effects of increasing mean mass flow rate, the mixing rate increased and the delay time decreased while the cycle period decreased. The response of the energy ratio was not consistent but changed within a small range, possibly because the changes in delay time and cycle period were not much different.

The effects of the combustion chamber volume from experimental data in Neumeier (1993) were similar to those in Keller et al. (1989). That is the increase in combustion chamber volume resulted in decreases in pressure amplitude and frequency. However, the energy ratio slightly changed. For this experiment, the tailpipe had a circular cross-section. The length and the diameter of the tailpipe were 1.9 m and 38 mm, respectively. Three volumes of combustion chamber were used, resulting in volume ratios of 0.7, 1.4, and 2.2, respectively. Mean mass flow rates were 5.3, 5.0, and 5.0 g/s and equivalence ratios were 0.74, 0.79, and 0.75 respectively. The measured pressure amplitudes were 6.4, 6.0, and 4.5 kPa whereas the operating frequencies were 55, 45, and 39 Hz, respectively. The resulting energy ratios were 0.57, 0.54, and 0.55, respectively. The small changes in energy ratios were possibly due to the geometry of the combustion chamber and reactant ports. As shown in Tang (1993), air and fuel were separately fed to the circular combustion chamber via ports at the circumference wall instead of the end wall opposite to the tailpipe. In addition, no stagnation plate was used in this pulse combustor.

For the same set of data, the pulse combustor with the volume ratio of 1.4 had more operating conditions. The variables, mean mass flow rate and equivalence ratio, were not systematically varied. Nevertheless, energy ratios were calculated to be in the range of 0.49-0.64. As discussed in Chapter 2, the concept of the energy ratio in this dissertation was similar to that in the pulse combustor model developed by Neumeier (1993), which was in the form of a transfer function based on frequency domain analysis. The energy ratio in the Neumeier model was correlated with pressure amplitude from experimental data, resulting in an inverse linear relationship. From such a relationship, the range of energy ratios for this experiment was 0.49-0.68. Although the values of energy ratios resulting from the two approaches were not matched case by case, they were generally in agreement.

In conclusion, the range of energy ratios evaluated from different Helmholtz pulse combustors with various operating conditions was 0.49-1.00. The energy ratio appears to be most affected by the geometry of the combustion chamber, especially the position of the stagnation plate. The magnitude of the energy ratio can be interpreted as an indicator of the Rayleigh criterion. That is a higher value of the energy ratio means that the oscillations of heat release rate and pressure are more in-phase with each other. The response of the energy ratio to changes in pulse combustor parameters can be explained by this interpretation. However, the quantitative response of the energy ratio to other parameters requires more complete data and detailed analysis, which is beyond the scope of this dissertation. Therefore, for convenience, the parameter study in the next section is performed by assuming that the energy ratio is constant for all conditions.

4.6 Model Parameter Study

An objective of the research is to study impingement heat transfer enhancement using a pulsating jet generated by a pulse combustor. In order to obtain a high enhancement factor, it is desirable to generate a pulsating jet with a high velocity ratio. This could be achieved by producing a high pressure amplitude in the combustion chamber while keeping the values of the other flow parameters constant. However, since flow parameters of the pulse combustor are nonlinearly coupled, this could be difficult. Thus, the objective of this section is to study the effects of input parameters of the pulse combustor on flow parameters, especially the velocity ratio. Two categories of parameters are separately studied: inlet flow and pulse combustor dimension. The inlet flow parameters are the mean mass flow rate and the equivalence ratio. The pulse combustor dimension parameters are the combustion chamber volume and the tailpipe length. The base case is the pulse combustor used for the impingement drying experiment as shown in Figure 3.1. Predicted parameters are pressure amplitude in the combustion chamber, pulsation frequency, and jet velocity ratio at the tailpipe exit.

The measured data for the base case were as follows: mean mass flow rate, $\dot{m}_m$ = 3.7 g/s; volume ratio, β = 5.2; tailpipe length, L = 0.2794 m; tailpipe diameter, D = 0.0254 m; tailpipe inlet temperature, T_{j2} = 1500 K; combustion chamber pressure amplitude, p_A = 6.5 kPa; and frequency, f = 155 Hz. The fuel was propane. Other parameters were adjusted to match the model results with measured data: equivalence ratio, ϕ = 0.5; energy input rate or mean heat source, $\dot{q}_m$ = 5.3 kW; jet (maximum) temperature at tailpipe exit, T_{j3} = 1200 K, and ambient temperature, T_a = 450 K. And the results were energy ratio, α = 0.94, mean velocity at the tailpipe inlet, u_{m2} = 31.0 m/s; velocity ratio at the tailpipe inlet, ε_2 = 2.8; mean velocity at the tailpipe exit, u_{m3} = 24.8 m/s, and velocity ratio at the tailpipe exit, ε_3 = 3.8.

The key assumption for the parameter study in this section is that the energy ratios for all cases are as high as that of the base case, which is 0.94. As discussed earlier, actual responses of the energy ratio to changes of other parameters are not yet determined. Nevertheless, it could also be assumed that the energy ratio is manageable by changing the stagnation plate position in each case. In addition, a high energy ratio is desirable for any operating condition in order to produce strong pressure oscillations. Therefore, since the energy ratio of 0.94 from the base case is reasonably high, this value is used for all other cases.

Effects of inlet flow parameters

There were two parameter studies in this part. The first study followed a common condition of laboratory experiments with pulse combustors, i.e., no forced cooling provided around the tailpipe wall. Two inlet flow parameters for this study were mean mass flow rate and equivalence ratio. The other parameter study was to find a condition that could produce a pulsating jet with a very high velocity ratio. This study was performed because resulting velocity ratios from the first study were not higher than the base case. An additional parameter for this study was jet temperature at the tailpipe exit.

For the first study, five values of mean mass flow rate were used: 3.7, 4.6, 5.5, 6.4, and 7.3 g/s. Equivalence ratio was varied in three steps: 0.5, 0.75, and 1.0, with corresponding adiabatic flame temperature or maximum temperature in the combustion chamber (T_C) of 1500, 1940, and 2370, respectively. Three additional assumptions for this part were as follows; ambient temperature remained the same for all cases (T_a = 450 K), there was no heat loss in the combustion chamber ($T_{j2} = T_C$), and the difference between jet (or maximum) temperature at tailpipe inlet and exit remained the same as the base case (T_{j2}-T_{j3} = 300 K). Results of pressure amplitude, frequency, and velocity amplitude ratio are shown in Figures 4.4, 4.5, and 4.6, respectively.

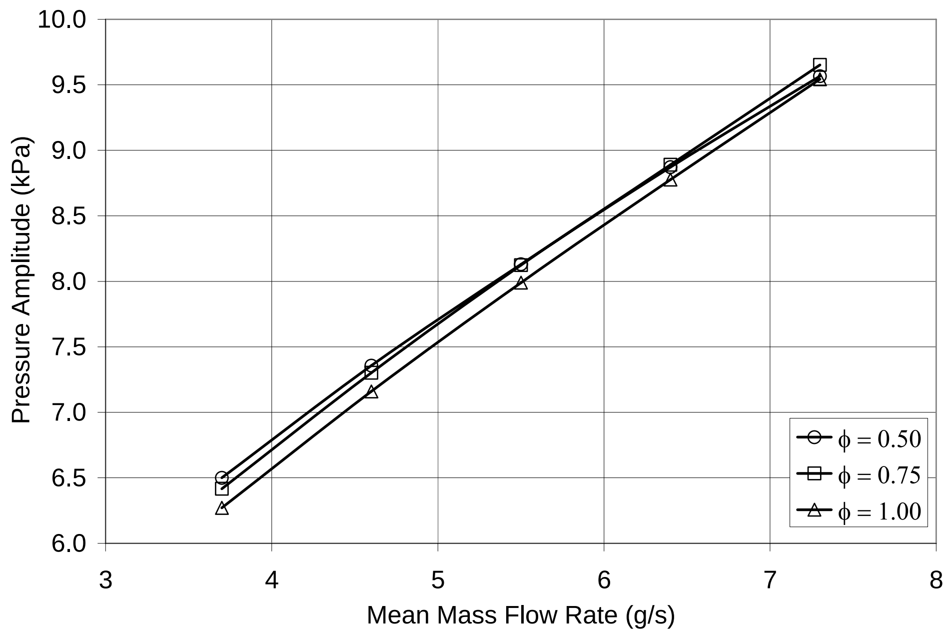

Figure 4.4: Effects of inlet flow parameters on combustion chamber pressure amplitude for the first parameter study.

The results showed nonlinear relationships between flow parameters. At the same equivalence ratio, pressure amplitude increased with increasing mean mass flow rate. This could be expected from the conditions of same equivalence ratio and energy ratio. When the total mean mass flow rate increases, the mean mass flow rate of fuel proportionally increases resulting in an increase in mean heat release rate. Due to the condition of constant energy ratio, the heat release amplitude increases, resulting in an increase in pressure amplitude. However, the effects of equivalence ratio on pressure amplitude were rather more complicated. At a low mean mass flow rate, pressure amplitude decreased with increasing equivalence ratio. At higher mean mass flow rates, pressure amplitude was greatest at medium equivalence ratio. From numerical experiments with other dimensions and flow parameters of pulse combustors, the relationship between equivalence ratio and pressure amplitude was not consistent. In some cases, pressure amplitude increased with equivalence ratio from low to medium and then remained at the same level at high equivalence ratio. This is because equivalence ratio directly affects the mean heat source which, in turn, affects temperature and density in the combustion chamber. All these parameters play a part in the pressure oscillation, which is the result of mass and temperature oscillation according to the ideal-gas law. Nevertheless, as shown in Figure 4.4, the effects of equivalence ratio on pressure amplitude were relatively small compared to the effects of mean mass flow rate.

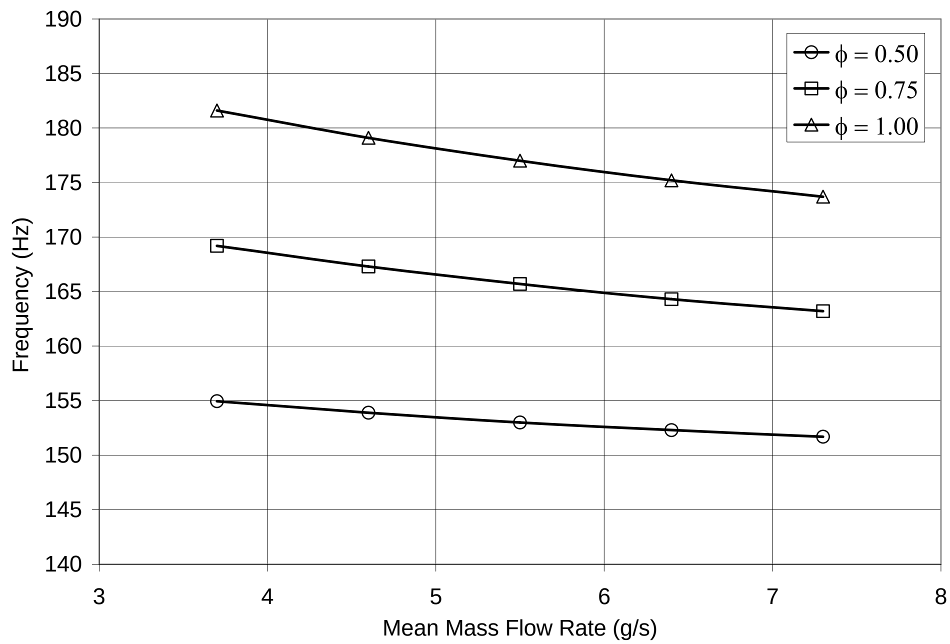

Figure 4.5: Effects of inlet flow parameters on pulsation frequency for the first parameter study.

The response of frequency was quite straight forward because the acoustic frequency only depends on system wavelength and mean speed of sound. The system wavelength depended on the dimensions of pulse combustor, which were constant in this study. Thus, the frequency in this study directly depended on the mean speed of sound or mean temperature in the tailpipe. As shown by the two-compartment model in Figure 4.3, the mean temperature in the tailpipe is affected by four parameters: combustion chamber temperature, jet temperature at the tailpipe exit, ambient temperature, and flow-reversal distance. In this study, combustion chamber temperature directly depends on equivalence ratio. Jet temperature at the tailpipe exit also depends on equivalence ratio because of the assumption of the same difference between jet temperature at tailpipe exit and combustion chamber. Ambient temperature around the tailpipe exit, in practice, depends on the configuration around the tailpipe exit. If a chamber or some kind of closed condition such as impingement surface with confinement is applied, ambient temperature would likely be at the same level as jet temperature. If the tailpipe exit is open, such as in the case of free jet or unconfined impingement, the temperature of fluids entering the tailpipe during flow reversal would actually be ambient temperature or slightly higher due to heating from hot exiting jet. In this study, the value of ambient temperature was the same for all cases. Finally, the maximum flow-reversal distance directly depends on the magnitude of velocity amplitude at the tailpipe exit. Thus, in Figure 4.5, the frequency decreased slightly with increasing mean mass flow rate because velocity amplitude increased at the tailpipe exit, drawing in more cool ambient air, but increased with equivalence ratio because combustion chamber temperature increased.

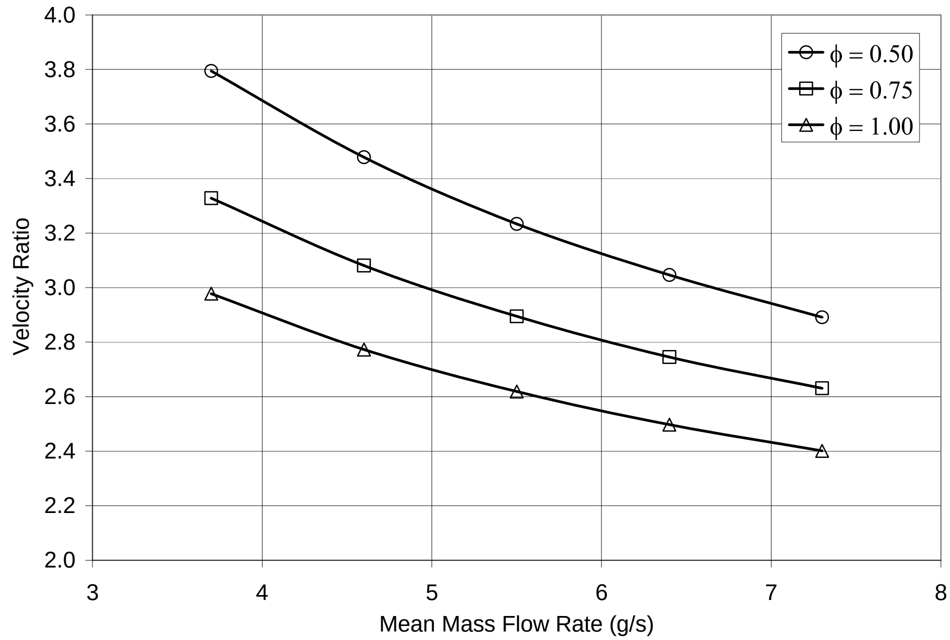

Figure 4.6: Effects of inlet flow parameters on velocity ratio at tailpipe exit for the first parameter study.

Figure 4.6 shows that velocity ratio decreases with increasing mean mass flow rate and equivalence ratio. These trends were rather unexpected as increasing mean mass flow rate and equivalence ratio meant an increase in pressure amplitude and heat source oscillation. However, model results show that both mean velocity and velocity amplitude increase with increasing mean mass flow rate and equivalence ratio. The velocity ratio decreases simply because the degree of the increase in velocity amplitude is less than that in mean velocity. These results suggests that, in order to have a high jet velocity ratio, both mean mass flow rate and equivalence ratio should be as low as possible for given pulse combustor dimensions.

However, it should be noted that, for a pulse combustor to have a stable oscillation, the combination of inlet flow parameters might not be arbitrary due to the requirement of the Rayleigh criterion. For example, the most stable condition of the pulse combustor used in the drying experiment was the base case of this study. It also should be noted that no stagnation plate was installed in that pulse combustor. If a stagnation plate was used to adjust the mixing rate and the delay time, as discussed in the previous section, other stable operating conditions might be possible.

A key condition of the first parameter study was that the difference between jet temperatures at tailpipe inlet and exit is constant. In order to find a condition that could generate a pulsating jet having a high velocity ratio, this condition was changed in the second study. Instead, the jet temperature at tailpipe exit was specified as another input parameter. Thus, the difference between jet temperatures at tailpipe inlet and exit increases with increasing equivalence ratio for each value of jet temperature at the tailpipe exit. In practice, this could be achieved by providing controllable forced cooling around the tailpipe wall. The values of three parameters in this study were: mean mass flow rate, $\dot{m}_m = 3.7$, 5.55, and 7.4 g/s; equivalence ratio, $\phi = 0.5$, 0.75, and 1.0; and jet temperature at tailpipe exit, $T_{j3} = 1000$, 1200, and 1400 K. Results of velocity ratio are shown in Figure 4.7.

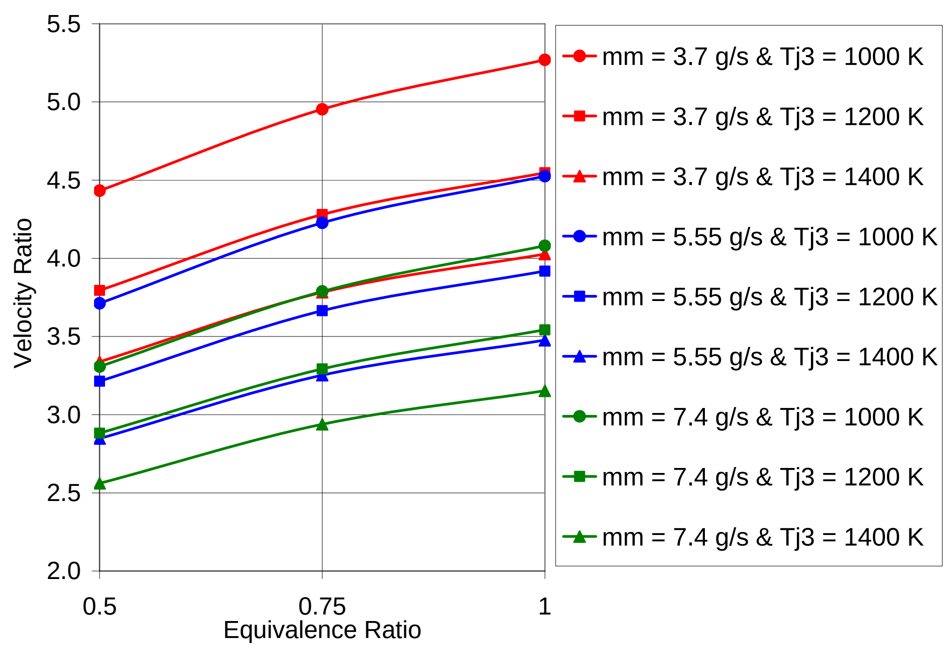

Figure 4.7: Effects of inlet flow parameters on velocity ratio at tailpipe exit for the second parameter study.

General trends were that velocity ratio increased with increasing equivalence ratio but decreased with increasing mean mass flow rate and tailpipe exit jet temperature. The highest velocity ratio ($\varepsilon = 5.3$) corresponded to the case with highest equivalence ratio ($\phi = 1.0$), lowest mean mass flow rate ($\dot{m}_m = 3.7$ g/s), and lowest jet temperature ($T_{j3} = 1000$ K). And the opposite directions of these parameters ($\phi = 0.5$, $\dot{m}_m = 7.4$ g/s, and $T_{j3} = 1400$ K) yielded the lowest velocity ratio ($\varepsilon = 2.6$). These results suggest that, for high velocity ratio purposes, the pulse combustor should be operated by first maintaining high equivalence ratio of reactants, then decreasing total mean mass flow rate to be as low as possible, and finally cooling the tailpipe as much as possible. It should be noted that, for impingement drying or heat transfer experiments, the highest jet velocity ratio from this criterion would not yield the highest net drying rate or heat flux because both jet temperature and mean velocity (mean energy rate of the pulsating jet at the tailpipe exit) are much lower than those for the case yielding lowest jet velocity ratio. The evaluation for heat transfer enhancement should be based on a corresponding steady jet with the same jet temperature and mean velocity.

Results for pressure amplitude showed that the case with highest velocity ratio had a pressure amplitude of 5.9 kPa, whereas the pressure amplitude from the case with lowest velocity ratio was 9.7 kPa. The pressure amplitude mainly depended on the mean mass flow rate, i.e., increased with increasing mean mass flow rate, as shown in Figure 4.8. The effects of jet temperature were not as prominent. And, unlike results in Figure 4.4, pressure amplitude generally decreased with increasing equivalence ratio.

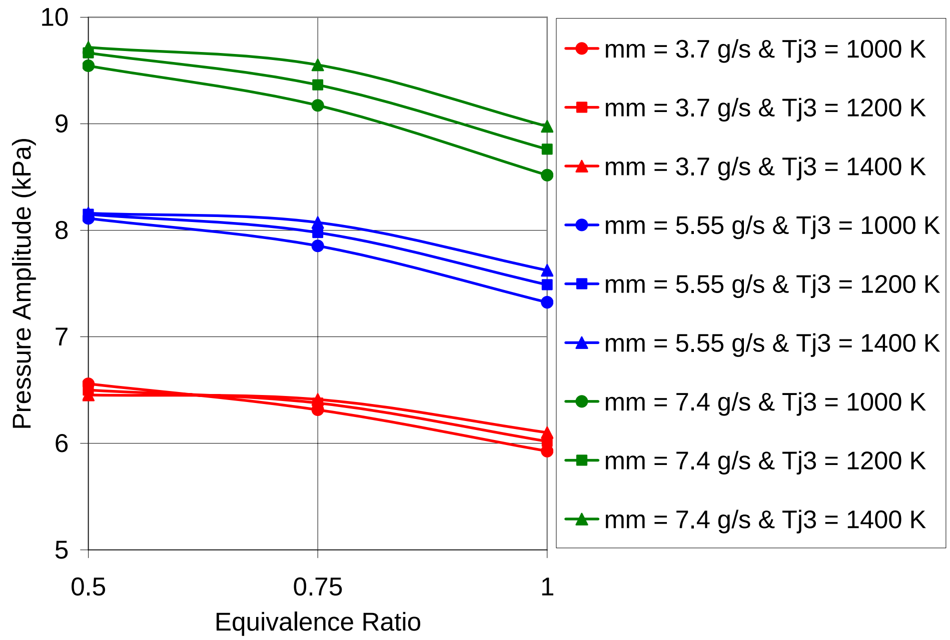

Figure 4.8: Effects of inlet flow parameters on combustion chamber pressure amplitude for the second parameter study.

The frequency response from this parameter study was not as straightforward as that from the first study. Figure 4.9 shows that trends of the response of frequency to equivalence ratio depend on mean mass flow rate. That is, with increasing equivalence ratio, frequencies increased, remained relatively the same, and decreased when mean mass flow rate was low, intermediate, and high, respectively. As with the first study, the frequency mainly depends on mean temperature in the tailpipe. This behavior is due to the balance between temperatures in the tailpipe inlet and tailpipe exit regions. Increasing equivalence ratio results in an increase in combustion chamber temperature and an increase in velocity ratio at the tailpipe exit, i.e., increasing temperature in the tailpipe inlet region but decreasing temperature in the tailpipe exit region at the same time. With low mean mass flow rate or jet velocity, fluid temperature in the tailpipe inlet region is more dominant than that in the tailpipe exit region. Thus, increasing equivalence ratio or combustion chamber temperature would increase mean temperature in the tailpipe. On the other hand, with high mean mass flow rate or jet velocity, fluid temperature in the tailpipe exit region becomes more dominant with cooler ambient air. Thus, the opposite trends occur. However, the overall range of frequencies from this study is relatively small, 141-164 Hz, compared to the first study, mainly due to the difference in the conditions of jet temperature at the tailpipe exit.

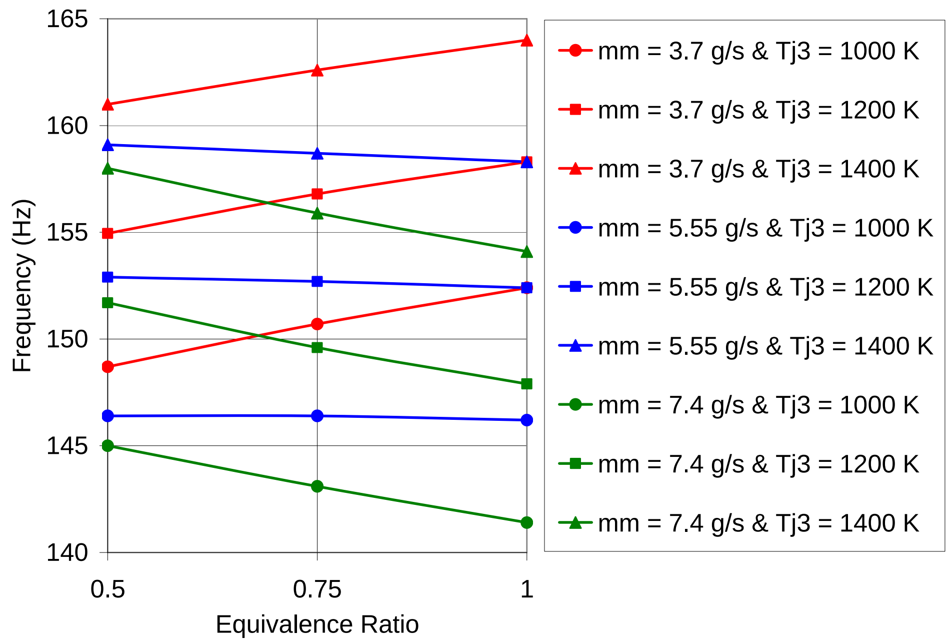

Figure 4.9: Effects of inlet flow parameters on pulsation frequency for the second parameter study.

In conclusion, the effects of inlet flow parameters on operating conditions of a pulse combustor are quite distinctive for different temperature conditions at the tailpipe exit. The parameter of primary interest is the velocity ratio at the tailpipe exit. The target is to produce a pulsating jet with the highest velocity ratio possible while maintaining stable oscillations. For the condition without tailpipe wall cooling, the strategy is to operate the pulse combustor with lowest mean mass flow rate and equivalence ratio possible. For the condition with tailpipe wall cooling, the strategy is to operate the pulse combustor with an optimum equivalence ratio for highest combustion chamber temperature at lowest mean mass flow rate and provide a great deal of cooling around the tailpipe wall to have lowest jet temperature possible.

Effects of pulse combustor dimensions

For this parameter study, the main variable is volume ratio, β, varied by changing either combustion chamber volume or tailpipe length. As the volume ratio of the base case was quite large ($\beta = 5.2$), the other cases were selected to have a smaller volume ratio, i.e., 5.2, 4.4, 3.6, 2.8, 2.0, and 1.2. Other input parameters were the same as those of the base case including the temperature at tailpipe exit. Therefore, mean velocities at the tailpipe exit were the same for all cases. As with the previous parameter studies, the parameters of interest were frequency, pressure amplitude, and velocity ratio.

According to the linear acoustic theory, the frequency, f, inversely depends on the system wavelength, λ, given a constant mean speed of sound in the tailpipe, c_{Tm}, i.e., $f = c_{Tm}/\lambda$. Due to the assumption that the temperatures at the inlet and the exit of the tailpipe and ambient temperature were constant, the resulting mean temperature and the mean speed of sound in the tailpipe were relatively constant for all cases. Thus, since the model used the linear acoustic theory for predicting pulsation frequency, the resulting frequency simply showed a linear relationship with the inverse of the system wavelength calculated from Equation (4.26), as shown in Figure 4.10. The system wavelength directly depends on the overall length of the pulse combustor, which is basically the combined effect of tailpipe length and combustion chamber volume. Either increasing the tailpipe length, L, or increasing the combustion chamber volume, V_C, would increase the system wavelength and decrease the frequency, or vice versa, as shown in Figure 4.11.

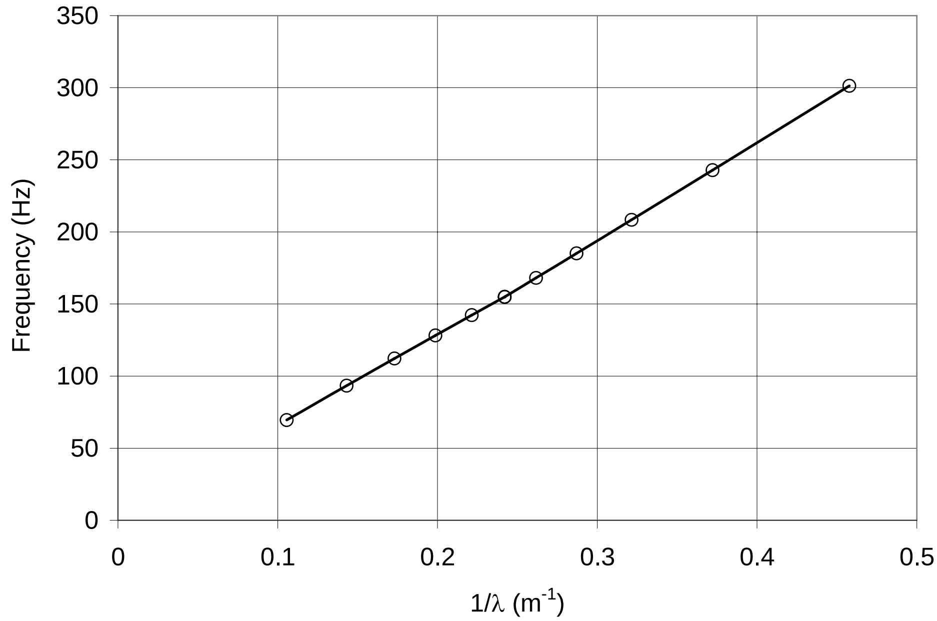

Figure 4.10: Relationship between system wavelength and pulsation frequency.

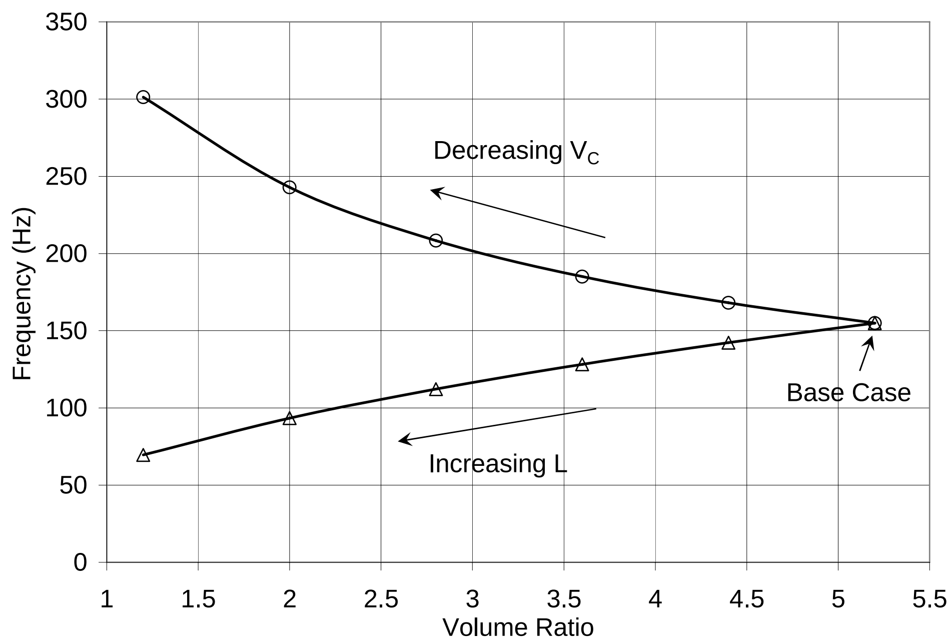

Figure 4.11: Effects of pulse combustor dimensions on pulsation frequency.

The effects of pulse combustor dimensions on pressure amplitude are shown in Figure 4.12.

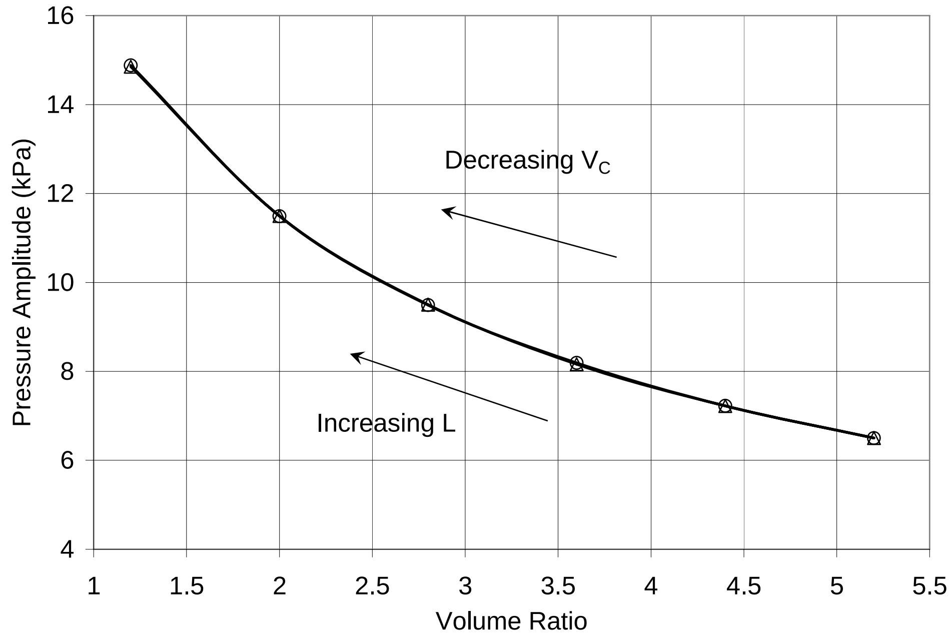

Figure 4.12: Effects of pulse combustor dimensions on combustion chamber pressure amplitude.

Interestingly, the same value of the volume ratio yielded the same value of pressure amplitude. This was not coincidental but was a response to the product of the frequency and the combustion chamber volume. This can be shown by substituting pressure and velocity functions as well as the solution for velocity amplitude into Equation (4.14) and rearranging to separate the mean heat source term, $\dot{q}_{Cm}$, and oscillating heat source terms, $\tilde{q}_C$, as follows.

$$\dot{q}_{Cm} = \left(aT_C + b - h_1\right)\dot{m}_{m1} \tag{4.36}$$

$$\begin{aligned}\tilde{q}_C = &\left(\frac{a-R}{R} - \frac{ap_a}{R\rho_{Tm}c_{Tm}^2}\right)\omega V_C p_A \cos(\omega t) + \frac{aAu_{m2}p_A}{R}\sin(\omega t) \\ &- \frac{a\omega V_C p_A^2}{R\rho_{Tm}c_{Tm}^2}\sin(\omega t)\cos(\omega t) - \left(h_1 - b\right)\tilde{m}_1\end{aligned} \tag{4.37}$$

where $\dot{m}_{m1}$ and $\widetilde{\dot{m}}_1$ are the mean value and the oscillating part of the inlet mass flow rate, $\dot{m}_1$, respectively. For this study, all parameters were constant, including the amplitude of heat source, except frequency, ω, combustion chamber volume, V_C, and pressure amplitude, p_A. From the definition of the amplitude of heat source by Equation (4.7), the integration of $\dot{q}_{C+}$ is equal to the integration of Equation (4.37) where the value of $\widetilde{\dot{q}}_C$ is greater than zero. Although it is not obvious analytically due to the nonlinearity of the equation, it can be observed numerically that the dominant terms for the integration during the positive cycle in Equation (4.37) are the first and last terms on the right-hand side. Therefore, the relationship between parameters can be simplified and written as

$$\dot{q}_{CA} \approx C_1 \omega V_C p_A + C_2$$

where C_1 is the product of constant parameters in the first term and C_2 is the integration of the last term, which is also a constant. And because the amplitude of heat source is constant for this parameter study, the relationship between the pressure amplitude and the product of the frequency and the combustion chamber volume is simply:

$$p_A \approx \frac{C}{\omega V_C}$$

where C is a constant parameter. Such a relationship for this parameter study is shown in Figure 4.13.

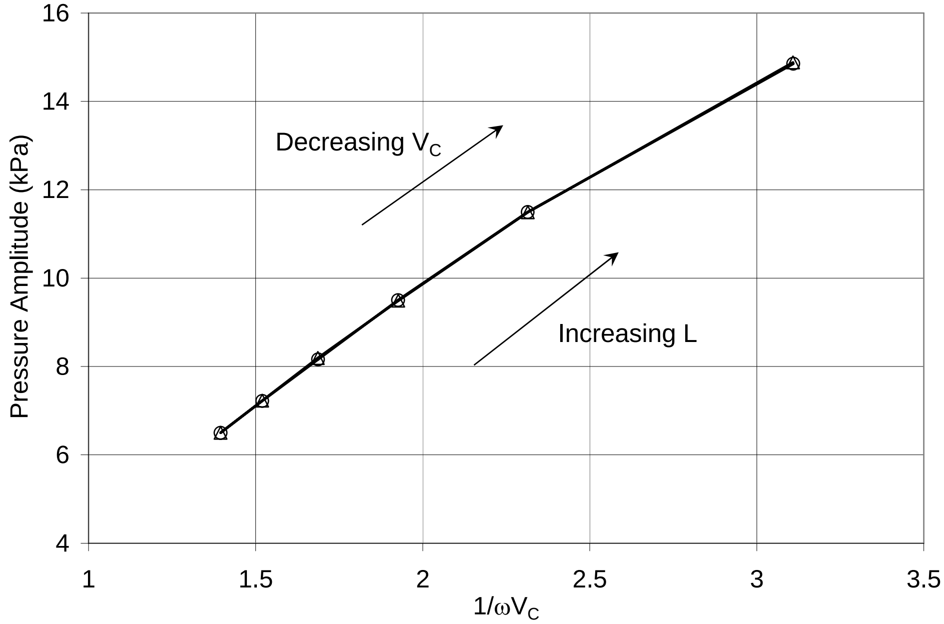

Figure 4.13: Relationship between combustion chamber pressure amplitude and product of frequency and combustion chamber volume.

When the tailpipe length is increased with the same combustion chamber volume, the volume ratio decreases and the frequency decreases. Thus, the term ωV_C decreases and the pressure amplitude increases. On the other hand, when the combustion chamber volume is decreased with the same tailpipe length, the volume ratio decreases but the frequency increases. The term ωV_C still decreases as the change of the frequency is relatively less than that of the combustion chamber volume, resulting in an increase in the pressure amplitude. The inverse relationship between the pressure amplitude and the term ωV_C is linked to the relationship between the pressure amplitude and the volume ratio through the relationship between the frequency and the system wavelength (Figure 4.10) and Equation (4.26) as follows.

From Figure 4.10,
$$\omega \propto \frac{1}{\lambda}$$

$$\omega V_C \propto \frac{V_C}{\lambda}$$

From Equation (4.26),
$$\frac{2\pi L}{V_C}\frac{V_C}{\lambda}\tan\left(\frac{2\pi L}{V_C}\frac{V_C}{\lambda}\right)=\frac{1}{\beta}$$

And $$\beta = \frac{V_C}{A_T L} \text{ or } V_C = \beta A_T L$$

$$\frac{2\pi}{A_T \beta} \frac{V_C}{\lambda} \tan\left(\frac{2\pi}{A_T \beta} \frac{V_C}{\lambda} \right) = \frac{1}{\beta}$$

Since, $$p_{CA} \propto \frac{1}{\omega V_C} \propto \frac{\lambda}{V_C} = \frac{C_3 \lambda}{V_C}$$

Thus, $$\frac{2\pi C_4}{A_T p_A \beta} \tan\left(\frac{2\pi C_4}{A_T p_A \beta} \right) = \frac{1}{\beta}$$

Since C_4 is a constant parameter, the pressure amplitude only depends on the volume ratio for this particular parameter study as shown in Figure 4.12.

As with the pressure amplitude, the velocity amplitude ratio only depends on the volume ratio (Figure 4.14). The velocity amplitude at the tailpipe exit was calculated from Equation (4.28), in which the mean density was constant and the mean speed of sound was relatively constant because the jet temperatures were constant. With the same assumptions as for the relationship of the pressure amplitude, Equation (4.28) can be rearranged to show that the velocity amplitude only depends on the pressure amplitude and the volume ratio, as follows:

$$u_{A3} = \frac{p_A}{\rho_{Tm} c_{Tm} \sin\left(\frac{2\pi C_4}{A_T p_A \beta} \right)}$$

Since the pressure amplitude is a function of the volume ratio, a fixed value of the volume ratio yields a fixed value of the velocity ratio, as shown in Figure 4.14.

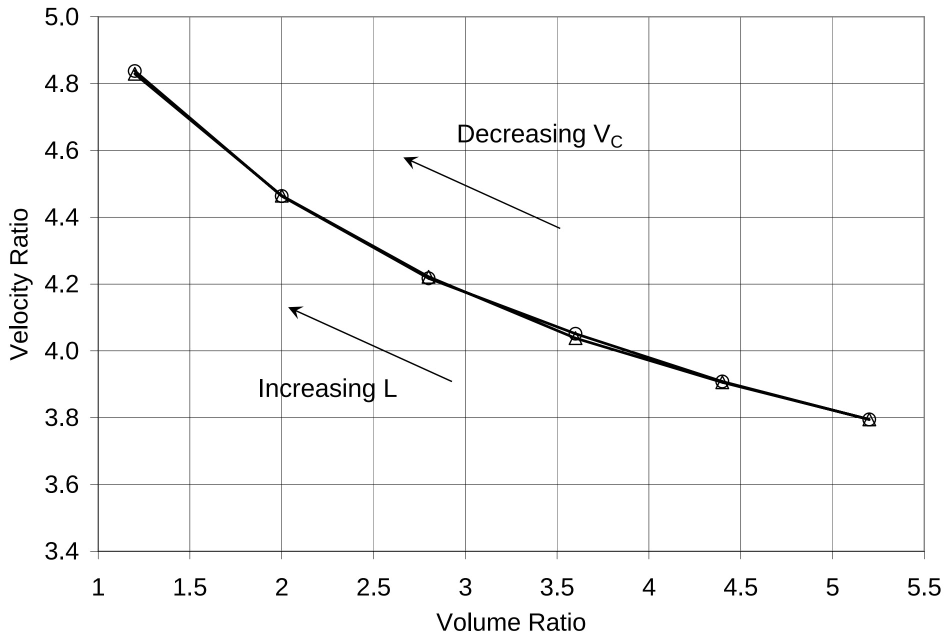

Figure 4.14: Effects of pulse combustor dimensions on velocity ratio at tailpipe exit.

In conclusion, the effects of pulse combustor dimensions predicted by the model are mainly related to the volume ratio. As the volume ratio decreases, the pressure amplitude and the jet velocity ratio increase. However, the frequency increases with decreasing combustion chamber volume (shorter system wavelength) but decreases with increasing tailpipe length (longer system wavelength). These effects can be used as a guideline for pulse combustor design or adjustment to achieve certain goals. For example, to generate a pulsating jet with a higher velocity ratio from an existing Helmholtz pulse combustor, the model suggests decreasing the volume ratio. And it can be achieved, provided that other parameters can be kept constant, by using a smaller combustion chamber or a longer tailpipe or the combination of both, depending on the requirement of frequency, i.e., higher, lower, or the same, respectively. The requirement of the frequency depends on applications. For heat transfer enhancement inside the tailpipe, it is commonly required to have a higher frequency for a higher enhancement factor. As for pulsating jet impingement heat transfer, as discussed later in Chapter 7, the frequency appears to have insignificant effects, for the cases studied, on time- and area-averaged heat fluxes with a practically large velocity ratio (~4) of the pulsating jet.

The combination of the results from the parameter studies in this section can be used as a guideline for a pulse combustor design to generate a pulsating jet with a high velocity ratio. For such applications that the nozzle or tailpipe diameter and flow parameters (jet temperature and mean velocity) at the tailpipe exit are determined first, the model suggests to have the highest temperature possible in the combustion chamber, i.e., equivalence ratio of 1.0. Then the temperature of the pulsating flow has to be cooled down along the tailpipe to the target temperature. This requires some cooling around the tailpipe wall and a certain length of the tailpipe. Then the volume of the combustion chamber should be as small as possible. The combustion chamber volume is typically limited by the requirement of the Rayleigh criterion, i.e., having the highest energy ratio possible. The design of combustion chamber geometry to satisfy the Rayleigh criterion is beyond the scope of the present work. However, the concept is that, as the operating frequency could be estimated by the resonant frequency of the pulse combustor, the flow path and mixing rate of reactants and the combustion delay time should be designed so that heat release rate oscillation is entirely in-phase with pressure oscillation.

4.7 Summary

The simplified model of Helmholtz pulse combustors consists of three submodels: a solution for the pulsating flow in the combustion chamber, a solution for the pulsating flow in the tailpipe, and an approximation of mean temperature in the tailpipe. The combustion chamber submodel is based on the conservation equations of mass and energy. The solution is the expression for the heat source in the energy equation. The tailpipe velocity submodel is based on the solution of linear wave equations in Ahrens (1979), which also yields the prediction of pulsation frequency. The submodel for the mean tailpipe temperature is based on the two-compartment assumption of cooler ambient air and hot gas in the tailpipe. The result from this model is used to calculate the mean speed of sound, required in the tailpipe velocity submodel and the frequency prediction. The information specific to an operating pulse combustor for the model is reduced to one parameter, the energy ratio, defined by the ratio between the amplitude and the mean value of heat source oscillation.

The energy ratio is basically an indicator of the Rayleigh criterion of the operating condition of a pulse combustor. Published data were used to evaluate a typical range of the energy ratio for operating pulse combustors. It appears that the energy ratio mainly depends on the geometry of reactant ports and the combustion chamber. For the pulse combustors at Sandia National Laboratories, the energy ratio was in the range of 0.6-1.0 whereas the pulse combustors at the Georgia Institute of Technology had the energy ratio of 0.5-0.7. The range of the energy ratio from the former cases was wider than those from the latter cases because of the use of a stagnation plate for adjusting the mixing rate and the delay time of reactants.

The model was used to study the effects of inlet flow parameters and pulse combustor dimensions on pulsating flow characteristics, compared to the operating condition of the pulse combustor used for the drying experiment in the preliminary work. The main objective was to obtain a basic understanding of how to generate a pulsating jet with the highest velocity ratio possible. The results suggested that, for given jet temperature and mean velocity at the tailpipe exit, the temperature in the combustion chamber should be as high as possible and the volume ratio of the pulse combustor should be as small as possible. Since the length of the tailpipe could be determined from the cooling requirement, the volume of the combustion chamber should be as small as possible, so long as the Rayleigh criterion is satisfied.

In the next chapter, the model is further simplified to calculate mass flow rate oscillation as an inlet boundary condition of the computational domain for CFD simulation.

CHAPTER 5
SIMULATION APPROACH

This chapter describes the numerical approach and procedure for the simulation of pulsating jet impingement heat transfer. The first section describes the numerical approach for the generation of a controllable pulsating jet at the tailpipe exit. The focus is on the inlet boundary condition of the computational domain. In order that both mean velocity and velocity amplitude at the tailpipe exit can be accurately determined, mass flow rate oscillation is used as the inlet condition. The model in the previous chapter is further simplified and used to calculate velocity oscillation at the tailpipe exit. The second section describes the numerical procedure used in this dissertation, including the V2F turbulence model, from the CFD software, FLUENT. The following section presents simulation results of the pulsating flow and jet impingement heat transfer from the PAD pulse combustor as a validation case.

5.1 Numerical Approach

As discussed in Chapter 3, the numerical approach for simulation of a pulsating flow in the tailpipe needs to be improved so that the velocity oscillation at the tailpipe exit can be accurately determined for both mean velocity and velocity amplitude. The technique used in the present work is to specify mass flow rate oscillation at the inlet boundary of an inlet chamber connected to the tailpipe. This section explains the simplifying conditions for the tailpipe pulsating flow and the calculation of velocity oscillation at the tailpipe exit from the inlet mass flow rate oscillation.

The inlet mass flow rate oscillation can be used with both incompressible and compressible flow models. The calculation of velocity oscillation at the tailpipe exit for an incompressible pulsating flow is straightforward because the velocity amplitude is constant along the tailpipe length. However, from the preliminary work presented in Section 3.3, the convergence rate from the incompressible flow model was extremely slow compared to that from the compressible flow model. In addition, the velocity amplitude along the tailpipe obtained from the compressible flow model was more physically reasonable than that from the incompressible flow. Therefore, the compressible flow model is used for the present work. As with the preliminary work, the compressible flow model is implemented by using the ideal-gas law for fluid density.

For simplicity, properties of air are used instead of those for combustion products. Other properties (viscosity, thermal conductivity, and specific heat capacity) are expressed by temperature-dependent polynomial functions. Another simplifying condition is that the walls of the pulse combustor are adiabatic so that jet temperature (maximum temperature in each oscillation cycle) at the tailpipe exit is easy to control, i.e., to maintain at the same level as the temperature at the tailpipe inlet. And, for the same temperature control reason, the tailpipe is required to be longer than the maximum distance ambient fluid could travel during flow reversal. The other key difference from the preliminary work is the addition of the inlet chamber, similar to the combustion chamber of a Helmholtz pulse combustor. Due to flow compressibility in the inlet chamber, the amplitude ratio of flow oscillation at the inlet boundary can be less than one (no flow reversal at the inlet) while the velocity ratios at tailpipe inlet and exit are larger than one. And, with the inlet chamber, the pulsating flow at the tailpipe inlet would be more physically reasonable in terms of velocity and temperature oscillations during both positive and negative cycles.

As shown in Section 3.3, the amplitude of velocity oscillation of the compressible pulsating flow in the tailpipe increases along the tailpipe length. The calculation of the velocity amplitude at the tailpipe exit is not as simple as the calculation in the case of the incompressible flow. Thus, the simplified model of Helmholtz pulse combustors, specifically the combustion chamber submodel, described in the previous chapter is further simplified to derive the relationship between the inlet mass flow rate and the tailpipe velocity oscillation. The two differences from the model of Helmholtz pulse combustors are the heat source in the combustion chamber and the pattern of inlet mass flow rate oscillation. The inlet boundary of the computational domain is the entrance or the open end of the inlet chamber, which is opposite to the end connected to the tailpipe. For the simulations, no heat source is required because fluid temperature is defined as desired at the inlet boundary. For the simulations, the pattern of inlet mass flow rate oscillation in the present work is a perfectly sinusoidal pattern as

$$\dot{m}_1 = \dot{m}_m \left(1 + \varepsilon_1 \sin(\omega t)\right)$$

where ε_1 is the amplitude ratio of the inlet mass flow rate oscillation. However, the mass flow rate oscillation would be the solution from the further simplified model. The amplitude, $\dot{m}_{A1}$, and the amplitude ratio, ε_1, of the resulting mass flow rate oscillation are defined with the same concept as the energy ratio in the previous chapter as follows.

$$\dot{m}_{A1} = \frac{\omega}{2}\int_0^{1/f} \dot{m}_{1+} dt, \qquad \dot{m}_{1+} = \begin{cases} \dot{m}_1 - \dot{m}_m & , \quad \dot{m}_1 \geq \dot{m}_m \\ 0 & , \quad \dot{m}_1 \leq \dot{m}_m \end{cases}$$

$$\varepsilon_1 = \dot{m}_{A1} / \dot{m}_m \tag{5.1}$$

As the two differences mentioned above are associated with the combustion chamber or the inlet chamber in this case, only the combustion chamber submodel is different from the previous chapter. As for the submodels of tailpipe velocity and mean temperature, all the assumptions and equations remain the same. The combination of conservation equations of mass and energy in the inlet chamber results in an explicit expression for inlet mass flow rate in terms of other flow parameters (pressure, temperature, and velocity) as follows. Note that all the symbols are the same as the model in the previous chapter except that the subscript C signifies the inlet chamber in this case.

The mass balance equation is

$$V_C \frac{d\rho_C}{dt} = \dot{m}_1 - \dot{m}_2$$

The energy balance equation without a source term is

$$V_C \frac{d}{dt}\left(\rho_C h_C - p_C\right) = h_C\left(\dot{m}_1 - \dot{m}_2\right)$$

$$V_C \rho_C \frac{dh_C}{dt} + V_C h_C \frac{d\rho_C}{dt} - V_C \frac{dp_C}{dt} = h_C\left(\dot{m}_1 - \dot{m}_2\right)$$

From the mass balance, $$V_C h_C \frac{d\rho_C}{dt} = h_C\left(\dot{m}_1 - \dot{m}_2\right)$$

Thus, $$V_C \rho_C \frac{dh_C}{dt} = V_C \frac{dp_C}{dt}$$

From $h_C = aT_C + b$, $$\frac{ap_C}{RT_C}\frac{dT_C}{dt} = \frac{dp_C}{dt}$$

$$\frac{1}{T_C}\frac{dT_C}{dt} = \frac{R}{ap_C}\frac{dp_C}{dt} \tag{5.2}$$

Integrating Equation (5.2), $$\ln T_C = \frac{R}{a}\ln p_C + C_1$$

Thus, $$T_C = C_{T_m} p_C^{R/a} \tag{5.3}$$

The constant parameter C_{T_m} is calculated, after the pressure term is determined as described later, such that the maximum value of temperature oscillation is equal to the desired inlet temperature. Equation (5.3) is the expected result for an isentropic process of an ideal gas with constant specific heats, where $R = c_p - c_v$, $a = c_p$, and $\gamma = c_p/c_v$ (Çengel and Boles, 2001).

Returning to the mass balance equation,

$$V_C \frac{d\rho_C}{dt} = \dot{m}_1 - \dot{m}_2$$

$$\frac{V_C}{R}\frac{d}{dt}\left(\frac{p_C}{T_C}\right) = \dot{m}_1 - \dot{m}_2$$

From Equation (5.3), $$\dot{m}_1 = \frac{V_C}{R}\frac{d}{dt}\left(\frac{p_C}{C_{T_m} p_C^{R/a}}\right) + \dot{m}_2$$

Substituting $\dot{m}_2$, $$\dot{m}_1 = \frac{V_C}{RC_{T_m}}\frac{d}{dt} p_C^{1-R/a} + \rho_C A_T u_2$$

$$\dot{m}_1 = \frac{V_C}{RC_{T_m}}\left(1-\frac{R}{a}\right)p_C^{-R/a}\frac{dp_C}{dt} + \frac{p_C A_T u_2}{RT_C}$$

In terms of T_C,

$$\dot{m}_1 = \frac{V_C}{RT_C}\left(1-\frac{R}{a}\right)\frac{dp_C}{dt} + \frac{A_T p_C u_2}{RT_C}$$

Finally,

$$\dot{m}_1 = \frac{1}{RT_C}\left[V_C\left(1-\frac{R}{a}\right)\frac{dp_C}{dt} + A_T p_C u_2\right] \tag{5.4}$$

Equations (5.3) and (5.4) serve as the inlet chamber submodel for this chapter. Combining this submodel with the submodels of tailpipe velocity and mean temperature as well as the desired specifications of tailpipe and pulsating jet parameters for the simulation, the variable left to be solved from Equation (5.4) is either the amplitude ratio of mass flow rate oscillation, ε_I, or the volume of the inlet chamber, V_C. For the validation case in this chapter, Equation (5.4) is used to search for V_C such that ε_I in Equation (5.1) is equal to 1.0, as an arbitrary choice, and the desired velocity ratio at the tailpipe exit is obtained. The process begins with specifying pulsation frequency, tailpipe diameter (or width), jet temperature, mean velocity (yielding mean mass flow rate), and velocity ratio at the tailpipe exit. The maximum distance of flow-reversal fluid travel can be calculated from Equation (4.34). Then the tailpipe length is chosen to be longer than such distance in order to ensure that the jet temperature at the tailpipe exit remains at the same level as the temperature in the inlet chamber. The volume of the inlet chamber or the volume ratio is required to be chosen initially in this step so that the system wavelength can be calculated from Equation (4.26).

In order to calculate pressure amplitude corresponding to the target velocity amplitude from Equation (4.28), another two parameters are required, mean density and mean speed of sound. The mean density is simply calculated from the target jet temperature because fluid temperatures at the tailpipe inlet and exit are almost the same. The mean speed of sound could be calculated from the mean tailpipe temperature estimated from the two-compartment model described in the previous chapter. However, from a comparison with simulation results, the mean speed of sound from this method yielded an inaccurate approximation in terms of mass flow rate amplitude ratio. This is possibly because the model is based on the linear acoustic theory in which the pulsation frequency is equal to the resonance frequency. As for the simulations, the frequency is specified or forced, as are the temperatures at the inlet boundary, impingement surface, and outlet boundary. The forced frequency is not necessarily equal to the resonance frequency of the system, which depends on mean temperature, mean speed of sound, and system wavelength ($f = c_m/\lambda$). Another reason for the inaccurate approximation is that fluid temperature entering the tailpipe during flow reversal in each case is not known until the simulation is run. As discussed later, for most of the simulation cases in this dissertation, the flow-reversal temperature depends on the jet temperature after heat is transferred to the impingement surface, which in turn depends on several parameters discussed in the following chapters. Therefore, for approximation purposes, the mean speed of sound can simply be calculated from the product of the specified frequency and the system wavelength. As it turned out, results from this method were more accurate than the two-compartment model for the simulations in the following chapters. As for the simulation of the validation case in this chapter, results from different methods for finding the mean speed of sound are not much different because the validation case is based on an actual operating condition of the PAD pulse combustor.

With the resulting pressure amplitude and other specified parameters, Equations (5.3) and (5.4) can be now used to calculate the inlet mass flow rate oscillation and its amplitude ratio, ε_I, evaluated by Equation (5.1). The process is repeated with a new value of the volume ratio until the resulting ε_I matches with the target value. It should be noted that the result of this model is only an approximation. In order that the pulsating jet in the simulation has the target velocity ratio, a final adjustment of ε_I from initial simulation results is necessary.

5.2 Numerical Procedure

This section describes the governing equations of unsteady turbulent flows and the V2F turbulence model as well as numerical schemes used in this dissertation from the commercial software, FLUENT version 6.3.

RANS Governing Equations

Since the pulsating flow in a pulse combustor is a turbulent flow, the governing equations for the simulation are Reynolds-Averaged Navier-Stokes (RANS) equations. Extra terms in the momentum equations are so-called Reynolds stresses. These terms are modeled, by most turbulence models, with the Boussinesq hypothesis, which assumes that a parameter called turbulent viscosity or eddy viscosity is isotropic. The V2F turbulence model used in this dissertation is based on this hypothesis and calculates the turbulent viscosity using four transport equations of turbulence parameters. Flow variables in the following governing equations are written as averaged quantities in RANS equations: pressure (p) velocity ($\vec{\upsilon}$), and temperature (T). For convenience, these governing equations are written in symbolic notation following the FLUENT 6.3 User's Guide (Fluent, 2006). The simulations in this chapter use cylindrical coordinates (with an axisymmetric circular tailpipe) whereas the simulations in the following chapters use Cartesian coordinates (with plane-symmetric slot tailpipes). The conversion from the symbolic notation to either coordinate system can be found in references such as Bird et al. (2002).

Continuity equation:

$$\frac{\partial \rho}{\partial t} + \nabla \cdot \left(\rho \vec{\upsilon}\right) = 0$$

Momentum equation:

$$\frac{\partial}{\partial t}\left(\rho \vec{\upsilon}\right) + \nabla \cdot \left(\rho \vec{\upsilon} \vec{\upsilon}\right) = -\nabla p + \nabla \cdot (\overline{\overline{\tau}} + \overline{\overline{\tau_t}})$$

$$\overline{\overline{\tau}} = \mu \left[\left(\nabla \vec{\upsilon} + \nabla \vec{\upsilon}^{T}\right) - \frac{2}{3} \nabla \cdot \vec{\upsilon} \overline{\overline{I}}\right]$$

$$\overline{\overline{\tau_t}} = \mu_t \left[\left(\nabla \vec{\upsilon} + \nabla \vec{\upsilon}^T \right) - \frac{2}{3} \left(\frac{\rho k_t}{\mu_t} + \nabla \cdot \vec{\upsilon} \right) \overline{\overline{I}} \right]$$

Energy equation:

$$\frac{\partial}{\partial t}(\rho E) + \nabla \cdot \left(\vec{\upsilon}(\rho E + p) \right) = \nabla \cdot \left(k_{eff} \nabla T \right)$$

$$E = h - \frac{p}{\rho} + \frac{\upsilon^2}{2}$$

$$h = \int_{T_{ref}}^{T} c_p dT$$

$$k_{eff} = k + \frac{c_p \mu_t}{\Pr_t}$$

where E is specific total energy, h is specific enthalpy, c_p is specific heat capacity, μ is dynamic viscosity, k is thermal conductivity, T_{ref} = 298.15 K, and turbulent Prandtl number, $\Pr_t$ = 0.85. Three fluid properties, dynamic viscosity, specific heat capacity, and thermal conductivity, are expressed by temperature-dependent polynomial functions added to the material database of the FLUENT software. The values of these properties are taken from the table of air properties at atmospheric pressure in Incropera and DeWitt (2002). As for the density of air, the ideal-gas law is used as the compressible flow model. Turbulence kinetic energy (k_t) and the turbulent viscosity (μ_t) in the Reynolds stress tensor term ($\overline{\overline{\tau_t}}$) and in the effective thermal conductivity (k_{eff}) are calculated by the V2F turbulence model as follows.

V2F Turbulence Model

First, note that the symbols for turbulence parameters (k, ε, v^2, and f) used in this sub-section follow symbols specifically used in the literature about turbulence models and the reference, FLUENT 6.1 v^2-f Turbulence Model Manual (Fluent, 2003). The definition of these symbols as used in other sections and chapters is listed in the List of Symbols. The V2F model solves four transport equations of turbulence parameters, two from the standard k-ε model (turbulence kinetic energy and dissipation rate, respectively) and another two for a velocity variance scale (v^2) and an elliptic relaxation function (f).

The latter two parameters were developed originally as a near-wall treatment for mildly separated flows. Nevertheless, it has been shown that this model is accurate for more complex flows and heat transfer, e.g., strongly separated flows (Durbin, 1995), unconfined and confined jet impingement heat transfer (Behnia et al., 1998 and 1999), pulsating channel flows (Scotti & Piomelli, 2002), and three-dimensional flows and heat transfer (Parneix et al., 1998, Etemad & Sundén, 2006). The governing equations for the V2F turbulence model in the FLUENT software can be written in symbolic notation as follows.

$$\frac{\partial}{\partial t}(\rho k) + \nabla \cdot (\rho k \vec{\upsilon}) = \overline{P} - \rho\varepsilon + \nabla \cdot \left[\left(\mu + \frac{\mu}{\sigma_k} \right) \nabla k \right]$$

$$\frac{\partial}{\partial t}(\rho \varepsilon) + \nabla \cdot (\rho \varepsilon \vec{\upsilon}) = \frac{C'_{\varepsilon 1} \overline{P} - C_{\varepsilon 2} \rho \varepsilon}{T} + \nabla \cdot \left[\left(\mu + \frac{\mu_t}{\sigma_\varepsilon} \right) \nabla \varepsilon \right]$$

$$\frac{\partial}{\partial t}\left(\rho \overline{\upsilon^2}\right) + \nabla \cdot \left(\rho \overline{\upsilon^2} \vec{\upsilon}\right) = \rho k f - 6 \rho \overline{\upsilon^2} \frac{\varepsilon}{k} + \nabla \cdot \left[\left(\mu + \frac{\mu_t}{\sigma_k} \right) \nabla \overline{\upsilon^2} \right]$$

$$f - L^2 \nabla^2 f = (C_1 - 1) \frac{\frac{2}{3} - \overline{\upsilon^2}/k}{T} + C_2 \frac{\overline{P}}{\rho k} + \frac{5 \overline{\upsilon^2}/k}{T}$$

where $$\overline{P} = 2\mu_t S^2 ,\ S^2 = \overline{\overline{S}} : \overline{\overline{S}} ,\ \overline{\overline{S}} = \frac{1}{2}\left(\nabla \vec{\upsilon} + \nabla \vec{\upsilon}^T \right)$$

The turbulent time scale, T, and length scale, L are defined as follows.

$$T' = \max\left[\frac{k}{\varepsilon}, 6\sqrt{\frac{\nu}{\varepsilon}} \right]$$

$$T = \min\left[T', \frac{\alpha}{\sqrt{3}} \frac{k^{3/2}}{\overline{\upsilon^2} C_\mu \sqrt{2S^2}} \right]$$

$$L' = \min\left[\frac{k^{3/2}}{\varepsilon}, \frac{1}{\sqrt{3}} \frac{k^{3/2}}{\overline{\upsilon^2} C_\mu \sqrt{2S^2}} \right]$$

$$L = C_L \max\left[L', C_\eta \left(\frac{\nu^3}{\varepsilon} \right)^{1/4} \right]$$

where ν is kinematic viscosity. The turbulent viscosity is calculated by

$$\mu_t = \rho C_\mu \overline{\upsilon^2} T$$

Constant parameters of the model have following values.

$$\alpha = 0.6,\ C_1 = 1.4,\ C_2 = 0.3,\ C_{\varepsilon 1} = 1.4,\ C_{\varepsilon 2} = 1.9,\ C_\eta = 70,$$
$$C_\mu = 0.22,\ C_L = 0.23,\ \sigma_k = 1,\ \sigma_\varepsilon = 1.3,\ C'_{\varepsilon 1} = C_{\varepsilon 1}\left(1 + 0.045\sqrt{k/\overline{\upsilon^2}}\right)$$

Computational domain and boundary conditions

Computational domains and boundary conditions are conceptually the same for all simulation cases and are shown in Figure 5.1. The computational domain consists of an impingement zone with confinement and a "pulse combustor" for the generation of a pulsating jet. Because flow reversal could occur at the boundaries, the quotations for "inlet" and "outlet" boundaries are used to indicate that the meaning relates to the direction of mean mass flow rate.

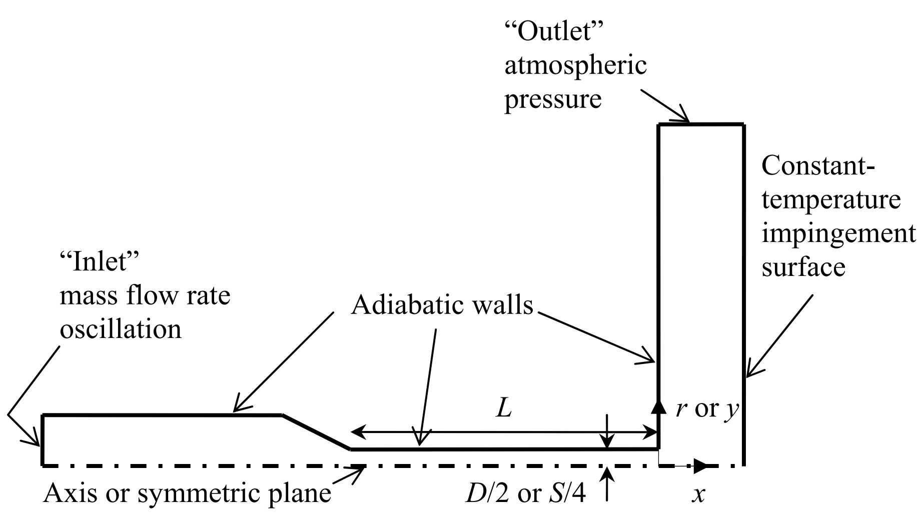

Figure 5.1: Computational domain and boundary conditions for simulation cases with a stationary surface.

For the cases with a stationary surface, an axis or a symmetry plane was used for a circular tailpipe or a slot tailpipe, respectively. Thus, the width of the tailpipe in the computational domain was equal to the radius ($D/2$) of the circular tailpipe or the half-width ($B/2 = S/4$) of the slot tailpipe, where S is the hydraulic diameter of the slot tailpipe. For the cases with a moving surface in Chapter 8, the computational domain covered both sides of the slot tailpipe centerline because the flow field was not symmetric. Tailpipe length, L, varied from case to case in such a way that, during flow reversal, fluid from outside the tailpipe could not reach the inlet chamber, to ensure that the temperature of the jet exiting the tailpipe would be controlled by the same inlet chamber temperature for all cases. The length of the impingement surface and the confinement wall was extended so that the area or the length of interest on the impingement surface near the stagnation point was not significantly affected by backflow conditions from the outlet boundary.

The boundary conditions at "inlet" and "outlet" boundaries were mass flow rate oscillation and atmospheric pressure, respectively. The inlet mass flow rate oscillation was expressed by a sine function.

$$\dot{m}_1 = \dot{m}_m \left(1 + \varepsilon_1 \sin(\omega t)\right)$$

All the walls had no-slip conditions and were adiabatic except the impingement surface, where the thermal condition was constant temperature. The temperature and turbulence parameters at the inlet and outlet boundaries were specified only for the inflows entering the domain. For the outgoing flow at the pressure outlet boundary, the simulation software calculated these flow quantities by extrapolating from interior cells. The turbulence parameters for the inflows at the boundaries were turbulent viscosity ratio (μ_t/μ) and turbulence intensity (I). The typical values of the turbulent viscosity ratio and the turbulence intensity at the inlet boundary were 1000 and 50%. For steady flow with the mean mass flow rate (as the initial condition of the pulsating flow), the resulting turbulence intensity at the center of the tailpipe exit was in the range of 3-5%, as for a fully-developed turbulent pipe or channel flow. For backflows at the outlet boundary, the turbulent viscosity ratio and the turbulence intensity were 1 and 1%, respectively. Note that the turbulence intensity was based on a reference velocity (u_{ref}), which was set to be the mean bulk velocity at the tailpipe exit in each respective case. The relationships among turbulence parameters are as follows.

Turbulence kinetic energy: $k = \frac{3}{2}\left(u_{ref} I\right)^2$

Dissipation rate of k: $\varepsilon = \rho C_\mu \frac{k^2}{\mu}\left(\frac{\mu_t}{\mu}\right)^{-1}$

where C_μ is a constant parameter in the V2F turbulence model. For the inflows at boundaries, FLUENT sets $\overline{\upsilon^2} = 2k/3$ and uses a zero-gradient condition for the f parameter of the V2F turbulence model. For boundary conditions at the walls, FLUENT internally imposes values for turbulence parameters, which typically were zero for k and $\overline{\upsilon^2}$. As for the values of ε and f at the walls, although the calculation is not provided in the User's Guide, it could be assumed that the following asymptotic solutions are used (Parneix et al., 1998):

$$\varepsilon_{wall} = 2\nu\left(\frac{k}{y^2}\right)_{wall} \quad \text{and} \quad f_{wall} = \frac{-20\nu^2}{\varepsilon}\left(\frac{\overline{\upsilon^2}}{y^4}\right)_{wall}$$

where y is the wall normal distance.

Numerical Schemes

The following numerical schemes were used for all simulation cases in this and following chapters. The discretization of space and time were second-order upwind and second-order implicit schemes, respectively. The solver was the pressure-based segregated algorithm, i.e., solving the governing equation for one variable at a time. The pressure-velocity coupling method was SIMPLE. For the cases with pulsating flows, one oscillation cycle was divided into 500 time steps, regardless of frequency. Scaled convergence criteria for each time step were $1\text{x}10^{-4}$ for momentum equations, $1\text{x}10^{-6}$ for the energy equation, and $1\text{x}10^{-3}$ for turbulence equations. Fine grids were used near all the walls, especially the impingement surface and the tailpipe wall, so that the nondimensional distance from the wall (y^+) of the grid cell next to the wall was not significantly greater than one at any time step. The value of y^+ being less than one for the V2F model, a common practice in the literature and also recommended by the technical support staff of the FLUENT software, is required so that the viscous sublayer next to the wall can be resolved and wall heat transfer can be predicted with relatively high accuracy. For steady jet impingement flows as initial conditions of pulsating flows, the scaled convergence criteria were decreased to 1×10^{-6} for all equations or until surface heat fluxes were insignificantly changed.

For the cases with a pulsating jet, the simulation was run until the oscillations of the flow and temperature fields, as well as surface heat transfer, were relatively stable. The evaluation of simulation results varied from case to case depending on the stability of flow oscillation. For most cases having very stable oscillations, in which the patterns of the oscillation from two successive cycles were repetitive or had less than 1% change in values over the whole cycle, flow characteristics, e.g., mean and amplitude values, were evaluated from the last cycle. For a few cases having less stable oscillations, in which peak values of successive cycles changed slightly, the flow characteristics were evaluated from the average of 5-10 cycles depending on the degree of the oscillation stability. In general, the simulations required about 30-40 cycles for each case.

5.3 Validation Case

Simulation results using the numerical approach and procedure described above were validated with available experimental results from the PAD pulse combustor (Figure 3.1) in Psimas et al. (2007). The measured results were surface heat fluxes from a pulsating jet with a similar condition as that for the drying experiment. The measurement technique, using temperature sensors embedded in an impingement plate, was based on a model of one-dimensional heat conduction in a semi-infinite solid which assumes that heat flux does not reach the back side of the plate during the testing period. This technique is a so-called inverse heat transfer problem, i.e., solving heat flux boundary condition from measured temperature data, in which the initial value for this case was at room temperature. The resulting time-averaged surface heat fluxes from the pulsating jet were 150, 140, and 40 kW/m^2, at the positions of r = 0, 20, and 40 mm from the stagnation point, respectively (r/D = 0, 0.8, and 1.6, respectively, where D = 25.4 mm is the tailpipe diameter).

The condition of the pulsating jet at the tailpipe exit for this case was as follows: mean mass flow rate, $\dot{m}_m$ = 4 g/s; jet temperature, T_j = 1200 K; frequency, f = 153.8 Hz (cycle period = 6.5 ms). The corresponding mean velocity was u_m = 26.8 m/s. The mean Reynolds number was about 4150 based on mean velocity, tailpipe diameter, and jet temperature. The target jet velocity ratio, ε, was 3.8. The computational domain, as shown in Figure 5.2, was designed so that the amplitude ratio of inlet mass flow rate oscillation, which was set to ε_I = 1.0 would yield the target jet velocity ratio. The resulting volume ratio was 5.9. It should be noted that the value of H in the reference was stated to be 25.4 mm or 1D. But from impingement conditions in more recent experiments with the same equipment, H was measured to be about 1.5″ or 38.1 mm. The difference was either a misstatement in the reference or the spacing was actually changed after that experiment. For this simulation, the value recently measured (H = 1.5D) was chosen.

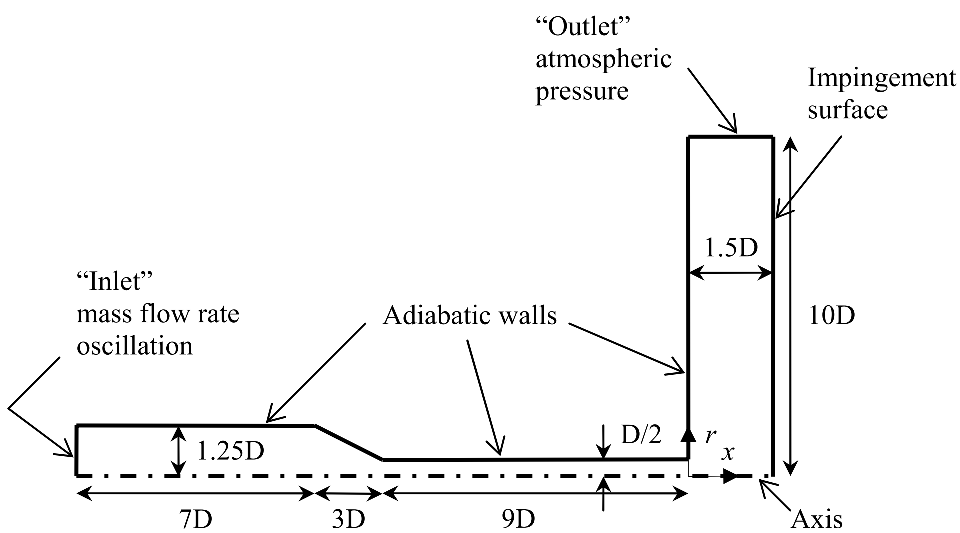

Figure 5.2: Computational domain for the validation case.

All the walls in the computational domain except for the impingement surface were adiabatic. The temperature of the impingement surface was held constant at 300 K. The temperature of the flow entering the domain at the inlet boundary was 1200 K. The outlet boundary condition was atmospheric pressure with backflow temperature of 300 K. Turbulence parameters at the inlet boundary were turbulent intensity of 50% and turbulent viscosity ratio of 1000. For backflows at the outlet boundary, turbulent intensity and turbulent viscosity ratio are 1% and 1, respectively.

Simulation Results

A grid independence study was performed by simulating steady jet impingement with the jet velocity at five times the mean velocity of the pulsating jet. The companion software of FLUENT, GAMBIT, was used to generate grid cells in the computational domain. The number of grid cells in the axial and radial directions for the base grid is 140x180 cells in the impingement zone, 150x57 cells in the tailpipe zone, and 208x101 cells in the inlet chamber zone. As for the grid independence study, the number of grid cells was doubled in both axial and radial directions such that the size of every grid cell was four times smaller than the base grid. Figure 5.3 shows profiles of local heat fluxes from both sets of grid, which are essentially the same. Figure 5.4 shows profiles of jet velocity and turbulence intensity from both sets of grids, which are also insignificantly different. Therefore, all simulation results presented in this chapter are from the original grid.

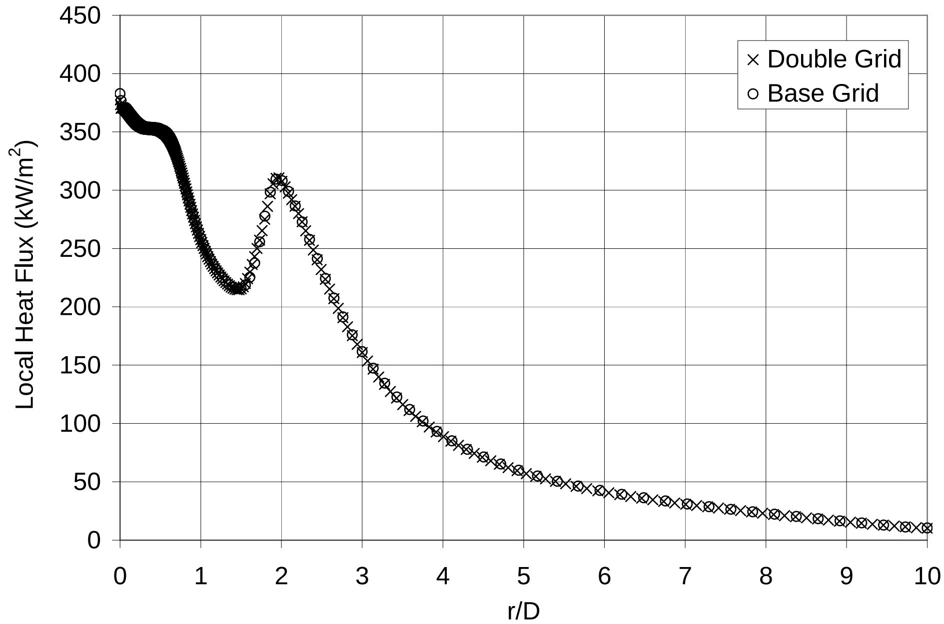

Figure 5.3: Local heat flux profiles from grid independence study for the validation case.

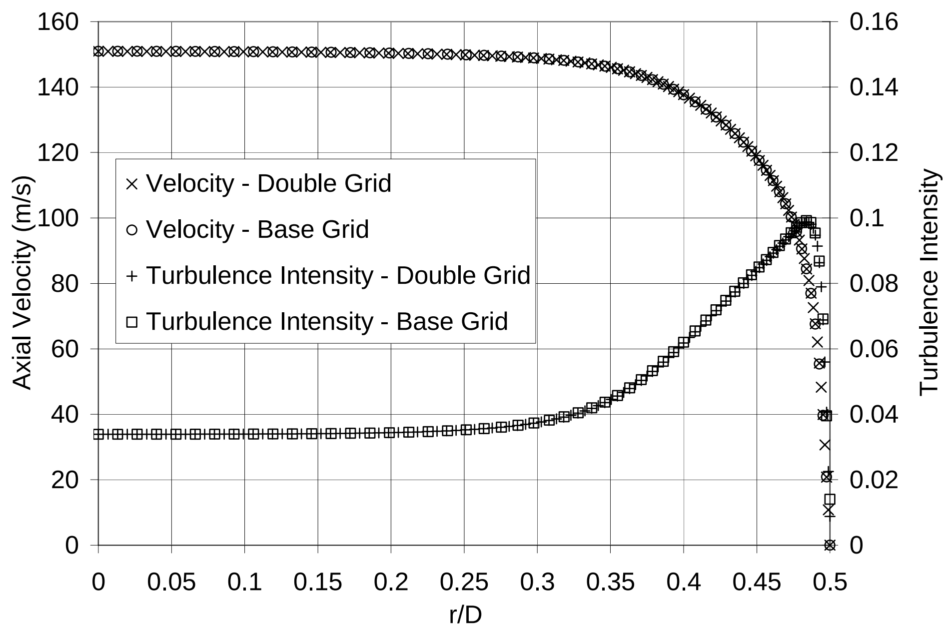

Figure 5.4: Profiles of axial velocity and turbulence intensity at tailpipe exit from grid independence study for the validation case.

Figure 5.5 shows the oscillations of jet velocity and temperature at the tailpipe exit and surface heat flux over one cycle. The mean velocity and velocity ratio were 26.6 m/s and 3.9, respectively, which showed that the numerical approach with mass flow inlet boundary condition works quite well. The temperature oscillation displays the behavior of mass conservation in the tailpipe, i.e., flow-reversal fluids flowing in and out of the tailpipe followed by fresh hot fluid at the end of the positive cycle of the velocity oscillation. The corresponding surface heat flux oscillation peaks at some delay time after fresh hot fluid begins to exit the tailpipe and then decreases during the flow-reversal period.

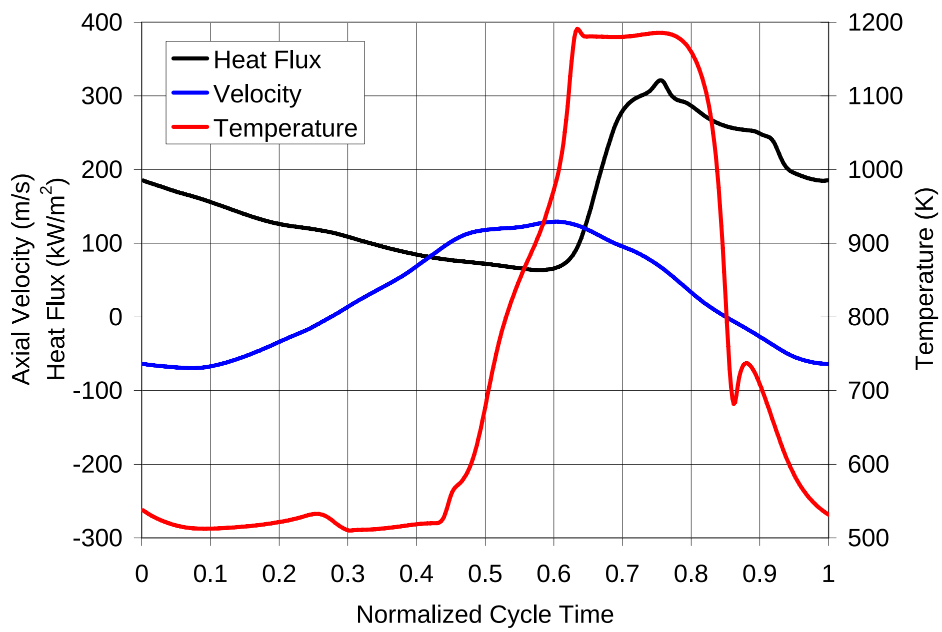

Figure 5.5: Oscillations of area-averaged velocity and mass-averaged temperature at tailpipe exit and area-averaged heat flux at impingement surface over $r \leq 1.5D$.

Figure 5.6 shows time-averaged local heat flux profiles from the steady jet and the pulsating jet compared with heat flux measurement data from Psimas et al. (2007). The temperature of the steady jet was 950 K, as the comparison in the reference was based on the same mean mass flow rate and the same mean temperature at the tailpipe exit. In general, simulation results for both steady and pulsating jet impingement were consistent with measurement data at *r/D* = 0 and 0.8, considering several assumptions were made especially for the pulsating jet. However, simulation results of heat fluxes at *r/D* = 1.6 were higher than the experimental data for both pulsating and steady jets. As surface heat flux directly depends on the temperature gradient in the boundary layer at the surface, these large differences in heat flux indicate that either the deceleration rates of the wall jet velocities or the entrainment rates of cooler air or the combination of both rates at such position in the experiment were higher than those predicted by the simulations. Since no further detailed measurement data of flow fields were available, actual physical reasons could not be identified. Nevertheless, these comparisons at least showed that the magnitudes of heat fluxes predicted by the simulations were generally at the same level as those from the experiment.

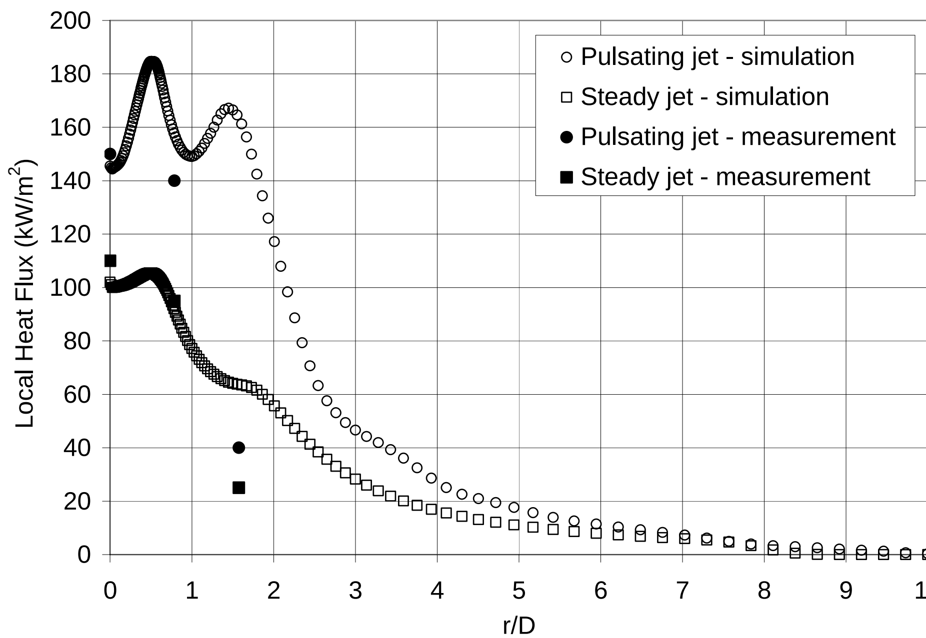

Figure 5.6: Time-averaged profiles of local heat fluxes from steady and pulsating jets compared to measurement data from Psimas et al. (2007).

For reference and comparison with the base case with a slot tailpipe in the next chapter, instantaneous results of this case are shown in Figures 5.7-5.11. In these Figures, τ is normalized cycle time with respect to the oscillation cycle of inlet mass flow rate, in which the positive cycle begins at $\tau = 0.0$. However, the positive cycle of jet velocity oscillation at the tailpipe exit begins at $\tau \sim 0.4$ due to the effects of fluid compressibility in the inlet chamber. The instantaneous velocity vectors, temperature contours, and local heat flux profiles during the positive and the negative cycles of velocity oscillation are shown in Figures 5.7 and 5.8, respectively, including the time-averaged profile of local heat flux (over $0 \leq \tau \leq 1.0$). The most left-hand triangle marker under the impingement surface indicates the position of $r = D/2$ or the edge of tailpipe exit. Then next markers indicate the positions of $r = D$, $2D$, $3D$, and so on. An interesting result is that the vortex propagating along with the wall jet does not eventually become a large re-circulating flow as was the case from preliminary simulation work. Two key differences are that the present case assumed compressible flow and had a lower mean jet velocity (26.6 vs. 50 m/s). As shown in the next chapter for the base case with the same compressible flow assumption and similar mean jet velocity but with a slot tailpipe, the vortex in that case eventually becomes a strong re-circulating flow near the stagnation point. Thus, the behavior of the vortex in this axisymmetric case was possibly due to the magnitude of wall jet velocity not being high enough for the vortex to grow into a large re-circulating flow.

Figures 5.9, 5.10, and 5.11 show instantaneous profiles of axial velocity, temperature, and turbulence intensity at the tailpipe exit, respectively. For all three figures, profiles in red and blue correspond to positive and negative cycles of jet velocity oscillation, respectively. The behavior of these profiles follows the flow characteristics discussed in previous chapters. From the instantaneous velocity profiles, fluids near the wall ($r/D = 0.5$) changed direction before the bulk flow. This behavior can be observed in instantaneous temperature profiles as well. As for the bulk flow, temperature did not reach the maximum value or jet temperature until $\tau = 0.7$ or near the end of the positive cycle because cooler fluids entering the tailpipe during flow reversal had to be driven out of the tailpipe first. Instantaneous turbulence intensity also showed typical profiles of fully-developed pipe flow at $\tau = 0.7$-0.8, corresponding to hot fresh fluid from upstream exiting the tailpipe. Patterns of instantaneous turbulence intensity profiles at other times in the cycle were largely affected by the flow-reversal fluid, which had higher turbulence intensity than the fresh fluid upstream.

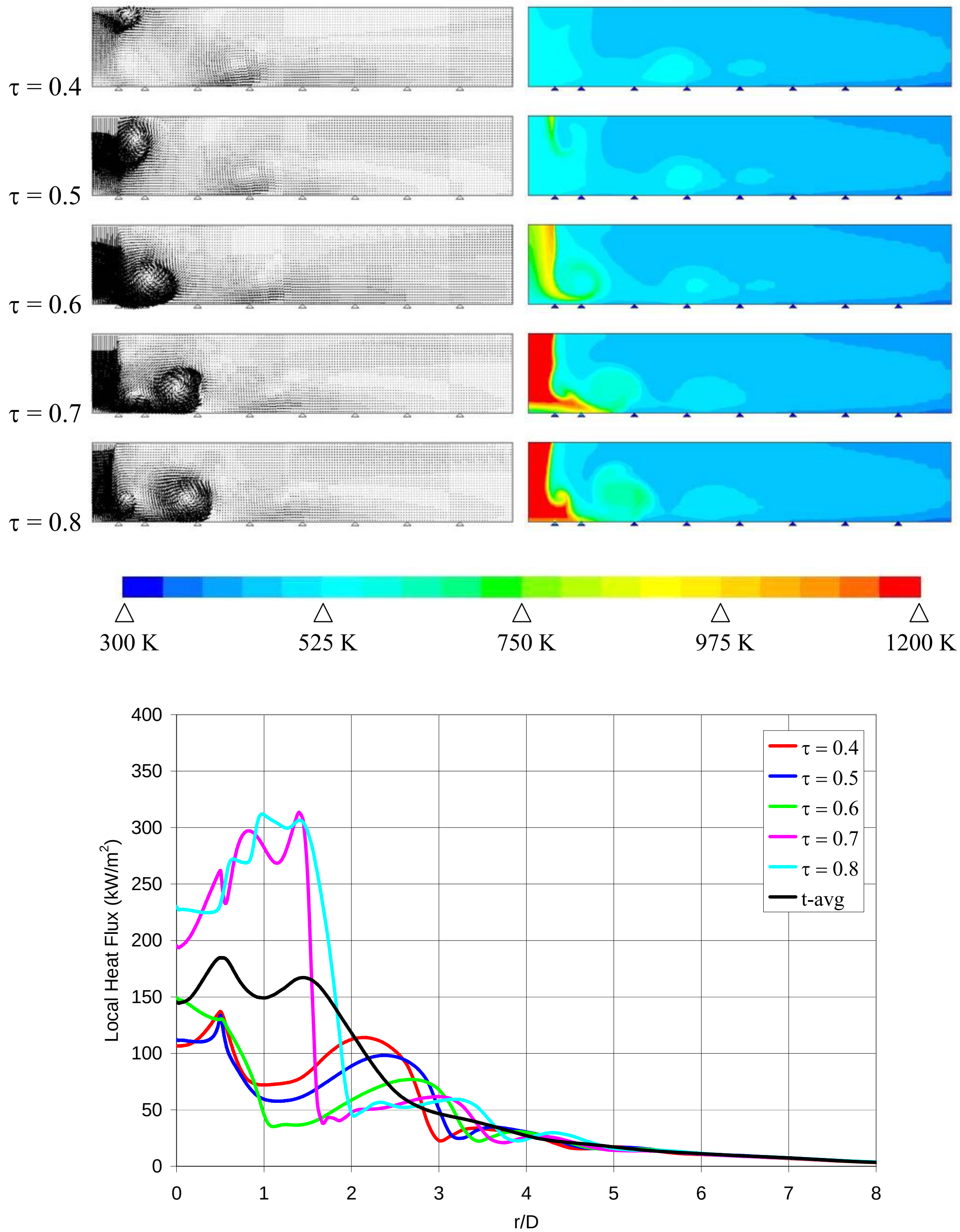

Figure 5.7: Velocity vectors, temperature contours and corresponding local heat flux profiles during positive cycle of jet oscillation for the validation case.

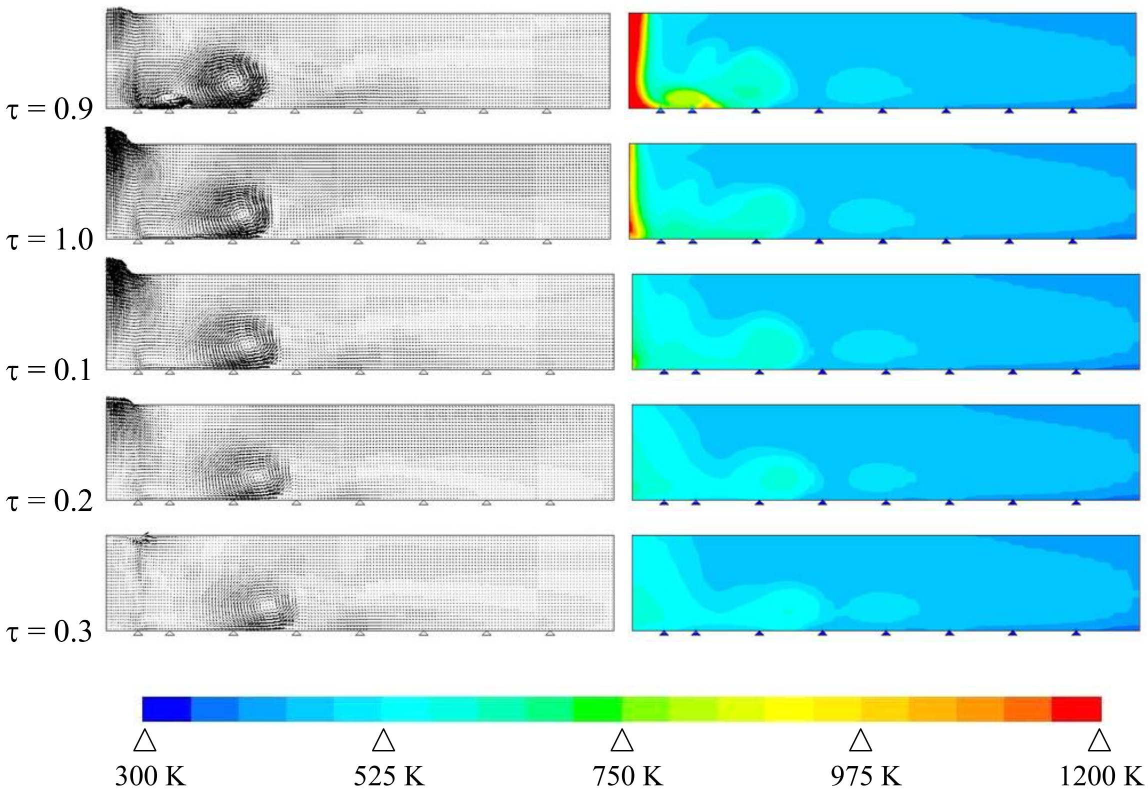

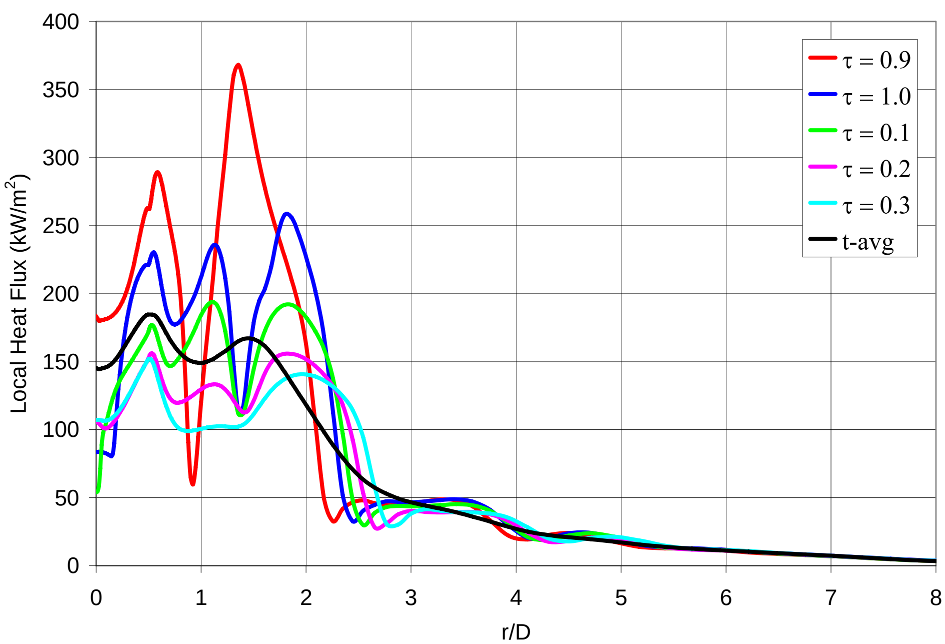

Figure 5.8: Velocity vectors, temperature contours and corresponding local heat flux profiles during negative cycle of jet oscillation for the validation case.

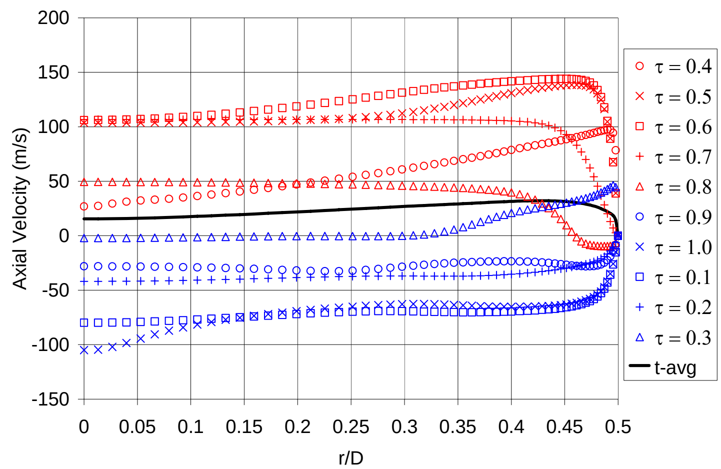

Figure 5.9: Instantaneous profiles of axial velocity at tailpipe exit for the validation case.

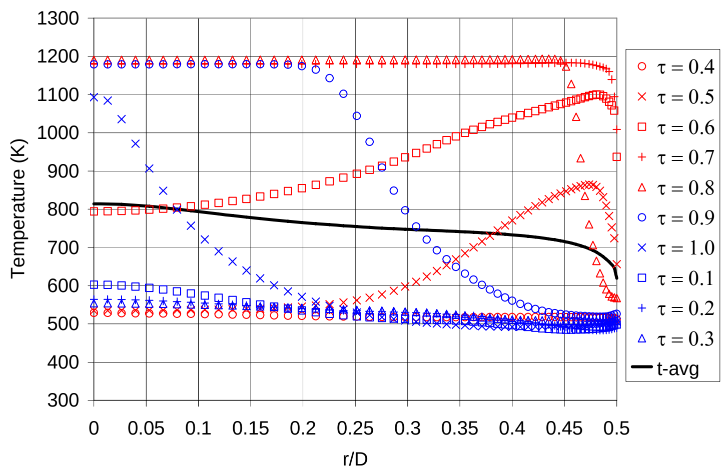

Figure 5.10: Instantaneous profiles of temperature at tailpipe exit for the validation case.

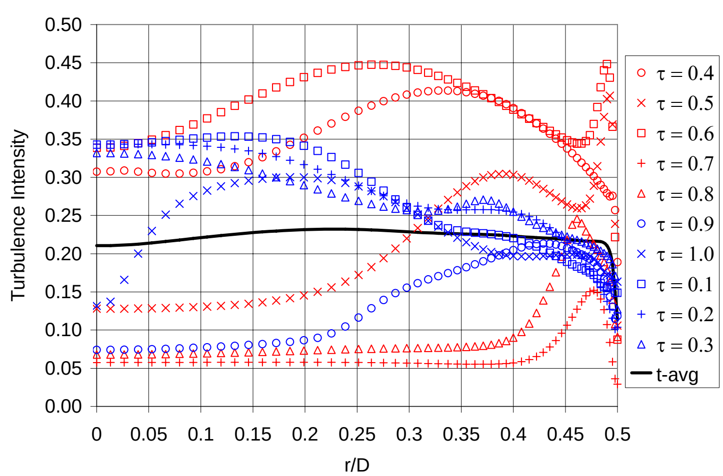

Figure 5.11: Instantaneous profiles of turbulence intensity at tailpipe exit for the validation case.

In order to evaluate practical heat transfer enhancement factors, two more steady jets with the same mean mass flow rate but different jet temperatures were simulated. Figure 5.12 shows the time-averaged profiles of area-averaged heat fluxes from the pulsating jet and three steady jets with T_j = 800, 950, and 1200 K. The simulated pulsating jet had a jet temperature or maximum temperature of 1200 K and a mean temperature of 740 K. In terms of energy input rate, the pulsating jet has a value 1.6, 1.3, and 1.0 times as high as that for steady jets with T_j = 800, 950, and 1200 K, respectively. Profiles of enhancement factors are shown in Figure 5.13. The maximum enhancement factors are 3.0, 2.1, and 1.4 with respect to the steady jets with T_j = 800, 950, and 1200 K, respectively. The position where the maximum enhancement factor occurs, about r/D = 2, coincides with the position at which vortices are still strong at the beginning of the negative cycle, τ = 0.9 in Figure 5.8.

These results for enhancement factor show that the operating condition of the pulsating jet does not yield a very high enhancement factor compared to the steady jet with equivalent energy rate (enhancement factor = 1.4 compared to the steady jet with T_j = 1200 K). For the comparison with the steady jet having T_j = 950 K, the enhancement factors were at the same level (1.4-2.1 from r/D = 0-2) as those from the comparison between pulsating and steady jets in the experiment at Sandia National Laboratories reviewed in Chapter 2. In that experiment, the jet temperatures of pulsating and steady jets were 1400 and 1200 K, respectively; the velocity ratio of the pulsating jet, ε = 4.7, and the nozzle-to-surface spacing ratio, H/D = 2-4. Although the conditions of the simulation and the experiment were quite different, the comparison is made to show that the simulation results are somewhat reasonable.

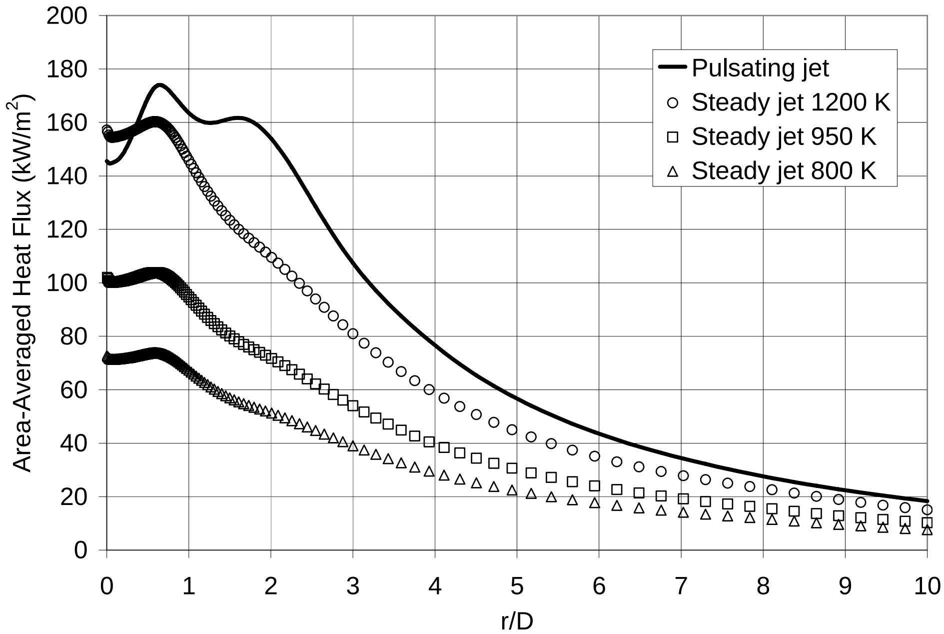

Figure 5.12: Time-averaged profiles of area-averaged heat fluxes from the pulsating jet and stead jets with different jet temperatures for the validation case.

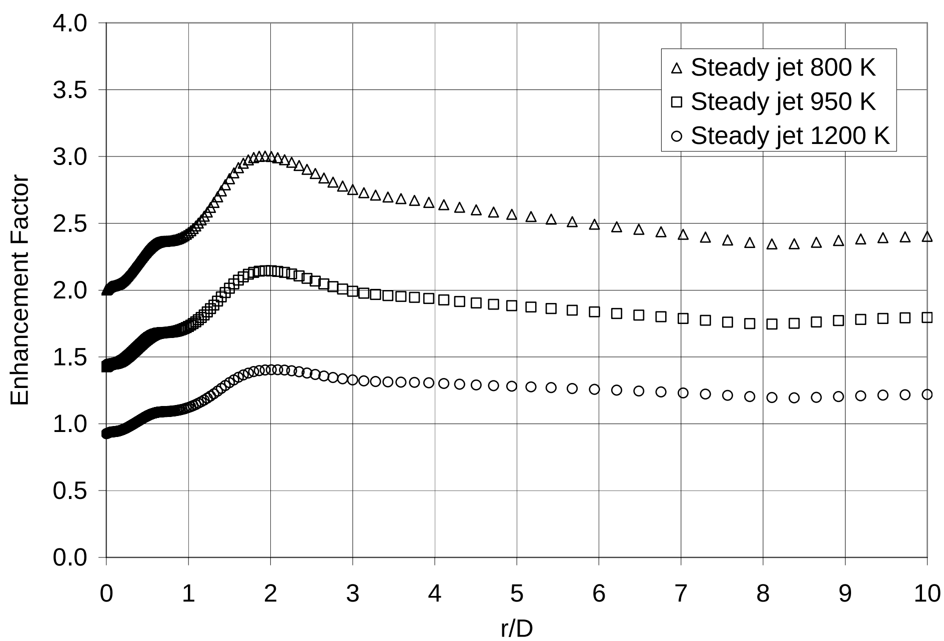

Figure 5.13: Enhancement factors corresponding to the profiles of area-averaged heat fluxes in Figure 5.12.

The operating condition of the pulsating jet from the Sandia experiment could have been used for the simulation and the validation of simulation results. However, it was not used because data on thermal conditions at the impingement surface, e.g., temperature profiles, were not available. In addition, the unconfined impingement condition was different from the cases of interest for the present work. As for the experiments with the PAD pulse combustor, future work includes the measurement of more data points of the heat flux profile along the impingement surface, with more operating conditions of pulsating and steady jets, so that the validation of simulation results can be performed with a higher confidence level.

As a part of the evaluation of the numerical approach, the effects of velocity ratio, ambient or backflow temperature, compressible flow model, and time-step duration were also studied. Figure 5.14 shows timed-averaged profiles of local heat flux with different velocity ratios. The effects of jet velocity ratio are most noticeable at the area near the stagnation point where the jets directly impinge onto the surface. However, the behavior of vortices is basically the same, resulting in a similar level of heat flux in the area beyond $r/D = 0.8$.

The effects of ambient temperature or backflow temperature at the outlet boundary are shown in Figure 5.15. Although the difference in temperature was as large as 400 K, the time-averaged profiles of local heat fluxes are essentially the same except for the area close to the outlet boundary, in which surface heat fluxes were the result of backflows entering the computational domain. However, the backflows appeared to be limited to the area near the outlet boundary because of large-scale re-circulating flows in the impingement zone blocking the backflows from entering further into the zone.

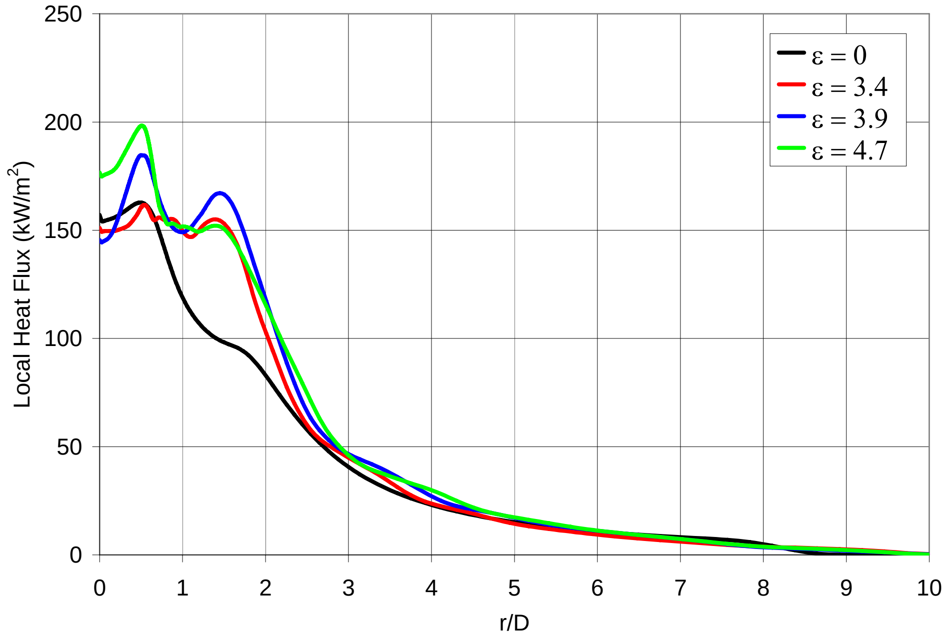

Figure 5.14: Time-averaged profiles of local heat fluxes of pulsating jets with different velocity ratios for the validation case.

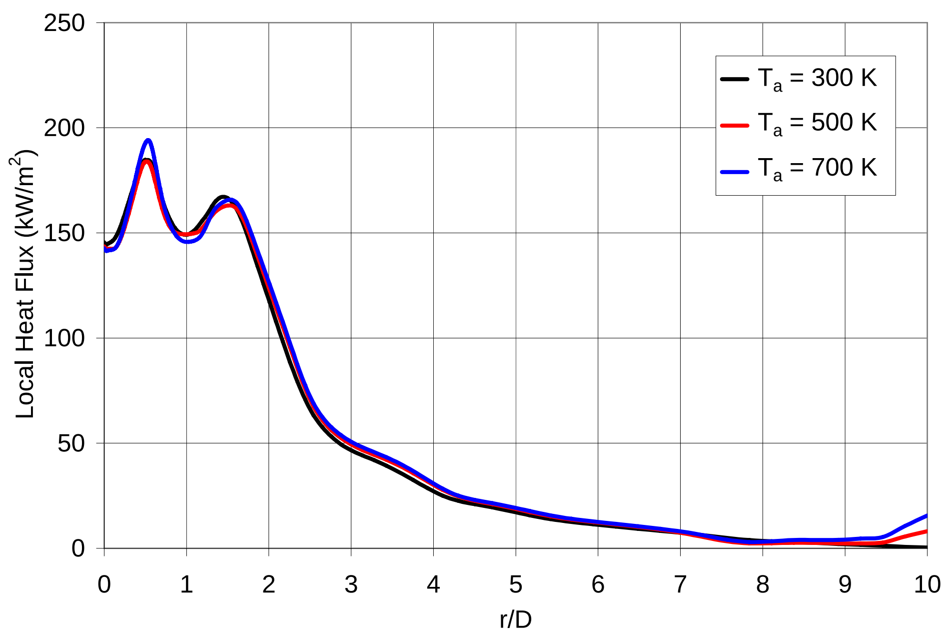

Figure 5.15: Time-averaged profiles of local heat fluxes of pulsating jets with different ambient temperatures for the validation case.

The effects of the size of time step are shown in Figure 5.16. The magnitude of the heat flux was slightly different for the two time steps. These profiles resulted from averaging over 10 cycles. The oscillation of heat flux from the case with the smaller time step was less stable than that from the base case, as shown in Figure 5.17, due to a less stable pressure oscillation in the inlet chamber, which in turn caused less stable velocity oscillation at the tailpipe exit. The pressure oscillation was less stable due to a larger vortex structure in the inlet chamber. Although this behavior might be more physically accurate, 500 time steps per cycle were still used for other simulation cases because the simulations with 1000 time steps per cycle need considerably more oscillation cycles to evaluate time-averaged results, which might not be much different from the base case. Furthermore, as shown in the next chapter, the results for the main numerical study are not significantly affected by the size of time step.

Finally, the effects of the density function or fluid compressibility are shown in Figure 5.18. The magnitude of time-averaged heat fluxes were generally at the same level. The main difference in terms of simulation results was the distance that vortices travel as shown in Figure 5.19. With an incompressible flow model, although vortices could propagate further, they were weaker than those from a compressible flow model. These effects can be seen from the magnitude of the second peak of local heat flux profiles in Figure 5.18. In terms of numerical performance, the convergence rate with the compressible flow model was 2.5 times faster than that with the incompressible flow model.

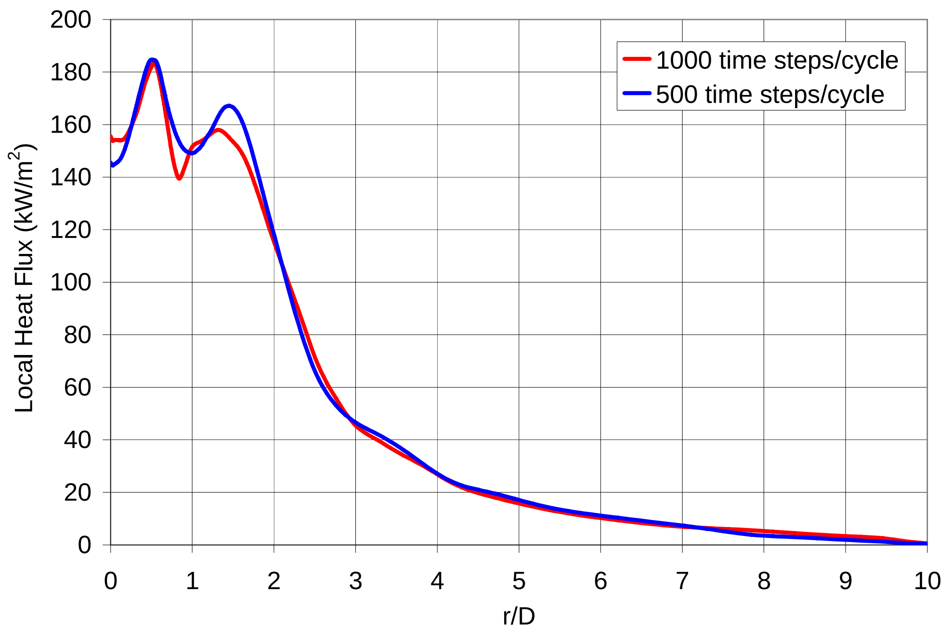

Figure 5.16: Time-averaged profiles of local heat fluxes at different time steps for the validation case.

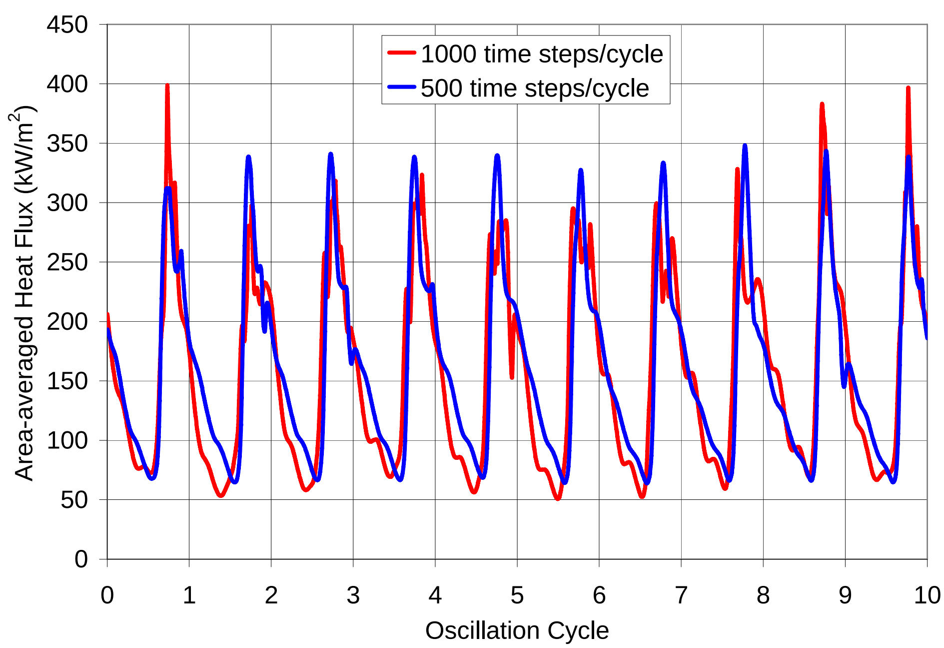

Figure 5.17: Oscillations of area-averaged heat flux ($r/D \leq 1.5$) at different time steps for the validation case.

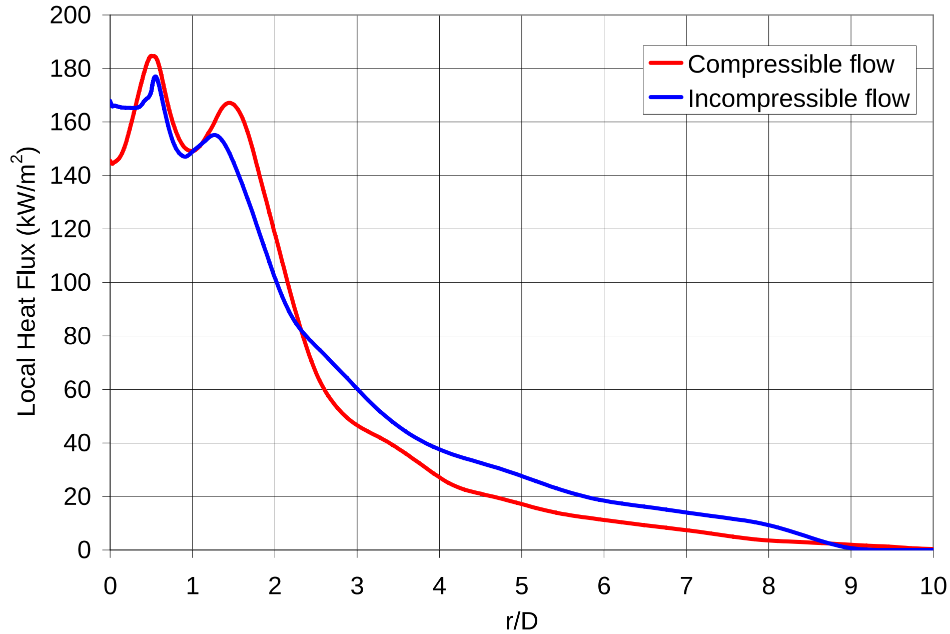

Figure 5.18: Time-averaged profiles of local heat fluxes of pulsating jets with different flow compressibility models for the validation case.

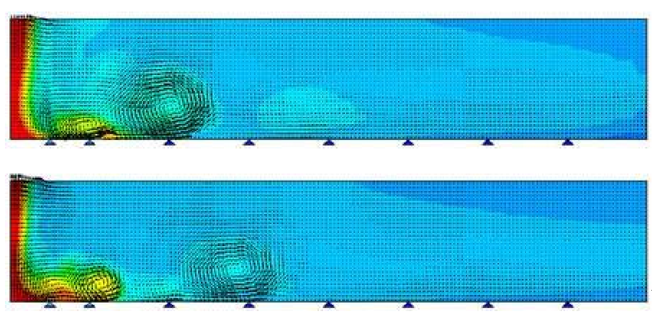

a) Compressible flow

b) Incompressible flow

Figure 5.19: Instantaneous velocity vectors and temperature contours at the beginning of negative cycle with different flow compressibility models for the validation case.

5.4 Summary

The numerical approach and procedure of the simulation worked quite well for the generation of a pulsating jet with a target velocity ratio. The main numerical approach was the relationship among inlet mass flow rate oscillation, volume ratio, and velocity ratio derived from the further simplification of mass and energy balances in the inlet chamber. The V2F turbulence model was chosen for the calculation of turbulent viscosity required in the RANS governing equations. Simulation results of impingement heat transfer were validated with heat flux measurement data from an experiment with the PAD pulse combustor. The predicted results were generally in agreement with experimental data. The key characteristic of the pulsating jet was that vortices did not grow and became large re-circulating flows. The maximum enhancement factor based on area-averaged heat fluxes coincided with the location where the vortices were still strong. The maximum enhancement factor varied from 1.4-3.0 depending on the temperature of the steady jet. Simulation results from parameter studies showed that the effects of jet velocity ratio, ambient temperature, time step size, and flow compressibility on time-averaged profiles of local heat flux were relatively small for the validation case.

CHAPTER 6

NUMERICAL EXPERIMENT

This chapter and the next two chapters present and discuss simulation results of the main numerical experiment of pulsating jet impingement heat transfer. The first section of this chapter describes the design of the numerical experiment and the selection of the variables for pulsating jet impingement heat transfer simulations. The second section presents the simulation results from the base case. The sensitivity studies of certain parameters are performed. The third section presents more detailed characteristics of pulsating jet flow and heat transfer. The following section discusses the effects of jet velocity ratio on impingement heat transfer. The final section identifies the mechanisms of heat transfer enhancement for the base case.

6.1 Design of Numerical Experiment

The operating condition of the pulsating jet and the impingement geometry from the validation case in the previous section could be used as a base case for this numerical experiment. However, since one parameter to be varied is surface velocity, the computational domain must be three-dimensional if a round nozzle is used with a moving impingement surface. Since significantly greater computational resources would be required for a three-dimensional domain, the simulations for the numerical experiment use a slot-type tailpipe, instead, so that even with a moving surface, the computational domain remains two-dimensional.

The numerical experiment was the simulation of a base case for pulsating jet impingement and the simulations of other cases in which one parameter was varied for each case. For the design of the base case of pulsating jet simulations, a reference steady jet had to be established first. The condition of reference steady jet impingement was designed in such a way that the magnitude of heat flux was at the same level as that from a typical impingement drying hood. First, a typical condition of steady jet impingement from an array of round nozzles (ARN) used in an impingement hood was applied with the Martin correlation for ARN to calculate the surface heat flux as a reference value. Then, the Martin correlation for single slot nozzle (SSN) was used to find the condition of a steady jet which yielded the same magnitude of heat flux as the reference value. This process resulted in jet velocity and temperature, nozzle width, nozzle-to-surface spacing, and surface area or length for evaluating area-averaged heat flux for the reference steady jet. For the pulsating jets of the base case of the simulations, two additional parameters were frequency and velocity ratio. After the condition of the base case was established, the numerical experiment was designed by varying only one parameter for each of the other cases. The parameters studied were frequency, mean jet velocity, nozzle width, and surface velocity.

The Martin correlation for ARN is

$$\overline{Nu} = \left[1 + \left(\frac{H/D}{0.6/\sqrt{g}}\right)^6\right]^{-0.05} \sqrt{g}\,\frac{1 - 2.2\sqrt{g}}{1 + 0.2(H/D - 6)\sqrt{g}}\,\mathrm{Re}^{2/3}\,\mathrm{Pr}^{0.42}$$

where g is relative opening area. The ranges of validity for this correlation are $2{,}000 \leq Re \leq 100{,}000$; $0.004 \leq g \leq 0.04$; and $2 \leq H/D \leq 12$. The optimum values of g and H/D, for maximum heat transfer per unit pumping power, are 0.0152 and 5.43, respectively. The optimization is based on a constant H.

The value of H for an impingement drying hood is usually determined by minimum spacing allowed within the restrictions of paper machine operation and maintenance, which is typically in the vicinity of 1″ or 25.4 mm. For the numerical experiment, H is set to be 30 mm. Hence, D = 5.5 mm for Martin's optimum geometry. Steady air jet velocity and temperature for this consideration are u_m = 100 m/s and T_j = 350°C (623 K), respectively. The Reynolds number of the steady jet is 9856, based on nozzle diameter and jet temperature at nozzle exit. But, for all Martin's correlations, gas properties are evaluated at the average value between jet and surface temperatures. The surface temperature, T_s, is set to be 373 K, approximately representing the evaporating temperature of water at the impingement surface during drying. Therefore, the temperature for the evaluation of gas properties is 498 K. Substituting in all required values, with Re = 14334 and Pr = 0.694, the results are Nu = 43.7, $h = Nu \cdot k/D$ = 320.7 W/K.m^2, and $q'' = h(T_j - T_s)$ = 80.2 kW/m^2.

The results from the correlation are validated with available industrial drying rate data of impingement paper drying hoods (Metso data in Johansson, 2005). Heat flux values are converted to drying rate by assuming that the drying process only requires the heat of water evaporation, 2257 kJ/kg. Figure 6.1 shows the comparison between results from the correlation and industrial data over a wide range of jet velocity and temperature. Results from the correlation are generally in agreement with the Metso data. Hence, Martin's correlations may be used as a reference for steady jet impingement heat transfer in this dissertation.

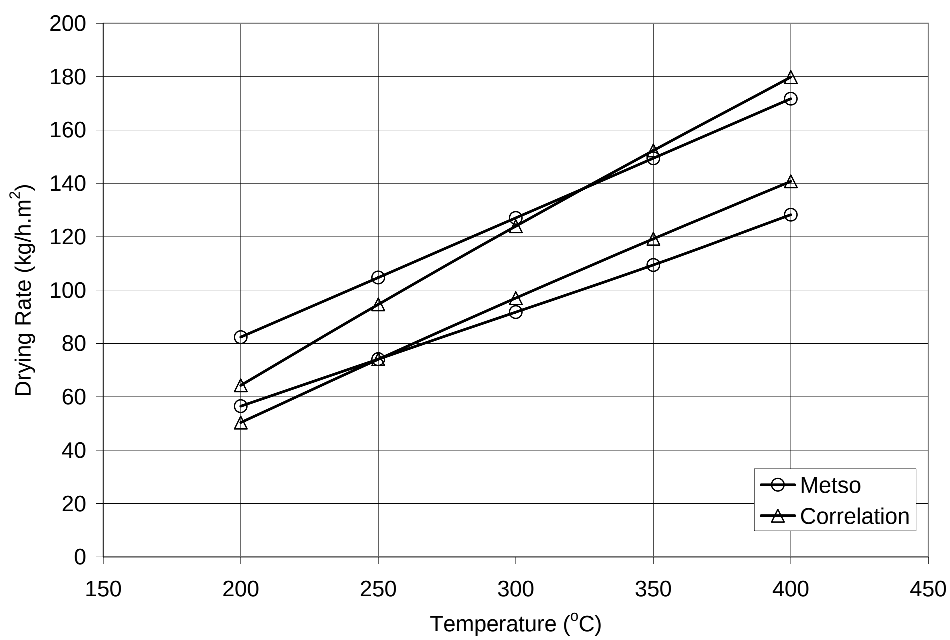

Figure 6.1: Comparison between drying rate data from Metso (Johansson, 2005) and equivalent drying rate from Martin correlation. Jet velocities are 90 & 130 m/s.

For comparison, the correlation for arrays of slot nozzles (ASN) is used to calculate jet velocity required to yield the same area-averaged heat flux from the typical condition of ARN.

$$\overline{Nu} = \frac{2}{3} g_0^{3/4} \left(\frac{2\,\mathrm{Re}}{g/g_0 + g_0/g} \right)^{2/3} \mathrm{Pr}^{0.42}$$

$$g_0 = \left[60 + 4\left(\frac{H}{S} - 2 \right)^2 \right]^{-1/2}$$

The ranges of validity for this correlation are $1{,}500 \le Re \le 40{,}000$; $0.008 \le g \le 2.5g_0$; and $1 \le H/S \le 40$. For the correlations of slot nozzle, S is the hydraulic diameter of a slot nozzle, where $S = 2B$ and B is the slot width. The optimum values of g and H/S for maximum heat transfer per pumping unit are 0.0718 and 5.037, respectively. For $H = 30$ mm, S would be 6.0 mm, and with $T_j = 623$ K and $q'' = 80.2$ kW/m^2, the jet velocity is 67.3 m/s. It is noteworthy that although the jet velocity of ASN is lower than that of ARN, the net mass flow rate, for the same coverage area, of ASN is about three times that of ARN.

From the optimization process in the Martin paper, an interesting aspect for this ASN correlation is that the optimum value of relative opening area, g_{opt}, for maximum heat transfer can be explicitly calculated for a given value of g_0, which is a function of H/S. That is $g_{opt} = g_0/\sqrt{2}$. This equation was used to calculate the reference distance for area-averaged heat fluxes for the simulation cases having single slot nozzles.

Variables for the numerical experiment

Variables for the experiment are nozzle width, mean jet velocity, jet velocity ratio, pulsation frequency, and surface velocity. In order to reduce the number of simulation cases, a set of variables is determined for a base case. Then only one variable, except jet velocity ratio, is changed for each simulation case. The jet velocity ratio is varied from zero (steady jet) up to about 5.0 for each simulation case.

The first parameter to be determined for the simulations is jet temperature. For impingement drying of paper, a typical range of jet temperature is 520-620 K (250-350°C). The upper limit of jet temperature depends on the properties of paper and drying fabric. However, higher jet temperatures (up to 450°C) have been used to increase energy efficiency without resulting in damage to the fabric or adversely impacting paper properties (Juppi and Kaihovirta, 2000). For a steady impingement hood, jet temperature can be easily controlled by mixing cooler air with hot combustion gas, in which the adiabatic flame temperature from the combustion process can be as high as 2300 K. In the case of a pulse combustor, such a mixing and cooling technique is not a common practice because it could adversely affect the desired flow characteristics of frequency, pressure amplitude, and velocity oscillation. Jet temperature is usually reduced by cooling the outside walls of the pulse combustor. But this method is not as effective as mixing cooler air. This is another issue for the development of a commercial-scale PAD system. For the time being, jet temperature for the simulations was set higher than that in a typical steady impingement system, i.e., 1000 K.

For impingement geometry, the nozzle-to-surface spacing is set to be the same as that in the correlation, i.e., H = 30 mm, which was kept constant for all the cases of numerical simulation. The nozzle width, B, was a variable for the numerical simulations. Following the Martin correlation for slot nozzles, the nozzle width in this dissertation was represented in terms of the hydraulic diameter of the nozzle, S (= 2B). The range of this variable in terms of nozzle-to-surface spacing ratio was H/S = 1, 2, 3, 4, and 5. The value for the base case was H/S = 3.

The next parameter to be determined is jet velocity for the base case. This parameter was calculated from the Martin correlation for single slot nozzles (SSN) so that area-averaged surface heat flux was at the same level as for a typical impingement drying hood, i.e., about 80 kW/m^2. The correlation for SSN is

$$\overline{Nu} = \frac{1.53}{y/S + H/S + 1.39} \mathrm{Re}^{\left[0.695 - \left(y/S + (H/S)^{1.33} + 3.06\right)^{-1}\right]} \mathrm{Pr}^{0.42}$$

The ranges of validity for this correlation are 3,000 $\leq Re \leq$ 90,000; 2 $\leq y/S \leq$ 25; and 2 $\leq H/S \leq$ 10, where y is lateral distance from the stagnation point or nozzle centerline. The surface area used to calculate area-averaged heat flux was the optimum value of the relative opening area for ASN with H/S = 3, resulting in y_{opt}/S = 2.8. The resulting jet velocity was 25 m/s. For convenience, jet velocity was rounded up to 30 m/s, which yielded an area-averaged surface heat flux of 90 kW/m^2. The Reynolds number, based on the hydraulic diameter and the mean value between jet and surface temperatures, was 4547, which is within the range of validity. Note that, with the same parameters, the heat flux from the correlation for ASN was slightly higher than that for SSN, i.e., 103 vs. 90 kW/m^2.

In summary, the parameters for the steady jet of the base case were S = 10 mm, H = 30 mm, u_j = 30 m/s, T_j = 1,000 K, and q'' = 90 kW/m^2 averaged over $0 \leq y \leq 2.8S$. For comparison, area-averaged heat fluxes calculated from Martin correlations for both ASN and SSN at different S (or H/S) are given in Table 6.1. In general, heat fluxes from multiple nozzles are slightly higher than those from a single nozzle with equivalent surface area.

Table 6.1: Heat fluxes comparison from Martin correlations for ASN and SSN

H/S	1	2	3	4	5
S (mm)	30	15	10	7.5	6
g_{opt}	0.088	0.091	0.088	0.081	0.072
y_{opt}/S	2.8	2.7	2.8	3.1	3.5
y_{opt} *(mm)*	85	41	28	23	21
Re	13,642	6,821	4,547	3,411	2,728
ASN q'' (kW/m^2)	71	92	103	106	105
SSN q'' (kW/m^2)	51	74	90	99	104

For pulsating jets, a key parameter is oscillation frequency (f). From the simplified model in Chapter 4, the system frequency of a pulse combustor depends on mean temperature in the tailpipe and pulse combustor dimensions. For an impingement drying hood which requires multiple nozzles, pulse combustion system characteristics, especially, resonance frequency might be more complicated than those from the system with a single tailpipe or nozzle. The oscillation frequency for the base case of the numerical experiment was somewhat arbitrarily chosen as 160 Hz, but was close to the frequency of an operating condition of the PAD pulse combustor. The other two cases for different frequencies were 320 and 80 Hz.

Jet velocity amplitude is presented as velocity ratio (ε) throughout this dissertation. Generally, the velocity ratio should be as high as possible for maximum heat transfer enhancement factor. However, from available data in the literature, typical values of high velocity ratios of operating pulse combustors were in the range of 4-5. Therefore, for the numerical experiment, the velocity ratio would be varied from 0-5 for the base case and other cases having the same mean jet velocity.

Mean jet velocity (u_j) is another key variable for the numerical experiment. If jet temperature and nozzle width are the same for different cases, the mean jet velocity represents the mean mass flow rate and energy rate of the impinging jet in each case. Since pulsating jet impingement heat transfer largely depends on jet velocity oscillation amplitude, an hypothesis or expectation is that if the maximum jet velocities for two different mean jet velocities are at the same level, the magnitude of heat flux could also be at the same level. In other words, a pulsating jet could yield both heat transfer enhancement and energy saving compared to a steady jet having a higher mean jet velocity.

The last variable for the design of the numerical experiment is the speed of the impingement surface (u_s) as, in industrial drying applications, wet materials would be moving along the manufacturing process. For modern paper machines, the machine speed is in the vicinity of 2000 m/min (6560 ft/min) or about 33 m/s. From the literature review, a moving surface generally results in a decrease in surface heat transfer compared to a stationary surface. For the numerical experiment, three levels of surface velocity (15, 30, and 45 m/s) were simulated with the conditions of the pulsating jet of the base case.

Table 6.2 summarizes the values of variables for the numerical experiment. Case 1 is the base case in which the values of parameters were determined from the above discussion. For other simulation cases, the parameters were varied one at a time (boldface in Table 6.2) with respect to those of the base case.

Table 6.2: Variables for the numerical experiment

Case	H (mm)	H/S	S (mm)	f (Hz)	ε	u_j (m/s)	u_s (m/s)
1	30	3	10	160	5	30	0
2	30	3	10	**80**	5	30	0
3	30	3	10	**320**	5	30	0
4	30	3	10	160	**11**	**15**	0
5	30	3	10	160	**3**	**45**	0
6	30	**1**	**30**	160	5	30	0
7	30	**2**	**15**	160	5	30	0
8	30	**4**	**7.5**	160	5	30	0
9	30	**5**	**6**	160	5	30	0
10	30	3	10	160	5	30	**15**
11	30	3	10	160	5	30	**30**
12	30	3	10	160	5	30	**45**

6.2 Simulation of the Base Case

The numerical procedure for the simulation was the same as that for the validation case in the previous chapter. This included the governing equations, the V2F turbulence model, ideal-gas density function, temperature-dependent fluid properties, second-order discretization schemes, and convergence criteria. The difference was that two-dimensional Cartesian coordinates were used instead of cylindrical coordinates.

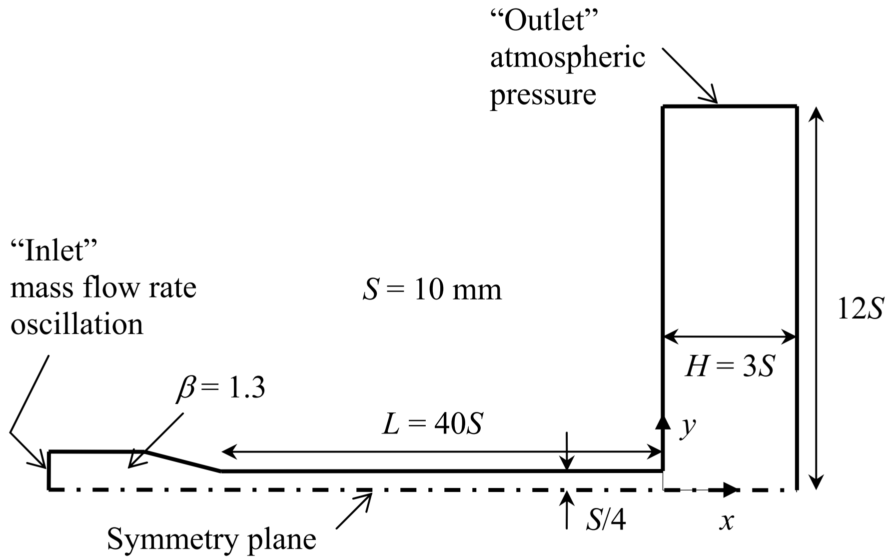

Figure 6.2: Computational domain for the base case

Figure 6.2 shows the computational domain for the base case. For convenience, the depth of the computational domain in the z-axis was set to 1 m so that the units of mass flow rates and heat fluxes were expressed with unit area, instead of unit length. The inflow temperature at the inlet boundary was 1000 K whereas the backflow temperature at the outlet boundary was 700 K. The temperature of the impingement surface was 373 K. The oscillation of inlet mass flow rate was

$$\dot{m}_1 = \dot{m}_m\left(1 + \varepsilon_1 \sin(\omega t)\right)$$

The mean mass flow rate, $\dot{m}_m$ = 26.48 g/s, was calculated from the target mean velocity, 30 m/s, the density corresponding to a jet temperature of 1000 K, 0.353 kg/m^3, and the cross-sectional area of the tailpipe, 0.0025 m^2. The frequency was 160 Hz. The dimensions of the computational domain were designed so that the velocity ratio at the tailpipe exit was approximately 5 with ε_1 = 1.0. However, the resulting velocity ratio from the simulation was 4.4. As discussed in the previous chapter, the difference in target and resulting velocity ratios was probably because the forced frequency of the pulsating flow was not the resonance frequency of the system. The calculation could be corrected by using the mean speed of sound from the acoustic relationship instead of from the mean temperature in the tailpipe. Nevertheless, the velocity ratio of 4.4 can be regarded as a high value for a pulsating jet generated by a pulse combustor under practical operating conditions. Therefore, this value was used for the base case and will be the reference velocity ratio for other cases as well.

Sensitivity Study of Numerical Parameters

Since there are virtually no available validation data from conditions similar to this numerical experiment, the validation of the simulation results was based on indirect comparison, i.e., the validation case in the previous chapter for axisymmetric pulsating jet impingement and the Martin correlation for steady jet impingement. A sensitivity study of several numerical parameters was also performed. It is assumed that if the simulation results and the parameter study appear consistent, it can be expected that the simulation results would be in agreement with experimental results (when available) as the numerical procedure is the same as that for the validation case in the previous chapter.

Figure 6.3 shows the comparison between the simulation results and the Martin correlation of single slot nozzle at two jet velocities. The plots are area-averaged heat fluxes from the stagnation point up to corresponding positions. The simulation results were consistent with the correlation results. The reference area or distance for this case was $y/S = 2.8$ as an optimum distance for multiple-jet nozzles with $H/S = 3$ in Table 6.1. Although the simulations were for a single nozzle, this distance will be used for the preliminary evaluation of simulation results among different cases or conditions. With $u_m = 30$ m/s, the area-averaged heat fluxes at $y/S = 2.8$ were 93 and 90 kW/m^2 from the simulation and the correlation, respectively. And with $u_m = 180$ m/s, the heat fluxes at such distance were 267 and 262 kW/m^2 from the simulation and the correlation, respectively.

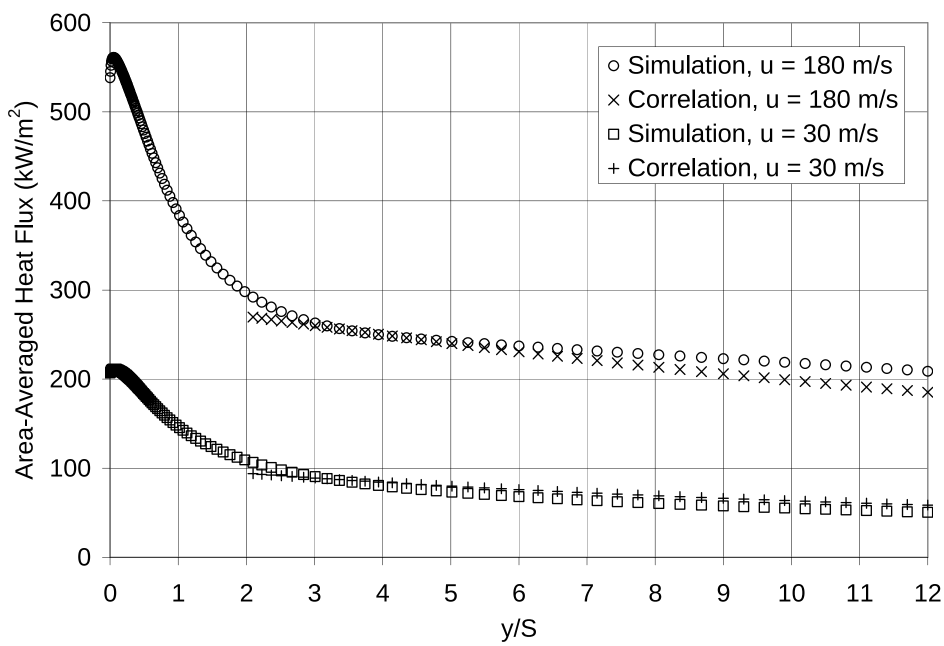

Figure 6.3: Profiles of area-averaged heat fluxes from steady jet simulations in comparison with Martin correlation for SSN for the base case.

The steady jet with u_j = 180 m/s was also used for a grid independence study as the maximum velocity of the pulsating jet would not be greater than this velocity. The number of grid cells in the *x* and *y* directions for the base grid was 125x139 cells in the impingement zone, 154x42 cells in the tailpipe zone, and 175x102 cells in the inlet chamber zone. For the grid independence study, the number of grid cells was doubled in both directions of the computational domain of the base case. Figure 6.4 shows the profiles of local heat flux from both sets of grids, which are essentially the same.

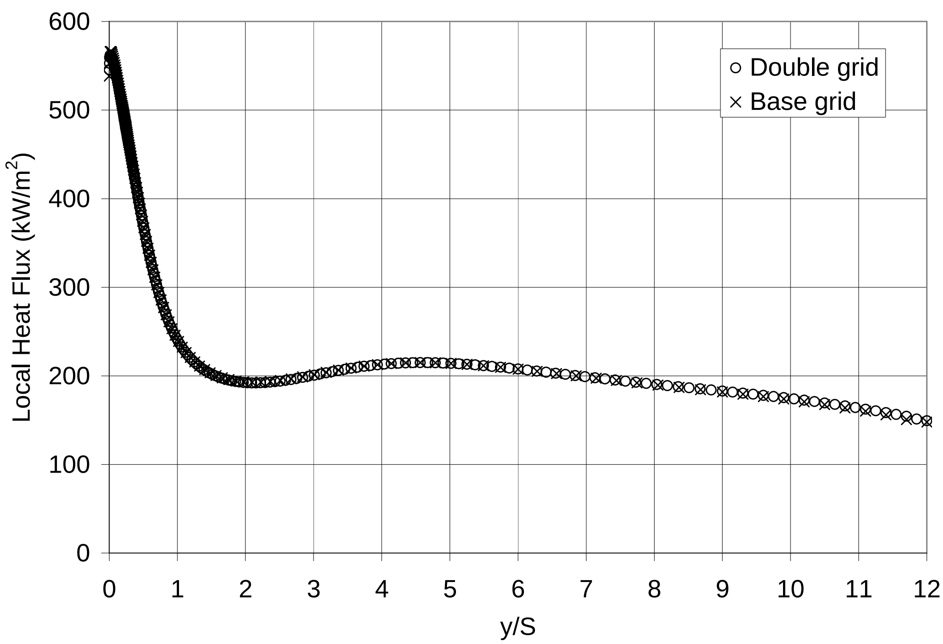

Figure 6.4: Local heat flux profiles from grid independence study with a steady jet and u_j = 180 m/s for the base case.

The next parameter study evaluates the effects of backflow temperature at the outlet boundary. Figure 6.5 shows the time-averaged profiles of local heat flux with three different levels of backflow temperature. The profiles are essentially the same up to about *y/S* = 7. Heat flux levels near the outlet boundary increase with increasing backflow temperature. These results indicate that pulsating flows are well contained in the impingement zone near the tailpipe exit due to re-circulating flows as shown in the following sections. For the base case, the temperature of the re-circulating flows was about 700 K, which was the result of heat loss from the impinging jet to the surface. This temperature would change corresponding to surface heat transfer from case to case. However, as the length of the impingement zone of computational domains was larger than the area occupied by the re-circulating flows, the overall energy balance in the impingement zone near the tailpipe exit and the stagnation point was not affected by different backflow temperatures. Therefore, the backflow temperature used for all simulation cases was the same as the base case, i.e., 700 K.

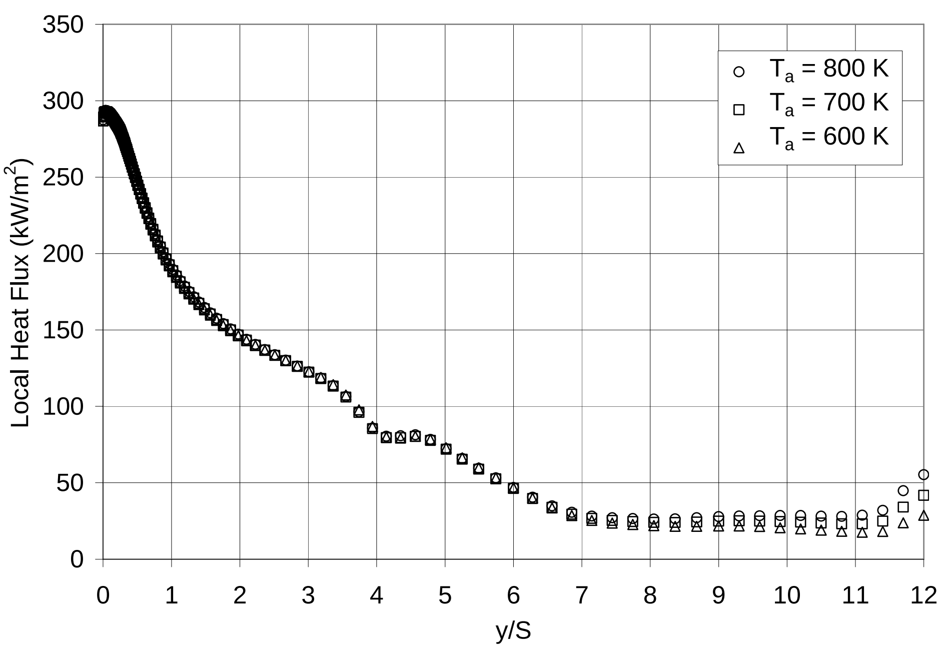

Figure 6.5: Effects of backflow temperature at outlet boundary for the base case – time-averaged profiles of local heat fluxes.

The effect of the size of time step was studied next. In the previous chapter, for the validation case, the simulation results were slightly different between two sizes of time steps in terms of oscillation stability due to the variation of vortex structures in the inlet chamber. However, for the base case, the size of time step had little effect on simulation results as shown in Figure 6.6. Hence, for all simulation cases, the number of time step per one oscillation cycle is set to be 500 time steps.

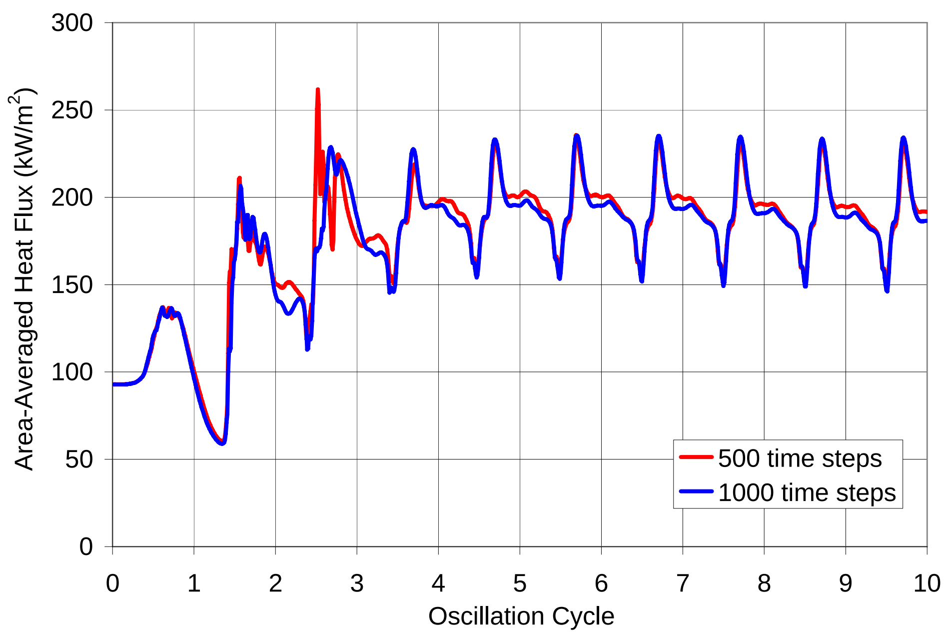

Figure 6.6: Effects of the size of time step for the base case – area-averaged heat fluxes over $y \leq 2.8S$.

As for the fluid compressibility, the compressible flow model results in more stable oscillation of surface heat transfer as shown in Figure 6.7. In addition, the variation or the amplitude of the oscillation from the incompressible flow model was larger than that from the compressible flow model. The time-averaged profiles of local heat fluxes were also different especially for locations away from the stagnation point as shown in Figure 6.8. This is due to the characteristics of vortices and re-circulating flows in the impingement zone as discussed in the following sections. The impinging jet with the incompressible flow model behaved rather like a quasi-steady flow, i.e., yielding higher heat fluxes during the positive cycle while yielding lower heat fluxes during the negative cycle than the impinging jet from the compressible flow, in which the effects of pressure on density and, thus, velocity, appeared to reduce the amplitude of heat flux oscillation. Although the incompressible flow model is commonly acceptable for simulating steady flows in this range of jet velocity, the compressible flow model is more physically reasonable for unsteady flows with large pressure variations. Therefore, the compressible flow model was used for all simulation cases.

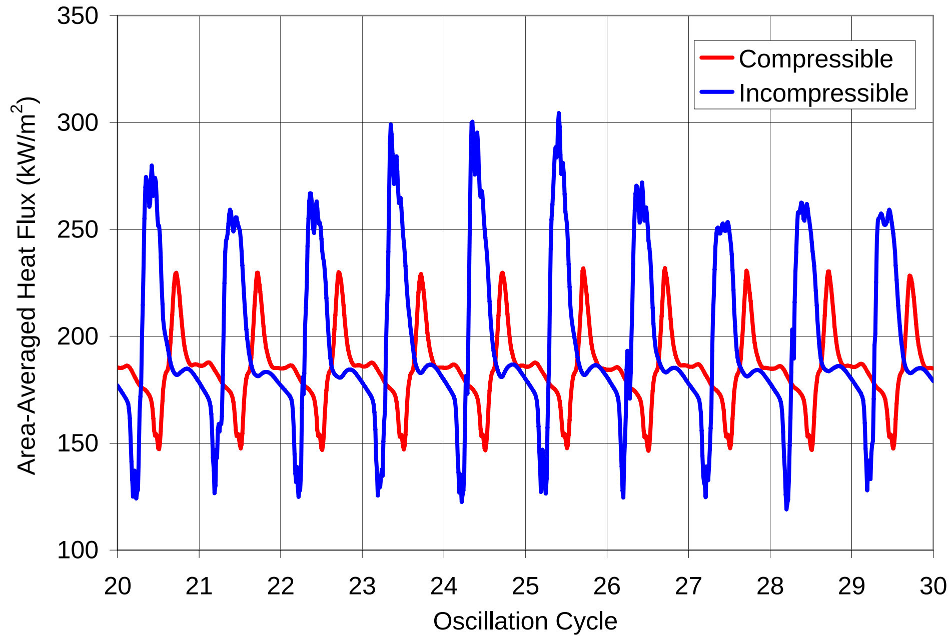

Figure 6.7: Effects of flow compressibility model for the base case – area-averaged heat fluxes over $y \leq 2.8S$.

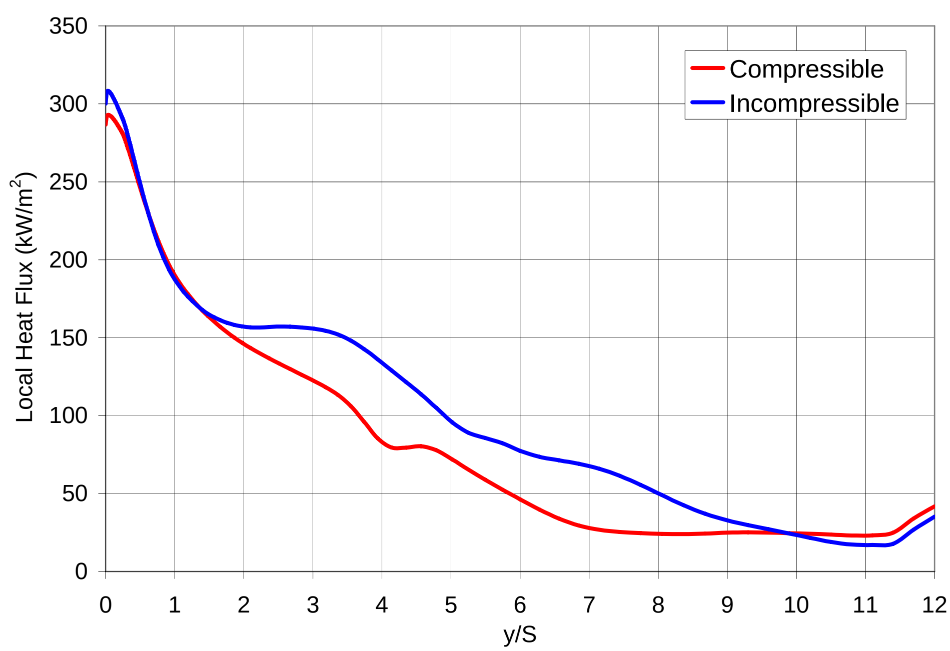

Figure 6.8: Effects of flow compressibility model for the base case – time-averaged profiles of local heat fluxes.

6.3 Flow and Heat Transfer Characteristics

This section presents and discusses the simulation results for the base case, focusing on the characteristics of pulsating flows at the tailpipe exit and in the impingement zone as well as the heat transfer characteristics at the impingement surface. Figure 6.9 shows the oscillations of area-averaged x-velocity, bulk temperature, and turbulence intensity at the tailpipe exit. In general, the characteristics of flow oscillations were similar to those in the validation case with a round tailpipe. The velocity ratio was about 4.4 with a mean velocity of about 30 m/s. The temperature varied from approximately 700 K to 1000 K. The minimum temperature was due to fluid in the impingement zone around the tailpipe entering the tailpipe during flow reversal, whereas the maximum temperature was due to fresh fluid from the inlet chamber. The turbulence intensity varied from about 15% to 55%. The values of the turbulence intensity were relative to the mean velocity, 30 m/s, not instantaneous velocity. The key characteristic was that the turbulence intensity was relatively low during the positive cycle or during the period when fresh fluid is exiting the tailpipe and higher during the flow reversal period as a result of impinging and re-circulating flows in the impingement zone.

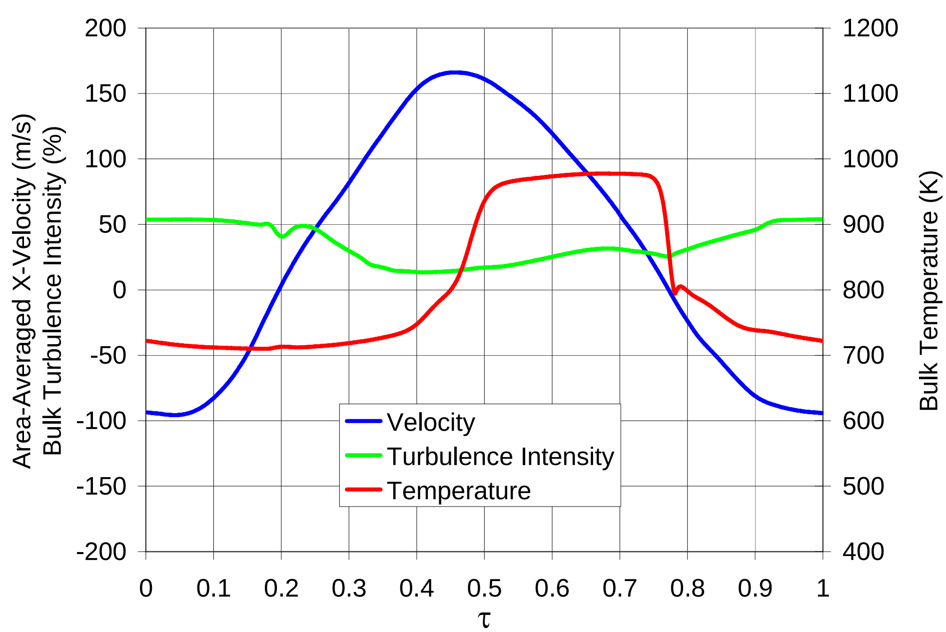

Figure 6.9: Flow oscillations at tailpipe exit for the base case.

The instantaneous profiles during one oscillation cycle for velocity, temperature, and turbulence intensity are shown in Figures 6.10-6.12, respectively. As with Figures 5.9-5.11 for the validation case in the previous chapter, the positive cycle is labeled in red while the negative cycle is in blue. The characteristics of velocity and temperature profiles were slightly different from those of the validation case with a round tailpipe. The main reason was possibly due to the Reynolds number. For this case, the Reynolds number based on mean velocity, jet temperature, and nozzle hydraulic diameter was 2460, compared to 4150 on the same basis for the validation case. The velocity profiles at high positive velocities in this case were close to the parabolic pattern of laminar channel flows. Fluid near the wall moved more slowly than bulk flow almost all the time except when the bulk flow was about to change direction. That was the reason why the temperature profile at $\tau = 0.5$ had lower values near the wall. Similar patterns of these profiles were also observed for the cases with a smaller nozzle width, in which the mean Reynolds numbers were lower and the patterns of the velocity profiles were even more similar to those of laminar flows. For the cases with a larger nozzle width, the patterns of these profiles were more similar to those of the validation case. That is, velocity profiles were flatter and temperatures near the wall changed faster with respect to the bulk flow temperature.

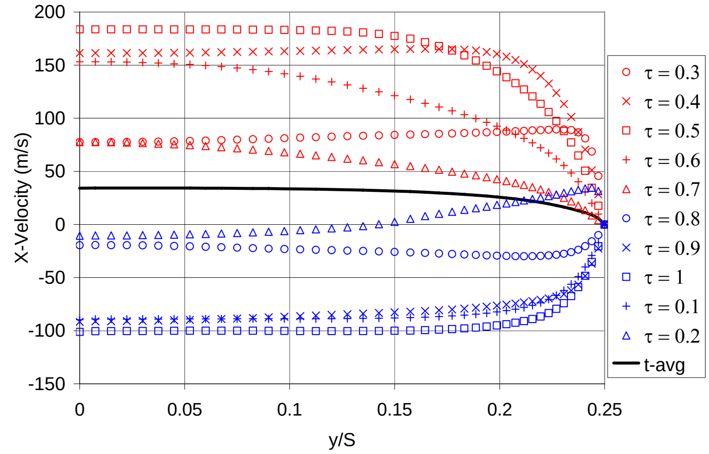

Figure 6.10: Instantaneous profiles of x-velocity at tailpipe exit for the base case.

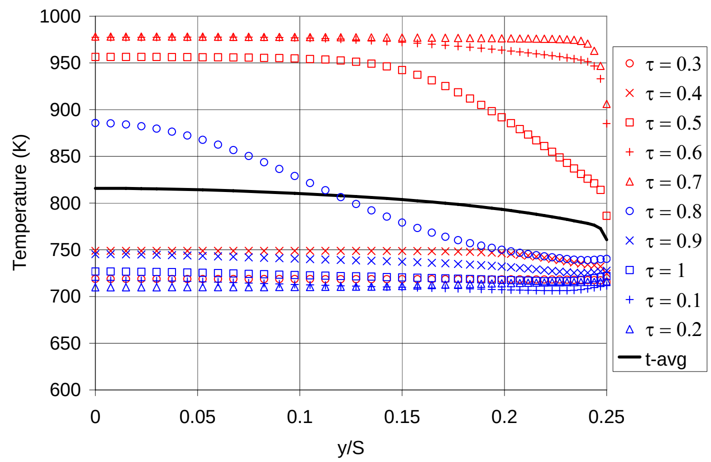

Figure 6.11: Instantaneous profiles of temperature at tailpipe exit for the base case.

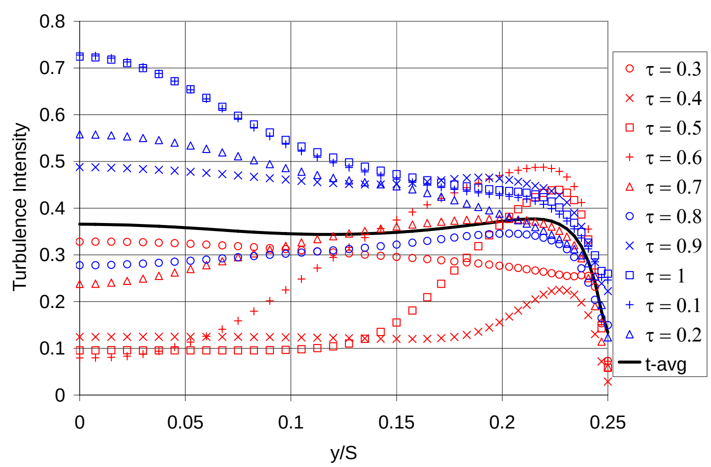

Figure 6.12: Instantaneous profiles of turbulence intensity at tailpipe exit for the base case.

Figures 6.13 and 6.14 show instantaneous velocity vectors and temperature contours in the impingement zone, as well as corresponding surface heat fluxes during the positive and the negative cycles of jet velocity oscillation, respectively. Note the normalized cycle time was based on the inlet mass flow rate oscillation. For this case, the positive cycle at the tailpipe exit began at $\tau = 0.3$. The triangle markers in the plots of velocity vectors and temperature contours indicated the locations of $y = S/4$, S, $2S$, $3S$, and so on. The key characteristics of the impinging flows were propagating vortices and re-circulating flows. The vortices began to form as soon as the jet exited the tailpipe and continued to propagate downstream along with the impinging jet. Compared to the vortices in the validation case, in which the wall jet velocity decreased rapidly with increasing distance away from the stagnation point due to the nature of axisymmetric flows, the vortices in this case were stronger and larger because of the slot type of the tailpipe (plane flow). The vortices forced the wall jet to curl up toward the confinement wall instead of flowing along the impingement surface as in steady jet impingement flows. At the end of the positive cycle, the vortices became re-circulating flows within the impingement zone and caused smaller secondary vortices as flow impinged on the confinement wall. During the negative cycle or tailpipe flow reversal period, the re-circulating flows continued providing heat transfer to the surface while some of the fluid entered the tailpipe. This is the main reason for high heat transfer enhancement from the pulsating jets for this numerical experiment. These vortices and re-circulating flows blocked backflow fluid at the outlet boundary from reaching the impingement zone around the tailpipe exit. This behavior was the reason why different backflow temperatures had little effect on surface heat transfer.

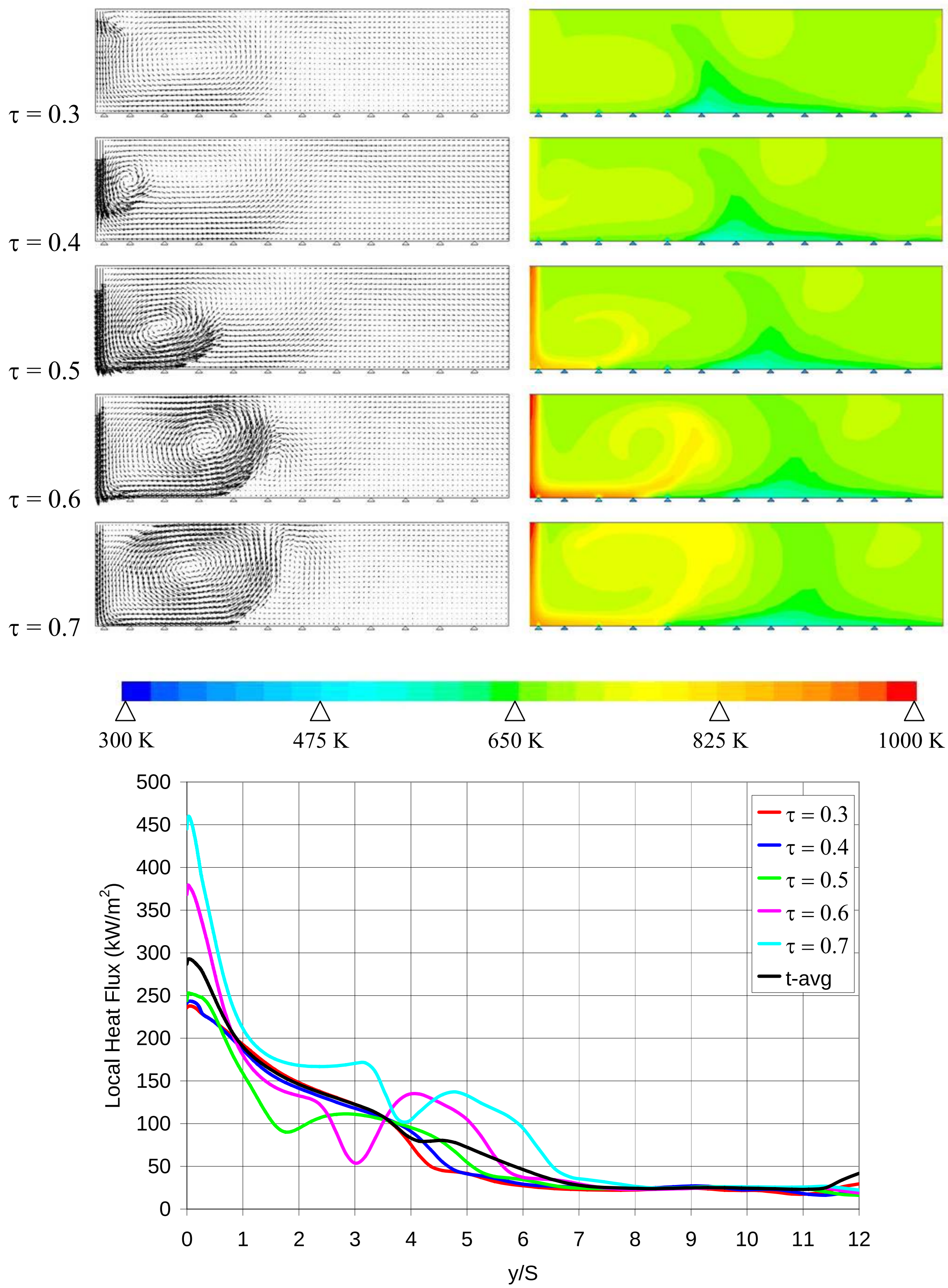

Figure 6.13: Velocity vectors/temperature contours and corresponding local heat flux profiles during positive cycle of jet oscillation for the base case.

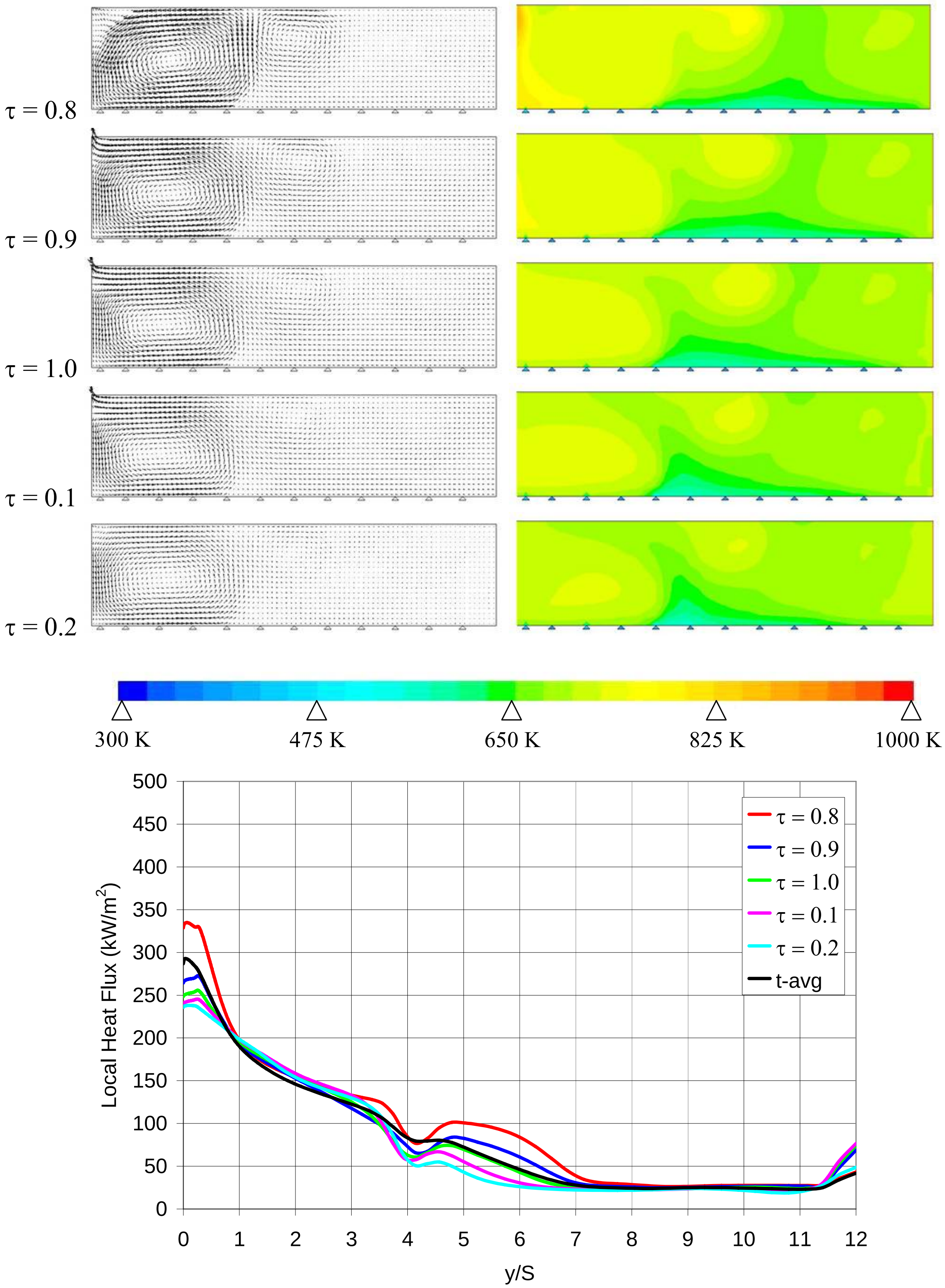

Figure 6.14: Velocity vectors/temperature contours and corresponding local heat flux profiles during negative cycle of jet oscillation for the base case.

Maximum heat transfer at the stagnation point occurred at the end of the positive cycle when the impinging jet with high velocity and temperature reached the surface. During the negative cycle, surface heat flux at the stagnation point continued to decrease whereas heat transfer on the surface away from the stagnation point was relatively constant due to the effects of re-circulating flows. Heat flux on the surface near the outlet boundary increased during the negative cycle because of backflow fluid entering the domain.

6.4 Effects of Jet Velocity Ratio

Results from preliminary work, with an incompressible flow model, showed that surface heat transfer increased with increasing velocity ratio. This was also the case for the base case as shown in Figure 6.15. The velocity ratio was varied by varying the amplitude ratio of inlet mass flow rate oscillation from 0.1, 0.2, 0.4, 0.6, 0.8, to 1.0, resulting in $\varepsilon = 0.5$, 0.9, 1.8, 2.9, 3.9, and 4.4, respectively. For the pulsating jets without flow reversal or $\varepsilon < 1.0$, stagnation point heat fluxes were lower than that of the steady jet and lowest at $\varepsilon = 0.9$. This is consistent with the theory of nonlinear dynamic behavior in boundary layers by Mladin and Zumbrunnen (1995). For the cases with flow reversal, the stagnation point heat flux was only slightly higher than the steady heat flux at $\varepsilon = 1.8$, and then significantly increased at $\varepsilon = 2.9$ or higher. These results correspond to the strength of re-circulating flows as shown in Figure 6.16. The re-circulating flow at $\varepsilon = 2.9$ became much stronger than that at $\varepsilon = 1.8$. As the velocity ratio increased, the strength or velocities of the re-circulating flows also increased.

The profiles of local heat fluxes in Figure 6.15 have a common pattern of a sharp drop at some distance from the stagnation point. Comparing the plots in Figures 6.15 and 6.16, the location of such drop coincides with the size of the re-circulating flow or the location where the wall jet curls up toward the confinement wall for each respective case. After the drop, heat fluxes slightly increased due to the effects of the smaller secondary vortices, as shown in Figures 6.13 and 6.14. Beyond the region of impact of the secondary vortices, heat flux levels were very low for all the cases of pulsating jets. At the area near the outlet boundary, heat flux levels increased because of the effects of the backflow entering the domain during the negative cycle (Figure 6.14).

The temperature contours in Figure 6.16 have the same color scale with those in Figures 6.14 and 6.15. The correlation between the strength or velocities and the temperatures of re-circulating flows was that the temperature decreased as the re-circulating flow became stronger as a result of increasing heat transfer to the surface. Some of the fluids from the re-circulating flows entered the tailpipe during the negative cycle. Hence, the minimum value of temperature oscillation at the tailpipe exit was determined by the temperature of the re-circulating flow, which decreased with increasing velocity ratio.

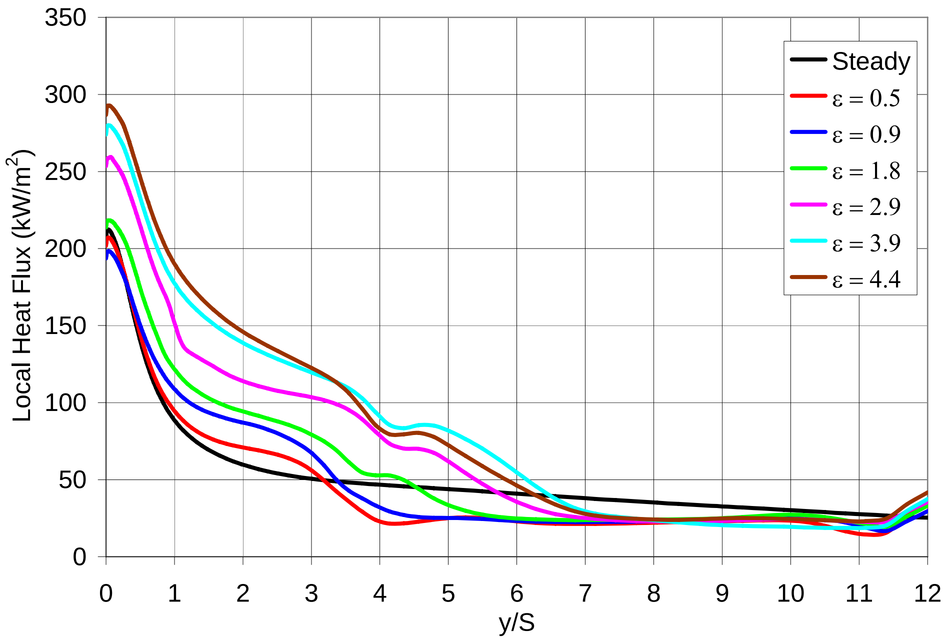

Figure 6.15: Time-averaged profiles of local heat fluxes from different velocity ratios for the base case.

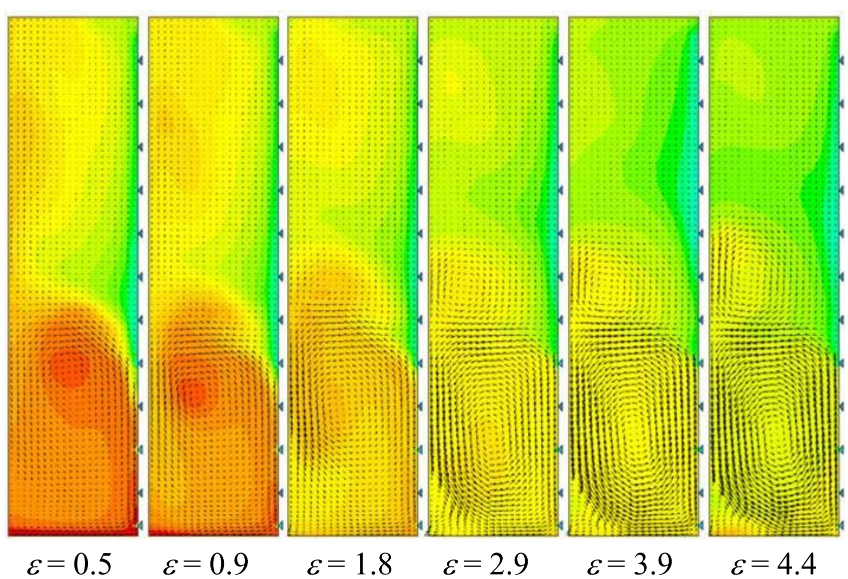

Figure 6.16: Instantaneous velocity vectors and temperature contours at the beginning of negative cycle from different velocity ratios for the base case.

In order to evaluate the heat transfer enhancement factor from the pulsating jets with respect to the steady jet, area-averaged heat fluxes were calculated from the profiles of local heat fluxes and are shown in Figure 6.17. The corresponding enhancement factor profiles are shown in Figure 6.18. The locations of the maximum values of enhancement factors coincide with the drops in local heat flux profiles or the size of the re-circulating flows for each respective case. The maximum enhancement factors were 1.1, 1.2, 1.4, 1.7, 1.9, and 2.0 at y/S = 3.0, 3.2, 3.4, 4.0, 4.0, and 3.7 for ε = 0.5, 0.9, 1.8, 2.9, 3.9, and 4.4, respectively. However, these values are based on the comparison with steady heat flux averaged over the same area for each case. In practice, multiple nozzles with optimum geometry are used for impingement drying applications. Those locations may not be at the optimum distance that yields maximum heat transfer for the steady jet. Furthermore, the optimum geometry for steady and pulsating jets is possibly not the same due to the different characteristics of the impingement flows. Simulations with multiple nozzles would have to be performed to evaluate more practical heat transfer enhancement. As for the present work, the simulation results from a single nozzle could be used as a preliminary indication by comparing area-averaged heat fluxes at a reference distance, y/S = 2.8, which is an optimum distance for H/S = 3 as discussed earlier. As it turned out, the enhancement factors at such distance were not much different from the maximum enhancement factors, i.e., 1.1, 1.2, 1.3, 1.6, 1.9, and 2.0 for ε = 0.5, 0.9, 1.8, 2.9, 3.9, and 4.4, respectively. The factor of 2.0 can be considered an encouraging result for the potential of pulsating jet impingement because the comparison was based on the same mean energy rates of pulsating and steady jets, therefore with no bias for the pulsating jet. Furthermore, the comparison was based on area-averaged heat fluxes and, thus, was more practical than that based on local heat fluxes, in which the enhancement factor could be much lower or higher at some location but with no practical value.

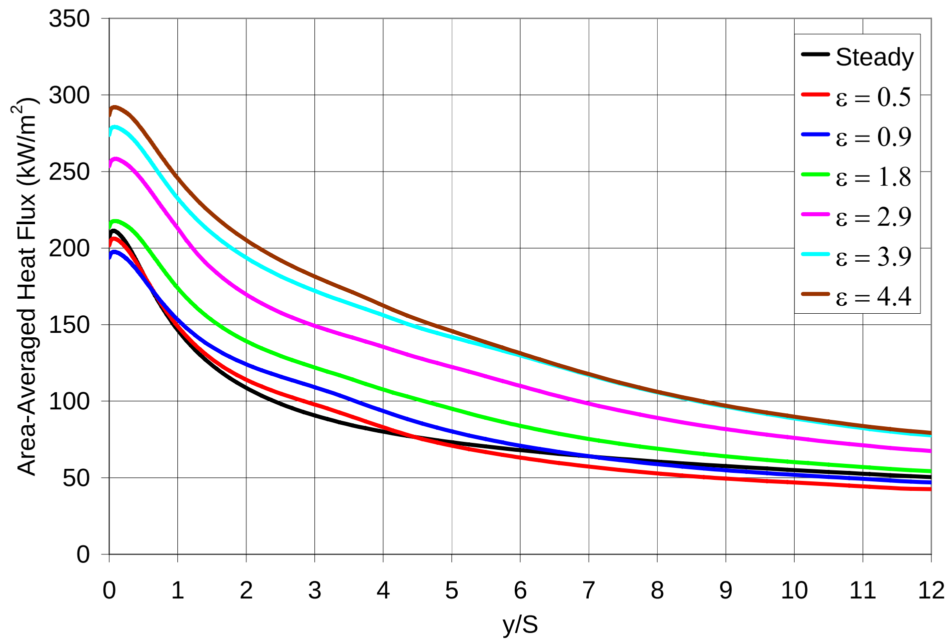

Figure 6.17: Time-averaged profiles of area-averaged heat fluxes from different velocity ratios for the base case.

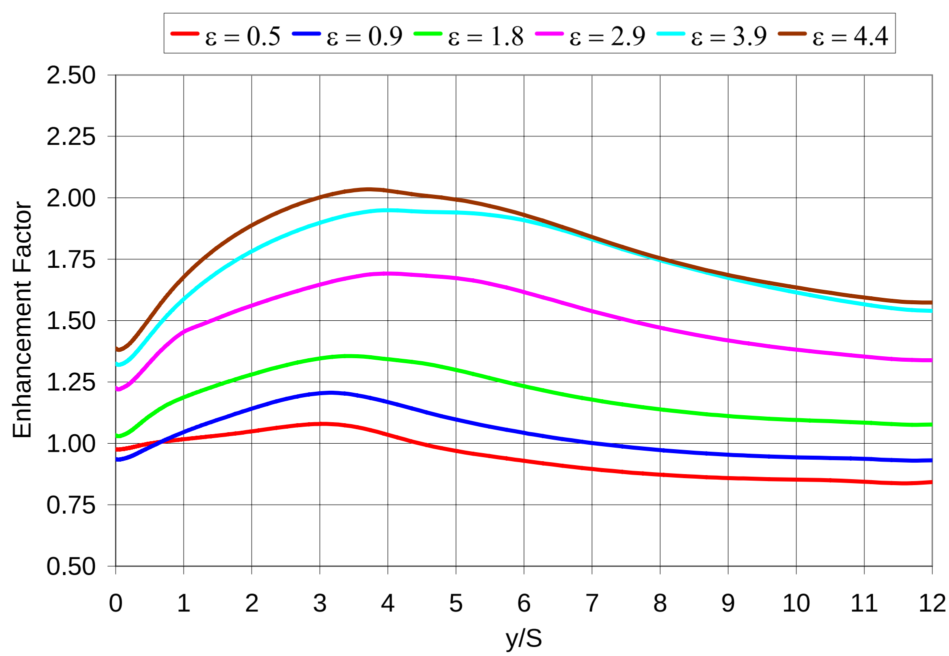

Figure 6.18: Profiles of heat transfer enhancement factors from different velocity ratios for the base case.

6.5 Mechanisms for Heat Transfer Enhancement

As shown in Section 6.3, the flow characteristic responsible for high heat transfer enhancement was strong re-circulating flow during the negative cycle continuing to provide heat transfer to the surface. Such a characteristic was not reportedly existent in other types or conditions of pulsating jets in the literature, in which vortices in most cases were generated from a round tailpipe and only propagated along the impingement surface farther away from the stagnation point (Eibeck et al., 1993; and Li, 2005). The vortices from the validation case in the previous chapter also had a similar behavior as those in the literature. Since the effects of strong re-circulating flows near the stagnation point are significant for heat transfer enhancement, the experimental validation of this characteristic is necessary for future work.

The condition of the pulsating jet for the validation case was comparable with that for the base case in terms of nozzle-to-surface spacing, frequency, mean velocity, and velocity ratio, i.e., H = 38.1 mm, f = 154 Hz, u_m = 26.6 m/s, and ε = 3.9 for the validation case whereas H = 30 mm, f = 160 Hz, u_m = 30 m/s, and ε = 4.4 for the base case in this chapter. The difference in jet temperatures was slightly larger, i.e., 1200 and 1000 K for the validation case and the base case, respectively. The main differences between the two cases were nozzle type (round vs. slot) and hydraulic diameter (25.4 vs. 10 mm). The resulting maximum enhancement factors were 1.4 and 2.0 for the validation case and the base case, respectively. Although the comparison between the two cases is not really straightforward, it could be observed that the key difference was in the characteristics of vortices and re-circulating flows. That is the vortices in the validation case could not grow and become a large, strong re-circulating flow as did those in the base case.

Such a difference is mainly due to the effects of nozzle type, not hydraulic diameter because, as shown in the next chapter, the pulsating jet with larger nozzle width also has similar characteristics of the re-circulating flow as the base case. As an axisymmetric flow, the velocity of the wall jet from the round nozzle decelerated very fast along the radial distance from the stagnation point, compared to that from the slot nozzle. This comparison shows that not only jet velocity ratio but also the magnitude of wall jet velocity plays an important role for generating strong re-circulating flows, thus, high heat transfer enhancement. It would be expected that if the pulsating jet in the validation case had the same velocity ratio but a higher mean velocity, or vice versa, such that re-circulating flow occurs in the impingement zone, the corresponding enhancement factor would be much higher.

In order to evaluate the contribution of the re-circulating flows, the velocity profiles in the impingement zone from the pulsating jets with $\varepsilon = 4.4$ and 0.5 were compared along with the steady jet velocity profile, as shown in Figure 6.19. The velocity ratio of 0.5 indicates that there was no flow reversal in the tailpipe. In other words, the pulsating jet continuously impinged onto the surface over the oscillation cycle with maximum temperature. On the other hand, the velocity ratio of 4.4 indicates that there was no jet exiting the tailpipe during the negative cycle. Furthermore, the temperature of jet impinging onto the surface was at the maximum level only during the half period of the positive cycle. Figure 6.19 shows the instantaneous profiles of the y- velocity in the impingement zone at $y/S = 1.5$ from the steady jet and the pulsating jets with $\varepsilon = 0.5$ and 4.4. The profiles from the pulsating jet with $\varepsilon = 0.5$ near the impingement surface ($x = 30$ mm) oscillated around the profile from the steady jet. Those profiles are indicative of wall shear stresses and boundary layers at the impingement surface. Hence, the time-averaged wall shear stress and boundary layer for the pulsating jet with $\varepsilon = 0.5$ was not much different than that from the steady jet, resulting in similar time-averaged heat fluxes at this location (Figure 6.15). As for the pulsating jet with $\varepsilon = 4.4$, the velocity profiles are very different, displaying the characteristics of re-circulating flow in the impingement zone. The profiles with high velocity magnitude near the impingement surface correspond to the impinging jet during the positive cycle, during which instantaneous jet velocities were higher than those from the steady jet and the pulsating jet with $\varepsilon = 0.5$. However, during the negative cycle, when there was no exiting jet from the tailpipe, the magnitude of the velocity profiles near the impingement surface from the pulsating jet with $\varepsilon = 4.4$ was still higher than that from the steady jet and than the maximum magnitude of the velocity profiles from the pulsating jet with $\varepsilon = 0.5$. This is apparently because the re-circulating flows were so strong that its circulating velocity is even higher than the steady jet velocity throughout the cycle. The strength of re-circulating flows was apparently sustained by the fluid drawn back into the tailpipe creating shear velocity near the confinement wall. The re-circulating flows became weaker at the end of the negative cycle. A new vortex was generated at the beginning of the next positive cycle, which then grew larger and stronger and finally became a strong re-circulating flow in the next negative cycle.

Corresponding instantaneous profiles of local heat fluxes for these three cases are shown in Figure 6.20. As with the velocity profiles near the impingement surface, even the minimum heat flux for the pulsating jet with $\varepsilon = 4.4$ was higher than the heat flux from the steady jet or the maximum heat flux from the pulsating jet with $\varepsilon = 0.5$. Therefore, it may be deduced that the two mechanisms responsible for heat transfer enhancement, considering jet velocity and temperature oscillation at the tailpipe exit for the two pulsating jets, are the high velocity of the exiting jet during the positive cycle and the strong re-circulating flow during the negative cycle. For the condition of the base case considered here, the jet velocity ratio should be at least 3.0 in order to create strong re-circulating flows and have a relatively high heat transfer enhancement factor compared to the corresponding steady jet.

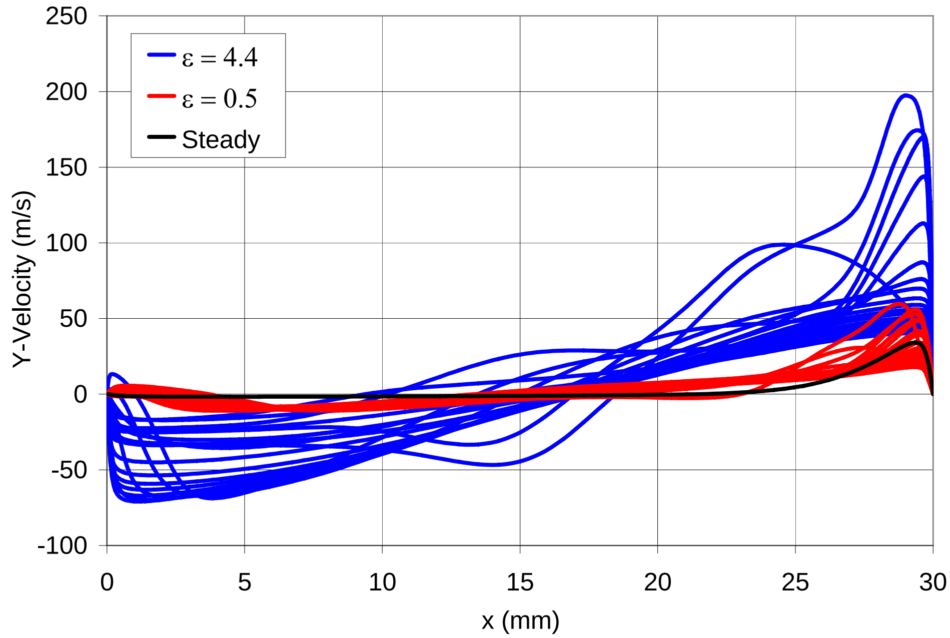

Figure 6.19: Instantaneous profiles of y-velocity at *y/S* = 1.5 for the base case.

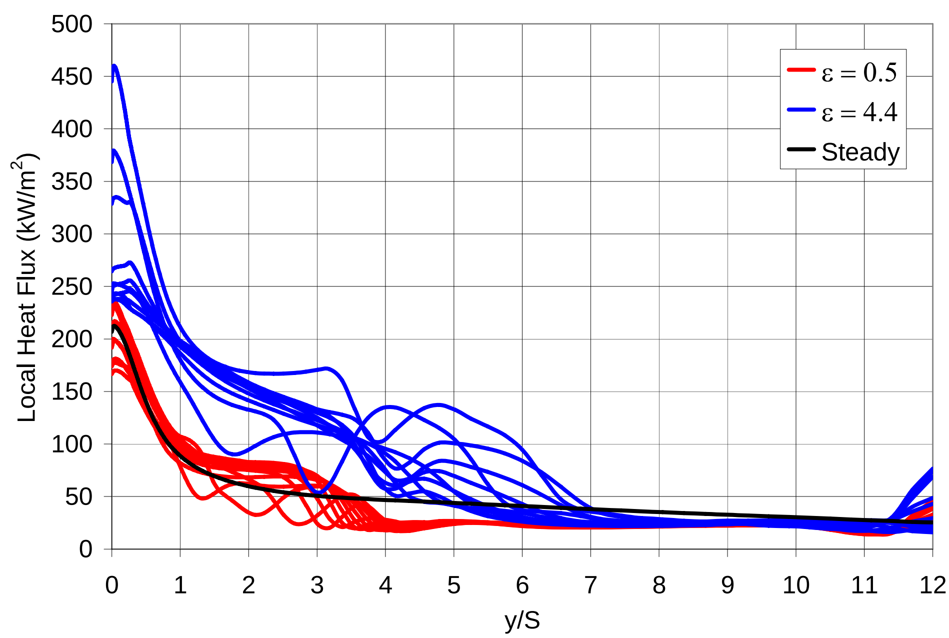

Figure 6.20: Instantaneous profiles of local heat fluxes corresponding to Figure 6.19.

6.6 Summary

The design of the numerical experiment or simulations was based on typical values of nozzle-to-surface spacing and heat flux level in industrial impingement hoods for paper drying. As discussed in Section 1.2, the simulations were limited to single nozzles in order to gain more understanding of the fundamental characteristics of pulsating flows in the impingement zone, prior to studying the effects of multiple nozzles. The slot nozzle or tailpipe was used so that the computational domain could remain two-dimensional with a moving impingement surface. The ranges of parameters were derived from the Martin correlation and the assumptions for operating pulse combustors. Simulation results for the base case were presented and discussed in this chapter. The numerical procedure for the simulations was the same as that for the validation case. The sensitivity of key numerical parameters was studied. The characteristics of the pulsating jet at the tailpipe exit were slightly different than those for the validation case because the base case had a lower mean Reynolds number than the validation case. However, the characteristics of vortices were quite different, i.e., the vortices from the slot nozzle were stronger than those from the round nozzle and eventually became large re-circulating flows in the impingement zone. The difference was possibly due to the different nature of the wall jet velocities between slot and round nozzles. A key parameter for heat transfer enhancement was jet velocity ratio. For the pulsating jet with $\varepsilon = 4.4$, the enhancement factor was as high as 2.0 based on area-averaged heat fluxes over a reference distance. Two mechanisms responsible for heat transfer enhancement were the high-velocity exiting jet during the positive cycle and the strong re-circulating flow during the negative cycle. And, in order to create relatively strong re-circulating flows and to obtain relatively high enhancement factor, the jet velocity ratio, for the conditions of the base case, should be at least 3.0.

CHAPTER 7

PARAMETER STUDY

This chapter discusses the effects of jet flow parameters, frequency, mean velocity, and nozzle width as compared to the base case. As with the base case, each case was simulated using a range of velocity ratios. A grid independence study was also performed for each case. However, simulation results presented in detail are from the cases that are meaningful for comparison with the base case. For the cases employing different nozzle widths, the simulation results were used to estimate heat transfer enhancement factors and energy saving factors for multiple nozzles.

7.1 Effects of Pulsation Frequency

A key parameter of a pulsating jet is pulsation frequency. This parameter seemingly plays an important role in heat transfer enhancement either from impinging jets without flow reversal (Mladin and Zumbrunnen, 2000) or a pulsating flow along the tailpipe wall (Dec and Keller, 1989). Yet, another experimental result (Gemmen et al., 1993) showed that frequency did not have a significant effect on mass transfer on a cylinder inside the tailpipe of the same pulse combustor as in Dec and Keller (1989). However, the conditions and the ranges of parameters for those experiments were quite different from the present work, in which large-amplitude pulsating jets were used with jet impingement geometry. Simulation results for three different frequencies, f = 80, 160, and 320 Hz, are shown in Figure 7.1 presenting the heat transfer enhancement factor, relative to steady jet impingement heat transfer. The comparison was based on time-averaged and area-averaged heat fluxes over the reference distance, $0 \leq y/S \leq 2.8$ and at the stagnation point, $y/S = 0$. As the maximum velocity ratios for the cases with f = 80 and 320 Hz were about 5.2, an additional case for the base case with f = 160 Hz was simulated so that the base case also had a maximum velocity ratio at 5.2. The trends for the cases with f = 80 and 160 Hz were quite similar over the whole range of velocity amplitude ratios. The trend for the case with f = 320 Hz was different from the other cases at low velocity amplitude ratios. The heat transfer enhancement factors at these points were significantly greater than the cases with a lower frequency. However, at higher velocity amplitude ratios, the enhancement factor approached the same values as those for the other two cases.

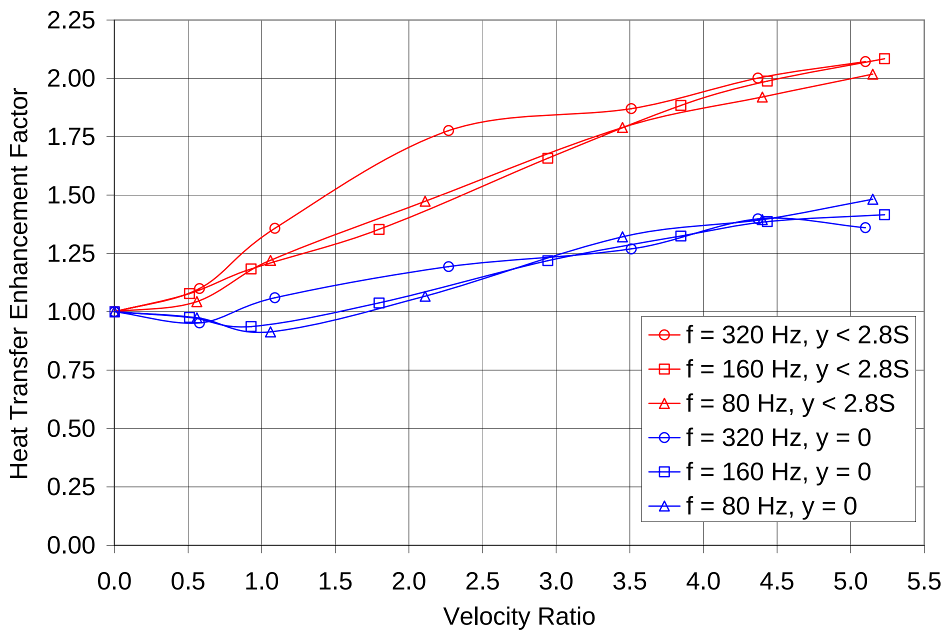

Figure 7.1: Heat transfer enhancement factors based on time- and area-averaged heat fluxes from different frequencies.

Figure 7.2 shows the maximum and minimum temperature at the tailpipe exit for the three cases. The trends are the same over the range of the velocity amplitude ratios. As discussed in the previous chapter, the minimum temperature at the tailpipe exit reflects the temperature of re-circulating flows or wall jets after they are subjected to heat loss at the impingement surface. Thus, the minimum temperature decreases with increasing velocity ratio due to increasing heat transfer to the surface. The maximum temperature slightly decreased with increasing velocity ratio, mainly due to the compressibility effects of higher mass flow rate in the inlet chamber. The effects of mass flow rate on temperature were observed in the simulation results for steady jets at u_m = 30 and 180 m/s, as for the initial condition and grid independence study, respectively. The temperatures at the tailpipe inlet were 1000 and 990 K whereas those at the tailpipe exit were 1000 and 985 K for u_m = 30 and 180 m/s, respectively. The decrease in the temperature at the tailpipe inlet for u_m = 180 m/s was due to a large pressure drop across the inlet chamber, from 12 to 7 kPa (gauge pressure). As for the case with u_m = 30 m/s, the pressure drop across the inlet chamber was much smaller, from 500 to 350 Pa (gauge pressure).

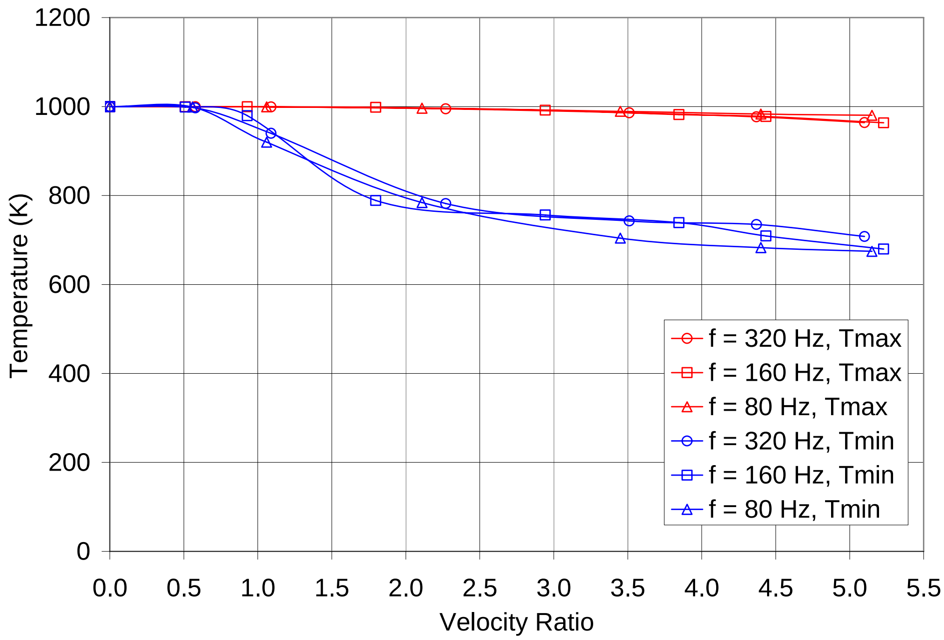

Figure 7.2: Maximum and minimum temperatures at tailpipe exit from different frequencies.

A general characteristic for pulsating jet impingement flows with a different frequency was that a pulsating jet with a lower frequency had a larger re-circulating flow region, as shown in Figure 7.3. This is because the wall jet could travel farther along the impingement zone as a result of the longer oscillation period. This characteristic resulted in a larger amplitude of surface heat flux oscillation for the case with a lower frequency.

However, the time-averaged values were about the same for the cases with different frequencies when the velocity amplitude ratio was large enough. Figures 7.4 and 7.5 demonstrate this behavior for the cases with $\varepsilon = 4.4$. The variation of stagnation point heat flux for the case with $f = 320$ Hz was clearly smaller than that for the case with $f =$ 80 Hz but the overall time-averaged profiles were not much different. The location, or the distance from the stagnation point, of the drop in the profiles increased with decreasing frequency indicating the size of the re-circulating flows or the location to where the wall jet could travel before curling upward.

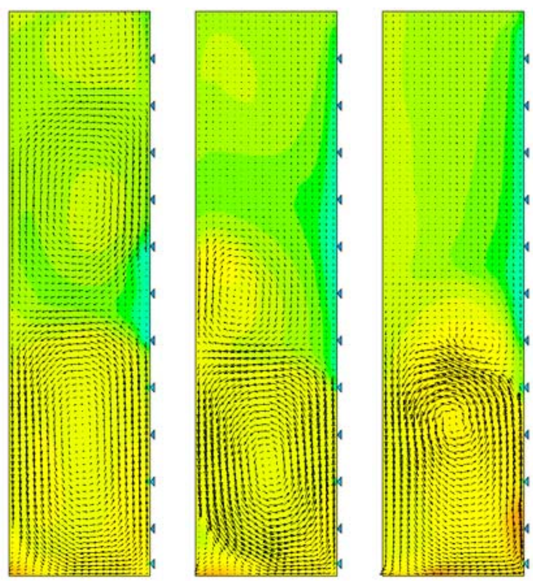

$f = 80$ Hz $f = 160$ Hz $f = 320$ Hz

Figure 7.3: Instantaneous velocity vectors/temperature contours from different frequencies with $\varepsilon = 4.4$.

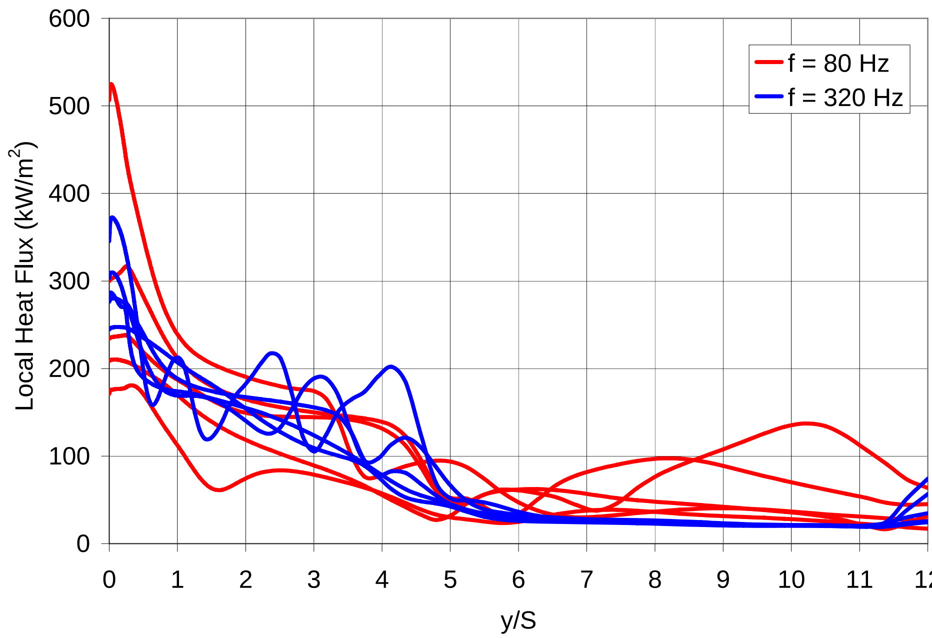

Figure 7.4: Instantaneous profiles of local heat fluxes from f = 80 and 320 Hz with ε = 4.4.

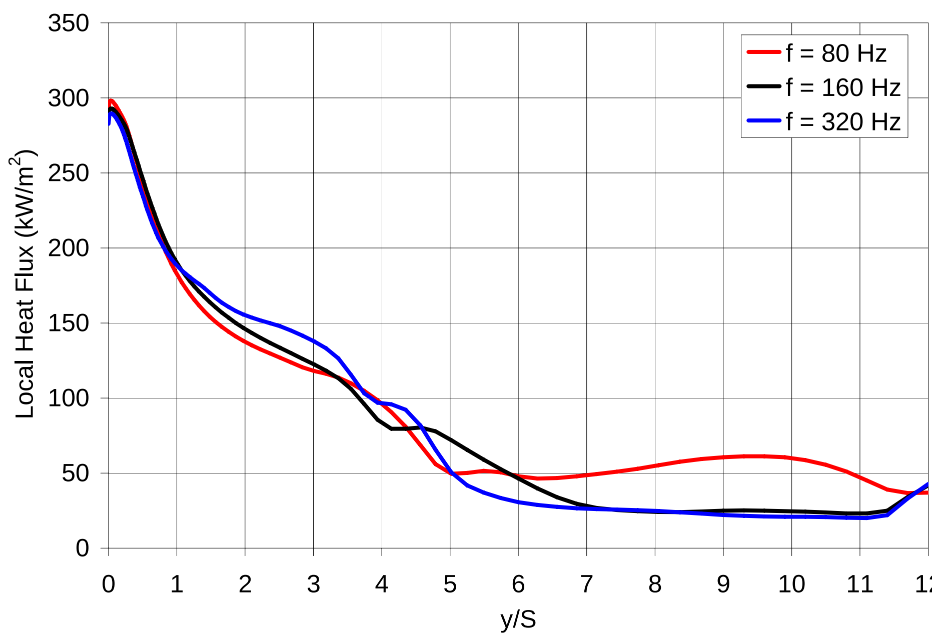

Figure 7.5: Time-averaged profiles of local heat fluxes from different frequencies with ε = 4.4.

As shown in Figure 7.1, at relatively low velocity amplitude ratio, especially at ε = 2.2, the result from the case with f = 320 Hz had the highest heat transfer enhancement factor, based on time- and space-averaged heat fluxes, compared to the cases with a lower frequency. This seems to be an optimum condition where the combination of both velocity amplitude and frequency has the greatest effect on surface heat transfer over the reference distance. Figure 7.6 shows instantaneous plots of velocity vectors for the cases with f = 80 and 320 Hz and with ε = 2.1 and 2.2, respectively. As with the cases with higher velocity ratios, the size of the re-circulating flows for the case with f = 80 Hz was larger than that for the case with f = 320 Hz. With a higher frequency, the pulsating jet velocity had a higher rate of acceleration resulting in a stronger re-circulating flow for the case with f = 320 Hz and, coincidentally, its size was about the same as the reference distance. Time-averaged profiles of local heat fluxes for these two cases are shown in Figure 7.7.

As the velocity amplitude ratio increased for each case, the re-circulating flows became stronger and larger. As a result, the time- and space-averaged heat fluxes were about the same over the reference distance as shown by the enhancement factors in Figure 7.1. Therefore, it could be deduced that the effects of oscillation frequency depend on the surface distance or area of interest as well as the magnitude of the velocity amplitude. For a pulsating jet with a low velocity ratio, a higher frequency could help increase surface heat transfer by creating stronger well-contained re-circulating flows as a result of a higher rate of jet acceleration. A parameter that appears to characterize this behavior is the Strouhal number, which typically represents the ratio between the oscillation frequency and the mean velocity (multiplied by a constant characteristic length). However, in this case, the magnitude of velocity n the Strouhal number should be velocity amplitude instead of mean jet velocity. This point should be further tested as the ranges of parameters in the present work are limited.

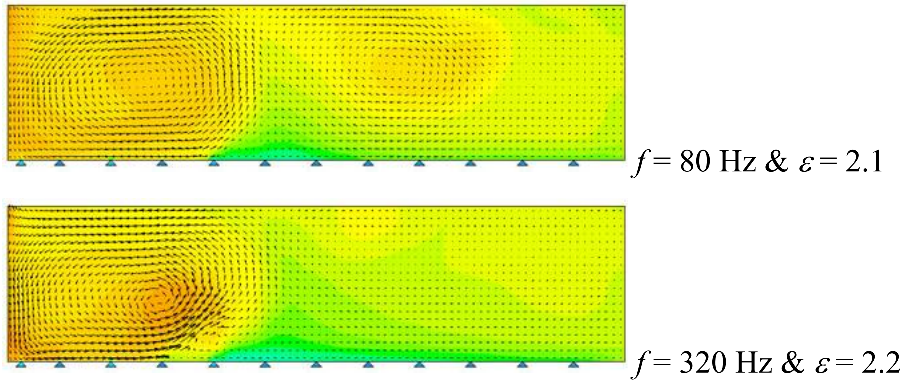

Figure 7.6: Instantaneous velocity vectors/temperature contours from f = 80 and 320 Hz with $\varepsilon \sim 2.2$.

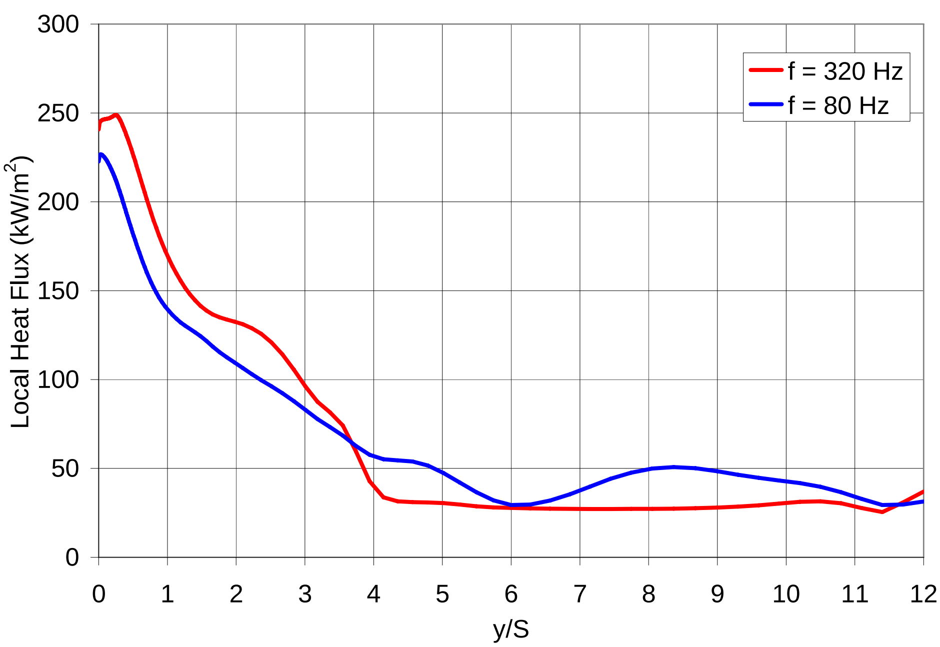

Figure 7.7: Time-averaged profiles of local heat fluxes from f = 80 and 320 Hz with $\varepsilon \sim 2.2$.

7.2 Effects of Mean Jet Velocity

As the large amplitude of jet velocity oscillation is mainly responsible for heat transfer enhancement, it would be interesting to compare the cases with the same maximum jet velocities but different mean velocities. A motivation is that, if a pulsating jet with a lower mean velocity could yield comparable heat transfer to that with a higher mean velocity, both heat transfer enhancement and energy saving could be achieved with respect to a corresponding steady jet. However, from the simulation results, this is not the case. Figure 7.8 shows the plots of time- and area-averaged surface heat fluxes for three different mean jet velocities with various velocity amplitude ratios. In order to compare the results more clearly, the x-axis was chosen to be maximum jet velocity instead of jet velocity ratio. The reference distance for area-averaged heat fluxes is 2.8*S* from the stagnation point. It is apparent from the plots in Figure 7.8 that, for the same maximum jet velocity, heat fluxes directly depend on the mean jet velocities (or mean energy rates) of the pulsating jets. The dependence on the mean energy rate can be observed via the temperature oscillations at the tailpipe exit. Figure 7.9 shows maximum and minimum temperatures during the oscillation cycle at the tailpipe exit for all three cases. The minimum temperature decreased with decreasing mean jet velocity. This trend was the result of the heat transfer process, not the boundary conditions. As the mean jet velocity decreased, the mean energy rate in the impinging jet also decreased. Therefore, after heat loss to the impingement surface, the temperature of the wall jet and re-circulating flow, as a function of the energy rate, was lower for the lower mean jet velocity case.

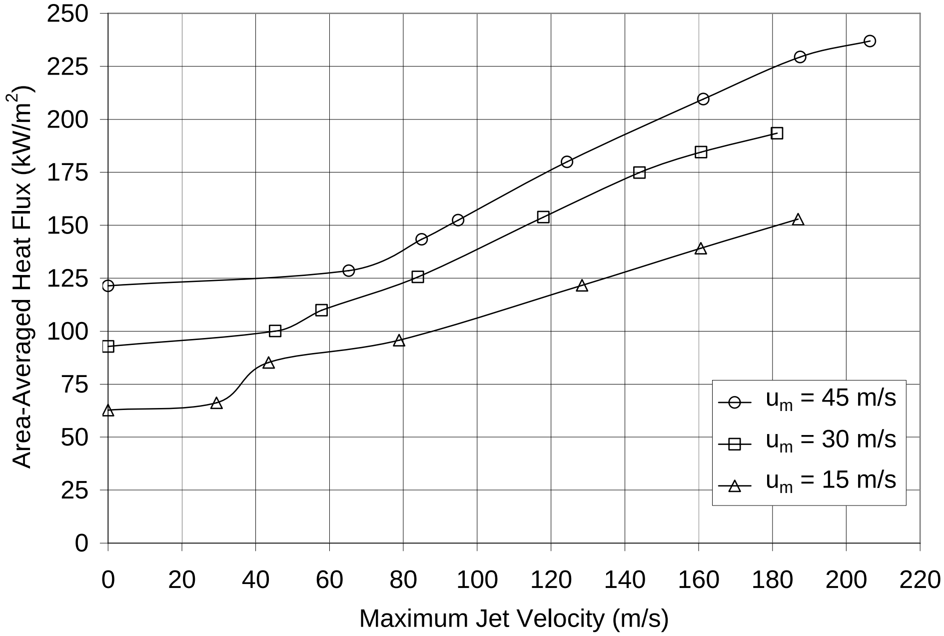

Figure 7.8: Time- and area-averaged heat fluxes over $y \leq 2.8S$ from different mean jet velocities.

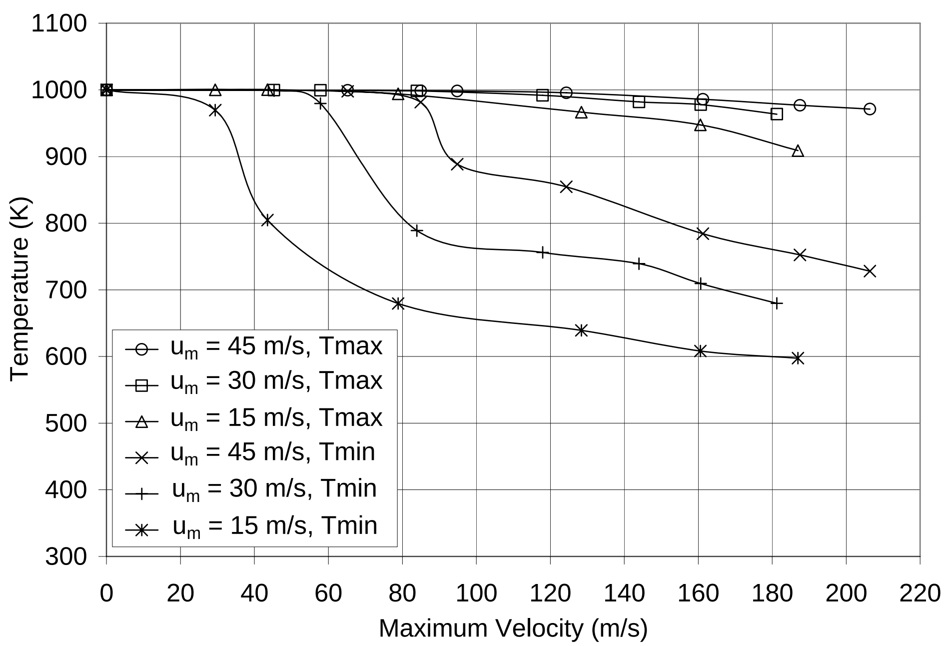

Figure 7.9: Maximum and minimum temperatures at tailpipe exit from different mean jet velocities.

Time-averaged profiles of local heat flux for the three cases with the same maximum jet velocity at 160 m/s are shown in Figure 7.10. Although the magnitude of heat flux from a lower mean jet velocity was less than that from a higher mean jet velocity, a practical parameter to be considered is the ratio of the surface heat flux at the impingement surface and the input energy rate, in other words, the energy efficiency. From Figure 7.10, it is apparent that the magnitude of heat flux for the case with u_m = 45 m/s was not three times that for the case with u_m = 15 m/s, meaning the energy efficiency was greater for the case with u_m = 15 m/s. Nevertheless, from another practical point of view for pulse combustor operation, generating high velocity amplitude from a low mean jet velocity could be more difficult than the other way around. Therefore, all aspects need to be optimized depending on the objective of the application, i.e., whether it requires high heat flux or high energy efficiency or something in between.

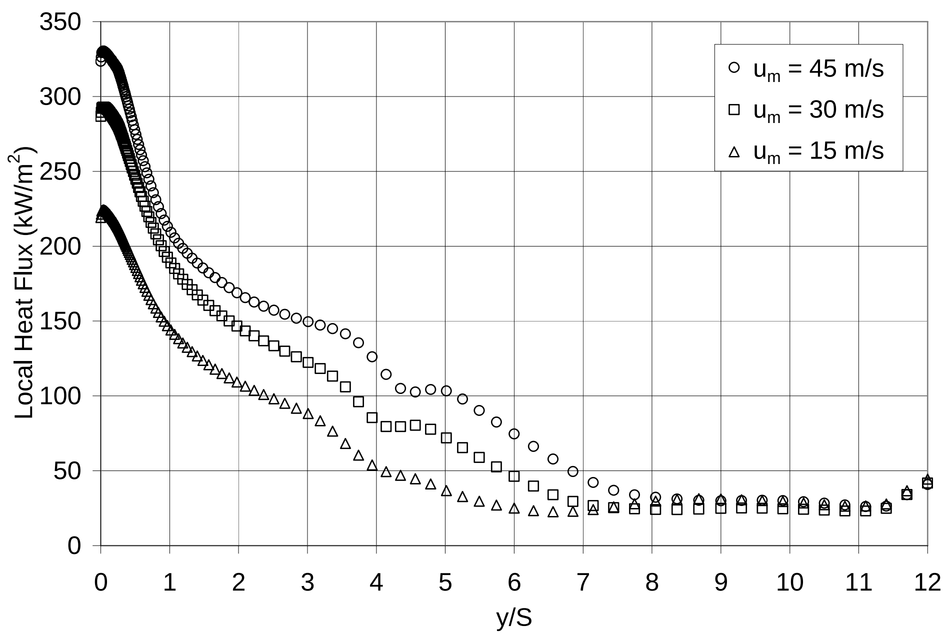

Figure 7.10: Time-averaged profiles of local heat fluxes from different mean jet velocities with maximum jet velocity of 160 m/s.

Figure 7.11 shows instantaneous velocity vectors and temperature contours for different mean jet velocities but with the same maximum jet velocity of 160 m/s. It is interesting that the size of the re-circulating flow is relatively the same for all three cases. This implies that the wall jet is being driven only during the acceleration phase of jet velocity from zero to the maximum value. After that, the impinging jet decelerates; the wall jet and the re-circulating flow lose momentum. In terms of fluid dynamics, the impingement surface would experience similar flow dynamics or shear stresses for all three cases. Thus, it is possible that if the mean energy rates of pulsating jets are at the same level, surface heat fluxes would also be at the same level for these three cases. As support for this argument, time-averaged profiles of local heat transfer coefficient calculated from the difference between the mean temperature at the tailpipe exit for each case and the surface temperature are shown in Figure 7.12. The values of heat transfer coefficient were comparable from the stagnation point up to about $y/S = 3$, where the bulk temperature of the fluid was about the same as that at the tailpipe exit. However, these profiles are only preliminary results. Simulations with different inlet temperatures should be performed for more definitive conclusions.

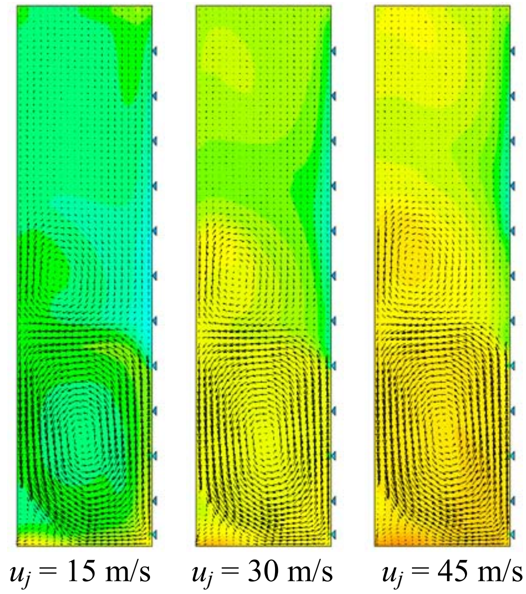

Figure 7.11: Velocity vectors/temperature contours from different mean jet velocities with maximum jet velocities of 160 m/s.

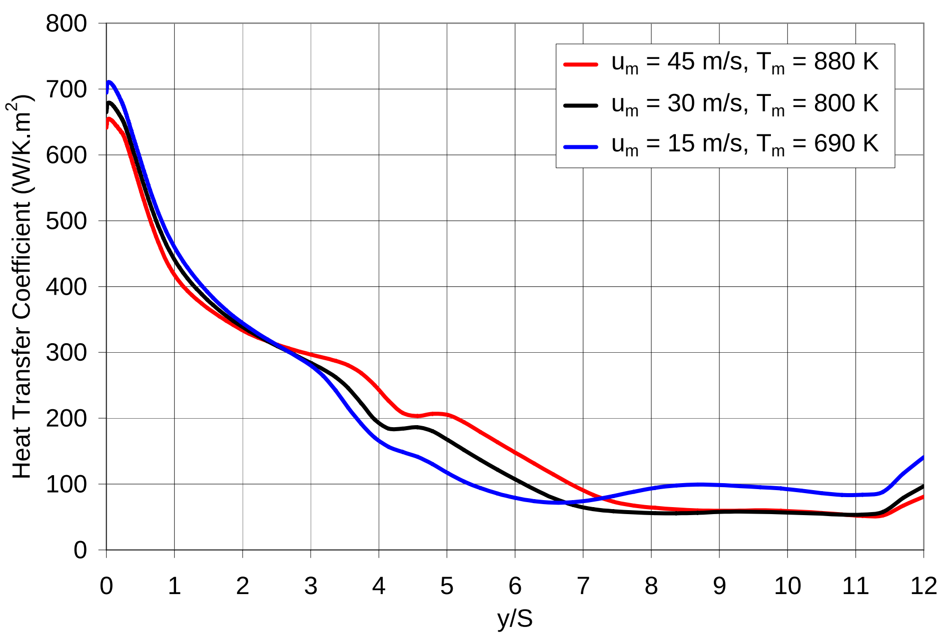

Figure 7.12: Time-averaged profiles of local heat transfer coefficient from different mean jet velocities with maximum velocity of 160 m/s.

7.3 Effects of Nozzle Width

One of the criteria for the design of the numerical experiment is that the nozzle-to-surface spacing is constant, H = 30 mm, as a minimum distance allowed in a typical impingement hood. Thus, the only other parameter of single-nozzle impingement geometry that could be varied is nozzle width. Four additional cases of different nozzle widths were simulated for comparison with the base case. The hydraulic diameter of the nozzles, S, was chosen to be 30, 15, 10, 7.5, and 6 mm so that the impingement spacing ratio, H/S, was 1, 2, 3, 4, and 5, respectively. The parameters of pulsating jets were the same as those of the base case, i.e., u_m = 30 m/s, ε = 4.4, and f = 160 Hz. Hence, the mean mass flow rates and mean input energy rates were different for each case.

Time-averaged profiles of local heat fluxes versus actual distances are shown in Figure 7.13. Heat flux levels directly depended on the width of the nozzle or tailpipe, or in other words, the mean energy rate. An interesting pattern is the position of the drop in the local heat flux profiles. Despite the difference in nozzle width, or mean mass flow rate, the vortices still travel to approximately the same distance as shown in Figure 7.14. This characteristic indicates that the driving force of the re-circulating flow comes from fluid at the center of the nozzle. Together with the conclusion from the previous section, it could be deduced that, at the same frequency, the size of re-circulating flow is determined by the maximum jet velocity of the fluids at the center of the nozzle, regardless of mean jet velocity or nozzle width.

In Figure 7.14, although the size of re-circulating flow was approximately the same, the re-circulating flows were strongest with the largest nozzle, S = H, due to it having highest mean mass flow rate. The secondary re-circulating flows were also most noticeable with the largest nozzle or highest mean mass flow rate. And the temperatures of the re-circulating flows were highest with the largest nozzle due to it having highest mean energy input rate.

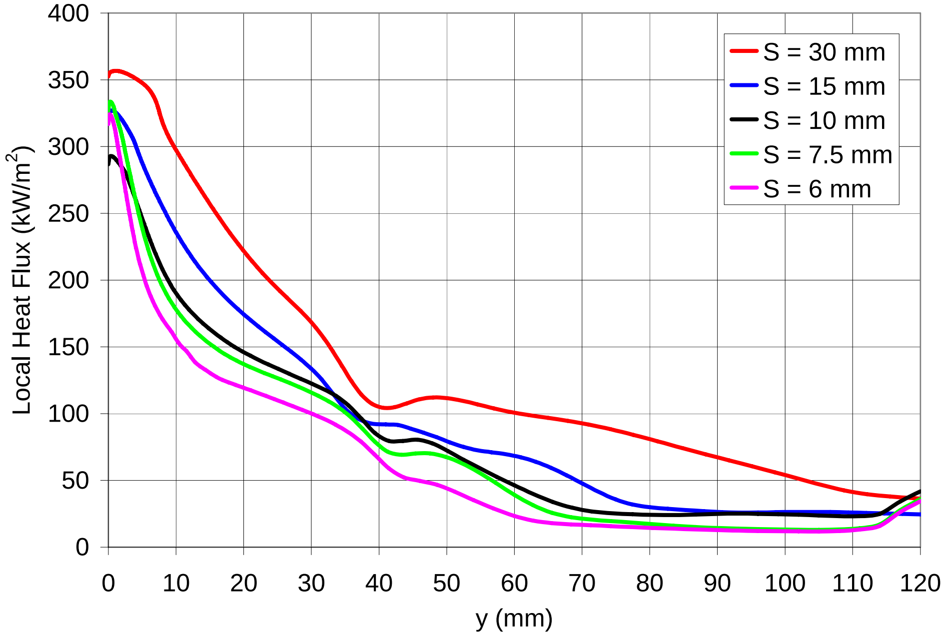

Figure 7.13: Time-averaged profiles of local heat fluxes from different nozzle widths versus actual distance, *y*.

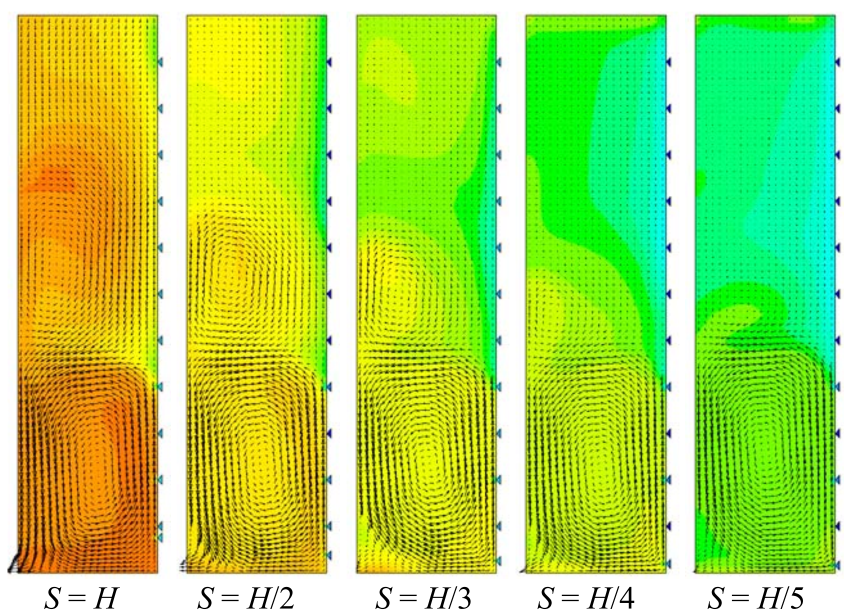

Figure 7.14: Velocity vectors/temperature contours from different nozzle widths at the beginning of negative cycle.

The time-averaged profiles of area-averaged heat fluxes corresponding to Figure 7.13 are shown in Figure 7.15. In general, the pulsating jets from larger nozzles yielded higher area-averaged heat fluxes than those from smaller nozzles but not in proportion to the increase in nozzle width or mean energy rate. As shown later, the results of pulsating jets from the smaller nozzles, *S* = 6 and 7.5 mm, were better than those from the larger nozzles in terms of energy efficiency and heat transfer enhancement as compared to a reference condition of steady jet impingement.

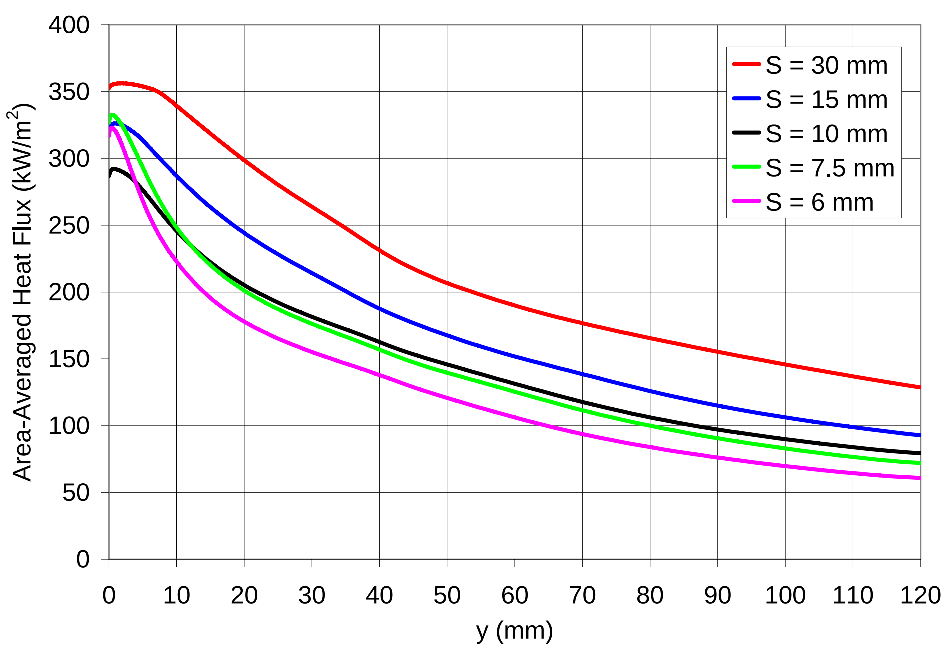

Figure 7.15: Time-averaged profiles of area-averaged heat fluxes from different nozzle widths versus actual distance, *y*.

Figure 7.16 shows plots of time-averaged local heat fluxes against corresponding non-dimensional distances, *y/S*. The positions of the drop in the profiles vary with nozzle width or the dimensionless parameter, *H/S*. That is, with respect to the nozzle width, the relative size of re-circulating flows decreased with decreasing relative nozzle-to-surface spacing. This characteristic is consistent with the preliminary simulation work, in which the tailpipe diameter was held constant and the nozzle-to-surface spacing was varied.

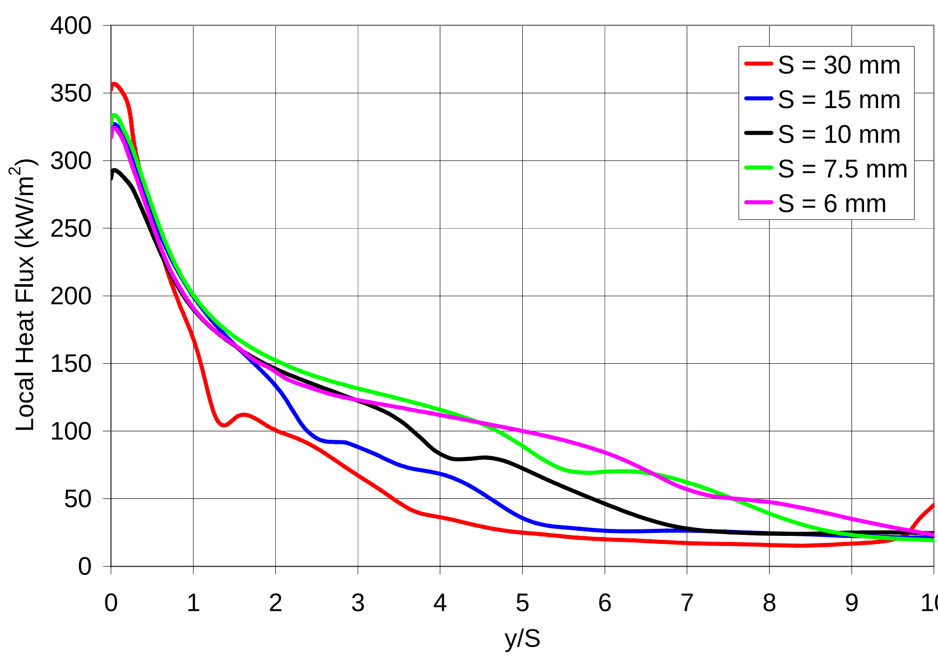

Figure 7.16: Time-averaged profiles of local heat fluxes from different nozzle widths versus non-dimensional distance, *y/S*.

In order to evaluate the heat transfer enhancement factor for each respective case, area-averaged heat fluxes were calculated for pulsating and steady jets, as shown in Figures 7.17 and 7.18, respectively. While pulsating jet impingement heat fluxes from different tailpipe widths were not much different with respect to corresponding non-dimensional distance, steady jet impingement heat fluxes were quite different with larger tailpipe width yielding lower heat flux than smaller nozzle width. Hence, enhancement factors from pulsating jets relative to corresponding steady jets were greatest at the largest tailpipe width as shown in Figure 7.19. The enhancement factors were based on the comparisons at the same nozzle width. In practice, steady jet impingement drying hoods are operated with optimum impingement geometry for maximum heat flux and energy efficiency. Therefore, a more meaningful comparison between pulsating and steady jets would be based on the optimum condition of the steady jets.

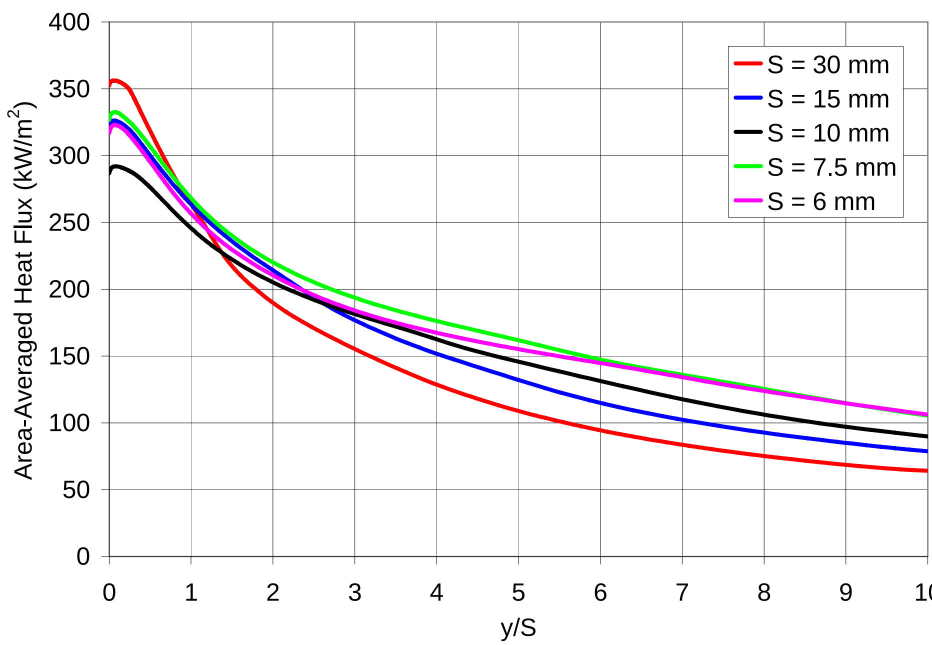

Figure 7.17: Time-averaged profiles of area-averaged heat fluxes from different nozzle widths versus non-dimensional distance, *y/S*.

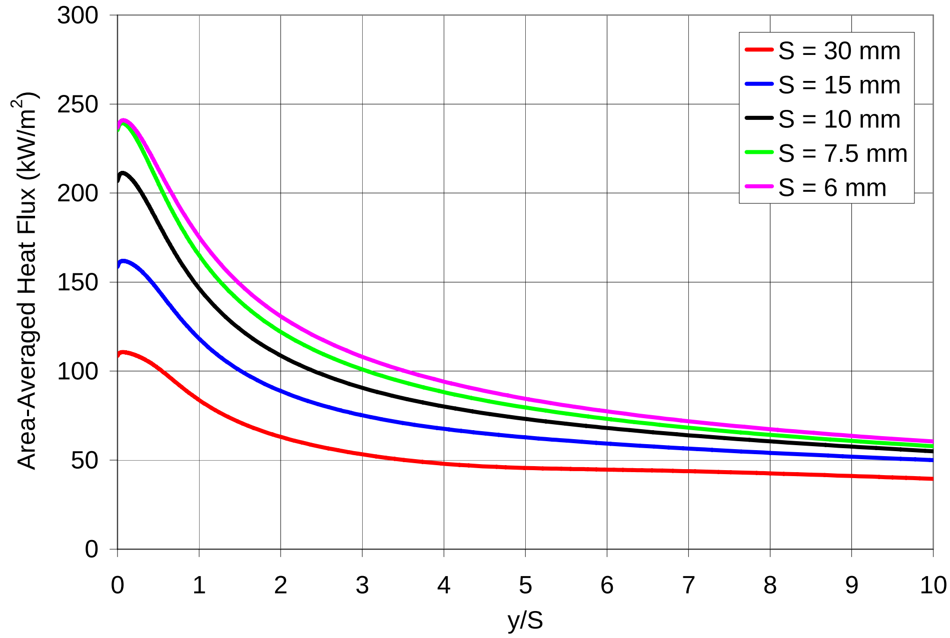

Figure 7.18: Area-averaged heat flux profiles from steady jets with different nozzle widths versus non-dimensional distance, *y/S*.

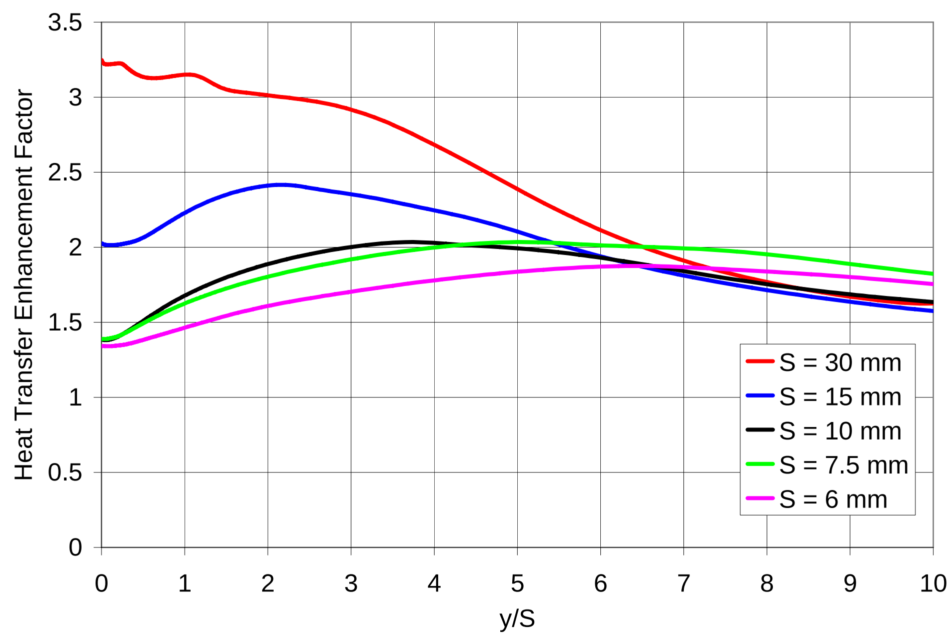

Figure 7.19: Heat transfer enhancement factor profiles from different nozzle widths versus non-dimensional distance, *y/S*.

The optimum value of H/S for steady jet impingement, based on the Martin correlation for ASN, is approximately five. From Figure 7.18, steady jet impingement with a single nozzle also yields maximum heat flux at $H/S = 5$ (for the range of H/S investigated). Therefore, this condition is used as a reference steady jet impingement heat flux for comparison with pulsating jets. Another factor to be considered is the magnitude of heat flux, which should be in the range of values equivalent to typical drying rates in impingement hoods. For this case, the heat flux level is chosen to be 100 kW/m^2 (~160 kg/h.m^2 for drying rate), corresponding to $y/S = 3.5$, which coincides with optimum nozzle-to-nozzle spacing for ASN with $H/S = 5$ as shown in Table 6.1. The heat flux from the simulation was also close to the correlation results, 105 and 104 kW/m^2 for ASN and SSN, respectively. Therefore, the reference condition is $S_0 = 6$ mm, $Y_0 = 3.5S_0 = 21$ mm, and $q_0'' = 100$ kW/m^2, where Y is the half distance of nozzle-to-nozzle spacing and the subscript 0 is for the reference condition. Furthermore, in order to evaluate both heat transfer enhancement and energy saving factors, additional assumptions must be made. The comparison is based on heat fluxes from multiple nozzles with different nozzle widths and different nozzle-to-nozzle spacings. Simulation results from a single nozzle are assumed to be equivalent to those from multiple nozzles, i.e., assuming that jet interactions and cross-flows have no effects on surface heat transfer. Figure 7.20 illustrates the reference condition of steady jet impingement heat transfer.

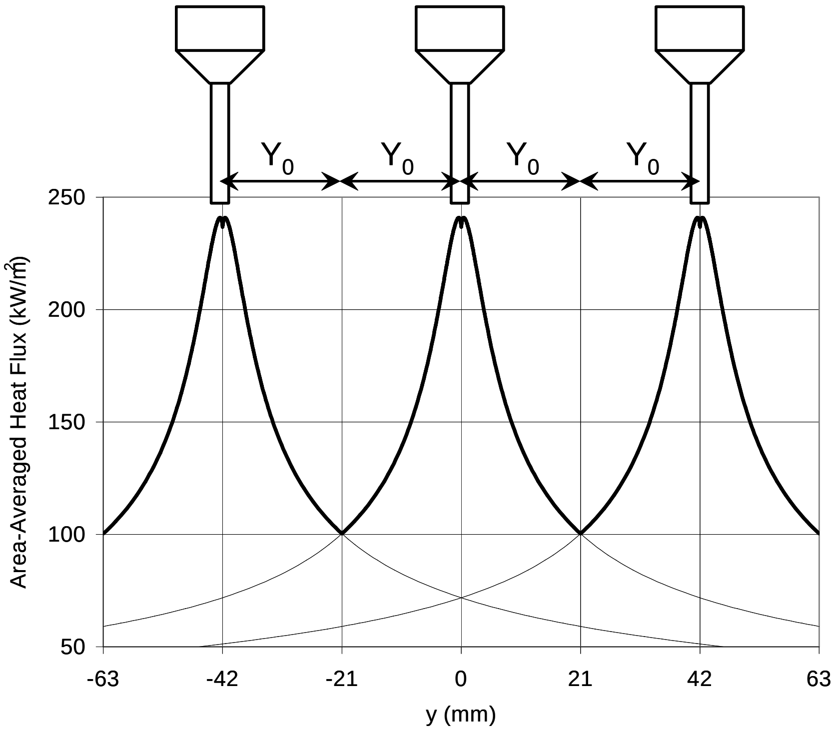

Figure 7.20: Reference condition of steady jet impingement heat transfer: $H/S_0 = 5$, $H = 30$ mm, $S_0 = 6$ mm, $Y_0 = 21$ mm, and $q''_0 = 100$ kW/m^2.

With the assumption that area-averaged heat fluxes from multiple nozzles are equal to area-averaged heat fluxes from single-nozzle simulation results at the same Y, the comparison could be easily done for either heat transfer enhancement or energy saving factors. First, consider the net input energy rate for multiple nozzles. The net input energy rate is equal to the input energy rate per nozzle multiplied by the number of nozzles in one unit area or unit length in this case. As the mean velocity and jet temperature are the same for all cases, the input energy rate per nozzle directly depends on the nozzle width or hydraulic diameter. The number of nozzles per unit length inversely depends on the nozzle-to-nozzle spacing, regardless of the nozzle width. Therefore, the net input energy rate for any condition is equal to $C \cdot S/Y$, where the value of the constant C is the same for all conditions. And due to the assumption above, the corresponding net heat flux for an impingement condition is the area-averaged heat flux from the simulation results at $y = Y$ with the same S. Since any single data point in Figure

7.17 has two corresponding values, q'' at y/S, it can be used to calculate the heat transfer enhancement factor and the energy saving factor compared to the reference condition.

For any point in Figure 7.17, the heat transfer enhancement factor is

$$qf = \frac{q''}{q''_0} = \frac{q''}{100}$$

And the corresponding energy saving factor is

$$ef = \frac{S_0/Y_0}{S/Y} = \frac{y/S}{Y_0/S_0} = \frac{y/S}{3.5}$$

With these definitions, a plot between heat transfer enhancement factors and corresponding energy saving factors for each nozzle width can be established, as shown in Figure 7.21.

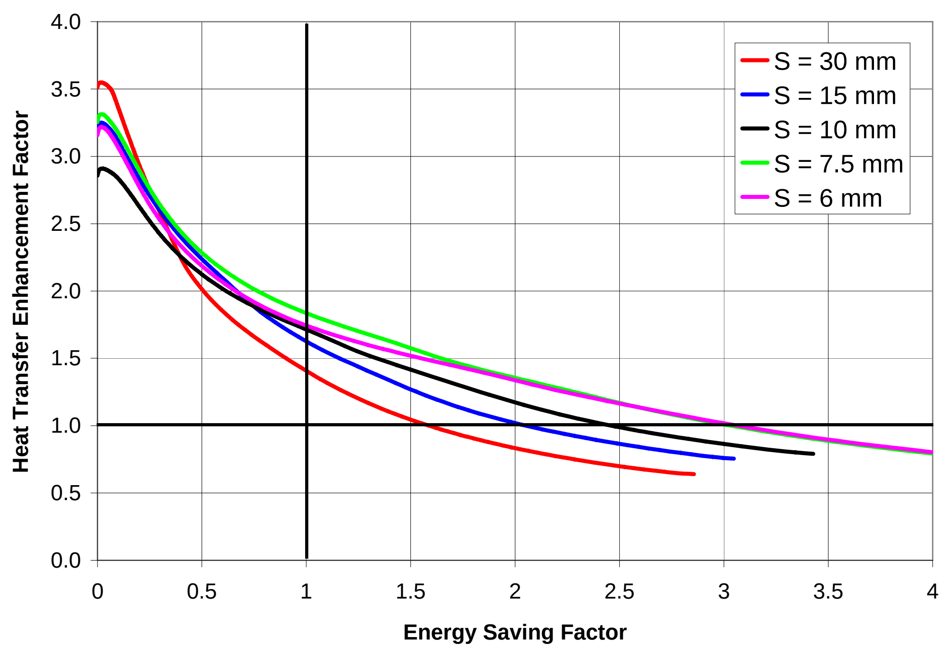

Figure 7.21: Heat transfer enhancement factor versus energy saving factor from different nozzle widths.

There are two reference lines of interest in Figure 7.21. The first line is the vertical line at the energy saving factor equal to one, indicating how much the pulsating jets could improve the area-averaged heat fluxes based on the same mean mass flow rate or energy rate input per unit area as that of the reference condition. The maximum heat transfer enhancement factor on this line is approximately 1.8 at the condition of $S = 7.5$ mm and $Y = 26$ mm ($H/S = 4$ and $Y/S = 3.5$). The second line is the horizontal line at the heat transfer enhancement factor equal to one, indicating how much the energy input could be reduced given the same area-averaged heat flux. The maximum energy saving factor on this line is approximately 3.0, so only 33% of the input energy rate of the reference condition is required. There are two conditions at this point: $S = 7.5$ mm at $Y = 79$ mm ($H/S = 4$ and $Y/S = 10.5$) and $S = 6$ mm at $Y = 64$ mm (H/S = 5 and Y/S = 10.7).

In general, the curve for the case with $S = 7.5$ mm or $H/S = 4$ appears to be the best overall in terms of both heat transfer enhancement and energy saving. The curve from the case with $S = 6$ mm or $H/S = 5$ is not much different in the area between the vertical and horizontal lines, which has positive benefits for both heat transfer enhancement and energy saving. From these results, it seems pulsating jet impingement heat transfer also requires small nozzles for optimum geometry conditions. The results for these improvement factors are very encouraging, especially the energy saving factor. However, these conditions are based on single-nozzle simulation results. Actual multiple-nozzle impingement conditions should be simulated to evaluate more realistic factors for both pulsating and steady jets.

7.4 Summary

The main effect of pulsation frequency is the amplitude of surface heat flux oscillation. Higher frequency yielded less fluctuation in surface heat flux. Time-averaged heat fluxes were approximately the same for different frequencies but the same velocity ratio. For a stationary surface, the effects of frequency are insignificant. But for a moving surface, high frequency could be preferable because a point on the surface would experience less fluctuation or more uniform heat transfer while moving through a series of impinging jets. At low velocity ratios, high pulsation frequency had more prominent effects due to the high acceleration rate of the jet causing stronger re-circulating flows compared to those for lower frequencies.

The resulting heat flux from a lower mean jet velocity with a high velocity amplitude was still lower than those from higher mean jet velocities but lower velocity amplitudes (same maximum jet velocities) because the mean energy rate was lower. If the mean energy rate was comparable for different mean jet velocities but the same maximum jet velocity, the magnitude of heat fluxes was possibly at the same level because the flow dynamics of the impinging jets and re-circulating flows were not much different. For the same frequency, the size of re-circulating flows appeared to be determined by the maximum jet velocity from the fluids at the center of tailpipe and independent of mean jet velocity and nozzle width.

Increasing tailpipe width, thus increasing mean mass flow rate and energy rate, increased area-averaged heat flux but not in the same proportion as the increase in energy rate. In other words, the energy efficiency was higher with smaller nozzle widths. From area-averaged heat flux data for steady and pulsating jets with various tailpipe widths, with simplifying assumptions, optimum conditions of nozzle width and nozzle-to-nozzle spacing for maximum heat transfer enhancement factor or maximum energy saving factor were determined. The best overall performance was from the pulsating jet with $H/S = 4$, in which the maximum heat transfer enhancement factor was 1.8 and the maximum energy saving factor was 3.0. As with steady jet impingement, the conditions with $H/S = 4$ or 5, or small nozzles, were preferred for pulsating jet impingement heat transfer.

CHAPTER 8
PULSATING JET IMPINGMENT ON A MOVING SURFACE

This chapter presents the simulation results of pulsating jet impingement heat transfer with a moving surface. The computational domain was double the size of that for a stationary surface since the plane symmetry can no longer be applied. The base case for this chapter had a jet velocity ratio of 4.3 and a surface velocity of 30 m/s (1800 m/min), which is in a typical speed range for modern paper machines. The effects of jet velocity ratio were studied in the same way as for the cases with a stationary surface. As for the effects of surface velocity, two more cases were simulated with surface velocities of 15 and 45 m/s. It should be noted that the ratios between the surface velocities and the mean jet velocity in these simulations (0.5-1.5) are higher than those in an impingement hood for paper drying (up to 0.4) because the mean jet velocity in these simulations (30 m/s) is lower than those in an impingement hood (~100 m/s).

8.1 Numerical Procedure

The numerical procedure for this chapter was the same as for the simulation cases with a stationary impingement surface except for the computational domain and the velocity of the impingement surface. Figure 8.1 shows a diagram of the computational domain, which is symmetric about the center line of the tailpipe or the x-axis. Grid generation was also symmetric about the x-axis. The number of grid cells was the same as for the base case with a stationary surface, except for the fine grids near the impingement surface. For the cases with a moving surface, the number of grid cells in the x-direction near the surface was adjusted to have 10 grid cells fewer than the stationary surface case because flow solutions did not converge even with a steady jet. This is possibly a result of the characteristic of the V2F turbulence model, which can be unstable if y^+ is too low or too high.

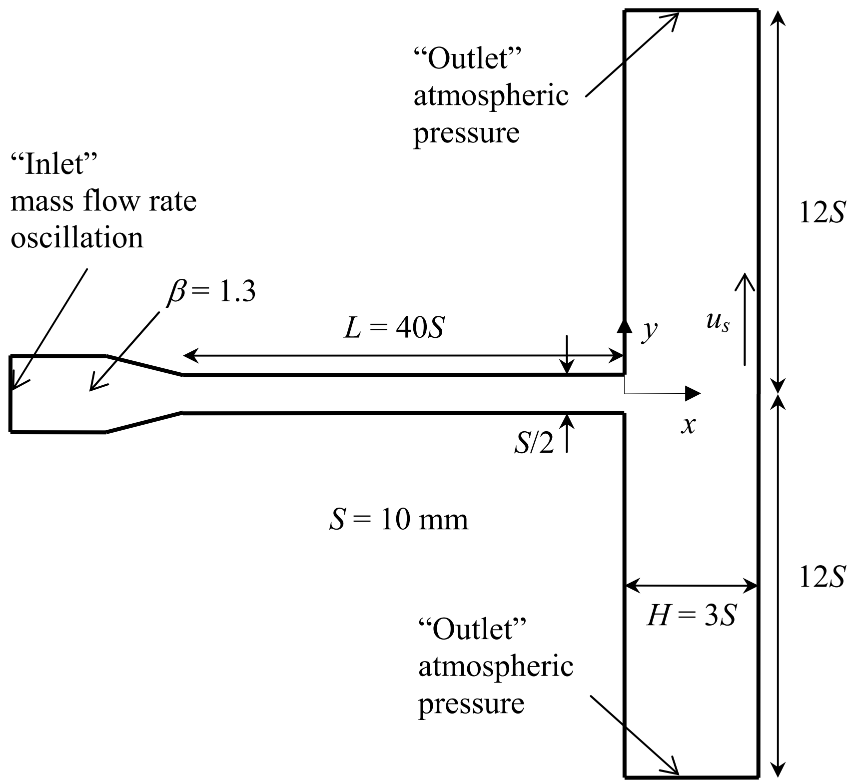

Figure 8.1: Computational domain for simulations with a moving surface.

As with the base case in Chapter 6, the key parameters were u_m = 30 m/s, f = 160 Hz, T_j = 1000 K, and H/S = 3. Backflow temperatures at the two outlet boundaries were 700 K. Three different surface velocities were simulated: 15, 30, and 45 m/s. The velocity ratio was varied in the same way as for the cases with a stationary surface, i.e., varying the amplitude ratio of inlet mass flow rate oscillation. Grid independence studies for all three surface velocities were performed in the same way as those for the base case with a stationary surface, i.e., using a steady jet with u_j = 180 m/s and double the grid cells in both directions. Results from the two sets of grids were not significantly different.

8.2 Flow and Heat Transfer Characteristics

As with the validation case and the base case with a stationary surface, basic flow characteristics are presented and discussed first. The base cases for this chapter were steady and pulsating jets with the surface velocity of 30 m/s. Figure 8.2 shows velocity vectors and temperature contours for the steady jet impingement flow. The impingement surface moves from left to right. On the right hand side of the tailpipe centerline, the wall jet flows along in the same direction as the moving surface. On the left hand side, the wall jet flows against the moving surface. As the surface velocity is considered relatively high, i.e., the ratio of u_s/u_j is 1.0, the effects of the moving surface on flow and heat transfer characteristics are different on either side of the tailpipe centerline and different from those with a stationary surface. For flow characteristics, the major difference from the stationary surface is on the left side of the tailpipe where the moving surface results in the wall jet moving toward the confinement wall. On the right side of the tailpipe, flow characteristics are similar to those with a stationary surface except that the surface moves along with the wall jet resulting in lower shear stress in the area near the jet centerline.

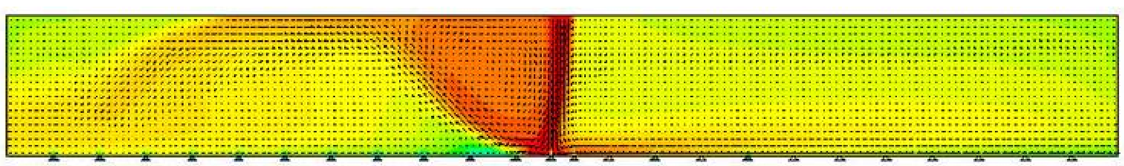

Figure 8.2: Velocity vectors/temperature contours of steady jet impingement on a moving surface with $u_s = u_j = 30$ m/s.

The local heat transfer profiles for steady jet impingement for a range of surface velocities are shown in Figure 8.3. The local heat flux profiles for a moving surface have similar patterns. As the surface velocity increases, the heat flux at the jet centerline decreases and shifts toward the right-hand side. An explanation is that, at $u_s = 15$ m/s, the impinging jet shifts toward the negative pressure created by re-circulating flows on the left-hand side of the jet. As the surface velocity increases, the impinging jet and the wall jet are increasingly dominated by the moving surface, resulting in the peak shifting slightly toward the right-hand side. And as the surface velocity increases, the shear stress or velocity gradient on the surface at the jet centerline decreases. Hence, the peak of the heat flux profiles decreases with increasing surface velocity.

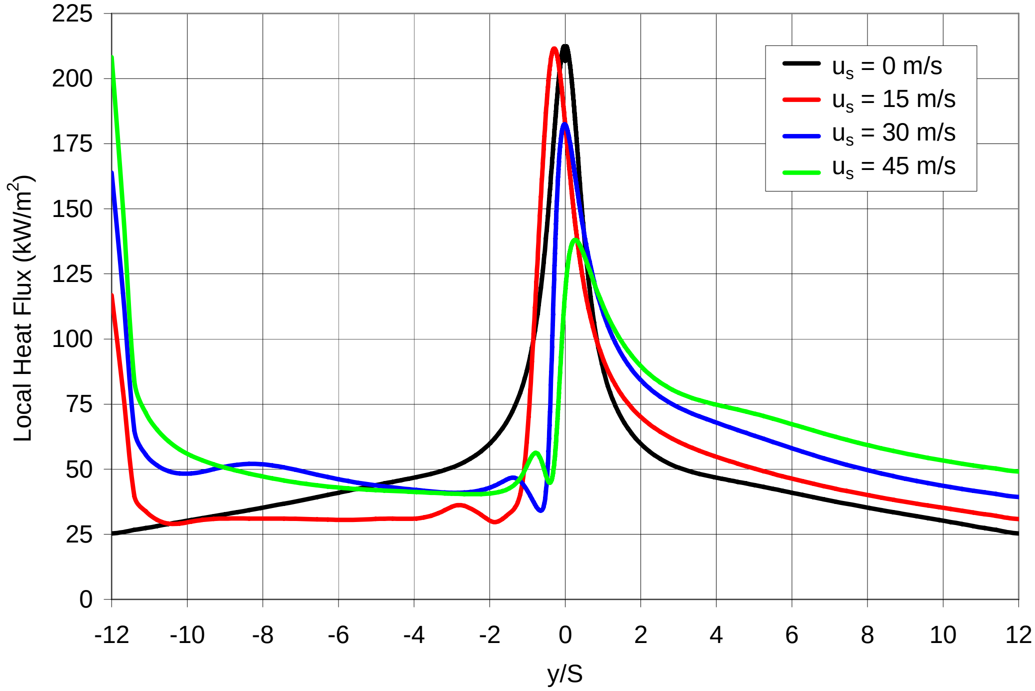

Figure 8.3: Local heat flux profiles of steady jet impingement from different surface velocities.

On the right side of the surface away from the centerline, heat flux levels increase with increasing surface velocity. The reason is also due to the domination of surface velocity; the velocity and temperature gradients near the surface are mainly caused by the moving surface, instead of the wall jet as the case with a stationary surface. On the left side of the centerline, where the direction of the moving surface is against the flow of the wall jet, the surface velocity has adverse effects, causing flow separation near the centerline of the surface. As the surface velocity increases, the position of flow separation is closer to the jet centerline. The wall jet is forced to flow up toward the confinement wall and reattach on the impingement surface near the outlet boundary at the left side. The outflow near the impingement surface explains why heat fluxes are extremely high at the outlet boundary on the left side for the cases with a moving surface; both velocity and temperature gradients are high because of the opposite directions of the outflow and the moving surface.

Figure 8.4 shows time-averaged profiles of local heat fluxes from the pulsating jet with $\varepsilon \sim 4.3$ for stationary and moving surfaces. The patterns of the profiles for the moving surfaces are similar. Basically, the patterns of these profiles are similar to those with a steady jet, with two distinctive features. The similar patterns are that, as the surface velocity increases, heat flux levels on the right side increase and the positions of flow separation on the left side are closer to the jet centerline. A main difference between profiles from the steady and pulsating jets is that maximum heat fluxes from the pulsating jet are relatively the same while those from the steady jet decrease with increasing surface velocity (Figure 8.3). The other key difference is that there are secondary peaks on the left side of the jet centerline. These differences are associated with the characteristics of vortices generated by the pulsating jet as shown in Figures 8.5 and 8.6.

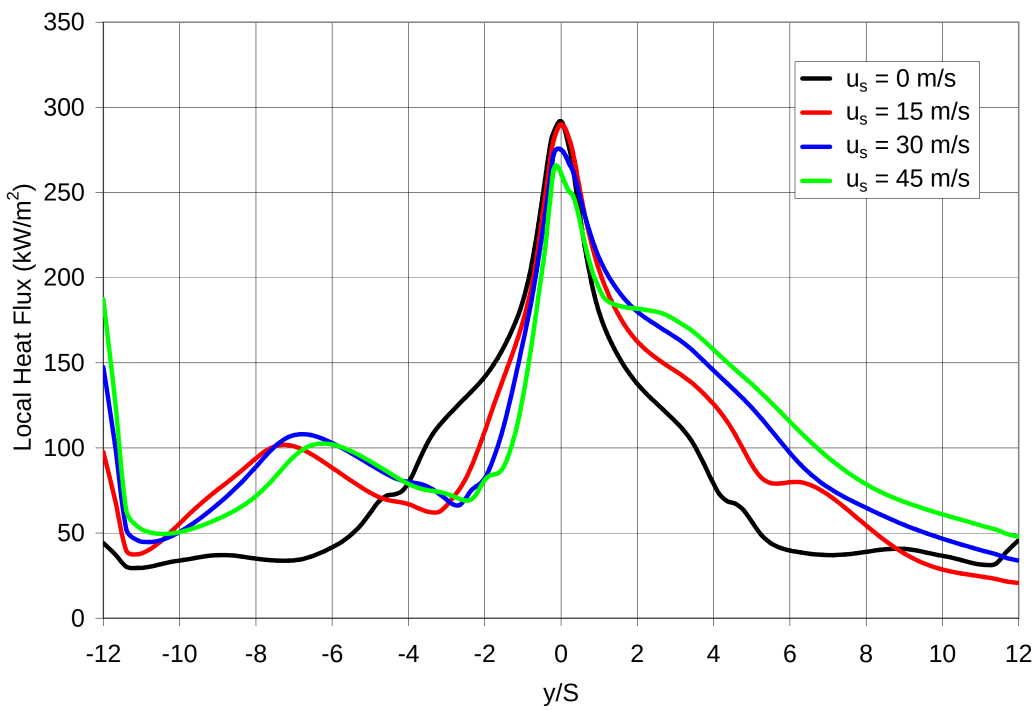

Figure 8.4: Time-averaged profiles of local heat fluxes from different surface velocities with $\varepsilon \sim 4.3$.

As with the validation case and the base case with a stationary surface in Chapters 5 and 6, respectively, instantaneous velocity vectors and temperature contours as well as corresponding local heat flux profiles during the positive and negative cycles of the base case in this chapter are shown in Figures 8.5 and 8.6, respectively. The pulsating jet has a velocity ratio of 4.3 and the velocity of the surface is 30 m/s, moving from left to right. Key characteristics are still vortices and re-circulating flows. However, the moving surface affects the vortices differently depending on the direction of the wall jet relative to the surface velocity. On the right side, the moving surface drags the vortices away from the jet centerline. On the left side, the moving surface pushes the vortices closer to the jet centerline causing smaller re-circulating flows and creating secondary re-circulating flows. The secondary re-circulating flows are responsible for secondary peaks in local heat flux profiles on the left side in Figure 8.4. As with the pulsating jet impinging on the stationary surface, maximum heat fluxes occur at the end of the positive cycle when the impinging jet velocity and temperature are highest and the re-circulating flows are strongest. And also, as with the pulsating jet impinging on the stationary surface, instantaneous heat fluxes during the negative cycle are relatively constant due to the effects of strong re-circulating flows.

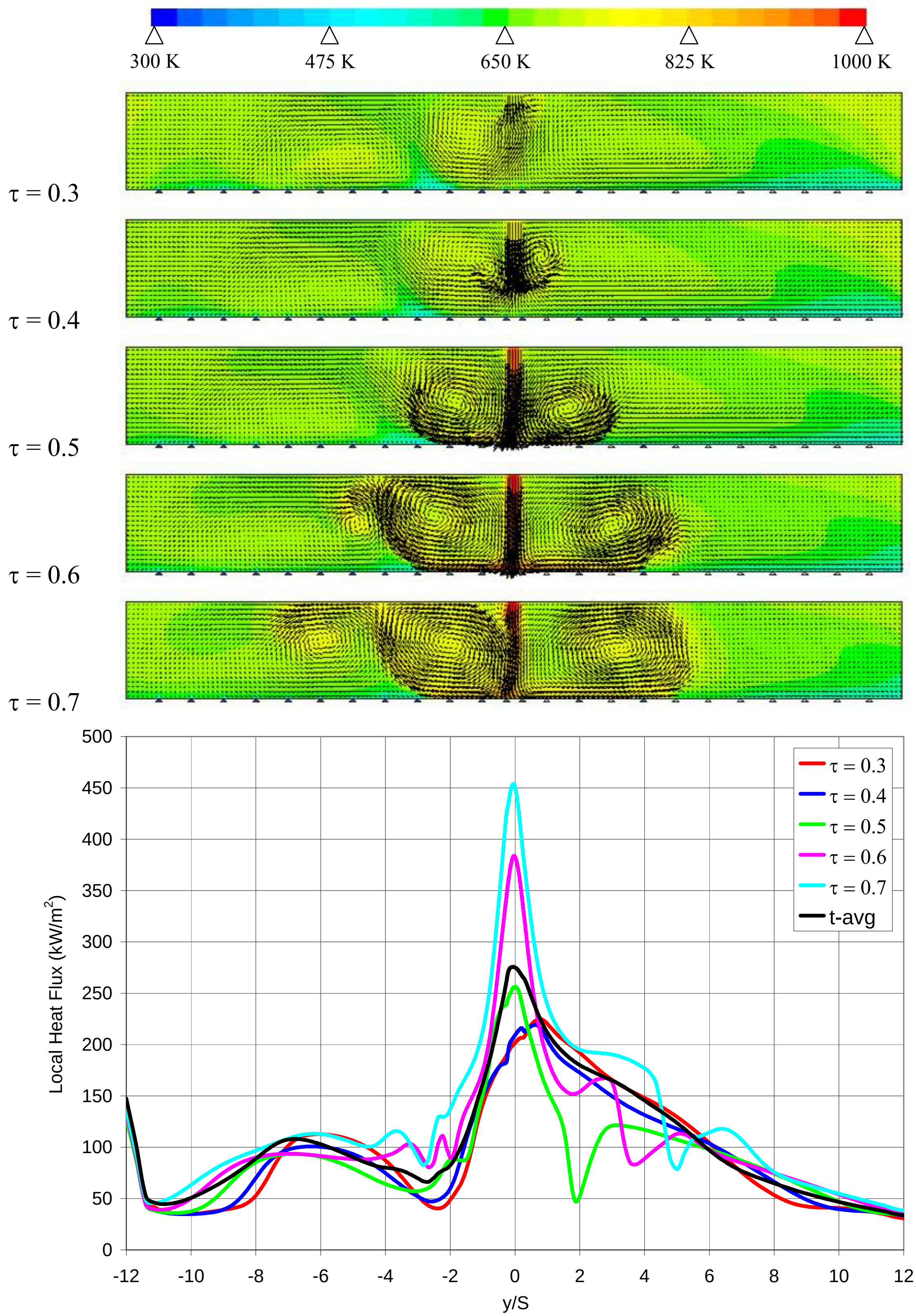

Figure 8.5: Velocity vectors/temperature contours and local heat flux profiles during positive cycle of jet oscillation for the base case with a moving surface.

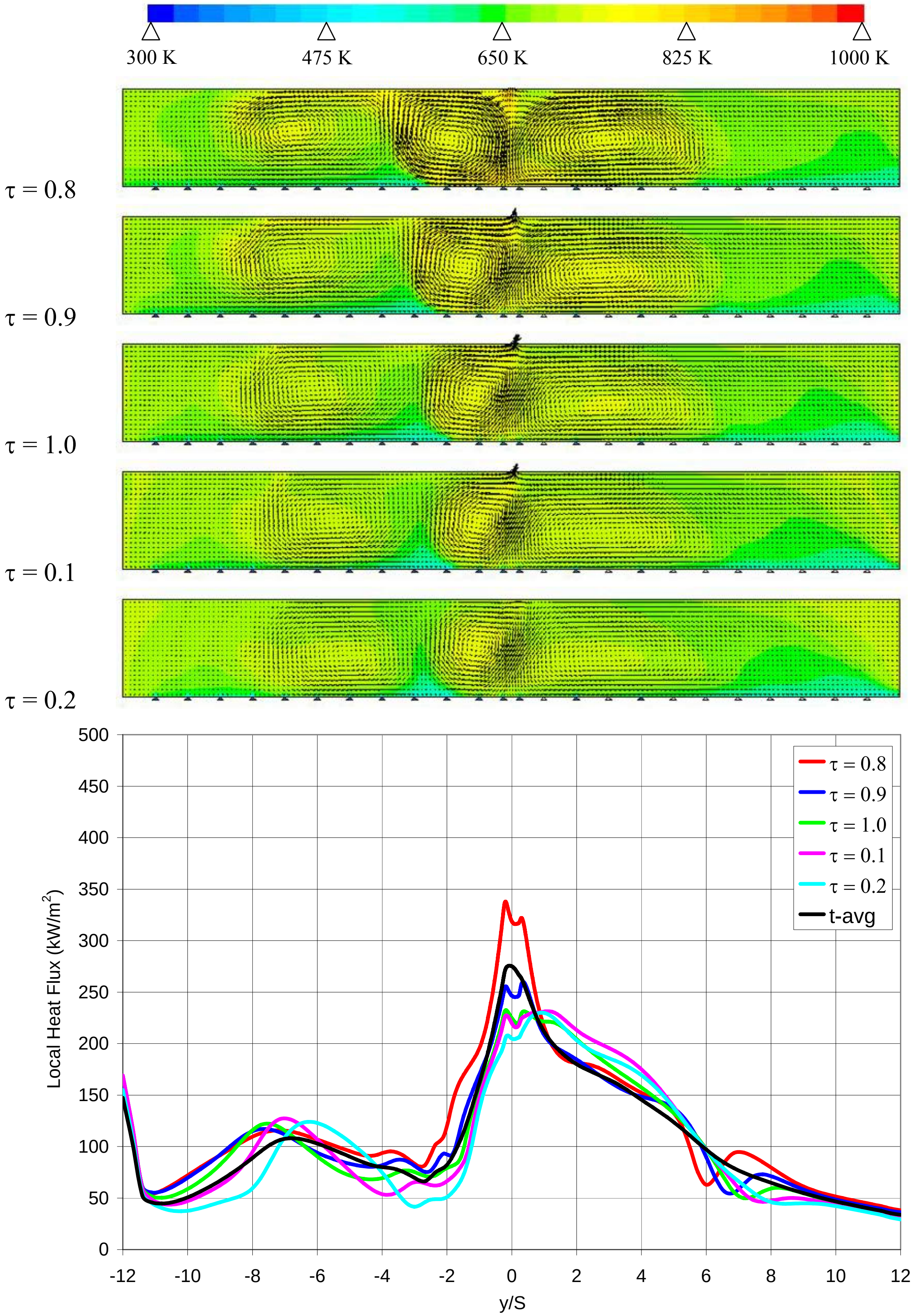

Figure 8.6: Velocity vectors/temperature contours and local heat flux profiles during negative cycle of jet oscillation for the base case with a moving surface.

8.3 Effects of Jet Velocity Ratio

The pulsating jet in the previous section had a velocity ratio of 4.3, which is about the same as the velocity ratio of the base case in the previous chapter. This section presents and discusses the effects of jet velocity ratio on flows and heat transfer characteristics of pulsating jets impinging on the moving surface with u_s = 30 m/s. The velocity ratio was varied by changing the amplitude ratio of inlet mass flow rate oscillation. The resulting velocity ratios at the tailpipe exit were slightly lower than those for the case with the stationary surface and even lower with a higher surface velocity, because the pulsating flows were no longer perfectly symmetric. The amount of fluids exiting and entering the tailpipe from either side of the center was not balanced because the pressure caused by re-circulating flows in the impingement zone was different to the left and the right sides of the jet centerline. As with all simulation cases in previous chapters, a grid independence study was performed for every case in this chapter.

Figure 8.7 shows time-averaged profiles of local heat flux for different velocity ratios, whereas Figure 8.8 shows instantaneous velocity vectors at the beginning of the negative cycle for corresponding velocity ratios. In terms of the magnitude of heat fluxes, there is a noticeable gap between the cases with $\varepsilon = 1.7$ and 2.6. For the pulsating jets with $\varepsilon \leq 1.7$, heat fluxes at the jet centerline were slightly lower than that from the steady jet because there was no heat transfer provided from vortices during the negative cycle. As shown in Figure 8.8, the vortices for these cases were dragged farther away from the jet centerline by the moving surface. The strength of these vortices increased with increasing velocity ratio. At $\varepsilon = 1.7$, the vortices were strong enough to help increase local heat fluxes at $2 \leq y/S \leq 5$, the region through which the vortices swept.

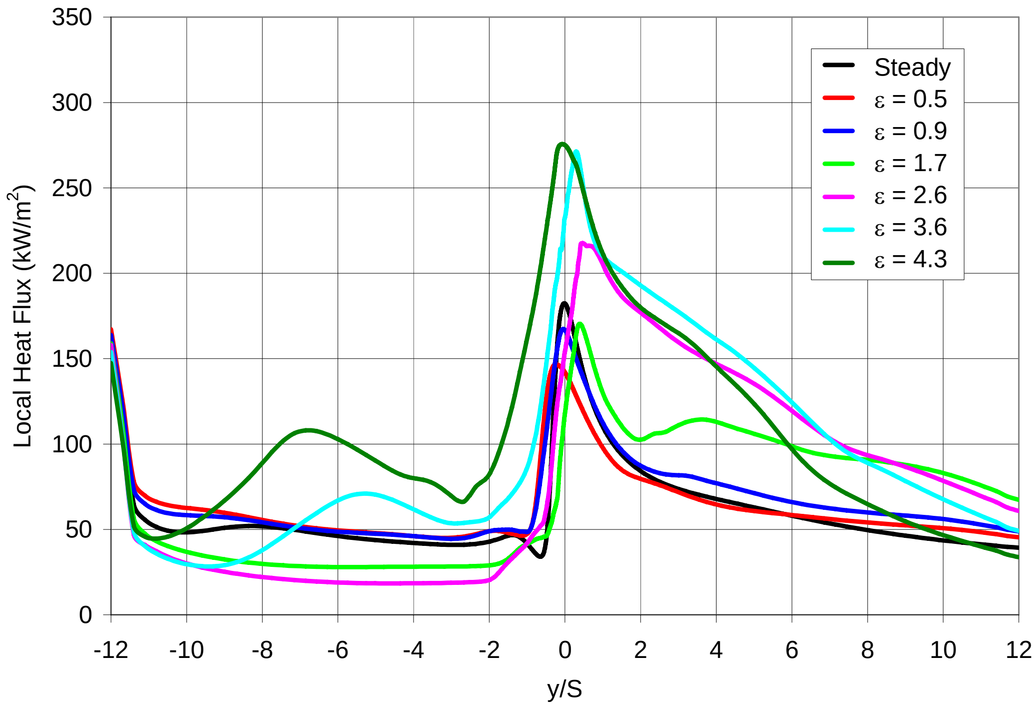

Figure 8.7: Time-averaged profiles of local heat fluxes from different velocity ratios with u_s = 30 m/s.

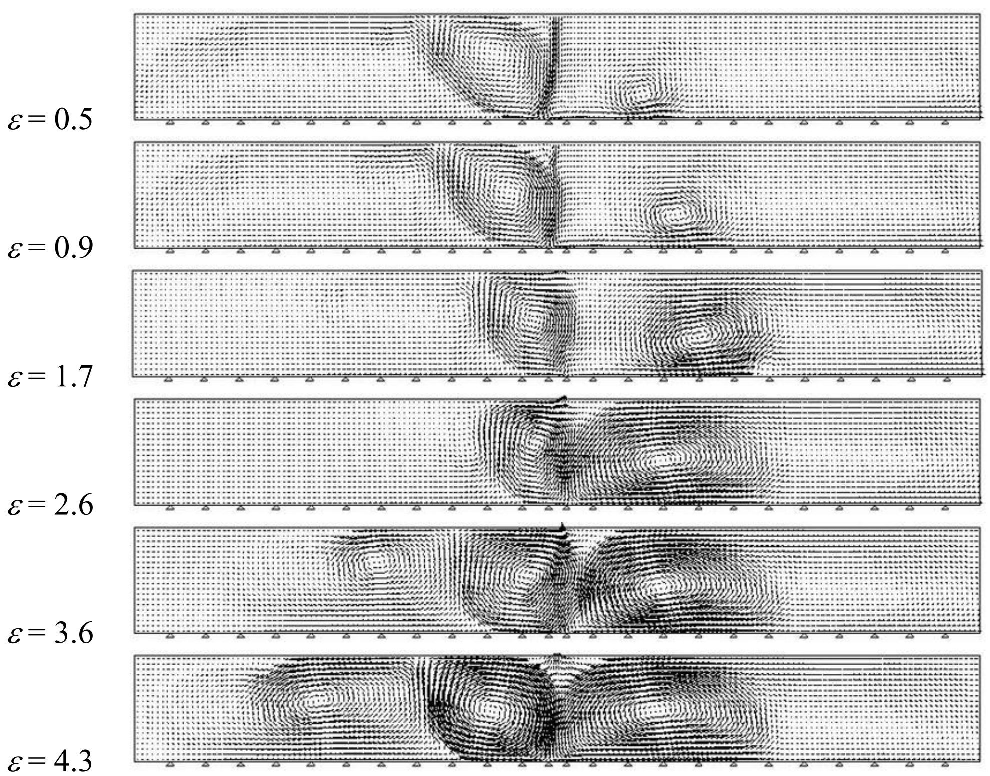

Figure 8.8: Velocity vectors at the beginning of negative cycle from different velocity ratios with u_s = 30 m/s.

As the velocity ratio increased further, the impinging jet and the vortices were stronger and became large re-circulating flows on the right side of the jet centerline, resulting in significant increases in heat flux. For the left side, the velocity ratio of the impinging jet had to be high enough, i.e., $\varepsilon = 3.6$ & 4.3, to overcome the counter-flow surface velocity and cause secondary re-circulating flows, as shown in Figure 8.8, providing significant heat transfer to the impingement surface. With these high velocity ratios, heat transfer enhancement factors over the reference distance were about the same as those for the case with a stationary surface as shown in Figure 8.9.

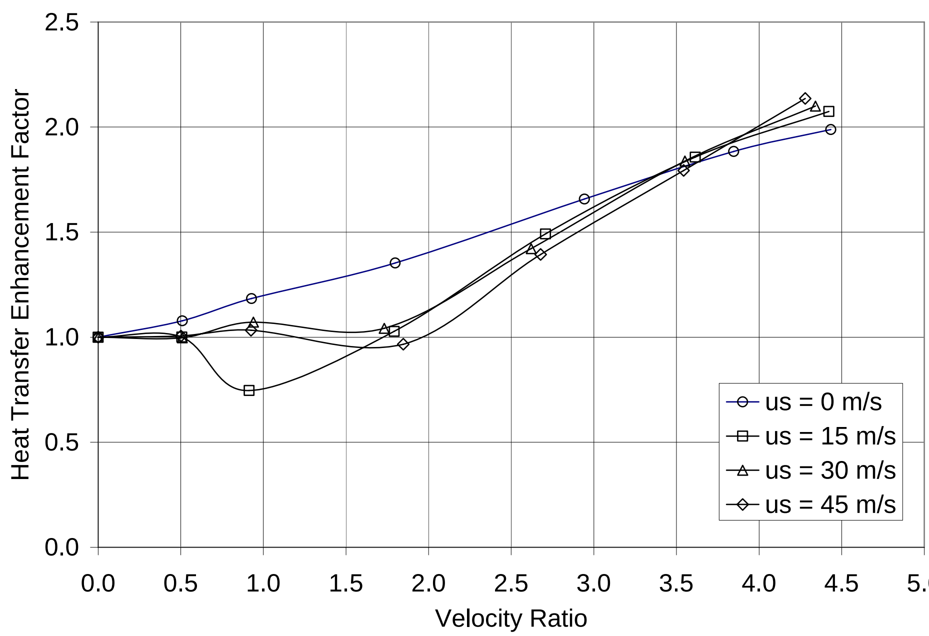

Figure 8.9: Heat transfer enhancement factors based on area-averaged heat fluxes over $-2.8 \leq y/S \leq 2.8$ from different surface velocities.

Figure 8.9 also includes enhancement factors from the cases with different surface velocities. The enhancement factors are based on the area-averaged heat flux from steady jet impingement with the same surface velocity for each respective case. The reference area or distance was $-2.8 \leq y/S \leq 2.8$. An obvious pattern of these plots is that while heat transfer on the stationary surface typically increases in a linear relationship with the velocity ratio, heat transfer on the moving surface requires relatively high velocity ratios to have significant enhancement, i.e., the velocity ratio has to be higher than 2.0. At the velocity ratio higher than 3.5, the enhancement factors are about the same and are almost independent of the surface velocity. However, it should be noted that net heat flux over the same area decreased with increasing surface velocity for impinging jets with the same velocity ratios, as shown later in Figure 8.10. Another interesting point in Figure 8.9 is that the enhancement factor is less than one for the case with $\varepsilon = 0.9$ and $u_s = 15$ m/s. This is because the location where the pulsating jet impinges onto the surface shifted to the right side, away from the centerline, as discussed in the following section.

8.4 Effects of Surface Velocity

This section discusses in more detail the combined effects of surface velocity and jet velocity ratio on the characteristics of re-circulating flows and surface heat transfer. Figure 8.10 shows the same data as Figure 8.9, but in terms of net area-averaged heat fluxes over the reference distance. In general, heat fluxes decreased with increasing surface velocity for the same jet velocity ratios, with the exception for the case with $\varepsilon =$ 0.9 and $u_s = 15$ m/s, which will be discussed later. Figure 8.11 shows the area-averaged heat fluxes over the reference distance on the left and right sides of the jet centerline separately. The effects of surface velocity on the magnitude of heat fluxes were not consistent for different velocity ratios. Rather, the magnitude of heat fluxes corresponded to the characteristics of the vortices or re-circulating flows in each respective case (Figure 8.12).

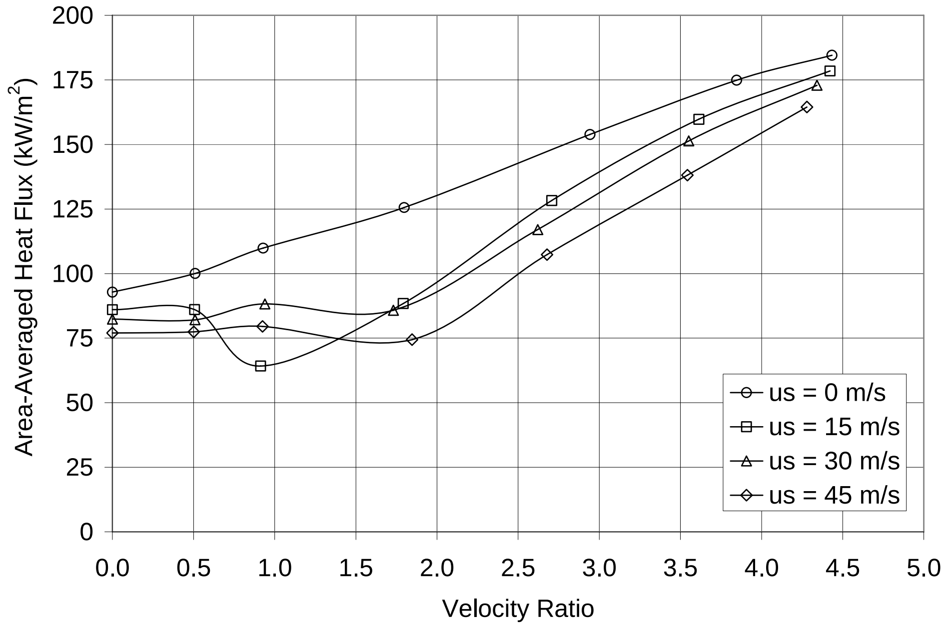

Figure 8.10: Area-averaged heat fluxes over -2.8 ≤ y/S ≤ 2.8 from different surface velocities.

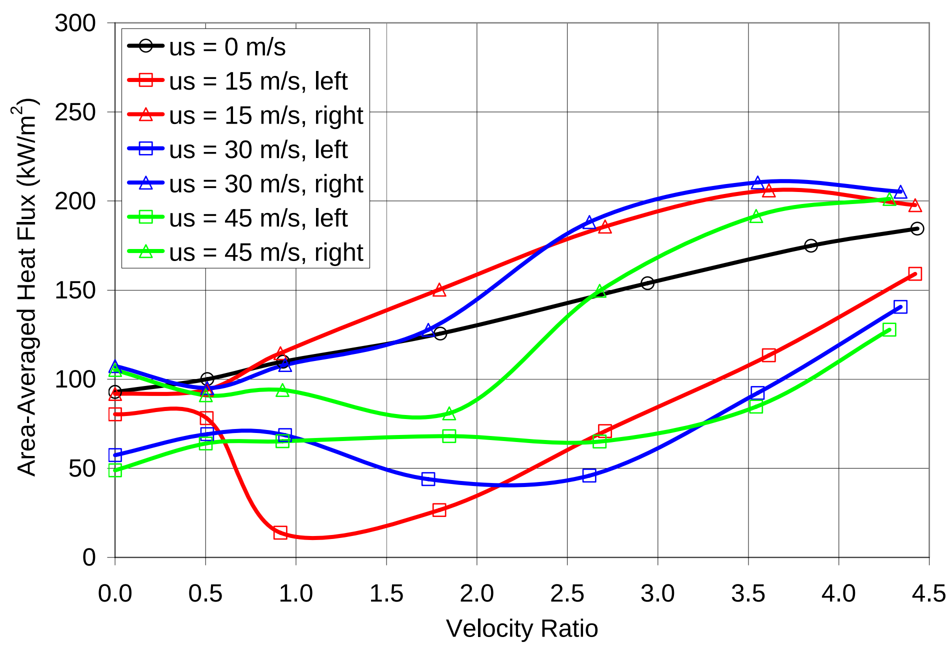

Figure 8.11: Area-averaged heat fluxes on either side of the tailpipe centerline from different surface velocities: left = over -2.8 ≤ y/S ≤ 0 and right = 0 ≤ y/S ≤ 2.8.

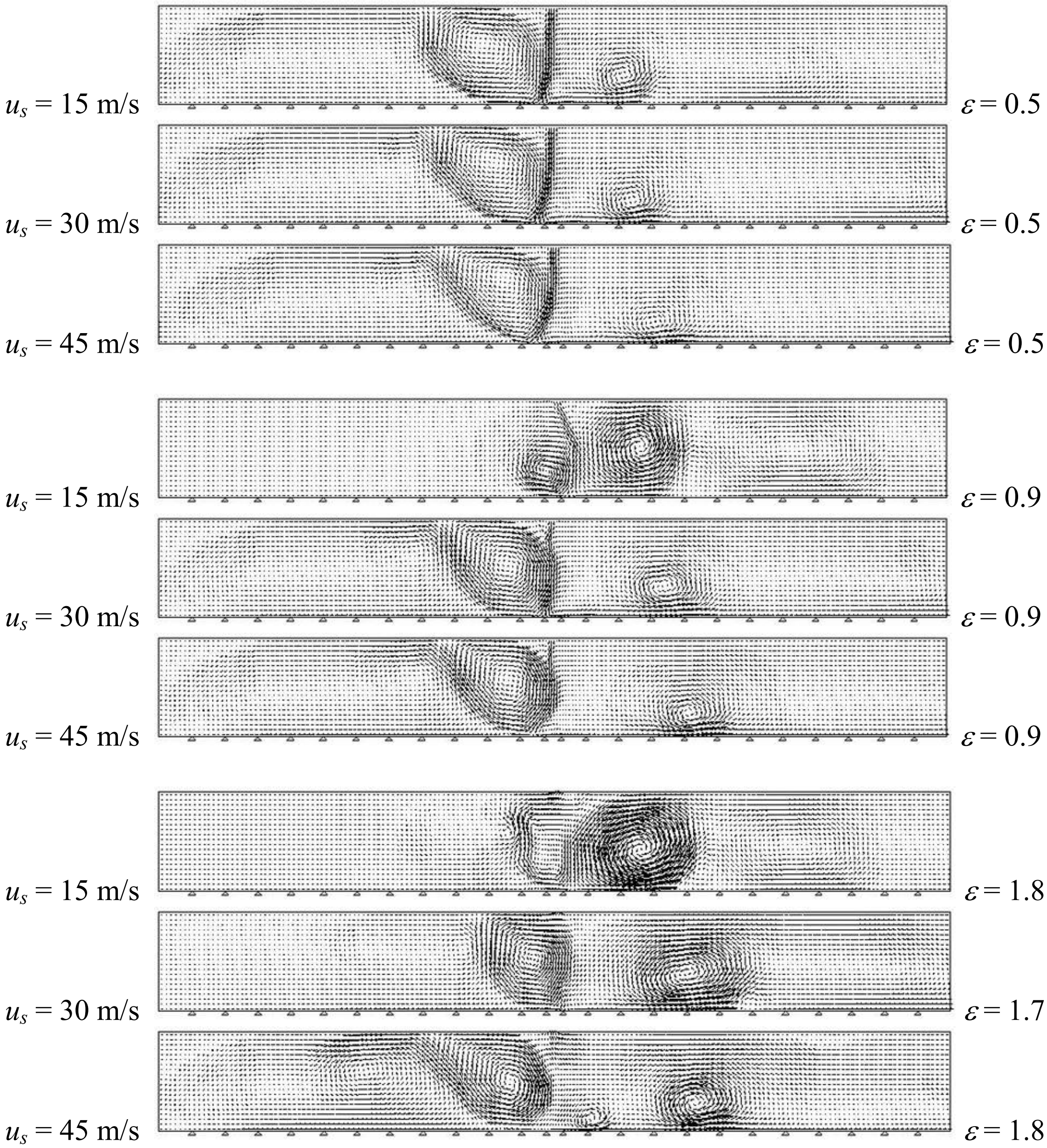

Figure 8.12: Instantaneous velocity vectors at the beginning of negative cycle from different surface velocities and jet velocity ratios.

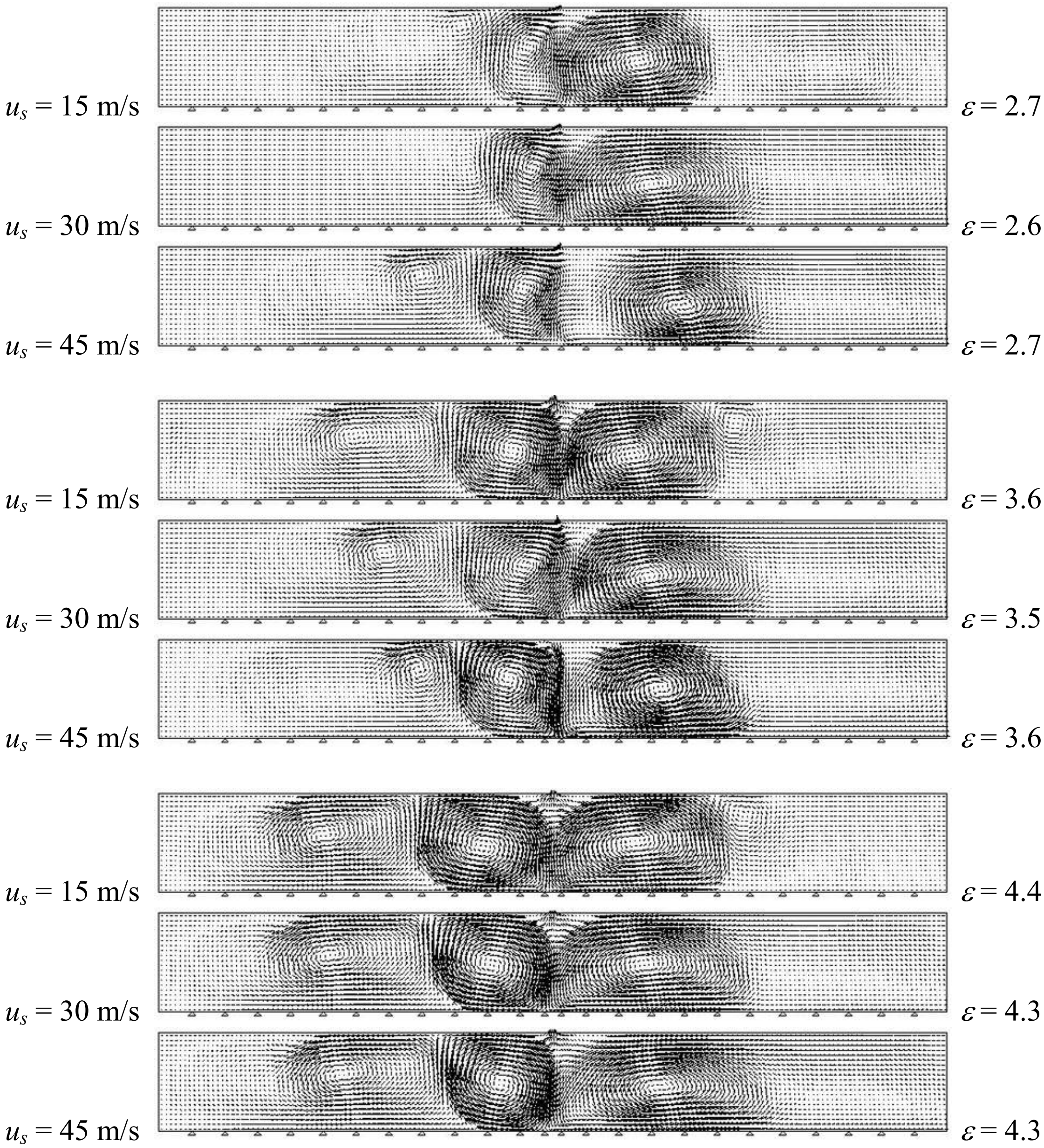

Figure 8.12 (continued)

The plots of heat fluxes on both sides of the jet centerline in Figure 8.11 corresponded to the characteristics of the vortices in each respective case. Figure 8.12 shows instantaneous velocity vectors at the beginning of the negative cycle at different surface velocities for each jet velocity ratio. These flow characteristics were the result of the interactions between the impinging jet velocity and the surface velocity. With $\varepsilon = 0.5$, the surface velocity dominated the flow fields. Vortices could not develop into large re-circulating flows because the moving surface dragged the vortices on the right side away from the impinging jet. The vortices became smaller and weaker as the surface velocity increased. With $\varepsilon = 0.9$, the impinging jet was stronger and the wall jet could flow farther away from the centerline. The vortices were also stronger but still not quite large enough to overcome high surface velocities. However, at u_s = 15 m/s, the vortices became large re-circulating flows that created negative pressure near the tailpipe exit. The large pressure difference in the impingement zone between the left and right sides of the tailpipe caused the exiting jet to impinge onto the right side of the centerline. This is the reason why the heat flux on the left side was very low for this case.

As the velocity ratio increased with the same surface velocity, the re-circulating flows became larger and stronger. For the same velocity ratio, a higher surface velocity resulted in smaller re-circulating flows on both sides of the centerline. The locations of re-circulating flows were also affected by the moving surface. With a higher surface velocity, the re-circulating flows on the right side were farther away from the centerline whereas the position of flow separation on the left side was closer to the centerline. In other words, the moving surface shifted flow characteristics along in the direction of the surface velocity. However, when the jet velocity ratio was high enough, the effects of surface velocity were less prominent.

For comparison to the case with u_s = 30 m/s and Figure 8.7, the time-averaged profiles of local heat fluxes at different velocity ratios are shown in Figures 8.13 and 8.14 for the cases with u_s = 45 and 15 m/s, respectively. An interesting pattern for the cases with u_s = 45 m/s is that there is secondary peak on the right side at $\varepsilon = 2.7$ and 3.5. This is caused by the re-circulating flows on the right side which were relatively strong but still slightly farther away from the centerline, as shown in Figure 8.12. Such a pattern is still noticeable at $\varepsilon = 4.3$ although the re-circulating flows were closer to the centerline. The secondary peak on the left side caused by secondary re-circulating flows was very small with $\varepsilon = 2.7$ and 3.5 and became much larger with $\varepsilon = 4.3$. If the surface velocity was lower, the secondary re-circulating flows could develop at lower jet velocity ratios.

The time-averaged profiles of local heat fluxes for the cases with u_s = 15 m/s are quite different from those with u_s = 30 and 45 m/s. The most interesting pattern is the case with $\varepsilon = 0.9$ in which the peak of the profiles is located at $y/S = 2$, instead of near the centerline. As discussed earlier, this is because strong negative pressure caused by re-circulating flows forced the pulsating jet to impinge to the right side of the centerline as shown in Figure 8.15, which also shows the pressure contours for the cases with u_s = 30 and 45 m/s for comparison. The position shift of the peak did not occur for the cases with u_s = 30 and 45 m/s and $\varepsilon = 0.9$ because the re-circulating flows on the right side were still small and farther away from the center.

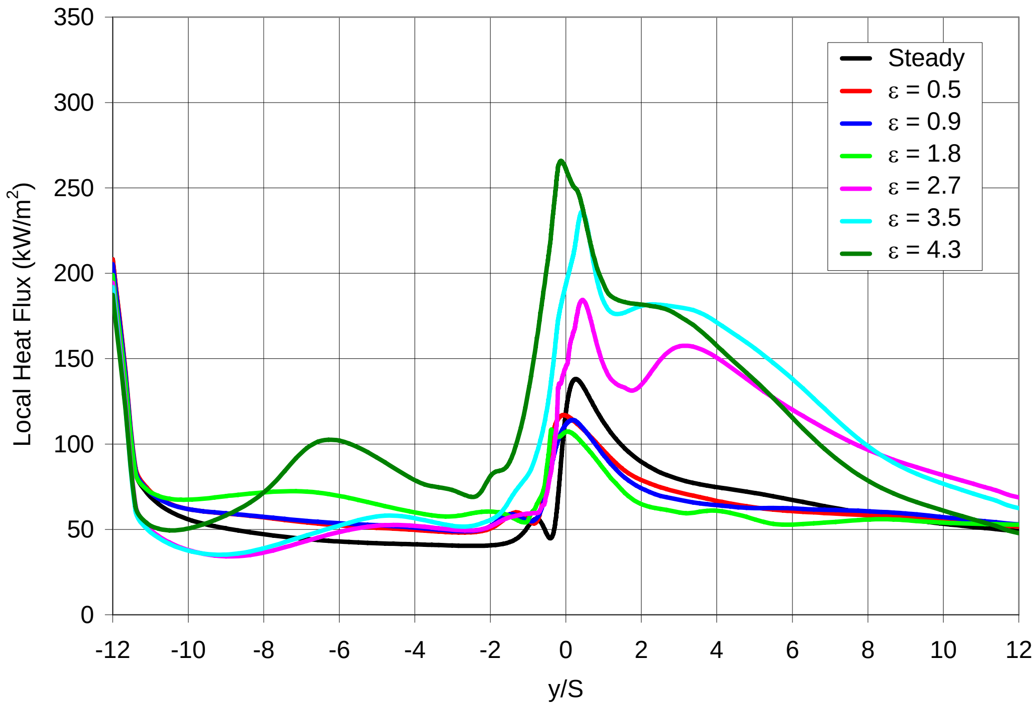

Figure 8.13: Time-averaged profiles of local heat fluxes from different velocity ratios with u_s = 45 m/s.

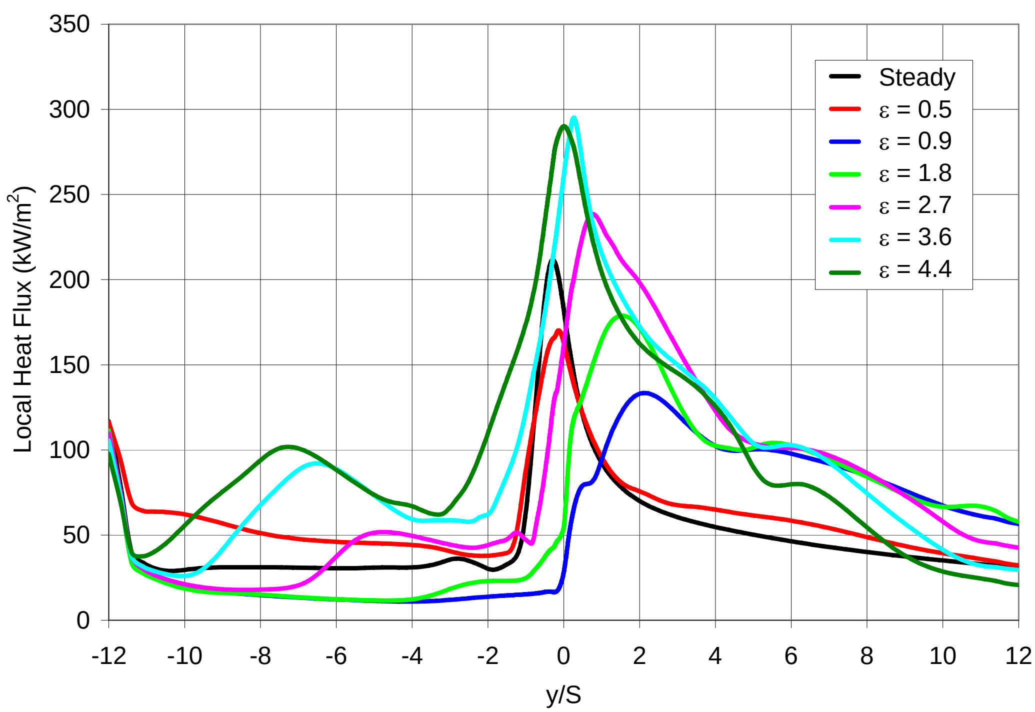

Figure 8.14: Time-averaged profiles of local heat fluxes from different velocity ratios with u_s = 15 m/s.

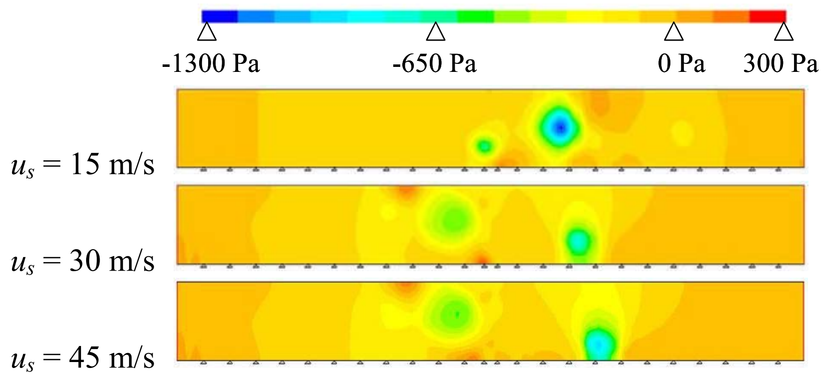

Figure 8.15: Instantaneous pressure contours at the beginning of negative cycle from different surface velocities with $\varepsilon = 0.9$.

As the velocity ratio increased ($\varepsilon = 1.8$ and 2.7), the location onto which the pulsating jet impinged (and the peak of the profiles) was closer to the center. The same driving force, i.e., pressure difference between the right and the left side in the impingement zone, determined the location for each case. Since re-circulating flows caused negative pressure, the stronger the re-circulating flows were, the stronger was the negative pressure. As the velocity ratio increased, the re-circulating flows on the left side became stronger, causing stronger negative pressure and less pressure difference between two sides of the centerline. At high jet velocity ratios, $\varepsilon = 3.6$ and 4.4, the patterns of the local heat flux profiles and the characteristics of vortices were similar to those with u_s = 30 m/s.

8.5 Summary

A general trend of the effects of surface velocity was that the magnitude of heat fluxes decreased with increasing surface velocity for the same jet velocity ratios. However, flow characteristics of pulsating jet impingement on the moving surface were quite different from those on a stationary surface. The main effect of the moving surface was that re-circulating flows on both sides of the centerline were dragged or shifted in the direction of the surface velocity. The profiles of local heat fluxes corresponded to the characteristics of re-circulating flows, which depended on the combined effects of surface and jet velocities. The interactions between the jet velocity and the surface velocity depended on the magnitude of both velocities. For the range of parameters considered here, the surface velocity dominated flow and heat transfer characteristics at relatively low velocity ratios, i.e., $\varepsilon = 0.5\text{-}1.7$. There was no significant heat transfer enhancement for these cases. However, at a practical and relatively high value of jet velocity ratio, $\varepsilon = 4.3$, the pulsating jet could still develop strong re-circulating flows even with a high surface velocity. The enhancement factors of area-averaged heat fluxes over the reference distance on both sides of the jet centerline for those cases were as high as the case with a stationary surface (about 2.0). The magnitude of heat fluxes on the left side of the jet centerline (or the upstream side relative to the moving surface) was lower than those on the right side because the moving surface pushed the re-circulating flows on the left side against the impinging jet but dragged the re-circulating flows along on the right side, resulting in smaller re-circulating flows on the left side than those on the right side.

CHAPTER 9

CONCLUSIONS

The results of the numerical studies and simulations can be summarized as two major contributions of the research. The first one is the strategy for pulse combustor design from the parameter studies with the simplified model of Helmholtz pulse combustors, which can be used as a guideline to generate a pulsating jet with a high velocity ratio at the tailpipe exit of a Helmholtz pulse combustor. The other main contribution is identification of the significance of strong re-circulating flows in impingement zones, which continue to provide heat transfer to the surface during the negative cycle of jet oscillation, resulting in considerable heat transfer enhancement as compared to corresponding steady jet impingement.

As shown by the simulation results, a key parameter for generating strong re-circulating flows is jet velocity ratio, which has to be at least 3.0 for the cases with single slot nozzles considered in this dissertation. As for the pulsating jets with round nozzles, the jet velocity ratio may need to be significantly greater than 3.0 to be able to create strong re-circulating flows in the impingement zone. Therefore, it is important to be able to generate a pulsating jet with the highest velocity ratio possible. From the parameter studies of the simplified model of Helmholtz pulse combustors, the strategy for pulse combustor design can be concluded by two requirements: one for the operating condition and the other for the dimensions of the pulse combustor. For the operating condition, it is recommended to have the highest temperature possible in the combustion chamber, which can be achieved by using the equivalence ratio of 1.0 or the stoichiometric ratio of fuel and air. As for the dimensions of the pulse combustor, it is recommended to have the smallest volume ratio possible (as long as the Rayleigh criterion can be satisfied), which can be managed by using a small combustion chamber or a long tailpipe or a combination of both. However, the pulsation frequency is also affected by a dimension change. Basically, if the overall dimension of the pulse combustor is smaller (shorter tailpipe or smaller combustion chamber), the pulsation frequency is higher, and vice versa. The effects on frequency can also play a role in pulse combustor design. For example, if it is required that the fluctuation of surface heat flux be small, the pulsation frequency should be higher. In this case, the volume ratio should be decreased by using a smaller combustion chamber.

From the literature review, strong re-circulating flows as those from the simulation results in this dissertation have not been reported in other types of pulsating jets. The significance of this characteristic is that, during the negative cycle when flow reversal occurs in the tailpipe, the strong re-circulating flow continues to provide heat transfer to the impingement surface, in addition to the high-velocity jet impingement during the positive cycle. As mentioned earlier, it appears that strong re-circulating flows can be created more easily by a pulsating jet from a slot nozzle (with a lower velocity ratio) than by that from a round nozzle because the magnitude of velocity of a plane-symmetric wall jet does not decrease as rapidly as that of an axisymmetric wall jet. Thus, slot nozzles appear to be more suitable for the PAD technology than round nozzles. As for the size of nozzles, based on the cases studied here, smaller nozzles are more effective than larger nozzles in terms of overall energy efficiency and heat transfer enhancement.

For practical implementation, the evaluation of heat transfer enhancement and energy saving factors based on the simulations results from single nozzles demonstrates a potential for the success of the PAD technology. The observed maximum enhancement and energy saving factors (1.8 and 3.0, respectively) are very encouraging for further development. It can be expected that if the jet velocity ratio is higher than the typical value considered here ($\varepsilon = 4.4$), the benefits from pulse-combustor jet impingement can be even greater. However, as a cautionary note, because several simplifying assumptions were applied with the numerical studies and simulations in this dissertation, these numerical results and conclusions need to be verified with laboratory experiments for further fundamental studies and practical development of the PAD technology.

CHAPTER 10

RECOMMENDATIONS FOR FUTURE WORK

Since the present work is an early phase of the PAD project, in which the ultimate goal is to develop a commercial-scale pulsating-jet impingement drying hood, there is obviously a great deal of work still to be done to accomplish that goal. Typical intermediate steps are successful demonstrations of the PAD technology to show it can significantly improve heat transfer/drying rate and/or energy efficiency with a laboratory-scale system and a pilot machine. Even with the laboratory scale, there is still a gap between the present work and the operating PAD system, in which the minimum requirement is an optimum condition of impingement geometry for an array of nozzles, for maximum heat transfer from pulsating jets. This chapter discusses needed next steps or plans for laboratory and numerical experiments aiming toward a successful demonstration of the laboratory-scale PAD system.

Basically, the next steps are a typical collaboration between laboratory and numerical experiments. First, measured data from laboratory experiments with at least one condition of multiple-nozzle pulsating jet impingement are required for the validation of simulation results. Then, CFD simulations should be performed to find an optimum condition of impingement geometry for maximum heat transfer from pulsating jets. Finally, laboratory experiments should be conducted to confirm the simulation results and evaluate the performance of the system. However, an initial task before all those steps is to confirm some of the simulation results from the present work, especially the difference between the performance of pulsating jets from a slot tailpipe and a round tailpipe. Meanwhile, the next cases for simulation work should be ones with multiple nozzles having the optimum conditions specified in Section 7.3 in order to confirm or re-evaluate the heat transfer enhancement and energy saving factors.

The first two parameters to be determined are the nozzle-to-surface spacing and the (hydraulic) diameter of the pulse combustor tailpipe. For the purpose of practical applications, the nozzle-to-surface spacing should be in the range of those in an impingement hood, i.e., 25-30 mm. This parameter should be the same for all conditions of the experiments. For the selection of tailpipe hydraulic diameter, it should be noted that the comparison between the PAD and conventional impingement systems should be for the optimum condition of each system, which is not necessarily the same. For steady jet impingement, the optimum condition for maximum heat transfer is H/S or $H/D \sim 5$. From the simulation results, however, the better performances from pulsating jets were also obtained at similar conditions, i.e., $H/S = 4$ and 5. Thus, for convenience and as an initial condition, the hydraulic diameters of round and slot tailpipes could be the same as those from steady jet impingement, i.e., H/S or $H/D \sim 5$. And, for the validation purpose of the simulation results in previous chapters, these parameters can be $H = 30$ mm and S or $D = 6$ mm. The aspect ratio of the slot tailpipe (length/width of cross-sectional area) should be large enough, at least 20, to ensure two-dimensional flows near the center of the tailpipe.

The next step for the laboratory experiment is to generate a pulsating jet with a high velocity ratio. The best case scenario is to generate a pulsating jet having the same condition as that in the numerical experiment, for validation purposes. However, if this is not practical, the most important condition is that the jet velocity ratio is as high as possible, or at least 4.0. Although the impingement condition would be multiple nozzles, several pulse combustors with single tailpipes could be used for the laboratory experiment. The parameter studies with the simplified model suggested that the pulse combustors should have small volume ratios and high temperature in the combustion chambers. However, a more challenging aspect is to operate a pulse combustor with high pressure amplitude while having a stable oscillation, meaning the oscillations of heat release and pressure must be substantially in-phase. The design of combustion chamber geometry to achieve this criterion is beyond the scope of the present work. Nevertheless, from the literature review, a simple technique is to use an adjustable stagnation plate such that the mixing rates between fresh reactants and remaining hot gas can be manipulated.

The combination of the adjustments of this plate and the supply pressure of the reactants should be able to allow the pulse combustors to operate with stable oscillations within a certain range of operating conditions.

The next step is to evaluate the performances of pulsating jets from a round tailpipe and a slot tailpipe in order to determine which type of tailpipe is more effective in terms of heat transfer enhancement. Ideally, this should be done with the optimum conditions of multiple-nozzle jet impingement geometry at equivalent net mean mass flow rate or energy rate per unit area and comparing net area-averaged heat fluxes. At this stage, however, preliminary assessment with single tailpipes should be adequate for the purpose of the laboratory-scale demonstration. And for a fair assessment, the comparison should be based on heat transfer enhancement factors relative to a corresponding steady jet for each type of tailpipe. This step is also to confirm a finding from the simulation results which showed that the pulsating slot jet yielded a higher enhancement factor that the pulsating round jet due to the effects of strong re-circulating flows.

Assuming that the pulsating jet from the slot tailpipe is more effective, the next step is a laboratory experiment with multiple nozzles to provide heat flux data as a validation case for the numerical simulation. This should be done for both steady and pulsating jet impingement. The number of nozzles should be at least three. The nozzle-to-nozzle spacing for both steady and pulsating jets can be initially set at the optimum distance from the Martin correlation for an array of slot nozzles, as described in Section 6.1. The number of heat flux data points should be enough to establish time-averaged profiles of local heat flux for both cases. As for a simple and cost-effective alternative for heat flux measurement, the technique used in the reference publication of the pulsating jet impingement heat transfer experiment at Sandia National Laboratories can be applied. This technique simply assumed the time-averaged heat flux from the pulsating jet as a steady heat flux which could be calculated back from a historical trend of surface temperature using a semi-infinite solid heat transfer equation. However, the accuracy of this technique should be evaluated as well.

The purpose of the laboratory experiment described above is to provide the conditions of pulsating and steady jets and impingement geometry and heat flux data as a validation case for numerical simulations. The computational domain for multiple-nozzle jet impingement can have an inlet chamber and a tailpipe for each nozzle. The numerical procedure and boundary conditions used in this dissertation should be effective. As for the turbulence model, if, for some reason, predictions from the V2F turbulence model are not consistent with the measured data, an alternative is the low-Re version of SST k-ω model which is also available in the simulation software FLUENT.

If the simulation results of the validation case are satisfying, the numerical experiment can be set up with one parameter left to be varied, i.e., nozzle-to-nozzle spacing. As with the manipulation of heat flux data in Section 7.3, the numerical experiment can have two separate goals for pulsating jet impingement: the optimum spacing for maximum heat transfer and the spacing for the same level of heat transfer as steady jet impingement heat transfer. The optimization process or the target search for these goals has to be done manually. In fact, this step can also be done with the laboratory experiment, if necessary resources are available. In any case, the simulations are still required because the characteristics of pulsating flows and heat transfer can be studied in detail, such as the interactions between pulsating jets and re-circulating flows. After the goals are achieved, maximum heat transfer enhancement and energy saving factors can be evaluated.

The final step for this phase of the PAD project is to validate or confirm the simulation results by performing sensitivity studies of the nozzle-to-nozzle spacing around those two conditions in the laboratory experiment. From the simulation results in Section 7.3, the enhancement and energy saving factors (1.8 and 3.0, respectively) were very impressive, especially the energy saving factor. Thus, the final results from the laboratory experiment can be expected to be encouraging and realistic enough for the project to move on to the next phase toward the ultimate goal.

APPENDIX

DERIVATION OF TAILPIPE VELOCITY AMPLIUTDE

The derivation for the solutions of pressure and velocity amplitude along the tailpipe length (Equations (4.17) and (4.18)) in Ahrens (1979), as well as the discussion about the limiting cases of frequency described in this Appendix, is provided by Professor Ahrens. The underlying assumptions in the linear acoustic theory are that the rest state of fluid has zero velocity with constant pressure and speed of sound corresponding to the rest-state temperature and that the changes in pressure and density are very small compared the rest-state values. Therefore, the conservation equations of mass and momentum and the equation of state for an ideal gas can be linearized with the values in the rest state. Then those three linearized equations can be combined to obtain the linear wave equations of pressure change, p_f, velocity change, u_f, and velocity potential, ϕ, as follows.

$$\frac{\partial^2 p_f}{\partial t^2} = c_0^2 \frac{\partial^2 p_f}{\partial x^2} \tag{A.1}$$

$$\frac{\partial^2 \phi}{\partial t^2} = c_0^2 \frac{\partial^2 \phi}{\partial x^2} \tag{A.2}$$

$$p_f = -\rho_0 \frac{\partial \phi}{\partial t} \tag{A.3}$$

$$u_f = \frac{\partial \phi}{\partial x} \tag{A.4}$$

where $p_f = p\text{-}p_a$, $u_f = u\text{-}u_0 = u$, $p_f << p_a$, $u << c_0$, and p_a, u_0, and c_0, are pressure, velocity, and speed of sound of the rest state ($u_0 = 0$), respectively.

The boundary condition at the exit of the tailpipe ($x = L$) is a pressure node:

$$p_f(L,t) = 0\,.$$

The boundary condition at the inlet of the tailpipe ($x = 0$) is the conservation of mass in the combustion chamber, assuming an isentropic process of an ideal gas:

$$\frac{V_C}{c_0^2}\frac{dp_f(0,t)}{dt} = -\rho_0 A_T u_f(0,t).$$

where V_C is the volume of the combustion chamber and A_T is the cross-sectional area of the tailpipe. Using the dimensionless parameters, $\tau = \frac{c_0 t}{L}$ and $\xi = \frac{x}{L}$, Equation (A.2) becomes

$$\frac{\partial^2 \phi}{\partial \tau^2} = \frac{\partial^2 \phi}{\partial \xi^2}$$

For a periodic solution, it can be assumed that

$$\phi = \Phi(\xi)\cos(\varpi\tau)$$

$$\varpi = \frac{\omega L}{c_0}$$

Hence, $$-\varpi^2\Phi(\xi) = \frac{\partial^2\Phi(\xi)}{\partial\xi^2}$$

in which a general solution is

$$\Phi(\xi) = A\cos(\varpi\xi) + B\sin(\varpi\xi)$$

With the boundary condition at the tailpipe exit, $\Phi(1) = 0$ (arbitrary constant),

$$A + B\tan\varpi = 0 \tag{A.5}$$

The boundary condition at the tailpipe inlet in the dimensionless form is

$$-\varpi^2\Phi(0) = \frac{1}{\beta}\frac{\partial\Phi(0)}{\partial\xi}$$

where $\beta = V_C/(A_T L)$ is the volume ratio of the Helmholtz pulse combustor. Thus,

$$A = -\frac{B}{\varpi\beta}. \tag{A.6}$$

From Equations (A.5) and (A.6),

$$\varpi\tan\varpi = \frac{1}{\beta} \tag{A.7}$$

$$\Phi(\xi) = B\left[\sin(\varpi\xi) - \tan\varpi\cos(\varpi\xi)\right]$$

$$\phi = B\left[\sin(\varpi\xi) - \tan\varpi\cos(\varpi\xi)\right]\cos(\varpi\tau)$$

From Equations (A.3) and (A.4),

$$p_f = -\frac{\rho_0 c_0 \overline{\omega}}{L} B\left[\sin(\overline{\omega}\xi) - \tan\overline{\omega}\cos(\overline{\omega}\xi)\right]\cos(\overline{\omega}\tau)$$

$$u_f = \frac{\overline{\omega}}{L} B\left[\cos(\overline{\omega}\xi) + \tan\overline{\omega}\sin(\overline{\omega}\xi)\right]\sin(\overline{\omega}\tau)$$

At $\xi = 0$ and $\tau = 0$, $$p_f = p_A = \frac{\rho_0 c_0 \overline{\omega}}{L} B \tan\overline{\omega}$$

where p_A is the pressure amplitude in the combustion chamber. Thus,

$$B = \frac{p_A L}{\rho_0 c_0 \overline{\omega} \tan\overline{\omega}}$$

Therefore, the final solutions are

$$p_f = p_A\left[\cos(\overline{\omega}\xi) - \frac{\sin(\overline{\omega}\xi)}{\tan\overline{\omega}}\right]\cos(\overline{\omega}\tau) \tag{A.8}$$

$$u_f = \frac{p_A}{\rho_0 c_0}\left[\frac{\cos(\overline{\omega}\xi)}{\tan\overline{\omega}} + \sin(\overline{\omega}\xi)\right]\sin(\overline{\omega}\tau) \tag{A.9}$$

These solutions, Equations (A.8) and (A.9), are equivalent to Equations (4.17) and (4.18) in Chapter 4, respectively.

From Equation (A.7), two limiting cases of the volume ratio, β, can be analyzed: $\beta \rightarrow 0$ and $\beta \rightarrow \infty$. The first case is a Schmidt or quarter-wave resonance tube. The second case is a Helmholtz resonator, where the flow in the tailpipe (neck) is usually assumed incompressible.

1. $\beta \rightarrow 0$: $\overline{\omega} \rightarrow \frac{\pi}{2}$ and $\tan\overline{\omega} \rightarrow \infty$

$$p_f = p_A \cos\left(\frac{\pi\xi}{2}\right)\cos\left(\frac{\pi\tau}{2}\right) = p_A \cos\left(\frac{2\pi x}{\lambda}\right)\cos\left(\frac{2\pi c_0 t}{\lambda}\right)$$

$$u_f = \frac{p_A}{\rho_0 c_0}\sin\left(\frac{\pi\xi}{2}\right)\sin\left(\frac{\pi\tau}{2}\right) = \frac{p_A}{\rho_0 c_0}\sin\left(\frac{2\pi x}{\lambda}\right)\sin\left(\frac{2\pi c_0 t}{\lambda}\right)$$

$$\lambda \equiv \frac{c_0}{f} = 4L$$

2. $\beta \rightarrow \infty$: $\tan\overline{\omega} \rightarrow \overline{\omega} \rightarrow \frac{1}{\sqrt{\beta}}$, $\sin(\overline{\omega}\xi) \rightarrow \overline{\omega}\xi$, $\cos(\overline{\omega}\xi) \rightarrow 1 - \frac{(\overline{\omega}\xi)^2}{2}$

$$\overline{\omega} \rightarrow \frac{\omega_s L}{c_0} = \overline{\omega}_s = \frac{1}{\sqrt{\beta}} \tag{A.10}$$

where ω_s is the radian frequency of a Helmholtz resonator:

$$\omega_s = c_0\sqrt{\frac{A_T}{V_C L}} = \frac{c_0}{L\sqrt{\beta}} \tag{A.11}$$

$$p_f = p_A(1-\xi)\cos\left(\frac{\omega_s L \tau}{c_0}\right) = p_A\left(1 - \frac{x}{L}\right)\cos(\omega_s t)$$

$$u_f = \frac{p_A}{\rho_0 c_0 \overline{\omega}}\sin(\overline{\omega}\tau) = \frac{p_A}{\rho_0 \omega_s L}\sin(\omega_s t) \tag{A.12}$$

Figure A.1 shows the relationship between the frequency and the volume ratio predicted by Equation (A.7) compared with the theory of a Helmholtz resonator, Equation (A.10). At a very large volume ratio, the frequencies from the two equations are very close. The difference becomes larger and larger when the volume ratio gets smaller and smaller. This is why Equation (A.7) is used for predicting the frequency in the simplified model in Chapter 4.

Similarly, the solution of acoustic model velocity amplitude and incompressible model velocity amplitude can be compared with each other for a wide range of the volume ratio. The acoustic model velocity amplitude at the tailpipe exit, $u_{A_{acoustic}}$, is calculated from Equation (4.28).

$$u_{A_{acoustic}} = \frac{p_A}{\rho_{Tm} c_{Tm} \sin\left(\frac{2\pi L}{\lambda}\right)} = \frac{p_A}{\rho_{Tm} c_{Tm} \sin\left(\frac{\omega L}{c_{Tm}}\right)} = \frac{p_A}{\rho_{Tm} c_{Tm} \sin(\overline{\omega})} \tag{A.13}$$

where $\overline{\omega}$ is calculated from Equation (A.7). The incompressible model velocity amplitude, which is constant along the tailpipe length, $u_{A_{incomp}}$, is calculated from Equation (A.12).

$$u_{A_{incomp}} = \frac{p_A}{\rho_{Tm}\omega_s L} = \frac{p_A}{\rho_{Tm}\left(\frac{\overline{\omega}_s c_{Tm}}{L}\right)L} = \frac{p_A}{\rho_{Tm} c_{Tm} \overline{\omega}_s} \tag{A.14}$$

where $\overline{\omega}_s$ is calculated from Equation (A.10). The comparison is done in terms of the ratio of the incompressible model velocity amplitude to the acoustic model velocity amplitude.

$$\frac{u_{A_{incomp}}}{u_{A_{acoustic}}} = \left(\frac{p_A}{\rho_{Tm} c_{Tm} \overline{\omega}_s}\right) \bigg/ \left(\frac{p_A}{\rho_{Tm} c_{Tm} \sin(\overline{\omega})}\right) = \frac{\sin(\overline{\omega})}{\overline{\omega}_s} \tag{A.15}$$

Figure A.2 shows the results calculated from Equation (A.15) at different volume ratios. These results suggest that the solution of velocity amplitude at the tailpipe exit from the Helmholtz resonator assumption used with the Helmholtz pulse combustor with a relatively small volume ratio is underpredicted. However, as with the frequency prediction, the difference between the two solutions becomes smaller when the volume ratio is larger.

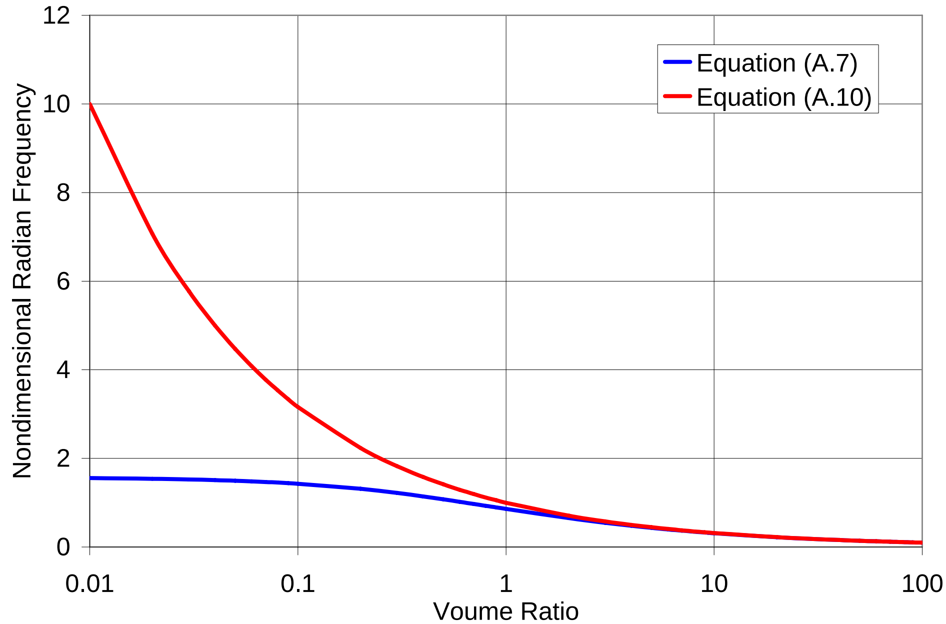

Figure A.1: Predictions of frequency for Helmholtz pulse combustor and Helmholtz resonator (Ahrens, 1979).

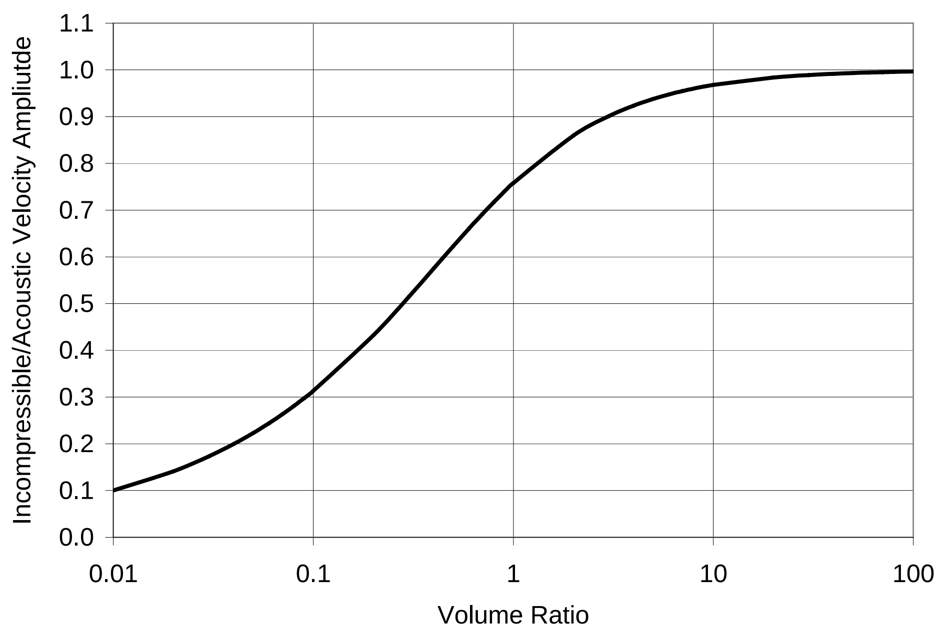

Figure A.2: Comparison between incompressible and acoustic model velocity amplitudes at tailpipe exit.

REFERENCES

2002 Manufacturing Energy Consumption Survey, Energy Information Administration, Department of Energy.

Ahrens, F. W., Kim, C., and Tam, S.-W. (1978). An analysis of the pulse combustion burner. *ASHRAE Transactions*, Vol. 84, Part I, pp. 488-507.

Ahrens, F. W. (1979). Prediction of heat transfer in pulse-combustion burners. In *Proceedings of the Symposium on Pulse Combustion Technology for Heating Applications*, Argonne, Illinois, pp. 46-66.

Angioletti, M., Di Tommaso, R.M., Nino, E., and Ruocco, G. (2003). Simultaneous visualization of flow field and evaluation of local heat transfer by transitional impinging jets. *International Journal of Heat and Mass Transfer*, Vol. 46, pp. 1703-1713.

Azevedo, L.F.A., Webb, B.W., and Queiroz, M. (1994). Pulsed air jet impingement heat transfer. *Experimental Thermal and Fluid Science*, Vol. 8, pp. 206-213.

Barr, P. K., Dwyer, H. A., and Bramlette, T. T. (1987). A one-dimensional model of a pulse combustor. In *Proceedings of the 1987 ASME-JSME Thermal Engineering Joint Conference*, Honolulu, Hawaii, pp. 283-290.

Barr, P.K. and Keller, J.O. (1990). Premixed combustion in an oscillating/resonant flow field part II: modeling the periodic reacting flow. *ASME Advanced Energy System Division*, Vol. 16, Thermal-Physical Aspects of Energy Conversion, pp. 23-39.

Barr, P.K., Keller, J.O., Bramlette, T.T., Westbrook, C.K., and Dec, J.E. (1990). Pulse combustor modeling: demonstration of the importance of characteristic times. *Combustion and Flame*, Vol. 82, pp. 252-269.

Behnia, M., Parneix, S., and Durbin, P.A. (1998). Prediction of heat transfer in an axisymmetric turbulent jet impinging on a flat plate. *International Journal of Heat and Mass Transfer*, Vol. 41, No. 12, pp. 1845-1855.

Behnia, M., Parneix, S., Shabany, Y., and Durbin, P.A. (1999). Numerical study of turbulent heat transfer in confined and unconfined impinging jets. *International Journal of Heat and Fluid Flow*, Vol. 20, pp. 1-9.

Bird, R.B., Stewart, W.E., and Lightfoot, E.N. (2002). *Transport Phenomena*, 2nd Edition, John Wiley & Sons, New York.

Bloom, F., Ahrens, F., and Patterson, T. (2007). Analysis of a nonlinear lumped parameter pulse combustor model. *Nonlinear Studies*, Vol. 14, No. 2, pp. 103-142.

Can, M., Etemoğlu, A.B., and Avci, A. (2002). Experimental study of convective heat transfer under arrays of impinging air jets from slots and circular holes. *Heat and Mass Transfer*, Vol. 38, pp. 251-259.

Can, M. (2003). Experimental optimization of air jets impinging on a continuously moving flat plate. *Heat and Mass Transfer*, Vol. 39, pp. 509-517.

Çengel, Y. A. and Boles, M. A. (2001). *Thermodynamics: An Engineering Approach, 4th Edition*. McGraw-Hill, New York.

Chance, J.L. (1974). Experimental investigation of air impingement heat transfer under an array of round jets. *Tappi Journal*, Vol. 57, No. 6, pp. 108-112.

Chaniotis, A.K. and Poulikakos, D. (2001). Modeling of continuous and intermittent gas jet impingement and heat transfer on a solid surface. *Proceedings of 2001 ASME International Mechanical Engineering Congress and Exposition*, New York, NY, HTD-Vol. 369-1, pp. 33-39.

Chaniotis, A.K., Poulikakos, D., and Ventikos, Y. (2003). Dual pulsating or steady slot jet cooling of a constant heat flux surface. *Journal of Heat Transfer*, Vol. 125, pp. 575-586.

Chung, Y.M. and Luo, K.H. (2002). Unsteady heat transfer analysis of an impinging jet. *Journal of Heat Transfer*, Vol. 124, pp. 1039-1048.

Clarke, P.H. and Craigen, J.G. (1976). Mathematical model of a pulsating combustor. 6th Thermodynamics and Fluid Mechanics Convention, the Institute of Mechanical Engineers, Paper C56/76, pp. 221-228.

Cokljat, D., Kim, S.E., Iaccarino, G., and Durbin, P.A. (2003). A comparative assessment of the V2F model for recirculating flows. *The 41st Aerospace Sciences Meeting and Exhibit*, Reno, Nevada, AIAA-2003-765.

Coulman, G.A., Vishwanath, P., Alhaddad, A., and Bartram, P.N. (1982). Experimental evaluation of a pulse-combustion computer simulation. In *Proceedings of Symposium on Pulse-Combustion Applications*, Vol. 1, Atlanta, GA., pp. 6-1 to 6-15.

Coussirat, M., van Beeck, J., Mestres, M., Egusquiza, E., Buchlin, J.-M., and Escaler, X. (2005a). Computational fluid dynamics modeling of impinging gas-jet systems: I assessment of eddy viscosity models. Journal of Fluids Engineering, Vol. 127, pp. 691-703.

Coussirat, M., van Beeck, J., Mestres, M., Egusquiza, E., Buchlin, J.-M., and Valero, C. (2005b). Computational fluid dynamics modeling of impinging gas-jet systems: II application to an industrial cooling system device. Journal of Fluids Engineering, Vol. 127, pp. 704-713.

Craft, T.J., Graham, L.J.W., and Launder, B.E. (1993). Impinging jet studies for turbulence model assessment—II an examination of the performance of four turbulence models. *International Journal of Heat and Mass Transfer*, Vol. 36, No. 10, pp. 2685-2697.

Dec, J. E. and Keller J. O. (1986). The effect of fuel burn rate on pulse combustor tail pipe velocities. *International Gas Research Conference*, pp. 498-507.

Dec, J.E. and Keller, J.O. (1989). Pulse combustor tail-pipe heat-transfer dependence on frequency, amplitude, and mean flow rate. *Combustion and Flame*, Vol. 77, pp. 359-374.

Dec, J. E. and Keller, J. O. (1990). Time-resolved gas temperatures in the oscillating turbulent flow of a pulse combustor tail pipe. *Combustion and Flame*, Vol. 80, pp. 358-370.

Dec, J. E., Keller, J. O., and Hongo, I. (1991). Time-resolved velocities and turbulence in the oscillating flow of a pulse combustor tail pipe. *Combustion and Flame,* Vol. 83, pp. 271-292.

Durbin, P.A. (1991). Near-wall turbulence closure modeling without "damping functions." *Theoretical and Computational Fluid Dynamics*, Vol. 3, pp. 1-13.

Durbin, P.A. (1995). Separated flow computations with the k-ε-v^2 model. *AIAA Journal*, Vol. 33, No. 4, pp. 659-664.

Dwyer, H.A., Bramletter, T.T., Keller, J.O., and Sanders, B.R. (1986). A numerical model of a pulse combustor. In *Progress in Astronautics and Aeronautics*, Vol. 105, Dynamics of Reactive Systems Part I: Flames and Configurations, Eds., Bowen J.R., Leyer, J.-C., and Soloukhin, R.I., AIAA, New York, pp. 349-364.

Eibeck, P.A., Keller, J.O., Bramlette, T.T., and Sailor, D.J. (1993). Pulse combustion: impinging jet heat transfer enhancement. *Combustion Science and Technology*, Vol. 94, pp. 147-165.

Erickson, R. and Zinn, B.T. (2002). One-dimensional numerical simulation of a pulse combustor using the linear eddy mixing model. *The 38th AIAA/ASME/SAE/ASEE Joint Propulsion Conference & Exhibit*, Indianapolis, Indiana, AIAA 2002-3718, pp. 1-10.

Etemad, S. and Sundén, B. (2006). Numerical investigation of turbulent heat transfer in a rectangular-sectioned 90° bend. *Numerical Heat Transfer, Part A*, Vol. 49, pp. 323-343.

Fernandes, E.C. and Heitor, M.V. (1996). Unsteady flames and the Rayleigh criterion. In *Unsteady Combustion*, Eds., Culick, F., Heitor, M.V., and Whitelaw, J.H., Kluwer Academic Publishers, Dordrecht, the Netherlands, pp. 1-16.

Fluent Inc. (2003). *FLUENT 6.1* v^2*-f Turbulence Model Manual*.

Fluent Inc. (2006). *FLUENT 6.3 User's Guide*.

Fureby, C. and Lundgren, E. (1993). One-dimensional models for pulsating combustion. *Combustion Science and Technology*, Vol. 94, pp. 337-351.

Garimella, S.V. (2000). Heat transfer and flow fields in confined jet impingement. *Annual Review of Heat Transfer*, Vol. 11, Ed., Tien, C.-L., pp. 413-494.

Gemmen, R.S., Keller, J.O., and Arpaci, V.S. (1993). Heat/mass transfer from a cylinder in the strongly oscillating flow of a pulse combustor tailpipe. *Combustion Science and Technology*, Vol. 94, pp. 103-130.

Gill, B.S. and Bhaduri, D. (1974). An analysis of Helmholtz pulsating combustion systems. *Indian Journal of Technology*, Vol. 12, pp. 151-153.

Gill, B.S. and Bhaduri, D. (1978). Prediction of pressure & frequency in Helmholtz pulsating combustion systems. *Indian Journal of Technology*, Vol. 16, pp. 171-176.

Hanby, V.I. (1969). Convective heat transfer in a gas-fired pulsating combustor. *Journal of Engineering for Power*, Vol. 91, Series A., No. 1, pp. 48-52.

Heikkilä, P. and Milosavljevic, N. (2002). Investigation of impingement heat transfer coefficient at high temperatures. *Drying Technology*, Vol. 20, No. 1, pp. 211-222.

Heikkilä, P. and Milosavljevic, N. (2003). Influence of impingement temperature and nozzle geometry on heat transfer—experimental and theoretical analysis. *Drying Technology*, Vol. 21, No. 10, pp. 1957-1968.

Hill, K.C. (1983). Paper Drying. In *Pulp and Paper Manufacture*, 3rd Edition, Vol. 7, Paper Machine Operations, Ed., Thorp, B.A., TAPPI & CPPA, pp. 282-305.

Huang, P.G., Mujumdar, A.S., and Douglas, W.J.M. (1984). Numerical prediction of fluid flow and heat transfer under a turbulent impinging slot jet with surface motion and crossflow. *ASME Paper* No. 84-WA/HT-33, pp. 1-8.

Hwang, S.D., Lee, C.H., and Cho, H.H. (2001). Heat transfer and flow structures in axisymmetric impinging jet controlled by vortex pairing. *International Journal of Heat and Fluid Flow*, Vol. 22, pp. 293-300.

Iaccarino, G. (2001). Predictions of a turbulent separated flow using commercial CFD codes. *Journal of Fluids Engineering*, Vol. 123, pp. 819-828.

Ibrahim, M.B. and Kochuparambil, B.J. (2005). CFD for jet impingement heat transfer with single jets and arrays. In *Proceedings of ASME Turbo Expo 2005: Power for Land, Sea and Air*, Reno-Tahoe, Nevada, pp. 1-15.

Incropera, F.P. and DeWitt, D.P. (2002). *Fundamentals of Heat and Mass Transfer*, 5th Edition, Wiley, New York.

Johansson, B.J. (2005). New revolutionary impingement dryer suitable for all grades. *Pulp & Paper*, Vol. 79, No. 7, pp. 40-42.

Juppi, K. and Kaihovirta, J. (2000). Impingement drying of printing papers at elevated temperatures. Tappi Engineering Conference, Atlanta, GA.

Kataoka, K., Sahara, R., Ase, H., and Harada, T. (1987a). Role of large-scale coherent structures in impinging jet heat transfer. *Journal of Chemical Engineering of Japan*, Vol. 20, No. 1, pp. 71-76.

Kataoka, K., Suguro, M., Degawa, H., Maruo, K., and Mihata, I. (1987b). The effect of surface renewal due to large-scale eddies on jet impingement heat transfer. *International Journal of Heat and Mass Transfer*, Vol. 30, No. 3, pp. 559-567.

Keller, J. O., Barr, P. K., Bramlette, T. T., Evens, L. J., and Marchant, R. N. (1989). Pulse combustion: demonstration of the characteristic mixing time in a commercial burner. *Combustion Science and Technology*, Vol. 66, pp. 127-137.

Keller, J.O., Gemmen, R.S., and Barr, P.K. (1990). Premixed combustion in an oscillating/resonant flow field part I: experimental investigation. *ASME Advanced Energy System Division*, Vol. 16, Thermal-Physical Aspects of Energy Conversion, pp. 1-22.

Keller, J.O., Eibeck, P.A., Bramlette, T.T., and Barr, P.K. (1993). Pulse combustion: tailpipe exit jet characteristics. *Combustion Science and Technology*, Vol. 94, pp. 167-192.

Kinstrey, R.B. and White, D. (2006). *Pulp and Paper Industry Energy Bandwidth Study*, Report for American Institute of Chemical Engineers and the Department of Energy's Industrial Technologies Program, Project No. 16CX8700.

Kudra, T. and Mujumdar, A.S. (2002). *Advanced Drying Technologies*. Marcel Dekker Inc., New York.

Kudra, T., Benali, M., and Zbicinski, I. (2003). Pulse combustion drying: aerodynamics, heat transfer, and drying kinetics. *Drying Technology*, Vol. 21, No. 4, pp. 629-655.

Kuhasalo, A., Niskanen, J., Paltakari, J., and Karlsson, M. (2000). Introduction to paper drying and principles and structure of a dryer section. In *Papermaking, Part 2, Drying*, Ed., Karlsson, M., Fapet Oy, Helsinki, Finland, pp. 14-53.

Lalwani, P.C., Das, K.L., Bhattacharyya, T.K., and Bhaduri, D. (1979). Heat transfer characteristics of a pulsating combustion system. *Mechanical Engineering Bulletin*, Vol. 10, No. 1 & 2, pp. 7-11.

Laurence, D.R., Uribe, J.C., and Utyuzhnikov, S.V. (2004). A robust formulation of the v2-f model. *Flow, Turbulence and Combustion*, Vol. 73, pp. 169-185.

Lee, D.H., Song, J., and Jo, M.C. (2004). The effects of nozzle diameter on impinging jet heat transfer and fluid flow. *Journal of Heat Transfer*, Vol. 126, pp. 554-557.

Lee, J.H., Dhar, B., and Soedel, W. (1985). A mathematical model of low amplitude pulse combustion systems using a Helmholtz resonator-type approach. *Journal of Sound and Vibration*, Vol. 98, No. 3, pp. 379-401.

Li, S. (2005). A numerical study of micro synthetic jet and its applications in thermal management. *Ph.D. Thesis*, the School of Mechanical Engineering, the Georgia Institute of Technology, Atlanta, Georgia.

Lien, F.-S. and Kalitzin, G. (2001). Computations of transonic flow with the v^2-f turbulence model. *International Journal of Heat and Fluid Flow*, Vol. 22, pp. 53-61.

Liewkongsataporn, W. (2006). Characteristics of pulsating flows in a pulse combustor tailpipe. *Master Thesis*, the School of Mechanical Engineering, the Georgia Institute of Technology, Atlanta, Georgia.

Liewkongsataporn, W., Patterson, T., Ahrens, F., and Loughran, J. (2006a). Impingement drying enhancement using a pulsating jet. In *Proceedings of the 15th International Drying Symposium*, Budapest, Hungary, pp. 939-945.

Liewkongsataporn, W., Patterson, T., and Ahrens, F. (2006b). A numerical study of axisymmetric pulsating jet impingement heat transfer. *The 13th International Heat Transfer Conference*, Sydney, Australia, JET-14.

Liu, X.D., Cao, C.W., and Lang, Z.H. (2001). Heat transfer between materials and unsteady airflow from a Helmholtz type combustor. *Drying Technology*, Vol. 19, No. 8, pp. 1939-1948.

Martin, H. (1977). Heat and mass transfer between impinging gas jets and solid surfaces. In *Advances in Heat Transfer*, *13*. Hartnett, J.P., and Irvine Jr., T.F., Eds., Academic Press, New York, pp. 1-60.

Meola, C., de Luca, L., and Carlomagno, G.M. (1996). Influence of shear layer dynamics on impingement heat transfer. *Experimental Thermal and Fluid Science*, Vol. 13, pp. 29-37.

Menter, F. R. (1994). Two-equation eddy-viscosity turbulence models for engineering applications. *AIAA Journal*, Vol. 32, No. 8, pp. 1598-1605.

Mladin, E.C. and Zumbrunnen, D.A. (1995). Dependence of heat transfer to a pulsating stagnation flow on pulse characteristics. *Journal of Thermophysics and Heat Transfer*, Vol. 9, No. 1, pp. 181-192.

Mladin, E.C. and Zumbrunnen, D.A. (1997). Local convective heat transfer to submerged pulsating jets. *International Journal of Heat and Mass Transfer*, Vol. 40, No. 14, pp. 3305-3321.

Mladin, E.C. and Zumbrunnen, D.A. (2000). Alterations to coherent flow structures and heat transfer due to pulsations in an impinging air-jet. *International Journal of Thermal Sciences*, Vol. 39, pp. 236-248.

Möller, S.-I. and Lindholm, A. (1999). Theoretical and experimental investigation of the operating characteristics of a Helmholtz type pulse combustor due to changes in the inlet geometry. *Combustion Science and Technology*, Vol. 149, pp. 389-406.

Narayanan, V., Seyed-Yagoobi, J., and Page, R.H. (2004). An experimental study of fluid mechanics and heat transfer in an impinging slot jet flow. *International Journal of Heat and Mass Transfer*, Vol. 47, pp. 1827-1845.

Narayanaswami, L. and Richards, G.A. (1996). Pressure-gain combustion: part I–model development. *Journal of Engineering for Gas Turbines and Power*, Vol. 118, pp. 461-468.

Neumeier, Y. (1993). Frequency domain analysis of a gas fired mechanically valved pulse combustor. *Ph.D. Thesis*, the School of Aerospace Engineering, the Georgia Institute of Technology, Atlanta, Georgia.

Nevins, R.G. and Ball, H.D. (1961). Heat transfer between a flat plate and a pulsating impinging jet. In *Proceedings of the 1961-1962 Heat Transfer Conference*, pp. 510-516.

Nomura, T., Nishimura, N., Hyodo, T., Tago, Y., Hasebe, H., and Kashiwagi, T. (1989). Heat and mass transfer characteristics of pulse-combustion drying process. In *Drying '89*, Ed., Mujumdar, A.S., pp. 534-549.

Parneix, S., Durbin, P.A., and Behnia, M. (1998). Computation of 3-D turbulent boundary layers using the V2F model. *Flow, Turbulence and Combustion*, Vol. 60, pp. 19-46.

Patterson, T., Ahrens, F., and Stipp, G. (2003). High performance impingement paper drying using pulse combustion technology. *TAPPI Engineering Conference*, Chicago, Illinois.

Pavlova, A. and Amitay, M. (2006). Electronic cooling using synthetic jet impingement. *Journal of Heat Transfer*, Vol. 128, pp. 897-907.

Perry, E.H. and Culick, F.E.C. (1974). Measurements of wall heat transfer in the presence of large-amplitude combustion-driven oscillations. *Combustion Science and Technology*, Vol. 9, pp. 49-53.

Pikulik, I.I., Poirier, N.A., and Sadeghi, M. (2006). Papridry™, a novel and rapid technique for paper drying. In *Proceedings of the 15th International Drying Symposium*, Budapest, Hungary, pp. 963-970.

Poh, H.J., Kumar, K., and Mujumdar, A.S. (2005). Heat transfer from a pulsed laminar impinging jet. *International Communications in Heat and Mass Transfer*, Vol. 32, pp. 1317-1324.

Polat, S., Huang, B., Mujumdar, A.S., and Douglas, W.J.M. (1989). Numerical flow and heat transfer under impinging jets: a review. *Annual Review of Numerical Fluid Mechanics and Heat Transfer*, Vol. 2., Eds., Chawla, T.C. and Tien, C.-L., pp. 157-197.

Polat, S. and Douglas, W.J.M. (1990). Heat transfer under multiple slot jets impinging on a permeable moving surface. *AIChE Journal*, Vol. 36, No. 9, pp. 1370-1378.

Polat, S., Mujumdar, A.S., Douglas, W.J.M. (1991a). Impingement heat transfer under a confined slot jet, part I: effect of surface throughflow. *The Canadian Journal of Chemical Engineering*, Vol. 69, pp. 266-273.

Polat, S., Mujumdar, A.S., Douglas, W.J.M. (1991b). Impingement heat transfer under a confined slot jet, part II: effects of surface motion and throughflow. *The Canadian Journal of Chemical Engineering*, Vol. 69, pp. 274-280.

Polat, S. (1993). Heat and mass transfer in impingement drying. *Drying Technology*, Vol. 11, No. 6, pp. 1147-1176.

Popiel, C.O. and Trass, O. (1991). Visualization of a free and impinging round jet. *Experimental Thermal and Fluid Science*, Vol. 4, pp. 253-264.

Psimas, M.J., Patterson, T., Ahrens, F., and Loughran, J. (2007). Heat transfer comparison of pulsating and steady flow jets. In *Proceedings of the 5th Asia-Pacific Drying Conference*, Vol. 2, Hong Kong, China, pp. 1243-1248.

Putnam, A.A., Belles, F.E., and Kentfield, J.A.C. (1986). Pulse combustion. *Progress in Energy and Combustion Science*, Vol. 12, No. 1, pp. 43-79.

Lord Rayleigh, J.W.S. (1945). Theory of resonators. In *The Theory of Sound*, Volume II, 2nd Edition (1st American Edition), Dover, New York.

Reuter, D., Daniel, B.R., Jagoda, J., and Zinn, B.T. (1986). Periodic mixing and combustion processes in gas fired pulsating combustors. *Combustion and Flame*, Vol. 65, pp. 281-290.

Richards, G.A. and Gemmen, R.S. (1996). Pressure-gain combustion: part II– experimental and model results. *Journal of Engineering for Gas Turbines and Power*, Vol. 118, pp. 469-473.

Saad, N.R., Polat, S., and Douglas, W.J.M. (1992). Confined multiple impinging slot jets without crossflow effects. *International Journal of Heat and Fluid Flow*, Vol. 13, No. 1, pp. 2-14.

Sailor, D.J., Rohli, D.J., and Fu, Q. (1999). Effect of variable duty cycle flow pulsations on heat transfer enhancement for an impinging air jet. *International Journal of Heat and Fluid Flow*, Vol. 20, pp. 574-580.

Scotti, A. and Piomelli, U. (2002). Turbulence models in pulsating flows. AIAA Journal, Vol. 40, No. 3, pp. 537-544.

Sheriff, H.S. and Zumbrunnen, D.A. (1999). Local and instantaneous heat transfer characteristics of arrays of pulsating jets. *Journal of Heat Transfer*, Vol. 121, pp. 341-348.

Shi, Y., Ray, M.B., and Mujumdar, A.S. (2002). Computational study of impingement heat transfer under a turbulent slot jet. *Industrial & Engineering Chemistry Research*, Vol. 41, pp. 4643-4651.

Smith, B.L. and Glezer, A. (1998). The formation and evolution of synthetics jets. *Physics of Fluids*, Vol. 10, No. 9, pp. 2281-2297.

Sundqvist, H. and Kiiskinen, H. (2000). Air impingement drying. In *Papermaking, Part 2, Drying*, Ed., Karlsson, M., Fapet Oy, Helsinki, Finland, pp. 126-144.

Tajiri, K. and Menon, S. (2001). LES of combustion dynamics in a pulse combustor. *The 39th AIAA Aerospace Sciences Meeting & Exhibit*, Reno, NV, AIAA Paper 2001-0194, pp. 1-13.

Tang, Y.M. (1993). An experimental investigation of the operation of a Helmholtz pulse combustor. *Ph.D. Thesis*, the School of Aerospace Engineering, the Georgia Institute of Technology, Atlanta, Georgia.

Tang, Y.M., Waldherr, G., Jagoda, J.I., and Zinn, B.T. (1995). Heat release timing in a nonpremixed Helmholtz pulse combustor. *Combustion and Flame*, Vol. 100, pp. 251-261.

Trávníček, Z. and Vít, T. (2006). Hybrid synthetic jet intended for enhanced jet impingement heat/mass transfer. *The 13th International Heat Transfer Conference*, Sydney, Australia.

Viskanta, R. (1993). Heat transfer to impinging isothermal gas and flame jets. *Experimental Thermal and Fluid Science*, Vol. 6, pp. 111-134.

Wang, S.J. and Mujumdar, A.S. (2005). A comparative study of five low Reynolds number k-ε models for impingement heat transfer. *Applied Thermal Engineering*, Vol. 25, pp. 31-44.

Wedel, G.L. (1979). Air impingement heat transfer. *TAPPI Engineering Conference*, Vol. 3, pp. 513-519.

Wilcox, D. C. (1994). *Turbulence Modeling for CFD*, DCW Industries, La Cañada, CA.

Wu, Z.H. and Mujumdar, A.S. (2006). R&D needs and opportunities in pulse combustion and pulse combustion drying. *Drying Technology*, Vol. 24, No. 11, pp. 1521-1523.

Wu, Z.H., Mujumdar, A.S., Liu, X.D., and Yang, L. (2006). Pulse combustion impingement to enhance paper drying. *The 15th International Drying Symposium*, Budapest, Hungary.

Wu, Z.H. (2007) Mathematical modeling of pulse combustion and its applications to innovative thermal drying techniques. *Ph.D. Thesis*, the Department of Mechanical Engineering, the National University of Singapore, Singapore.

Yan, X.T. and Saravanan, Y. (2004). Numerical analysis of local heat transfer from a flat plate to a pair of circular air impinging jets. In *Proceedings of 2004 ASME International Mechanical Engineering Congress*, Anaheim, CA, pp. 629-644.

Zbicinski, I., Smucerowicz, I., Strumillo, C., Kasznia, J., and Stawczyk, J. (1998). Experimental investigations on pulse combustion drying process. In *Proceedings of the 11th International Drying Symposium*, Vol. C, Halkidiki, Greece, pp. 1960-1966.

Zinn, B.T. (1996). Pulse combustion applications: past, present and future. In *Unsteady Combustion*, Eds., Culick, F., Heitor, M.V., and Whitelaw, J.H., Kluwer Academic Publishers, Dordrecht, the Netherlands, pp. 113-137.

Zuckerman, N. and Lior, N. (2005). Impingement heat transfer: correlations and numerical modeling. *Journal of Heat Transfer*, Vol. 127, pp. 544-552.

Zumbrunnen, D.A. and Aziz, M. (1993). Convective heat transfer enhancement due to intermittency in an impinging jet. *Journal of Heat Transfer*, Vol. 115, pp. 91-98.